

New solid proton conductors:
Functionalized mesoporous SiO₂ materials
for application in high temperature PEM
fuel cell membranes

Von der Naturwissenschaftlichen Fakultät der
Gottfried Wilhelm Leibniz Universität Hannover
zur Erlangung des Grades

Doktor der Naturwissenschaften
- Dr. rer. nat. -

genehmigte Dissertation
von

Dipl.-Chem. Roland Marschall

geboren am 24.05.1980 in Hannover

2008

Referent: Prof. Dr. Jürgen Caro
Korreferent: Prof. Dr. Josef-Christian Buhl
Tag der Promotion: 04.06.2008

Für meine Eltern

(...) „Jawohl mit Wasser“, sagte Cyrus Smith, „mit Wasser, das durch elektrischen Strom zerlegt worden ist. **In jener Zeit wird die Elektroenergie ungeahnte Möglichkeiten eröffnet haben**, es ist überhaupt einzigartig, wie sich die verschiedensten Erfindungen durch geheimnisvolle Übereinstimmung immer wieder ergänzen. **Die so zerlegten Elemente des Wassers, Wasserstoff und Sauerstoff, werden auf unabsehbare Zeit hinaus die Energieversorgung der Erde sichern.** Eines Tages werden Dampfer und Lokomotiven keine Kohlebunker mehr führen, sondern Gastanks, aus denen komprimierte Gase durch Rohre in die Heizkessel strömen. **Das Wasser ist die Kohle der Zukunft.**“(...)

Jules Verne, Die geheimnisvolle Insel (1874).

Erklärung

Hierdurch erkläre ich, dass ich die Dissertation „New solid proton conductors: Functionalized mesoporous SiO₂ materials for application in high temperature PEM fuel cell membranes“ als Mitarbeiter des Instituts für Physikalische Chemie und Elektrochemie der Gottfried Wilhelm Leibniz Universität Hannover selbstständig verfasst und alle benutzten Hilfsmittel sowie evtl. zur Hilfeleistung herangezogene Institutionen vollständig angegeben habe.

Die Dissertation wurde nicht schon als Diplom- oder ähnliche Prüfungsarbeit verwendet.

Hannover, 07.04.2008
Dipl.-Chem. Roland Marschall

Danksagung

An dieser Stelle möchte ich mich bei allen ganz herzlich bedanken, die zum Gelingen dieser Arbeit beigetragen haben.

Zuerst möchte ich mich natürlich bei Prof. Dr. Michael Wark für die sehr gute Betreuung meiner Doktorarbeit in den letzten drei Jahren bedanken, vor allem, weil er mich jederzeit in allen Belangen unterstützt hat, und mich durch kritisches Hinterfragen und Motivieren, aber auch durch beruhigende Gespräche zur rechten Zeit immer wieder auf das Wichtige fokussiert hat.

Natürlich danke ich auch Prof. Dr. Jürgen Caro, in dessen Arbeitsgruppe ich nach meiner Diplomarbeit nun auch meine Doktorarbeit anfertigen durfte, und der immer ein offenes Ohr für fachliche Diskussionen und Anregungen für meine Arbeit hatte.

Prof. Dr. Josef-Christian Buhl danke ich für die sehr gute Betreuung im Rahmen des Promotionsprogramms des ZFM während der letzten drei Jahre, und für die Anfertigung des Gutachtens zu meiner Arbeit.

Des Weiteren bedanke ich mich bei Prof. Dr. Max Lu von der University of Queensland, der mir die Gelegenheit gab, bei meinem Forschungsaufenthalt in Brisbane drei wundervolle Monate im faszinierenden Australien zu verbringen. Diese Zeit hat mir in vielerlei Hinsicht die Augen geöffnet, und ich bin unglaublich dankbar für diese einmalige Erfahrung. Natürlich danke ich auch Dr. Lianzhou Wang für die wissenschaftliche Betreuung während meiner Zeit in Brisbane.

Außerdem danke ich Dr. Jiří Rathouský vom J. Heyrovský Institut für Physikalische Chemie in Prag für die jederzeit gute Zusammenarbeit, auch während meines Forschungsaufenthalts.

Natürlich möchte ich mich bei meinen Kooperationspartnern aus dem DFG-SPP 1181 für die Zusammenarbeit bedanken, bei Prof. Dr. Georg Grathwohl, Dr. Dietmar Koch, Dr. Michael Jeske und Dr. Michaela Wilhelm vom Institut für Keramische Materialien und Komponenten der Universität Bremen für die Bereitstellung der Polysiloxane zur Fertigung von Kompositmembranen, und bei Prof. Dr. Thomas Frauenheim, Dr. Christof Köhler, Dr. Welch L. Cavalcanti und Pia Tölle vom BCCMS der Uni Bremen für die theoretisch-chemischen Berechnungen.

Dr. Dominique Gomes und Dr. Suzana P. Nunes vom GKSS in Geesthacht danke ich für die gute Zusammenarbeit bei der Herstellung der Kompositmembranen mit den zur Verfügung gestellten Polyoxadiazolen.

Birgit Beiße, Songül Noyun und Falk Heinroth vom Institut für Anorganische Chemie der Leibniz Universität Hannover danke ich für die Unterstützung bei IR-, TG- und Stickstoffadsorptionsmessungen.

Dr. Armin Feldhoff und Frank Steinbach danke ich für die Hilfe in allen Fragen zu REM und TEM, für Probenpräparation, und für TEM-Messungen.

Ganz besonders möchte ich mich bei Inga Bannat, Britta Seelandt und Katrin Wessels bedanken; für die gemeinsame Zeit in Labor und Büro, für die langen Sitzungen am TEM und die tollen Bilder, für die vielen gemeinsamen Tagungserlebnisse, aber auch einfach für die Unterstützung und die passenden Motivationsschübe zur richtigen Zeit.

Weiterhin möchte ich mich bei allen weiteren Mitarbeitern des Arbeitskreises für die Hilfsbereitschaft bedanken, bei Mirko Arnold, Daniel Albrecht, Cathrin Boeckler, Christian Dunkel, Stefan Frisch, Yvonne Gabbey-Uebe, Kerstin Janze, Julia-Maria Martynczuk, Melanie Minnermann, Torsten Oekermann, Yvonne Selk, Monir Sharifi, Sven Wiebcke und Viktor Yarovyj.

Des Weiteren gilt mein Dank den Mitarbeitern sowohl der Elektronikwerkstatt als auch der mechanischen Werkstatt für ihre Tatkraft und Hilfe.

Für die finanzielle Unterstützung danke ich dem Land Niedersachsen und dem Ministerium für Wissenschaft und Kultur für die Förderung durch ein Georg-Christoph-Lichtenberg-Stipendium.

Schließlich danke ich ganz herzlich meinen Eltern, denen ich diese Arbeit widme, für die ununterbrochene Unterstützung während des Studiums und der Doktorarbeit, die zu jeder Zeit immer ein offenes Ohr für meine Probleme hatten und für mich da waren. Genau wie meine besten Freunde Hendrik und Dennis und meine Freundin Welchy, die während der letzten Jahre alle viel Geduld mit mir haben mussten, aber sich nie beschwert haben.

Zusammenfassung

Für die Erhöhung der Betriebstemperatur von Polymer-Elektrolyt-Membran (PEM) Brennstoffzellen werden alternative Membransysteme gesucht, die bei einer Temperatur von 140 bis 180 °C arbeiten, dabei eine hohe Protonenleitfähigkeit zeigen und außerdem bei möglichst geringer Befeuchtung arbeiten. Vorteile der Erhöhung der Betriebstemperatur von diesen PEM Brennstoffzellen sind ein Wegfall von Befeuchtungssystemen, eine verbesserte Elektrodenkinetik und eine erhöhte Toleranz des für den Betrieb notwendigen Elektrokatalysators gegenüber Kohlenstoffmonoxid-Vergiftung. Ein Forschungszweig in der Untersuchung neuer PEMs ist die Herstellung von Kompositmembranen. Kompositmembranen bestehen meist aus einem protonenleitfähigen Polymer, dessen Eigenschaften (Protonenleitfähigkeit, mechanische Stabilität, thermische Stabilität, Wasseraufnahme und -rückhalt) durch den Einbau anorganischer Additive verbessert werden. Durch die gezielte Synthese dieser Additive können die Eigenschaften der Kompositmembranen eingestellt werden.

In dieser Arbeit wird über die Synthese neuartiger Festkörper-Protonenleiter auf Basis von mesoporösen SiO₂ - Materialien berichtet, welche anschließend in verschiedenartige Polymere eingebettet werden, um neue Kompositmembransysteme herzustellen. Der Fokus dieser Arbeit liegt dabei deutlich auf der Synthese der Additive. Mesoporöse SiO₂ - Materialien werden mit unterschiedlichen Porensystemen, Porendurchmessern und Partikelgrößen synthetisiert. Damit diese Materialien protonenleitfähig werden, wird die extrem hohe innere Oberfläche dieser Materialien mit Alkoxysilanen funktionalisiert, deren funktionelle Endgruppen anschließend in hydrophile, protonenleitende Gruppen umgewandelt werden. Beispiele derartiger Gruppen sind u. a. Sulfonsäure (SO₃H), Phosphonsäure (PO₃H₂) und Imidazol.

Neben der ausführlichen strukturellen Charakterisierung dieser neuartigen Systeme wird die Protonenleitfähigkeit der synthetisierten organisch-anorganischen Hybride mittels Impedanzspektroskopie ermittelt. Die kleinen Porendurchmesser des Si-MCM-41-Wirtsmaterials (ca. 3 nm) erwiesen sich als vorteilhaft für hohe Protonenleitung. Bei den unterschiedlichen funktionellen Gruppen zeigten SO₃H funktionalisierte Materialien die höchsten Protonenleitfähigkeiten. Die relative Feuchtigkeit (RH) und die Dichte der funktionellen Gruppen, d.h. die Beladung mit protonenleitfähigen organischen Resten, haben ebenso einen entscheidenden Einfluss auf die Protonenleitung wie die Partikelgrößen. In Einklang mit theoretisch-chemischen Berechnungen wurden die besten Ergebnisse dabei für SO₃H funktionalisiertes Si-MCM-41 gefunden, welches bei hoher Beladung und 100 % RH eine extrem hohe Protonenleitfähigkeit für einen Festkörper-Protonenleiter von 0.2 S/cm erzielte.

Die synthetisierten Festkörper-Protonenleiter wurden in unterschiedliche Polymere (Nafion[®], Polysiloxan und Polyoxadiazol) eingebettet. Die hergestellten Additive haben einen entscheidenden positiven Einfluss auf die Eigenschaften der resultierenden Kompositmembranen. Durch eine sehr gute Verteilung der Additive in den jeweiligen Polymeren ohne jegliche Segregation konnten eine erhöhte Protonenleitfähigkeit, auch bei Temperaturen weit oberhalb 100 °C und bei geringer Feuchtigkeit bis zu 5 % RH, verbesserter Wasserrückhalt und eine Steigerung in mechanischer und thermischer Stabilität erzielt werden.

SCHLAGWORTE: Brennstoffzellen, mesoporöse Materialien, Protonenleitfähigkeit

Abstract

For increasing the working temperature of polymer electrolyte membrane (PEM) fuel cells, alternative membrane systems are under investigation, working at temperatures from 140 to 180 °C, under low relative humidity (RH) conditions and, nevertheless, showing high proton conductivities. Advantages of higher working temperatures of PEM fuel cells are the abolition of humidification systems, improved electrode kinetics and higher tolerance of the for operation required electro catalyst against carbon monoxide poisoning. One area of research in the investigation of PEMs is the development of composite membranes. Composite membranes mostly consist of a proton conductive polymer, whose properties (proton conductivity, mechanical stability, thermal stability, water uptake and water retention) are improved by the incorporation of inorganic additives. Via specific synthesis of these additives, the properties of the composite membranes can be tailored.

In this work, the synthesis of new solid proton conductors based on mesoporous SiO₂ materials is reported, which are subsequently incorporated into different polymers to fabricate new composite membranes.

The focus of this work clearly lies on the synthesis of the additives. Mesoporous SiO₂ materials are synthesized with different pore systems, different pore sizes and different particle sizes. For enabling proton conductivity in these materials, the very high internal surface of these materials is functionalized with alkoxy silanes, whose functional end groups are subsequently converted into hydrophilic, proton conductive groups. Examples for such groups are sulfonic acid (SO₃H), phosphonic acid (PO₃H₂) and imidazole.

Besides the detailed structural characterization of these novel systems, the proton conductivities of the synthesized organic-inorganic hybrids are determined via impedance spectroscopy. The small pore diameter of Si-MCM-41 host material (approx. 3 nm) is proved to be advantageous for high proton conductivity. In the different functional groups, SO₃H functionalized materials showed the highest proton conductivities. The RH and the density of functional groups, meaning the loading with proton conductive organic rests, have as well a crucial influence on the proton conductivity as the particle sizes. In accordance to theoretical-chemical calculations, the best results thereby were found for SO₃H functionalized Si-MCM-41, which achieved at high loading and 100 % RH an extreme high proton conductivity for a solid proton conductor of 0.2 S/cm.

The synthesized solid proton conductors were imbedded into different polymers (Nafion[®], polysiloxane and polyoxadiazole). The synthesized additives have an essential positive influence on the properties of the resulting composite membranes. Via a very good distribution of the additives in the respective polymers without any segregation, increased proton conductivities, even at temperatures highly above 100 °C and under low humidification down to 5 % RH, improved water retention and enhanced mechanical and thermal stability could be achieved.

KEYWORDS: fuel cells, mesoporous materials, proton conductivity

Table of Contents

1 INTRODUCTION	1
2 FUNDAMENTALS	5
2.1 The Fuel Cell	5
2.1.1 History	6
2.1.2 Fuel Cell Principles	9
2.1.3 PEMFC and DMFC	12
2.1.4 Thermodynamics and kinetics of H ₂ /O ₂ fuel cells.....	16
2.1.4 Proton conductive polymer membranes for PEMFCs.....	21
2.1.5 Proton conductivity mechanisms.....	26
2.1.6 Membrane improvements with additives	30
2.2 Mesoporous SiO ₂ materials	32
2.2.1 Amphiphilic molecules.....	33
2.2.2 Micellar structures and self-assembly	36
2.2.3 Nanoporous silica materials, M41S and SBA	39
2.2.4 Formation processes of mesoporous materials.....	47
2.2.5 Detemplation and surface properties of amorphous silica.....	51
2.2.6 Surface functionalization of mesoporous silica: grafting and co-condensation	55
3 EXPERIMENTAL	61
3.1 Analytical methods	61
3.1.1 Impedance spectroscopy	62
3.1.2 X-ray diffractometry	71
3.1.3 Infrared spectroscopy	73
3.1.4 Sorption measurements	75
3.1.5 Electron microscopy	78
3.1.6 Electron-dispersive X-ray spectroscopy and electron energy-loss spectroscopy	83

Table of Contents

3.1.7 Thermal analysis.....	85
3.1.8 Computational modeling	86
3.1.9 Ion exchange capacities	88
3.2 Syntheses	89
3.2.1 Synthesis of pristine mesoporous silica hosts	90
3.2.2 Functionalization of mesoporous silica hosts via grafting	91
3.2.3 Functionalization via co-condensation	93
3.2.4 Thiol-oxidation to SO ₃ H.....	95
3.2.5 Imidazole anchorage/formation processes.....	96
3.2.6 Phosphonic acid formation	101
4 RESULTS	103
4.1 Pristine mesoporous silica	103
4.1.1 Si-MCM-41 via homogeneous precipitation	103
4.1.2 Si-SBA-15	109
4.1.3 Si-SBA-16	113
4.1.4 Si-MCM-41 nanoparticles	116
4.1.5 Silica host summary	120
4.2 Functionalization via grafting.....	121
4.2.1 Functionalization of mesoporous silica with SO ₃ H groups via grafting	121
4.2.2 Proton conductivity of grafted SO ₃ H functionalized silica materials.....	128
4.2.3 N-Imidazole functionalization of Si-MCM-41 via grafting	139
4.2.4 Imidazole functionalization of Si-MCM-41 via grafting and peptide bonding	145
4.2.5 Imidazole functionalization of Si-MCM-41 via grafting and in-situ formation	149
4.2.6 Summary of grafting results	155
4.3 Functionalization via co-condensation	157
4.3.1 Functionalization of mesoporous silica with SO ₃ H groups via co-condensation	158
4.3.2 Functionalization of mesoporous silica with PO ₃ H ₂ groups via co-condensation	170
4.3.3 Functionalization of mesoporous silica with imidazole groups via co-condensation	173
4.3.4 Summary on proton conductivities of functionalized Si-MCM-41 materials synthesized via co-condensation	176
4.3.5 Mesoporous Si-MCM-41 nanoparticles functionalized with SO ₃ H groups via co-condensation	178
4.4 Composite membranes containing SO₃H functionalized Si-MCM-41 particles....	189
4.4.1 Composite membranes and MEAs with polysiloxanes	189

4.4.2 Composite membranes with polyoxadiazole.....	198
4.4.3 Composite membranes with Nafion [®]	203
4.4.4 Summary of composite membranes containing SO ₃ H functionalized Si-MCM-41 particles.....	207
5 CONCLUSION.....	209
APPENDIX.....	215
A Abbreviations and Symbols.....	215
B Table of figures.....	219
C Tables.....	226
D Chemicals.....	227
E Publications arisen from this work.....	228
Journal Publications.....	228
Posters.....	230
Talks on Conferences.....	231
F Curriculum vitae.....	232

1 Introduction

The world population is increasing with dramatic velocity. With the actual tendency, the world population will reach 9 billion people in 2050. But with an increasing number of people, the demand for energy simultaneously increases. In contrast, our supplies of non-renewable fossil fuels are running out. Human kind is therefore searching for new ways of energy generation, to fulfill its need for comfort and mobility, and to overcome this kind of energy crisis. Along with that, this new way of energy generation must be an environmental friendly technique, due to the fact that our environment is already highly polluted. The growing ozone hole, rising sea levels and other climate change phenomena show us in an unfriendly way that nature can not tolerate more careless treatment from human beings. Therefore, the production of coke, nitrogen oxides and carbon dioxides must be reduced. This must happen not only forced by political restrictions, but voluntarily in every country.

Solar and wind energy technologies are two alternative and promising technologies to use natural energy for transforming it into electrical energy for our households in an environmentally friendly way. These techniques can also be used to produce clean hydrogen for another interesting application. A very clean possibility exists to convert chemical energy into electrical energy, namely via the reaction of hydrogen with oxygen to water, in a special reaction assembly. This assembly is called a fuel cell.

In general, a fuel cell consists of two electrodes, which are separated via an electrolyte (solid/liquid). This electrolyte has to be gas-tight, and electrons generated at the anode

can be used to generate electrical work. One area of fuel cell research is focused on the improvement of proton exchange membrane (PEM, also: polymer electrolyte membrane) fuel cells. Actual PEM fuel cells are working at temperatures around 80 °C, and are mostly designed for small electrical devices and mobile applications, e.g. for service equipments in cars as auxiliary power units (APU). The working principle is simple: hydrogen is oxidized at the electrode surface to protons, which diffuse through the electrolyte membrane from the anode to the cathode, while the generated electrons reach via an electrical outer circuit the cathode side, where they react with oxygen and the protons to water. So, the electrode-separating electrolyte membrane must be a proton conductor, but should not conduct electrons, and has to separate the gases.

The most often used membrane material for PEM fuel cells is Nafion[®]. It consists of a hydrophobic fluorocarbon polymer backbone with grafted hydrophilic side chains with very acidic sulfonic acid (SO₃H) end groups. The SO₃H groups are required for the proton conductivity as well as for the attachment of water molecules. Nafion[®] membranes in fuel cells can reach proton conductivities of 0.2 S/cm at 80 °C in water-rich environments of 100% relative humidity (RH).¹ Unfortunately, 80 °C is the highest working temperature for Nafion[®], because it cannot keep water inside the pores at higher temperatures, and the structure is destroyed.² But water is needed for the proton conduction mechanisms occurring in this material.^{3,4}

The goal of this work is to develop new solid proton conductors as additives for polymer membranes for PEM fuel cells working at elevated temperatures, namely 140 to 180 °C. The increased working temperature brings several advantages: higher CO tolerance towards catalyst poisoning⁵, facilitated cooling devices for the fuel cell, better electrode kinetics for higher efficiencies, and higher efficiency due to gaseous and non-

¹ M. Hogarth, X. Glipa, ETSU Technical Report F/02/00189/REP, 2001.

² M. Elkerling, A. A. Kornyshev, U. Stimming, *J. Phys. Chem. B* 101 (1997) 10807.

³ C.J.T. de Grotthuss, *Ann. Chim.* 58 (1806) 54.

⁴ K. D. Kreuer, W. Weppner, A. Rabenau, *Angew. Chem. Int. Ed.* 21 (1982) 208.

⁵ Q. Li, R. He, J.O. Jensen, N. J. Bjerrum, *Chem. Mater.* 15 (2003) 4896.

liquid water.⁶ Especially the automotive industry is becoming more and more interested in high-temperature PEM fuel cells (HT-PEMFC).

For this reason, the synthesis of new solid proton conductors as additives for proton conductive polymers comes to the fore. For achieving a better water uptake, higher water retention, higher mechanical stability and throughout higher proton conductivity, organic polymers are often modified by incorporation of hydrophilic inorganic fillers and/or inorganic proton conductors, like heteropolyacids^{7,8,9}, solid boron phosphates^{10,11}, zirconium oxides and phosphates^{12,13}, SiO₂ particles^{14,15,16,17,18}, TiO₂^{19,20} or zeolite mordenite²¹, to prepare composite membranes for proton conduction.

This work presents new solid proton conductors basing on highly ordered mesoporous SiO₂ materials. These kind of materials were synthesized for the first time in 1992 from scientists of the Mobil Research and Development Corporation^{22,23}, called the M41S-materials. Depending on the synthesis conditions (e.g. the template), they showed huge surface areas of more than 1000 m²/g. Beck *et al.* used for their synthesis the self-

⁶ K. Ledjeff-Hey, F. Mahlendorf, J. Roes, *Brennstoffzellen – Entwicklung, Technologie, Anwendung*, 2nd Edition, C. F. Müller Verlag, Heidelberg, 2001.

⁷ Y.S. Kim, F. Wang, M. Hickner, T.A. Zawodzinski, J.E. McGrath, *J. Membr. Sci.* 212 (2003) 263.

⁸ S.M.J. Zaidi, S.D. Mikhailenko, G.P. Robertson, M.D. Guiver, S. Kaliaguine, *J. Membr. Sci.* 173 (2000) 17.

⁹ S. M. J. Zaidi, M. I. Ahmad, *J. Membr. Sci.* 279 (2006) 548.

¹⁰ S.D. Mikhailenko, S.M.J. Zaidi, S. Kaliaguine, *J. Chem. Soc., Faraday Trans.* 94 (1998) 1613.

¹¹ S.D. Mikhailenko, S.M.J. Zaidi and S. Kaliaguine, *Catal. Today* 67 (2001) 225.

¹² V.S. Silva, B. Ruffmann, H. Silva, V.B. Silva, A. Mendes, L.M. Madeira, S. Nunes, *J. Membr. Sci.* 284 (2006) 137.

¹³ G. Alberti, M. Casciola, A. Donnadio, R. Narducci, M. Pica, M. Sganappa, *Desalination*, 199 (2006) 280.

¹⁴ M. Watanabe, H. Uchida, Y. Seki, M. Emori, P. Stonehart, *J. Electrochem. Soc.* 143 (1996) 3847.

¹⁵ H. Y. Chang, C. W. Lin, *J. Membr. Sci.* 218 (2003) 295.

¹⁶ J. D. Halla, M. Mamak, D. E. Williams, G. A. Ozin, *Adv. Funct. Mater.* 13 (2003) 133.

¹⁷ Y.-H. Su, Y.-L. Liu, Y.-M. Sun, J.-Y. Lai, D.-M. Wang, Y. Gao, B. Liu, M. D. Guiver, *J. Membr. Sci.* 296 (2007) 21.

¹⁸ B. P. Ladewig, R. B. Knott, A. J. Hill, J. D. Riches, J. W. White, D. J. Martin, J. C. Diniz da Costa, G. Q. (Max) Lu, *Chem. Mater.* 19 (2007) 2372.

¹⁹ E. Chalkova M.V. Fedkin, D.J. Weselowski, S.N. Lvov, *J. Electrochem. Soc.* 152 (2005) 1.

²⁰ P. Kalappa, J.-H- Lee, *Polym. Int.* 56 (2007) 371.

²¹ S.-H. Kwak, T.-H. Yang, C.-S. Kim, S.-B. Park, S.-K. Min, H.-W. Rhee, *Electrochim. Acta*, 50 (2004) 653.

²² C. T. Kresge, M. E. Leonowicz, W. J. Roth, J. C. Vartuli, J. S. Beck, *Nature* 359 (1992) 710.

²³ J. S. Beck, J. C. Vartuli, W. J. Roth, M. E. Leonowicz, C. T. Kresge, K. D. Schmidt, C. T. W. Chu, D. H. Olson, E. W. Sheppard, S. B. McCullen, J. B. Higgins, J. L. Schlenker, *J. Am. Chem. Soc.* 114 (1992) 10843.

organization of surfactant molecules and their affinity to inorganic components, resulting in mesostructured composites of surfactant and inorganic material. Since their discovery, a lot of knowledge in this field of materials has been developed due to immense research (a good overview gives Ref. 24).

This kind of materials was chosen because of the high potential in functionalization possibilities of these materials. By functionalizing with e.g. SO_3H as protogenic groups, these materials can become proton conductive. In addition, their long range ordered mesopores can help to guide proton through their pore channels, and should be advantage for water storage, facilitating the water management in a fuel cell membrane. Different synthesis strategies are used in this work to enable high loadings of protogenic groups in the inorganic mesoporous powders, called either grafting or co-condensation method. Via co-condensation, usually higher loadings can be achieved.²⁴

Finally, these new solid proton conductors are incorporated into different polymer materials, to investigate the influence of the powders on the conductivities and stabilities of the polymers. A good connection between the polymer and the inorganic particles is here of high importance²⁵, a covalent anchorage of advantage. The so formed composite membranes are investigated concerning proton conductivity, and used to build membrane electrode assemblies (MEAs) for single cell fuel cell performance testing.

²⁴ F. Hoffmann, M. Cornelius, J. Morell, M. Fröba, *Angew. Chem. Int. Ed* 45 (2006) 3216.

²⁵ S. J. Miller, W. J. Koros, D. Q. Vu, *Stud. Surf. Sci. Catal.* 170, Part B (2007) 1540.

2 Fundamentals

This section introduces the fundamentals of fuel cells and mesoporous silica materials. A defined knowledge of the processes occurring in fuel cells, especially in the fuel cell membranes, is necessary for understanding this complicate system with all its components, and is of course needed to tailor the properties of the aimed solid proton conductors synthesized in this work. As these materials are functionalized ordered mesoporous SiO₂ materials, their properties and formation mechanisms must be understood to tailor the desired materials for the aspired application. The functionalization of the resulting powders for being proton conductive is possible via several methods, and the principles of these reactions must be known for the optimum reaction conditions and successful anchorage of proton conductive groups.

2.1 The Fuel Cell

In the following chapters general principles of fuel cells are presented. Beginning with a historical overview, from the first fuel cell-like discovery from Sir William Grove, the working conditions and principles of different fuel cell types are introduced and explained in detail. Typical examples for fuel cells are shown, coming from low

temperature fuel cells like PEM or direct methanol fuel cells (DMFC) to high temperature fuel cells like solid oxide fuel cells (SOFC). After a part concerning fuel cell thermodynamics and kinetics and fuel cell efficiency, compared to typical Carnot heat engines, the focus lies on the different kinds of fuel cell membranes for PEM and DMFC application. Examples of proton conductive polymers for PEMFC or DMFC membranes are presented, including the polymers used in the present work, and their properties and mechanisms of proton conductivity under fuel cell operation. Possible modifications and additives, including their influence on membranes properties like stability, water retention or fuel cross-over, are introduced. Finally, the chosen additives of this work are introduced, explaining the proposed mechanisms of water storage and proton conductivities of the target composite membranes.

2.1.1 History

The principle of a fuel cell was first described by the German scientist Christian Friedrich Schönbein, who published his work in January 1839. He found in his experiments a measurable voltage between two platinum wires, if they are dipped into an electrolyte solution (sulfuric acid) and flushed with hydrogen and oxygen gas, respectively.

At the same time, the Welsh lawyer and physicist Sir William Grove made experiments with the electrolysis of water to hydrogen and oxygen. He found this experiment to be reversible under certain conditions. Together with the work of Schönbein, he developed the first fuel cell in 1843, which he called “galvanic gas battery”²⁶, and which produced electrical voltage via the so-called “cold combustion” of hydrogen and oxygen gas (Figure 1). In two glass tubes, platinum wires have been incorporated and flushed with hydrogen or oxygen. Hydrogen was oxidized at the electrode surface, which could migrate through the electrolyte (diluted sulfuric acid) to the other glass tube, reacting

²⁶ www.diebrennstoffzelle.de, January 2008.

with oxygen to water. In his experiment, Grove connected 4 single cells together to the first kind of fuel cell stack.²⁷

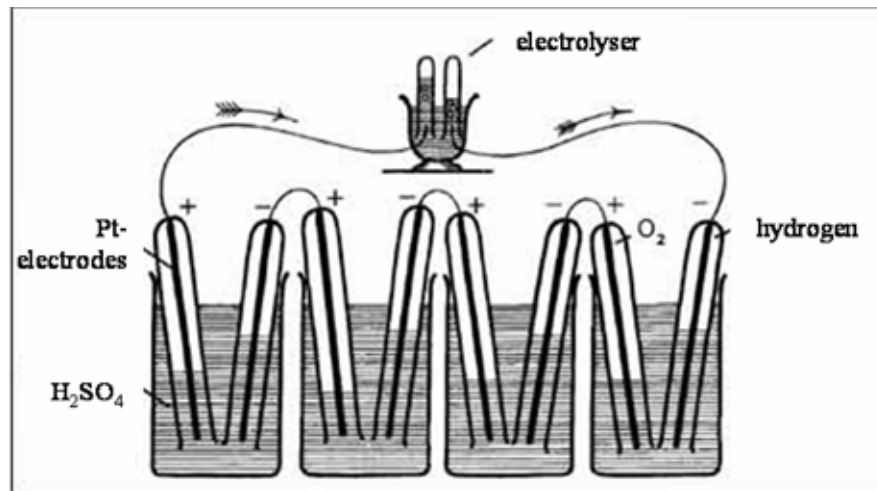


Figure 1. Scheme of the first fuel cell developed by Sir William Grove.²⁶

Unfortunately, the research on this system was not further followed up for several reasons. The electrochemical processes in the fuel cell have not been understood completely, and several years later, 1866, Werner von Siemens constructed the first dynamo machine. This invention was quite better understood, and together with the steam engines at this time, less complicated concerning fuels and construction materials for power generation. The fuel cell could not become accepted against this trend and the later invented combustion engines, although already at 1887 the German Scientist Wilhelm Ostwald proposed the big potential of fuel cells and an efficiency of 83 %.^{26,27} Although this proposal lead to several construction ideas during the beginning of the 20th century, the still existing material corrosion problems for construction could not be overcome. With the beginning understanding of corrosion processes, the fuel cell principle was rediscovered.

Francis Thomas Bacon reconstructed the original concept fundamentally. Instead of the very expensive platinum, he used cheaper nickel gauzes, and as electrolyte he used the less corrosive alkali potassium hydroxide. He named the cell “Bacon cell” in 1932, the

²⁷ www.initiative-brennstoffzelle.de, January 2008.

2 Fundamentals

first alkaline fuel cell (AFC). 27 years later, he constructed a truly working fuel cell providing 5 kW of power.

Spaceflight research brought several inventions to the fuel cell system, also caused due to the reason that money was not the most important driving force for the development of new fuel cell constructions, but the footrace into space. In 1955, the chemist Willard Thomas Grubb used for the first time an ion-exchange membrane as electrolyte, based on sulfonated polystyrene. Together with the chemist Leonard Niedrach, who discovered the deposition of platinum on this membrane as catalyst for the oxidation of hydrogen and the reduction of oxygen, he constructed the Grubb-Niedrach fuel cell, the first PEMFC.²⁸ As these two scientist worked for General Electric, who provided technique to the National Aeronautics and Space Administration (NASA) of the United States (US), this development found its way into the space crafts of the Gemini space project, the first commercial use of a fuel cell. For the Apollo space program, the company Pratt & Whitney licensed the patents of the Bacon cell, and with new light-weight construction properties, they supplied the NASA spacecrafts of that time with AFCs. AFCs are the up to now most used fuel cells in space crafts, having more than 65.000 working hours on more than 87 crewed space shuttle flights, showing the big reliability of this system.²⁹

With new developments in efficient hydrogen fuel generation (hydrogen production from natural gas, hydrogen produced with solar and wind energy), fuel cells are still of increasing interest, not only in mobile applications, but also for stationary use, as power supplies for home heating and emergency power generators, e.g. in hospitals. However, the mobile application is still one of the most forcing factors in fuel cell development. Especially the automotive companies are increasing their research for an environmental friendly way of car engines basing on fuel cells, like Daimler-Chrysler (since 2007: Daimler) with the NECAR-series from 1994 to 2000. The Volkswagen AG just

²⁸ www.fctec.com, January 2008.

²⁹ J. H. Hirschenhofer, *Fuel Cell Handbook*, 1st edition, Morgantown, West Virginia, 1998.

proposed “...the first Volkswagen with a fuel cell drive that is affordable and suitable for everyday use...” for 2020.³⁰

2.1.2 Fuel Cell Principles

Every fuel cell consists of two electrodes, an anode and a cathode. On the anode side, the oxidizing fuel is continuously fed (hydrogen for example), while on the cathode side oxygen or air stream is applied. The gases are applied via bipolar plates with an embedded flow field, being responsible for a homogeneous gas supply to the electrodes. Both reaction rooms are separated via an electrolyte blocking layer, which can be a solid (e.g. a membrane) or a liquid (e.g. phosphoric acid H_3PO_4) electrolyte. At the anode, fuel is oxidized, and the generated electrons are merging through an electrical circuit to the cathode, generating electrical work for an electrical consumer. For charge equalization, ionic charge carriers diffuse through the electrolyte. Figure 2 shows the most important fuel cell principles in comparison. They can be divided in low-temperature (up to 200 °C) and high temperature application. In the following, the different types are described, beginning with the low-temperature devices.

³⁰ Press release Volkswagen AG, October 2006.

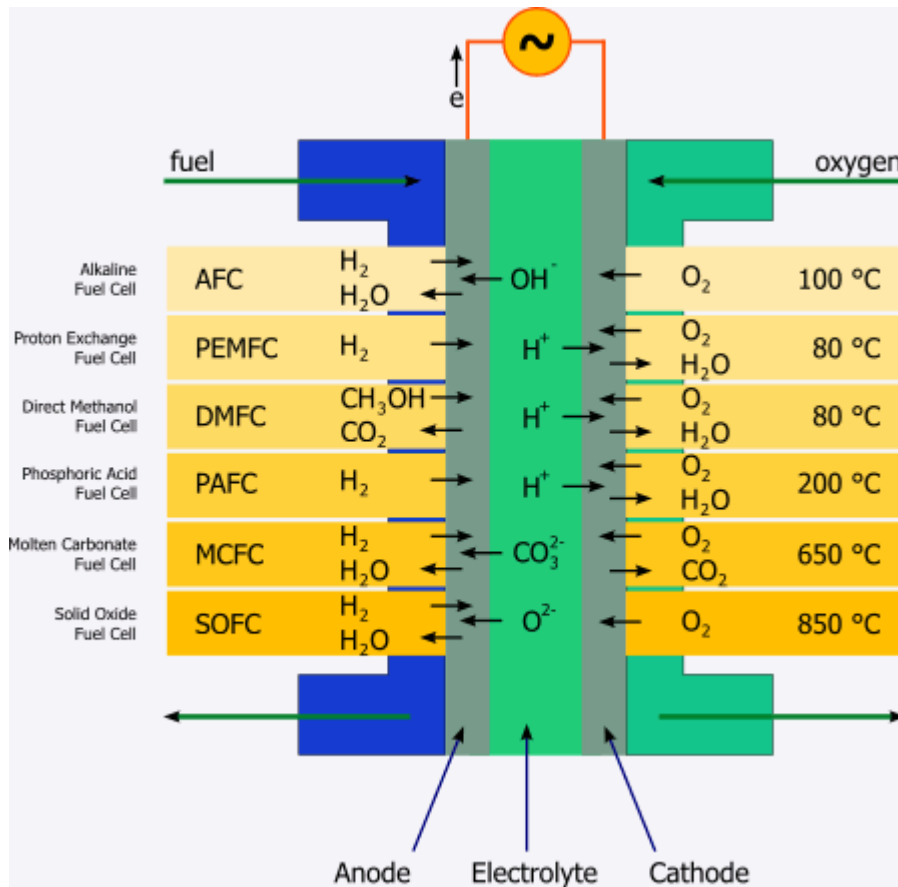


Figure 2. Different fuel cell types for comparison.³¹

AFCs are presently used in cars, space crafts and submarines. The electrolyte separating the electrodes is a 30-50 % potassium hydroxide (KOH) solution, and the fuels are pure hydrogen and oxygen gas. The ionic charge carriers are hydroxide ions (OH⁻), which are diffusing from the cathode to the anode side, in the opposite direction to the electrons. The appropriate working temperatures are between 60 and 100 °C. This type of fuel cell needs no warm-up time, is immediately operational, and the average efficiencies are between 50 and 60 %. Their advantage is the very fast cathode reaction at the given working temperature, but in contrast, the removal of carbon dioxide (CO₂) out of the fuel cell and air restrict their application possibilities.³²

³¹ ezb-dresden.de/de/fuelcells, January 2008.

³² www.pemfc.de, January 2008.

PEMFCs and DMFCs are very similar and described in detail in chapter 2.1.3.

Phosphoric acid fuel cells (PAFC) are mostly used for power generation, in combined heat and power plants (CHPs) and in automotive applications. The liquid electrolyte of this fuel cell type is a concentrated H_3PO_4 at working temperatures from $160\text{ }^\circ\text{C}$ to $200\text{ }^\circ\text{C}$, as for fuel either hydrogen or methane can be used at the anode. The charge carriers are protons, and the efficiencies lie around 55 %, but PAFCs need a warm-up time of around 30 minutes from a stand-by mode. In addition, they need expensive platinum catalysts, show low current and power densities, and are mostly very big and heavy. But however, coupled to CHPs, they show overall efficiencies of around 85 %.

In the high-temperature sector, two important fuel cell technologies are of importance. Molten carbonate fuel cells (MCFC) are working at temperatures of around $650\text{ }^\circ\text{C}$. The electrolyte is a molten mixture of lithium carbonate and potassium carbonate ($\text{Li}_2\text{CO}_3/\text{K}_2\text{CO}_3$) with carbonate-ions (CO_3^{2-}) as charge carriers. Possible fuels are methane, bio gas or natural gas, because due to the high working temperatures, the gases can be reformed internally to hydrogen. MCFC are mostly used for power generation, their flexible fuel gas household is a big advantage, and their efficiencies are between 60 and 65 %. In contrast, MCFCs need several hours warm-up time, and the very aggressive molten salts can cause severe corrosion problems, which lead to an increase altering time of the components.

Solid oxide fuel cells (SOFC) are the fuel cells with the highest working temperatures of 800 to $1000\text{ }^\circ\text{C}$. As electrolyte, a solid ion conductor is used, e.g. yttrium stabilized zirconium dioxide (Y:ZrO_2). This material is a pure oxygen ion conductor, due to the oxygen vacancies produced via yttrium-doping, so the charge carriers are O^{2-} -anions merging via oxygen vacancies from the cathode to the anode side. Like in MCFCs, natural gases can be used for fuels due to the high working conditions internal reforming. They are used in stationary power generators, their efficiencies lie between 55 and 65 %, and their solid electrolyte makes them easy to handle. But also like MCFCs, SOFCs have a long warm-up time of several hours, and their components have an accelerated altering process due to the high temperatures. Actual research on SOFCs concentrates on thinner and alternative electrolyte layers for lower working

temperatures.³³ Table 1 summarizes the ongoing reactions in the different fuel cell types presented.

Table 1. Anode and cathode reactions in different fuel cell types.

	PEMFC		DMFC
Anode	$H_2 \rightarrow 2H^+ + 2e^-$		$CH_3OH + H_2O \rightarrow CO_2 + 6H^+ + 6e^-$
Cathode	$\frac{1}{2}O_2 + 2H^+ + 2e^- \rightarrow H_2O$		$\frac{3}{2} O_2 + 6H^+ + 6e^- \rightarrow 3 H_2O$
	AFC		PAFC
Anode	$H_2 + 2OH^- \rightarrow 2H_2O + 2e^-$		$H_2 \rightarrow 2H^+ + 2e^-$
Cathode	$\frac{1}{2}O_2 + H_2O + 2e^- \rightarrow 2OH^-$		$\frac{1}{2}O_2 + 2H^+ + 2e^- \rightarrow H_2O$
	MCFC		SOFC
Anode	$H_2 + CO_3^{2-} \rightarrow H_2O + CO_2 + 2e^-$		$H_2 + O^{2-} \rightarrow H_2O + 2e^-$
Cathode	$\frac{1}{2}O_2 + CO_2 + 2e^- \rightarrow CO_3^{2-}$		$\frac{1}{2}O_2 + 2e^- \rightarrow O^{2-}$

2.1.3 PEMFC and DMFC

PEMFC and DMFC are very similar. As the focus of the present work lies on additives for membranes used in PEMFCs or DMFC, these fuel cell types are presented in more detail.

Figure 3 presents the working principle of a PEMFC, only showing schematically the basic module of a PEMFC, the membrane electrode assembly (MEA), consisting of the PEM pressed together with electrodes on both sides. At one electrode (anode), hydrogen molecules are split at a Pt catalyst surface into hydrogen atoms adsorbed on the catalyst. These atoms are then oxidized to protons, which can diffuse through the PEM, while the

³³ P. Holtappels, U. Vogt, T. Graule, *Adv. Eng. Mater.* 7 (2005) 292.

generated electrons can be used via an outer electrical circuit to produce electrical work. At the cathode side, oxygen is reduced to O^{2-} -anions, reacting with electrons and the protons to the only chemical byproduct of this system, water.

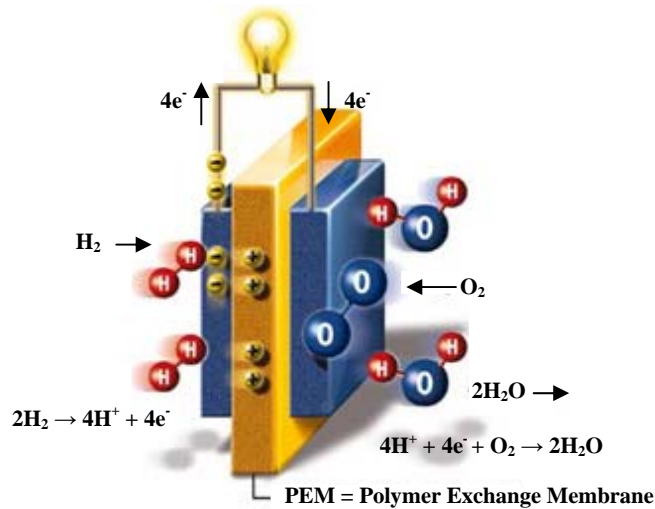


Figure 3. Working principle of a PEMFC single cell.²⁸

The electrodes themselves are porous and highly conductive carbon sheets, so that the gases can reach the membrane and the catalyst homogeneously. Therefore, they are also called gas diffusion layers (GDL). Figure 4 shows a MEA with these layers and the occurring reactions in detail.

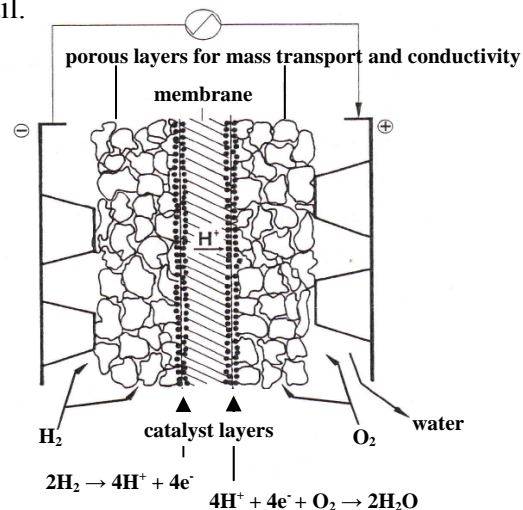
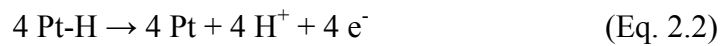


Figure 4. Detailed cross section of a MEA.³⁴

³⁴ C. H. Hamann, W. Vielstich, *Elektrochemie*, Wiley-VCH, Weinheim, 3rd Edition, 1998.

2 Fundamentals

Mostly, the GDLs are hydrophobized, so that the product water occurring on the cathode side can be transported away from the membrane. And, as already mentioned, the GDLs are covered with highly disperse platinum nanoparticles. The Pt catalyst is needed due to the high activation energy of hydrogen and oxygen dissociation, which is lowered at a Pt surface. Normally, the following reactions occur at the Pt surface at the anode side, where in a first step a platinum-hydrogen intermediate is formed, which then dissociates with hydrogen oxidation.



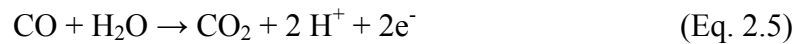
At the anode side, the recombination of protons, electrons and oxygen takes place.



The overall reaction is then



If the used fuel gases are polluted with CO, the reaction in Eq. 2.1 cannot take place, because the CO irreversibly blocks all adsorption sites on the catalyst surface. By increasing the working temperature to higher than 100 °C, the catalyst poisoning tendency is reduced due to the formation of non-blocking CO₂,



and the fuel cell is still able to work. At 80 °C, the maximum acceptable CO concentration in fuel gas is around 20 ppm (parts per million), but at 130 °C 1000 ppm.⁵

The slowest of all reactions is the cathodic oxygen reduction, which is 100 times slower than the hydrogen reaction.³⁵ But this reaction is also proposed to be improved with higher working temperatures.

To build a single cell PEMFC, additional bipolar plates are used around the MEA. The bipolar plates are responsible for the sufficient gas transport and water back-transport from the MEA, for which purpose they have a channel-like distribution system (flow field). In addition, the bipolar plates are also responsible for heat evacuation to cooling circles and the electrical contacting.

However, a single fuel cell does not produce enough voltage, only 1.229 V at 25 °C and 1 bar. To overcome this problem, a number of single cells are connected in a row, to a fuel cell stack. Figure 5 shows schematically a fuel cell stack, introducing also the bipolar plates.

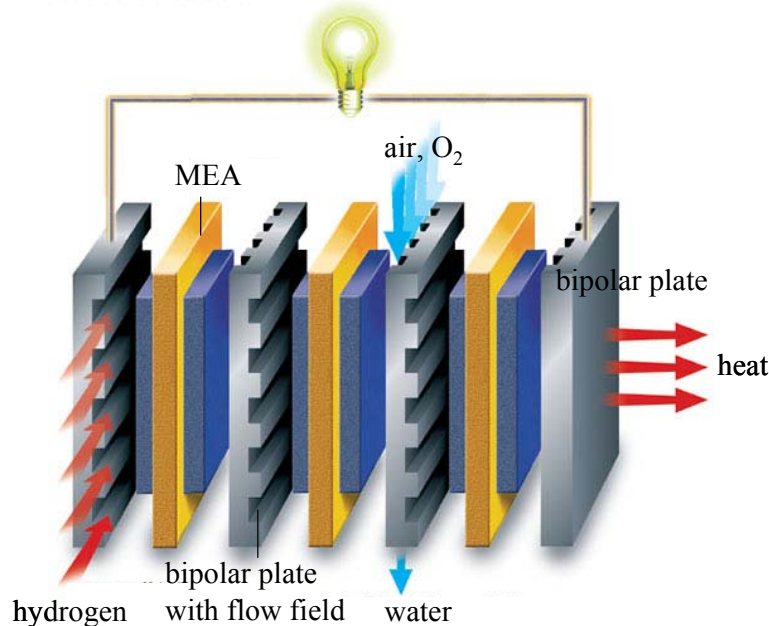
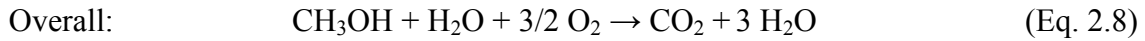
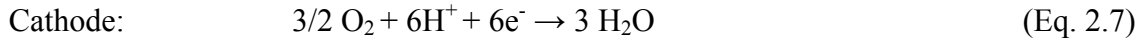
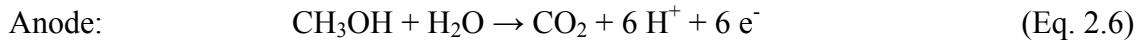


Figure 5. PEMFC stack with construction elements.²⁸

DMFCs work in the same principle, but methanol is used as fuel at the anode. In a first reaction, methanol is oxidized to CO_2 . The generated electrons and protons merge in the same way like in the PEMFC to the cathode reacting with oxygen to water.

³⁵ J. F. Shackelford, *Werkstofftechnologie für Ingenieure*, Pearson, 6th Edition, 2005.



Various reaction intermediates may be formed during methanol oxidation.³⁶ Some of these CO-like species are irreversibly adsorbed on the surface of the electrocatalyst and severely poison Pt for the occurrence of the overall reaction, which has the effect of significantly reducing the fuel consumption efficiency and the power density of the fuel cell in the same way like in the PEMFC case. But in the same way, this problem can be solved with a working temperature higher than 100 °C. However, DMFCs show lower power densities than PEMFC, which might correlate with the slow methanol oxidation reaction kinetics, involving the transfer of six electrons. The methanol oxidation at a Ru-Pt catalyst is three times slower than the oxidation of hydrogen on Pt.³⁷ Another drawback compared to the PEMFC is the tendency of methanol cross-over through the membrane to the cathode side, resulting in fuel leakage and efficiency loss.¹⁵

2.1.4 Thermodynamics and kinetics of H_2/O_2 fuel cells

One of the most important facts making fuel cell systems so interesting is their thermodynamic efficiency. A theoretical maximum efficiency of about 95 % for an ideal hydrogen-oxygen fuel cell, which is significantly higher than the efficiency of a Carnot heat engine, is responsible for the immense research efforts in this field. In contrast to Carnot machines, fuel cells directly produce electrical energy out of chemical energy, while the Carnot principle works via two intermediate conversion steps, including heat and mechanical energy. Figure 6 illustrates this circumstance.

³⁶ R. Parsons, T. Van der Noot, *J. Electroanal. Chem.* 257 (1988) 9.

³⁷ A. S. Aricò, S. Srinivasan, V. Antonucci, *Fuel Cells* 1 (2001) 133.

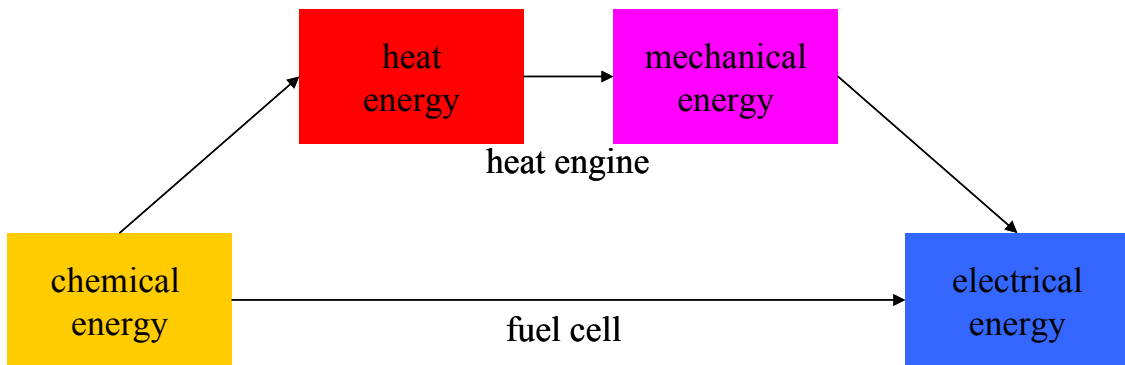


Figure 6. Energy conversions in a Carnot or fuel cell process.

Comparing the ideal efficiencies of both machines, the advantage of the fuel cell becomes clear. The ideal efficiency of a hydrogen-oxygen fuel cell is calculated from the free reaction enthalpy $\Delta_R G^0$ and the standard formation enthalpy $\Delta_f H^0$ of water for the reaction between hydrogen and oxygen forming gaseous water.

$$\eta_{\max}^{\text{fc}} = \frac{\Delta_R G^0}{\Delta_f H^0} = \frac{-228.6 \text{ kJ/mol}}{-241.8 \text{ kJ/mol}} = 0.945 = 94.5 \% \quad (\text{Eq. 2.9})$$

In general, with the relation $\Delta G = \Delta H - T\Delta S$, Eq. 2.9 can be written as

$$\eta_{\max}^{\text{fc}} = \frac{\Delta_R G^0}{\Delta_f H^0} = \frac{\Delta_f H^0 - T \cdot \Delta_R S^0}{\Delta_f H^0} = 1 - \frac{T \cdot \Delta_R S^0}{\Delta_f H^0} \quad (\text{Eq. 2.10})$$

Depending on the standard reaction entropy $\Delta_R S^0$ of the applied reaction used for the fuel cell, theoretically, efficiencies higher than 100 % are possible.

In contrast, the efficiency of a Carnot heat engine is calculated from the temperature dependence between the inlet temperature T_1 and the outlet temperature T_2 , where $T_1 > T_2$.

$$\eta_{\max}^{\text{he}} = \frac{T_1 - T_2}{T_1} = 1 - \frac{T_2}{T_1} \quad (\text{Eq. 2.11})$$

Figure 7 compares the efficiencies of the ideal H_2/O_2 fuel cell with the Carnot machine efficiency.³⁸ T_2 is set to 300 K for this rough calculation (higher T_2 might be more realistic), and T_1 is increasing on the x axis. For the fuel cell efficiency, the temperature corresponds to the working temperature.

As the efficiencies are in both cases temperature dependent, the thermodynamic efficiency for a heat engine increases with increasing temperature difference between the inlet and the outlet, while for a fuel cell with increasing working temperature, the ideal efficiency deteriorates. At a temperature around 1450 °C, both systems have the same ideal efficiency and change the efficiency lead. But until this temperature, a fuel cell is still the better energy converter, due to thermodynamics.

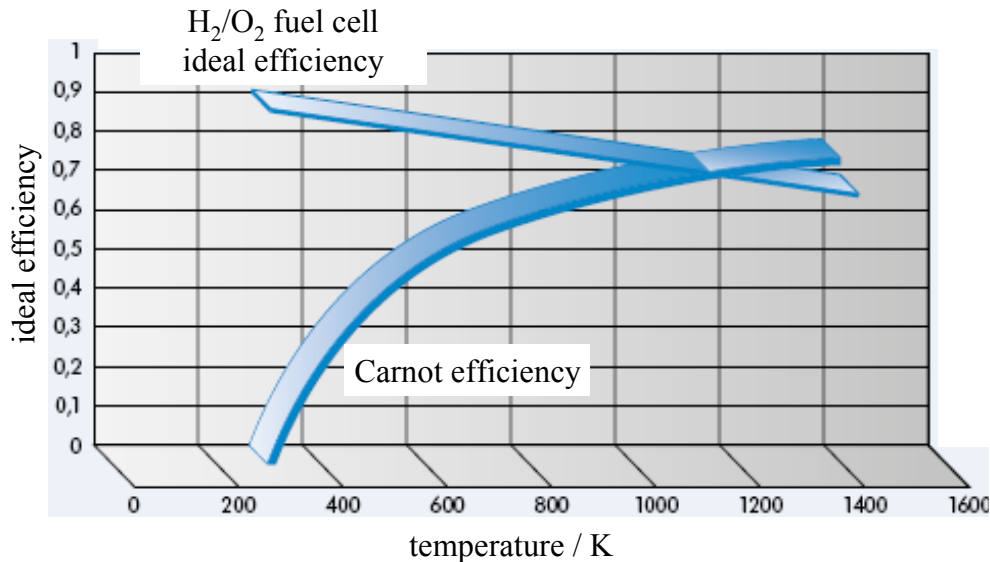


Figure 7. Ideal efficiencies of a hydrogen-oxygen fuel cell against the Carnot efficiency.³⁸

Besides the thermodynamics, fuel cell electrode kinetics is a critical point restricting the ideal thermodynamical efficiency down to about 60 %. Figure 8 points out the several voltage losses in a fuel cell polarization curve due to electrode kinetics. The output voltage will be less than the open circuit voltage when current is drawn by a load. The resulting voltage U is determined by subtracting all voltage losses, summarized as ΔU ,

³⁸ www.asue.de, January 2008.

from the ideal open circuit voltage. ΔU_{rev} is the reversible voltage loss caused by reversible overvoltages. ΔU_A is the voltage loss due to activation process for the slow electrochemical reactions occurring at the electrodes as current is drawn, also caused by cathode and anode polarizations.

For ΔU_R resistive and capacitive voltage losses are responsible, also called impedance losses. They are associated with the flow of electrons and ions in the electrodes and the electrolyte. Finally, voltage losses due to inadequate concentration of reactants and lacking diffusion to the reaction sites can occur, abbreviated with ΔU_{diff} .

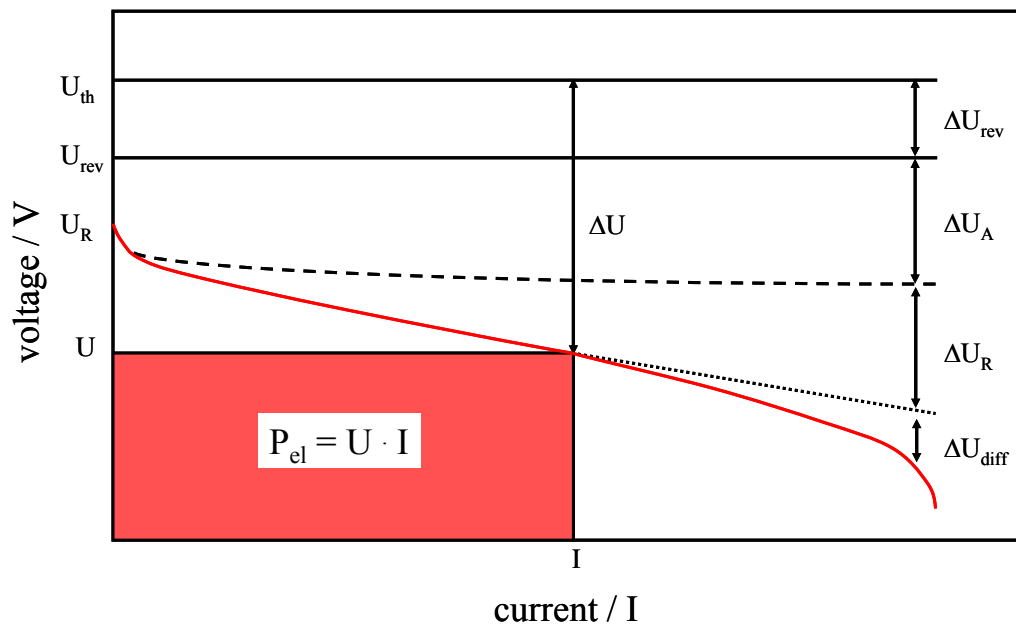


Figure 8. Voltage losses in fuel cell operation due to electrode kinetics. Resulting polarization curve in red.³⁹

The overall voltage losses are summarized and calculated to

$$\Delta U = \Delta U_{\text{rev}} + \Delta U_A + \Delta U_R + \Delta U_{\text{diff}} \quad (\text{Eq. 2.12})$$

³⁹ M. Ciureanu, S. D. Mikhailenko, S.Kaliaguine, *Catal. Today* 82 (2003) 195.

while the resulting accessible voltage corresponds to

$$U = U_{\text{th}} - \Delta U \quad (\text{Eq. 2.13})$$

It can also be seen in Figure 8 from the current-voltage curve that increasing currents result in a lower potential, being controlled by the region of activation, impedance and diffusion losses. A nearly linear potential drop for the ohmic and capacitive voltage losses can be seen throughout a long current region, while at high currents the concentration losses are significantly coming into fore. A compromise between current and voltage losses must be found resulting in an efficient fuel cell operation. With increasing working temperatures the voltage losses can be reduced and the electrode kinetics improved. Although the thermodynamical efficiency goes down with increasing temperature, the kinetics determines the overall efficiency, resulting in about 60 %. For example, in SOFCs the resulting efficiencies lie around 65 %, in general slightly higher than for PEMFC due to the better kinetics, as for the thermodynamical efficiency the situation is opposite.

Increasing the working temperatures of PEMFCs to more than 100 °C should result in higher efficiencies, where one factor would be the enhanced kinetics, e.g. reduced ΔU_A .

2.1.4 Proton conductive polymer membranes for PEMFCs

An electrolyte membrane for PEMFC application must fulfill several requirements:

- High proton conductivity
- Low gas and/or fuel permeability
- Electrical insulator
- Good water uptake with low swelling
- Mechanically and thermally stable
- Chemically and electrochemically stable
- Long lifetime
- Easy to recycle

Two types of polymers dominate research efforts: sulfonated aromatic polymers (e.g. sulfonated polyetheretherketone SPEEK or sulfonated polysulfone SPSU) and perfluorinated sulfonic acid (SO₃H) membranes like Nafion[®]. These membranes both exhibit phase separated domains consisting of an extremely hydrophobic backbone, which gives morphological stability, and extremely hydrophilic functional groups. These functional groups aggregate to form hydrophilic nanodomains which act as water reservoirs.⁴⁰ The key features of these membranes are shown in Figure 9.

Nafion[®] has very wide channels compared to SPEEK and very good connectivity between the channels. In contrast, the channels of SPEEK are more branched, but also dead-end channels exist.

⁴⁰ K.D. Kreuer, *Solid State Ionics* 136 (2000) 149.

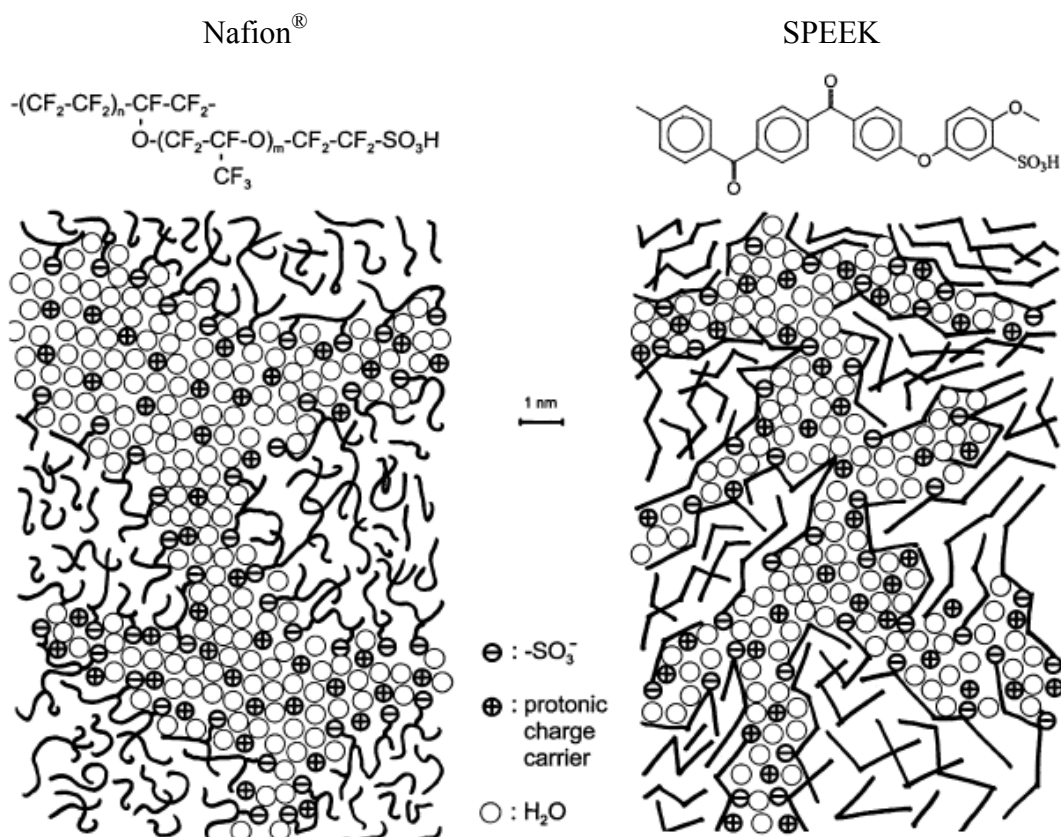


Figure 9. Nafion and SPEEK membranes with their nanodomains.⁴¹

As perfluorinated polymers are strong and stable in both oxidative and reductive environments, sulfonated aromatic polymers show better mechanical strength and are chemically and thermally stable even at elevated temperatures.⁴² The biggest problem of SPEEK-type membranes is a dependence of the proton conductivity on the sulfonation degree. At reduced levels of sulfonation the aromatic polymers have lower water contents and reduced conductivity $<10^{-2}$ S/cm.⁸ However, if the degree of sulfonation is increased to improve conductivity, the mechanical properties of the membrane deteriorate.¹¹ A degree of sulfonation of about 60 % (related to a maximum sulfonation of all aromatic rings) seemed to be a good compromise.⁴³ Another proposed solution is to produce composite membranes with controlled mechanical, physical and chemical

⁴¹ K. D. Kreuer, *J. Membr. Sci.* 185 (2001) 29.

⁴² B. Smitha, S. Sridhar, A. A. Khan, *J. Membr. Sci.* 259 (2005) 10.

⁴³ M. Horgarth, X. Glipta, *High Temperature Membranes for Solid Polymer Fuel Cells*, 2001.

properties. The proton conductivity of SPEEK and Nafion[®] strongly depends on the water content. Proton conductivity mechanisms in water-rich membranes are introduced in chapter 2.1.5.

Polysulfone is another example out of the sulfonated aromatic polymer family; the structure is shown in Figure 10. The SPSUs are also highly mechanically stable and show good properties for use in fuel cells.^{44,45,46}

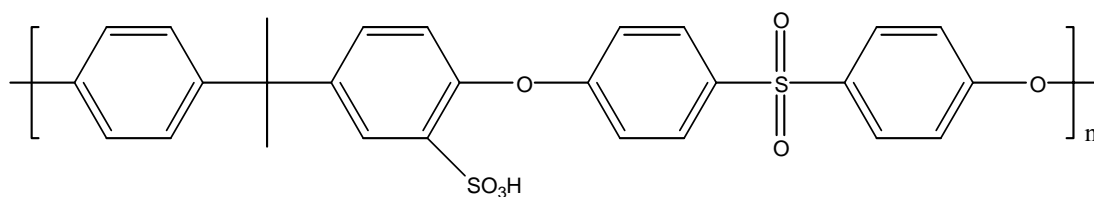


Figure 10. Structural unit of sulfonated polysulfone (SPSU).⁴⁷

Another, but structural completely different type of proton conductive membranes are functionalized polysiloxanes. These types of materials were used for proton conductivity for the first time in 1992.⁴⁸ The actual trend is to use mixed functionalized polysiloxanes with sulfonic acid and benzimidazole moieties,⁴⁹ as Kreuer *et al.* already proposed in 1998 nitrogen-based heterocyclic systems for use as proton conductive groups.⁵⁰ The mixed system should provide water-free proton conductivity due to the polymer structure of the polysiloxanes, where the sulfonic acid groups provide excess protons needed for the proton conductivity, which is then fulfilled via the benzimidazole groups (see Figure 11).

⁴⁴ J. Kerres, A. Ullrich, F. Meier, T. Häring, *Solid State Ionics* 125 (1999) 243.

⁴⁵ P. G. Dimitrova, B. Baradie, D. Foscallo, C. Poissonon, J. Y. Sanchez, *J. Membr. Sci.* 185 (2001) 59.

⁴⁶ C. Manea, M. Mulder, *J. Membr. Sci.* 206 (2002) 417.

⁴⁷ F. Lufrano, I. Gatto, P. Staiti, V. Antonucci, E. Passalacqua, *Solid State Ionics* 145 (2001) 47.

⁴⁸ I. Gautier-Luneau, A. Denoyelle, J. Y. Sanchez, C. Ponsignon, *Electrochim. Acta* 37 (1992) 1615.

⁴⁹ M. Jeske, C. Soltmann, C. Ellenberg, M. Wilhelm, D. Koch, G. Grathwohl, *Fuel Cells* 1 (2007) 40.

⁵⁰ K. D. Kreuer, A. Fuchs, M. Ise, M. Spaeth, J. Maier, *Electrochim. Acta* 43 (1998) 1281.

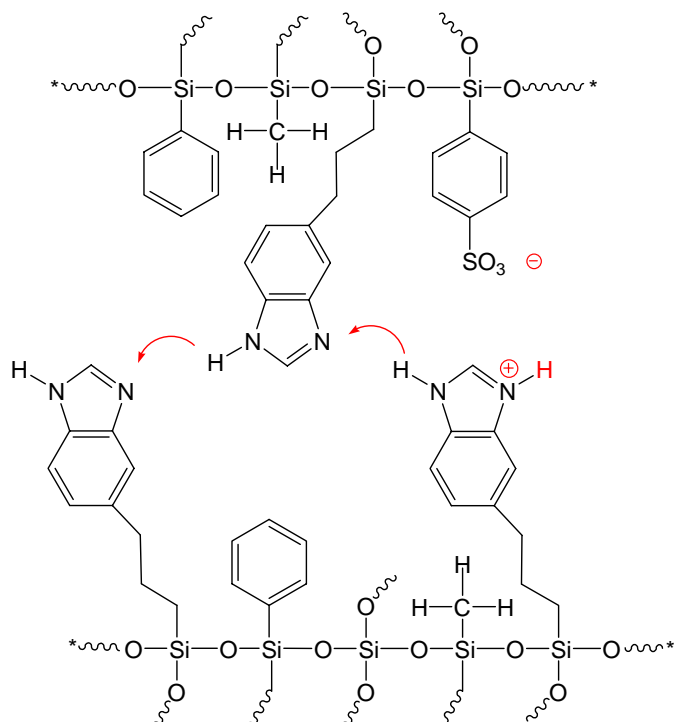


Figure 11. Ideal structure of functionalized polysiloxane.⁴⁹

Finally, another aromatic system with basic character has become recent interest in fuel cell research, namely polyoxadiazole polymers (Figure 12). The conjugated heterocyclic ring containing (C=N) pyridine-like nitrogen with the electron lone pair which does not participate of the aromatic sextet makes polyoxadiazoles and their derivatives potential candidates for application in fuel cells when doped and/or sulfonated.

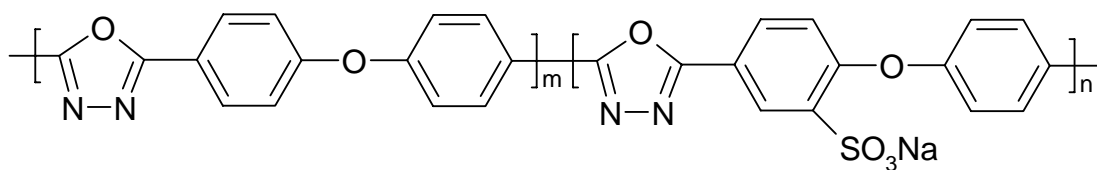


Figure 12. Structural unit of sulfonated polyoxadiazole.⁵¹

Recently, sulfonated polyoxadiazole membranes with high thermal stability, high degradation stability and good mechanical properties have been reported. High proton

conductivity values within the order of magnitude of 10^{-2} S/cm at 80 °C and RH = 20 % are due to the high ionic exchange capacities of these polymers, up to 2.7 mmol/g.⁵¹ Figure 13 depicts the structure and the water uptake mechanism into the polymer between the chains.

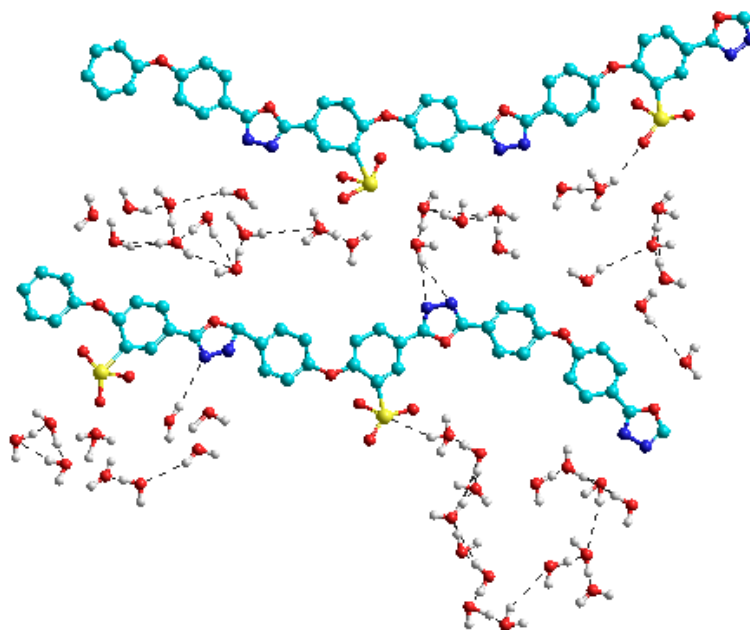


Figure 13. Polymer chains of sulfonated polyoxadiazoles including incorporated water. White: hydrogen, red: oxygen, dark blue: nitrogen, light blue: carbon, yellow: sulfur.⁵¹

In this work, Nafion[®] as well as polysiloxanes and polyoxadiazoles were used to build composite membranes.

⁵¹ D. Gomes, J. Roeder, M. L. Ponce, S. P. Nunes, *J. Power Sources* 175 (2008) 49.

2.1.5 Proton conductivity mechanisms

In literature, three different proton conductivity mechanisms are discussed. These are:

- Surface diffusion along functional groups
- Grotthuss mechanism³, structure diffusion with proton trajectories
- Vehicle mechanism, diffusion of mobile species present in the Grotthuss mechanism

Mostly, these mechanisms cannot be separated from each other, and they occur simultaneously, or together.

One example for surface diffusion is the cluster-model for Nafion[®].⁵² The protons are transported from one SO₃H groups to another via the side chains, which count into the clusters formed after swelling. Figure 14 illustrates the modified cluster model, which is an improvement of the old model.⁴² Following new results, the formed clusters are non-ordered and have different diameters, connected via channels.

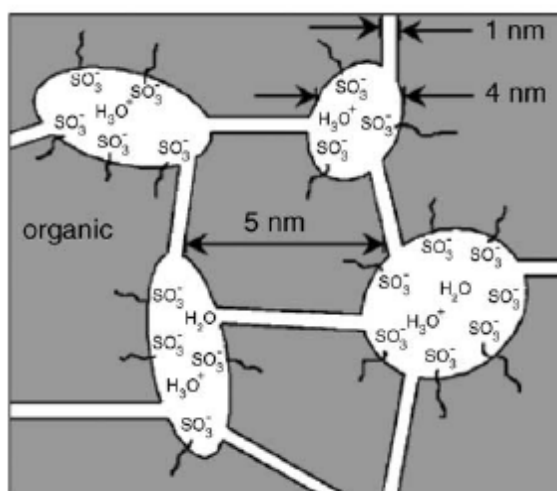


Figure 14. Random-cluster-network model.⁴²

⁵² T. D. Gierke, W. Y. Hsu, in *Perfluorinated Ionomer Membranes*, Eds. A. Eisenberg, H. L. Yeager, ACS Symposium Series No. 180, American Chemical Society, Washington, DC, 1982.

Surface conductivity can also take place in surface functionalized acid membranes, like zirconium phosphate.^{53,54} In addition, some remaining water molecules help to transfer protons (Figure 15).

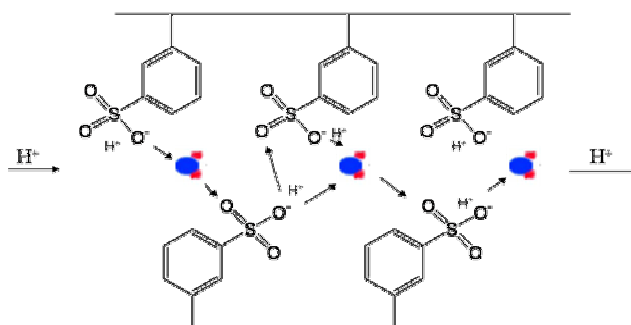


Figure 15. Surface conductivity mechanism in solid acid membranes.⁵⁵ Water molecules are colored (oxygen: blue, hydrogen: red).

As Nafion[®] takes up a lot of water, the Grotthuss mechanism, with protons provided by the hydrophilic side chains and SO₃H groups, overlies this mechanism. The Grotthuss mechanism is in principle a hopping of a proton from one water molecule with hydrogen bond breaking and formation. Figure 16 shows schematically this mechanism. Activation energies for this mechanism lie between 13.5 and 38.5 kJ/mol.⁵⁶

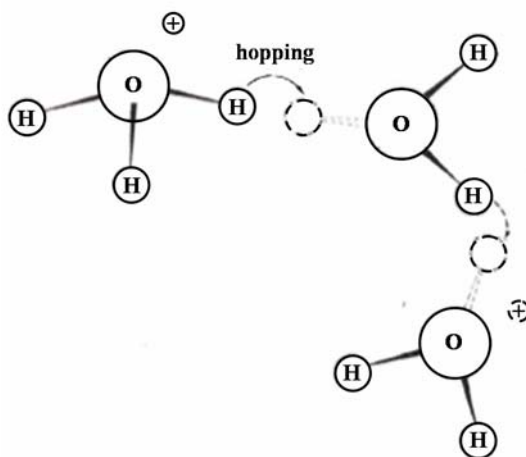


Figure 16. Grotthuss mechanism.

⁵³ G. Alberti, M. Casciola, U. Costantino, A. Peraio, T. Rega, *J. Mater. Chem.* 5 (1995) 1809.

⁵⁴ G. Alberti, M. Casciola, *Solid State Ionics* 97 (1997) 177.

⁵⁵ W.H.J. Hogarth, J.C. Diniz da Costa, G.Q.(Max) Lu, *J. Power Sources* 142 (2005) 223.

⁵⁶ P. Colomban, A. Novak in P. Comlomba (ed.) *Proton conductors*, Cambridge University press, Cambridge, 1992.

In detail, two intermediate ions are formed in the proton transfer process of the Grotthuss mechanism to solvate the excess proton, namely the Eigen-ion (H_9O_4^+) and the Zündel-ion (H_5O_2^+), shown in Figure 17. Theoretical calculations have been performed to prove the presence of these ions in the Grotthuss mechanism.^{57,58,59}

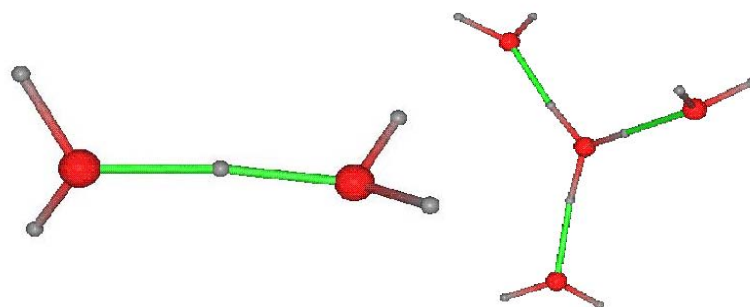


Figure 17. Zündel- and Eigen-ion.⁵⁷

In 2002, the “presolvation” concept of Tuckerman was proposed and proven, saying that the “Proton-receiving species must be “pre-solvated” like the species into which it will be transformed in the proton-transfer reaction”.⁶⁰ The estimated transfer time of a proton from the Zündel-ion to the Eigen-ion was calculated to be 1.5 ps, whereas NMR measurements found 1.3 ps. Then, the proton is transferred from the Zündel-ion complex again to an Eigen-ion. Figure 18 illustrates this mechanism and also depicts the presolvation shell.

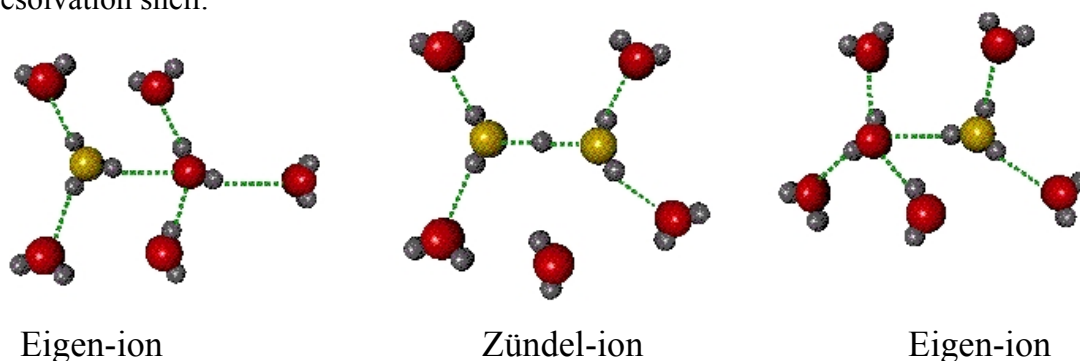


Figure 18. Proton transfer from Eigen-ion over Zündel-ion to Eigen-ion. Charged oxygen atoms are yellow.⁶⁰

⁵⁷ M. E. Tuckerman, K. Laasonen, M. Sprik, M. Parrinello, *J. Phys. Chem.* 99 (1995) 5749.

⁵⁸ M.E. Tuckerman, K. Laasonen, M. Sprik, M. Parrinello, *J. Chem. Phys.* 103 (1995) 150.

⁵⁹ D. Marx, M. E. Tuckerman, M. Parrinello, *Nature* 397 (1999) 601.

⁶⁰ M. E. Tuckerman, D. Marx, M. Parrinello, *Nature* 417 (2002) 925.

In the Eigen-ion, the central hydronium-ion (H_3O^+) is solvated by three water molecules via hydrogen bonds. The proton receiving water molecule is four-times coordinated via hydrogen bonds. To form the Zündel-ion, the proton-receiving oxygen breaks one hydrogen bond to be only three-times coordinated, as in an Eigen-ion, and forms the Zündel-complex. The free molecule coordinates then to the former charged oxygen, being then four-times coordinated, and the hopping proton is completely transferred to the other oxygen. The now charged oxygen has only three hydrogen bonds; a new Eigen-ion is formed.

A kind of Zündel-like behavior is also possible and proposed for water-free systems based on pure imidazole. Ab-initio calculations from Münch *et al.* showed that imidazole can act in a same way like water, as proton receiving and delivering species,⁶¹ and therefore a Grotthuss-like mechanism in pure imidazole is assumed.⁵⁰ These computational data used Schuster *et al.* to investigate different protogenic groups anchored to heptyl spacers (SO_3H , imidazole, phosphonic acid groups PO_3H_2) in water-free environment with focus on water-free proton conductivity, which all can act in a Grotthuss-like conduction mechanism.⁶² Imidazole shows for example resonance stabilization in protonated constitution, acting analogue to a single water molecule forming a positively charged molecule by binding an additional proton (Figure 19). Two imidazole groups are needed of course for the proton transport. If the imidazole is immobilized or anchored to a spacer, the type of anchorage is important for the conductivity mechanism. This will be shown and discussed in chapters 4.2.3, 4.2.4 and 4.2.5.

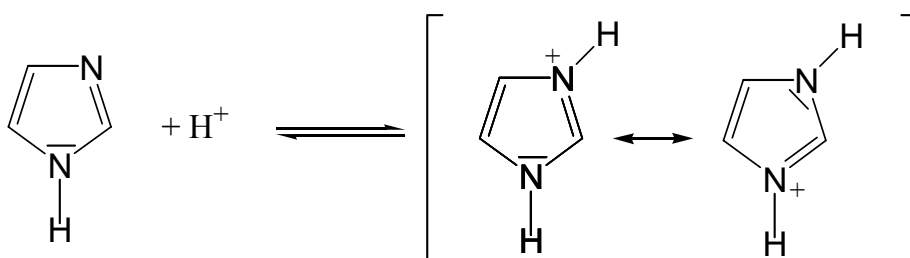


Figure 19. Imidazole resonance-stabilization.⁶³

⁶¹ W. Münch, K. D. Kreuer, W. Silvestri, J. Maier, G. Seifert, *Solid State Ionics* 145 (2001) 437.

⁶² M. Schuster, T. Rager, A. Noda, K. D. Kreuer, J. Maier, *Fuel Cells* 5 (2005) 355.

⁶³ K. P. C. Vollhardt, N. E. Schore, *Organische Chemie*, 3rd Edition, Wiley-VCH, Weinheim, 2000.

2.1.6 Membrane improvements with additives

As already mentioned before, inorganic additives incorporated into the polymer matrix are often used to improve the water uptake, the water retention and the mechanical stability of polymer membranes, and throughout to achieve higher proton conductivity. The proton conductivity mechanism is then facilitated via surface transport occurring along the exposed acid/hydrophilic sites on the surface (inter-layers or pores) which are either involved in the interactions between particles and polymer themselves, or responsible for water domains within the structure which promote the transport similar to polymer membranes. It is this latter water assisted transport which is likely to be the most dominant. Figure 20 illustrates this behavior, the green circle represent incorporated inorganic particles as additives.

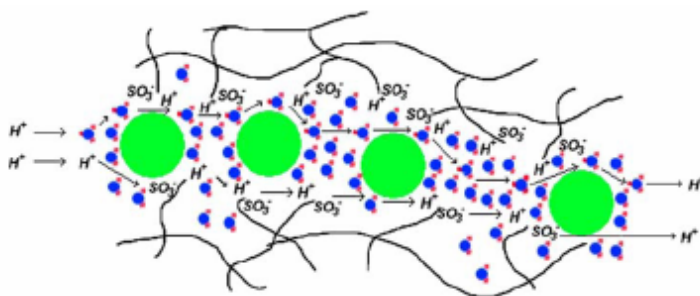


Figure 20. Proton transport in composite membranes.⁵⁵ Additives are shown as green balls, water molecules colored in blue (oxygen) and red (hydrogen).

For example, many composite membranes have been produced using Nafion[®] to improve its properties. Among the already given examples, the influence of addition of silica to Nafion[®], as studied by Antonucci *et al.*⁶⁴, was to improve the retention of water in the membrane and to enable the operation of the fuel cell above 130 °C. A similar method for retaining water in Nafion[®] at higher temperatures by incorporating silica as well as titanium dioxide into a Nafion[®] composite to enable its use in DMFC was

⁶⁴ P.L. Antonucci, A.S. Arico, P. Creti, E. Ramunni, V. Antonucci, *Solid State Ionics* 125 (1999) 431.

studied by Baradie *et al.*⁶⁵ This membrane exhibited a significant improvement in proton conductivity but did not retard methanol crossover. A significant improvement in the conductivity of Nafion[®], at elevated temperatures, by incorporating perfluorinated ionomers in Nafion[®] matrix and by doping it with heteropolyacids (HPA) such as phosphotungstic acid and phosphomolybdenic acid in Nafion[®] was targeted and achieved by Bahar *et al.*⁶⁶ A similar attempt to attain improved ionic conductivity and high power density with the incorporation of HPAs in Nafion[®] 117 membrane was made by Tazi and Savadogo.⁶⁷ Water uptake in the Nafion[®] with incorporated HPA was 60 %, while the pure Nafion[®] membrane only exhibited 27 %. Thus a substantial improvement in ionic conductivity was observed. Zirconium phosphate nanoparticles are for example also used to improve the properties of Nafion[®] membranes.¹³ With the dispersed inorganic phase, synthesized by *in situ* formation, the stability of the proton conductivity can strongly increased of about 20 °C at 85 % RH. Titanium dioxide, protonated zeolites and other silica materials are additional possibilities to fabricate composite membranes with Nafion[®]. Watanabe *et al.* improved the water uptake of Nafion[®] with incorporated silica particles (7 nm) from 17 to 43 wt.-%.¹⁴ Chalkova *et al.* showed with Nafion[®]-TiO₂ composite membranes that a high surface area of the inorganic filler plays a key role in the improvement of the power density of the composite membrane.¹⁹ The proton conductivity of Nafion[®] at 80 °C can also be increased by addition of the protonated zeolite mordenite in the Nafion membrane.²¹ Of course, these concepts can also be applied on other polymer membranes, like the aromatic SPEEK membranes^{8,11,12,20}, or also polysiloxanes and the new polyoxadiazoles.⁶⁸

As new kind of inorganic additives for PEMFC membranes, this work presents the use of new solid proton conductors based on mesoporous SiO₂. The only report on using mesoporous silica materials as additives, but anyway functionalized with a HPA, was

⁶⁵ B. Baradie, J.P. Dodelet, P. Guay, *J. Electroanal. Chem.* 489 (1998) 209.

⁶⁶ B. Bahar, A.R. Hobson, J.A. Kolde, D. Zuckerbrod, US Patent, 5,547,551 (1996).

⁶⁷ B. Tazi, O. Savadogo, *Electrochimica Acta* 45 (2000) 4329.

⁶⁸ D. Gomes, I. Buder, S.P. Nunes, *J. Polym. Sci., Part B: Polym. Phys.* 44 (2006) 2278.

presented by Zaidi *et al.* incorporating them into SPEEK, leading to promising proton conductivities.⁶⁹

New examples using functionalized mesoporous silica materials as additives are shown in section 4. Our concept is to immobilize several proton conductive species on the large internal surface of the mesoporous SiO₂ materials, investigating the proton conductivity properties as solid proton conductors, and then incorporating them in different proton conductive polymers to improve their properties. The high water uptake capability and water retention of the mesoporous SiO₂, also of the produced product water on the cathode side, will be of advantage for the solid proton conductors itself as for the composite membranes. The mesoporous SiO₂ systems used in this work are presented in the following chapters.

2.2 Mesoporous SiO₂ materials

The following chapters introduce the class of mesoporous silica⁷⁰ materials, whose synthesis depicts one of the most important parts of this work. First, the general synthesis of mesoporous silica materials will be presented; introducing the use of amphiphilic structure-directing templates and their self-organization process for enabling highly ordered porous structures in silica during a sol-gel process, including also several detemplating possibilities. The different used surfactants and block-copolymers will be presented for enabling different porous structures in silica materials. In addition, possibilities for size control of the synthesized porous materials will be shown, enabling a pathway to mesoporous nanoparticles. Afterwards, the surface functionalization procedures will be introduced, namely post-synthetically grafting and

⁶⁹ S.M.J. Zaidi, M.I. Ahmad, *J. Membr. Sci.*, 279 (2006) 548.

⁷⁰ Silica describes better the amorphous non-stoichiometric phase of the materials of the formula SiO_{2-x}(OH)_{2x}

in-situ co-condensation process, to enable organic moieties on the surface of the host silica materials. The advantages and problems will be discussed, giving an insight in the complicate chemical processes during functionalization.

2.2.1 Amphiphilic molecules

Amphiphilic molecules consist of a hydrophilic part, the so called head group, and a hydrophobic part. Hydrophobic or hydrophilic parts can be present several times in one molecule.^{71,72,73}

Since these two complete physically different parts exist in one molecule, amphiphilic molecules have a high affinity to interfaces. Their accumulation at surfaces reduces surface and interfacial tensions drastically. This property makes amphiphilic molecules able to build supramolecular aggregates called micelles, to protect their hydrophobic parts against a polar external solvent. Also possible are inverse micelles, where the head groups stick together and the hydrophobic parts protect against a non-polar solvent.⁷⁴ In the following, the focus lies on the most prominent groups of amphiphilic molecule, surfactants.

Figure 21 shows micellar and inverse micellar formation of a typical surfactant, consisting of charged hydrophilic head group and a long hydrophobic carbon chain rest. To protect against the external solution (blue = water, green = oil), the surfactant molecules stick together to disc like or spherical supramolecular aggregates.

⁷¹ F. M. Menger, J. S. Kneiper, *Angew. Chem.* 112 (2000) 1980.

⁷² J. Haldar, V. K. Aswal, P. S. Goyal, S. Bhattacharya, *Angew. Chem. Int. Ed* 30 (2001) 1228.

⁷³ M.S. Bakshi, A. Kaura, R. K. Mahajan, *Colloids Surf. A* 262 (2005) 168.

⁷⁴ H. Rehage, *Chemie in unserer Zeit* 39 (2005) 36.

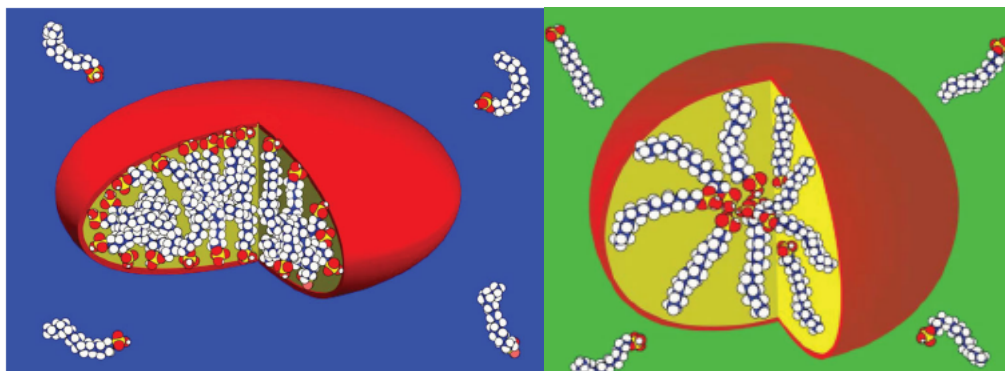


Figure 21. Micelle formation in different media.⁷⁴

Surfactants are classified concerning their molecular structure. One differentiates between anionic, cationic, non-ionic and amphoteric surfactants, which all have a long alkyl rest (C_n) as hydrophobic part and only differ in the chemical nature of their head group. Most of the surfactants have abbreviation resulting from their chemical structure, which are often used in literature. One example is hexadecyltrimethylammonium bromide ($C_{16}TMABr$), which is also called Cetyltrimethylammonium bromide. Its abbreviation is therefore CTAB. CTAB is the most famous example of a cationic surfactant.

One example for an anionic surfactant is sodium dodecylsulfate ($C_{12}OSO_3Na$), which is often abbreviated as SDS. It has also an alkyl chain, but connected to a sulfate group. Normally, sodium is used as counter ion. Figure 22 shows some examples for the four kinds of surfactant types, including CTAB and SDS.

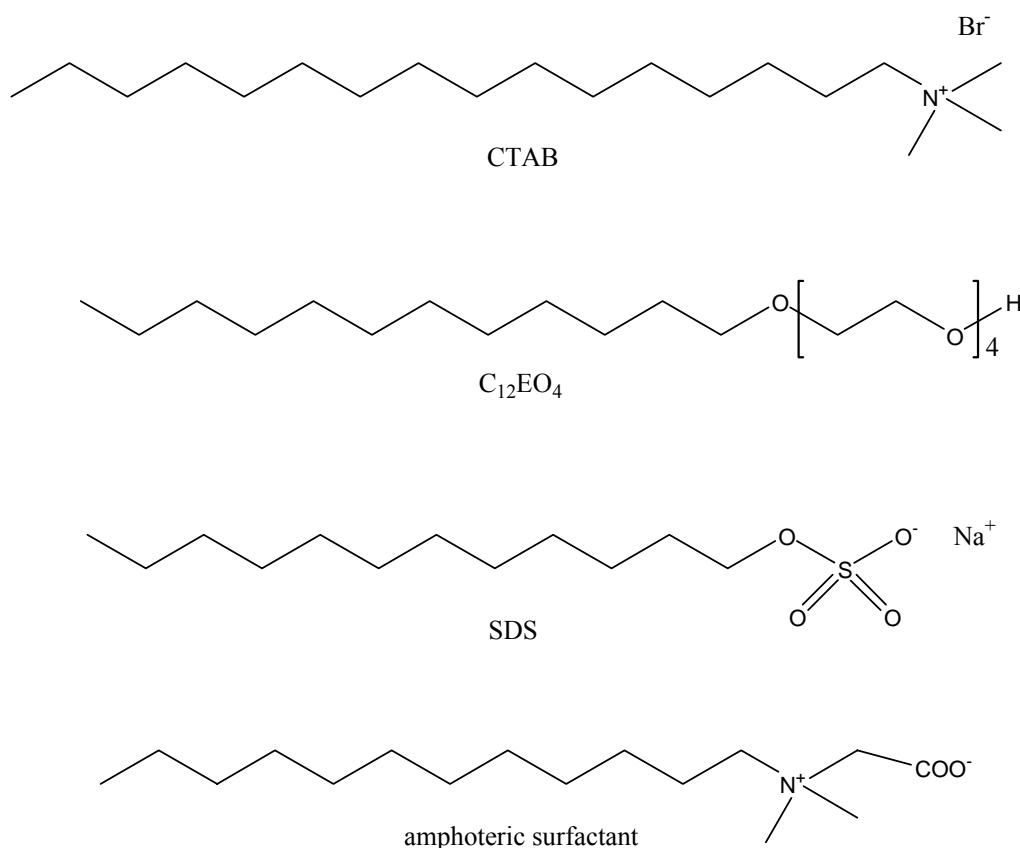


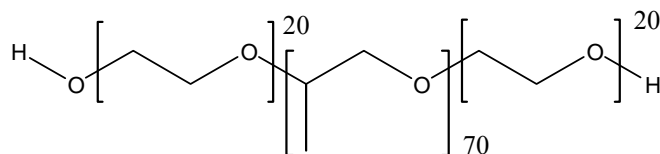
Figure 22. Surfactants with different chemical head groups.⁷⁴

Tetraethyleneglycol monododecylether is an example for a non-ionic surfactant. The C_{12} chain ends in a hydrophilic head consisting of four ethylene oxide (EO) blocks. As the number x of EO blocks is indicated as EO_x , tetraethyleneglycol monododecylether has the abbreviation C_{12}EO_4 . To complete the row, an example of an amphoteric surfactant, where the head group includes a cationic and an anionic group, is shown.

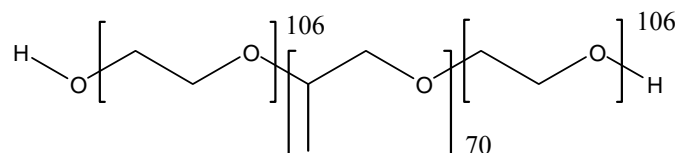
Another class of amphiphilic molecules is block-copolymers. These macromolecules are also able to form micellar structures, but are, in contrast to most surfactants, uncharged.⁷⁵ To build supramolecular structures, hydrophilic A-blocks (e.g. polyethylene oxide EO) and hydrophobic B-block (e.g. poly-propylene oxide PO) must be connected in one molecule. Diblock-copolymers AB or Triblock-copolymers ABA are

⁷⁵ S. Bagshaw, E. Prouzet, T. Pinnavaia, *Science* 269 (1995) 1242.

possible. The two most prominent and most often used Triblock-copolymers are shown in Figure 23.



(EO)₂₀(PO)₇₀(EO)₂₀, Pluronic P123



(EO)₁₀₆(PO)₇₀(EO)₁₀₆, Pluronic F127

Figure 23. Triblock-copolymers P123 und F127.⁷⁶

2.2.2 Micellar structures and self-assembly

Surfactants and block-copolymers form micelles in aqueous systems, which can have several structures. The micellar structure hereby depends on the concentration of the amphiphilic molecule in water. At low concentrations, no micelles are formed, most of the amphiphilic molecule organize themselves at the interface air-liquid or are homogenously dispersed. Above a certain surfactant concentration in water, the critical micelle concentration (cmc), micellar structures are formed, and the amphiphilic molecules begin to aggregate to spherical micelles. In addition, micelle formation

⁷⁶ G. Wanka, H. Hoffmann, W. Ulbricht, *Macromolecules* 27 (1994) 4145.

depends also on temperature. The solubility of an amphiphilic molecule escalates at a certain, molecule characteristic temperature. This point is called Krafft-point.^{77,78}

From the thermodynamically point of view, micellar structures are formed due to the gain in entropy caused by the lowering of contact area between water and the hydrophobic chains. The hydrophobic chains inside the micelle are connected via van-der-Waals interactions. The hydrophilic head groups instead form contorted surfaces due to electrostatic repulsion. But a micelle is not a static system; equilibrium exists between the micellar system and the ambient solution. A fast (with a C₁₆-chain about 1 ms) exchange of amphiphilic molecules between the micelle and the solution takes place, as already indicated in Figure 21.

After reaching the cmc, spherical micelles are formed. When the concentration of surfactants is further increased, the second cmc (cmc2) is reached where the spherical micelles are transformed into cylindrical or rod-like micelles. The structure transformation is caused by the increase of the solutions ion strength due to more added surfactants, the spherical micelles become elongated. With further increasing surfactant concentration, mesophases or lyotropic phase are formed.

Systems are called mesophases when their degree of ordering of the system is similar to a crystal, but not endless expanded. The molecules exhibit a preferred orientation, but the ordering is still lower than in a solid crystal. Examples for mesophases are the lyotropic crystals formed by amphiphilic molecule in water, depending on temperature and concentration. Figure 24 shows this behavior exemplarily with the phase diagram for CTAB/water.

After crossing the cmc2 by increasing the surfactant concentration, the cylindrical micelles are formed. These micelles are still separated from each other dispersed in the solution. With further increasing the amount of surfactant, these cylindrical micelles assemble themselves in a hexagonal liquid crystal phase H₁. The reasons for that are not clear, but one reason might be the minimization of repulsive interaction via this regular

⁷⁷ M. Almgren, W. Brown, S. Hvidt, *Colloid Polym. Sci* 273 (1995) 2.

⁷⁸ K. Bryskhe, S. Bulut, U. Olsson, *J. Phys. Chem. B* 109 (2005) 9265.

ordering. Also a gain in entropy is possible while water molecules are set free around the area of the micelle, favoring the formation of a lyotropic phase.

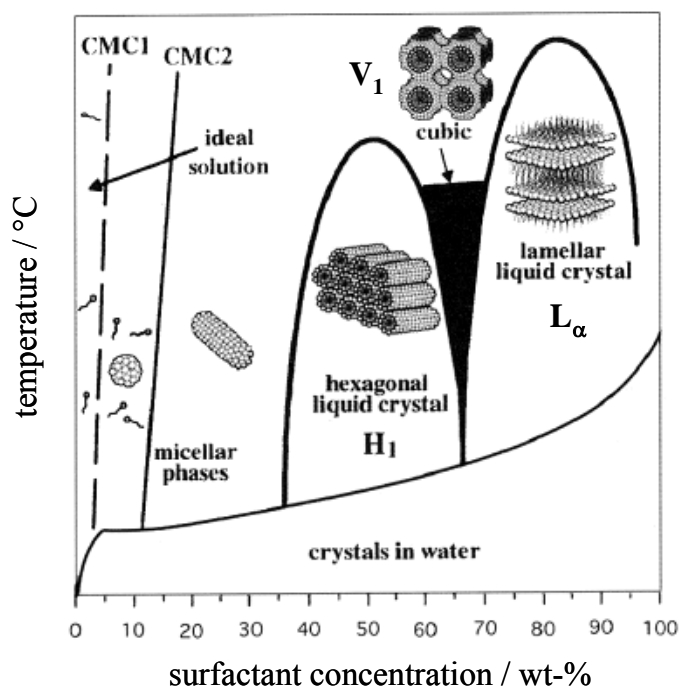


Figure 24. Phase diagram for the binary system CTAB in water.⁷⁹

Other lyotropic phases are formed when the surfactant concentration is again further increased, resulting in a cubic phase V_1 or a lamellar phase L_α , where the surface tension of the micelles continuously deteriorates. However, the shape of the micelles in solution can be changed by additives.⁸⁰ Counter ions near to the micelle surface have for example a strong influence elongating the micelles.⁸¹ And the addition of alcohols like methanol results in growth of the micelles.⁸² Recent research also showed that even

⁷⁹ C. J. Brinker, Y. Lu, A. Sellinger, H. Fan, *Adv. Mater.* 11 (1999) 579.

⁸⁰ H. Wellmann, Dissertation: *Synthese und Charakterisierung von Halbleiter-Nanokristallen in keramischen Matrices*, University Bremen, 2000.

⁸¹ S. Ikeda, *Colloid Polym. Sci.* 269 (1991) 49.

⁸² M. T. Anderson, J. E. Martin, J. Odinek, P. Newcomer, *Chem. Mater.* 10 (1998) 311.

below the cmc, small amounts of micelles already exist, being helpful in the electrochemical deposition on ZnO.⁸³

The existence of lyotropic phases is essential for the formation of the different structures of mesoporous materials. These structures are introduced in the following chapter.

2.2.3 Nanoporous silica materials, M41S and SBA

Porous materials can be clearly distinguished to the usual dense solids synthesized in solid state chemistry. Instead of high temperatures (~1000 °C) or pressures for the synthesis of crystalline and dense solids, less dense or porous materials are mostly produced at lower temperatures under kinetically control, meaning that the produced solids are not obtained in their thermodynamically stable phase, but in a metastable phase. A good example for this kind of synthesis procedure is hydrothermal synthesis.⁸⁴ In a closed reaction vessel with an aqueous medium, at temperature slightly above 100 °C and pressures therefore higher than 1 bar, special reaction conditions are taking place, with which metastable solid phases can be synthesized. The principle behind is the Ostwald step rule, saying that crystallization from solution occurs via several thermodynamically unstable (metastable) phases. When the reaction is stopped at a given time, it is possible via hydrothermal synthesis to synthesize one exact metastable phase out of these crystallization steps. This is not possible via classical solid state chemistry, where mostly all the small activation energies for metastable phase transitions are completely skipped due to the high reaction temperatures. The synthesis of quartz is an example for a hydrothermal synthesis.

⁸³ C. Boeckler, T. Oekermann, A. Feldhoff, M. Wark, *Langmuir* 22 (2006) 9427.

⁸⁴ A. Rabenau, *Angew. Chem.* 97 (1985) 1017

The synthesis of nanoporous⁸⁵ materials is also possible via kinetic reaction control, at temperatures between 25 and 200 °C. The pores in these materials are obtained via incorporation molecules or molecule aggregates while crystallizing matter around these templates. The templates incorporated are called “guest” molecules, if the condensed matter formed is called the host. If the molecules (aggregates) influence the formed crystal or porous structure, the templates are called structure directing agents (SDA).

Nanoporous materials are classified via IUPAC⁸⁶ concerning their pore diameters in three different groups, shown in the following Table 2 with some examples.

Table 2. Nanoporous materials following IUPAC.⁸⁷

pore diameter	material	example
< 2 nm	microporous	zeolites, zeosiles
2 – 50 nm	mesoporous	Si-MCM-n, Si-SBA-n
> 50 nm	macroporous	inverse opal, porous glass

But although the diameters are classified, the pore size distributions of the materials can differ. Zeolites, microporous aluminosilicates, and zeosiles, microporous silicates, show a very narrow pore size distribution, as sketched in Figure 25.

Mesoporous materials have first been synthesized in 1992 from Beck et al.^{22,23} when these Mobil scientists synthesized the M41S mesoporous silica materials. They used the lyotropic phases of amphiphilic molecules described in chapter 2.2.2 for structuring and preparing inorganic-organic composites which exhibit, after calcinations, highly ordered porous structures made from amorphous inorganic material. Their pores have been significantly larger than the so far known zeolites, whose micropores are not accessible for larger molecules in catalysis.

⁸⁵ accepted notation for pores < 200 nm, G. P. Androustopoulos, C. E. Salmas, *Ind. Eng. Chem.* 39 (2000) 3747.

⁸⁶ International Union of Pure and Applied Chemistry, www.iupac.org, April 2008.

⁸⁷ K. S. W. Sing, D. H. Everett, R. A. Haul, L. Moscou, R. A. Pierotti, J. Rouquerol, T. Siemieniowska, *Pure Appl. Chem.* 57 (1985) 603.

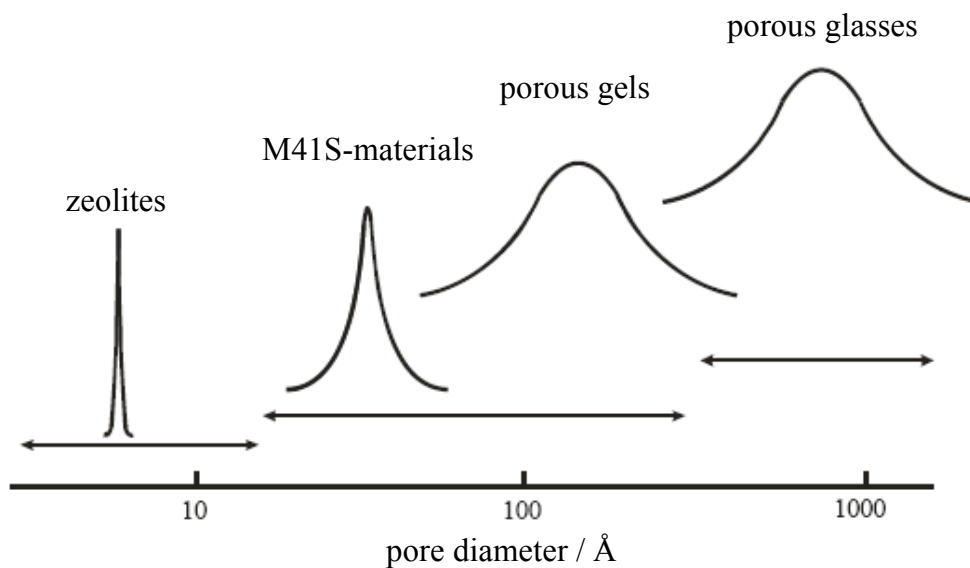


Figure 25. Pore widths and pore size distribution of nanoporous materials.⁸⁸

The most famous example of the M41S family is Si-MCM-41 (MCM = Mobil Composition of Matter) exhibiting a hexagonally ordered pore structure of one-dimensional channels, belonging to the space group $P6mm$. Figure 26 shows schematically the composite of silica and surfactant CTAB of Si-MCM-41.

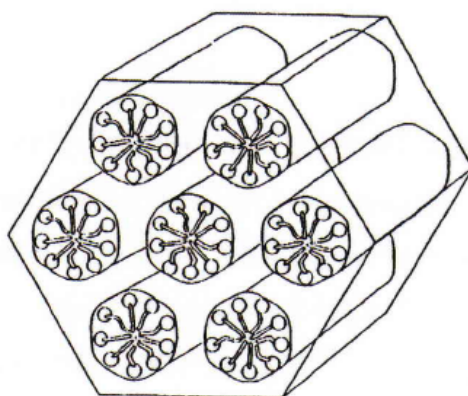


Figure 26. Si-MCM-41 structure model with incorporated surfactants (taken from Ref. 89).

⁸⁸ P. Behrens, *Adv. Mater.* 5 (1993) 127.

The pore size of Si-MCM-41 can be tuned from 2 nm to 10 nm, with walls between 0.7 and 1 nm for a typical synthesis, which are only two to three layers of silica.^{22,90,91} And because its pores are comparably large, they can be directly seen in transmission electron microscopy (TEM, Figure 27).

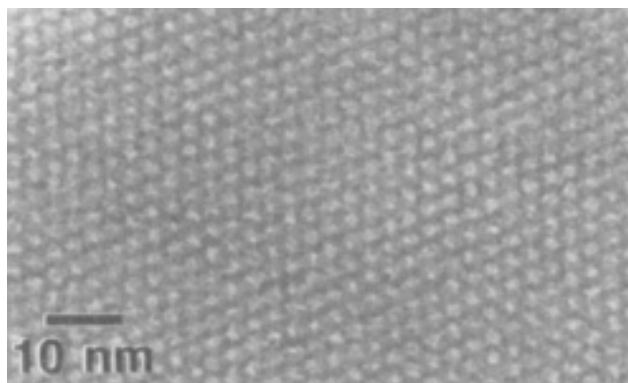


Figure 27. TEM-micrograph of Si-MCM-41.²³

The pores of Si-MCM-41 are not round, they are formed nearly hexagonally. Only when the wall thickness is increased to 1 nm, the pores are nearly perfect round shaped.⁹² Figure 28 depicts this circumstance additionally.

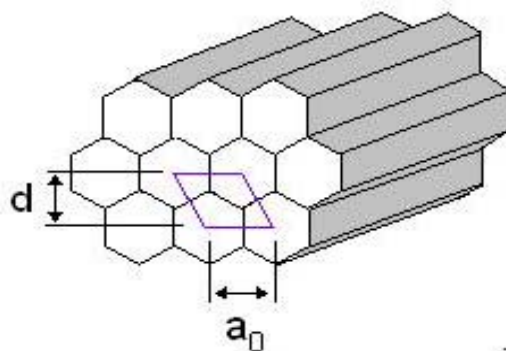


Figure 28. Scheme of hexagonally shaped pore in Si-MCM-41 with structural indices.

⁸⁹ B. Ufer, Dissertation, Leibniz Universität Hannover, 2007.

⁹⁰ A. Sayari, M. Kruk, M. Jaroniec, I. Moudrakovski, *Adv. Mater.* 10 (1998) 1376.

⁹¹ C.-Y. Chen, H.-X. Li, M. Davis, *Microporous Mater.* 2 (1993) 17.

⁹² A. Corma, *Chem. Rev.* 97 (1997) 2373.

The walls of Si-MCM-41 are made of amorphous silica, so no crystalline reflections can be observed in X-ray powder diffraction measurements along the channel direction. In the direction of the pore opening, the hexagonal periodicity of the materials produces X-ray reflections due to the short range ordering of the materials, but only $hk0$ -reflections. From 2θ -angles between 0.5 and 10, lattice constants a_0 can be calculated, giving an insight in the pore sizes and wall thicknesses (together with sorption measurement results). More details are described in the experimental section 3. But due to their large pores and thin walls, mesoporous materials of M41S-type feature low external surface areas ($< 10 \text{ m}^2/\text{g}$) and a large internal surface (around $1000 \text{ m}^2/\text{g}$).

The Mobil scientist synthesized the M41S materials because they were searching for a catalytic active material having large pores for large molecules, applicable in heterogeneous catalysis. Si-MCM-41 itself nevertheless shows no catalytic activity. Only substituting framework silicon via metal atoms, e.g. aluminum^{23,93,94}, boron^{95,96}, iron⁹⁷, manganese⁹⁸, titanium^{99,100,101}, vanadium^{102,103} or zirconium¹⁰⁴ generates catalytic centers in mesoporous materials.

Si-MCM-41 is usually synthesized in a hydrothermal process, using CTAB as surfactant and tetraethyl orthosilicate (TEOS) as silicon source. Rathousky *et al.* presented in 1998 a new method called “homogeneous precipitation” for the synthesis of Si-MCM-41, which is used in this work exclusively (chapter 3.2.1).¹⁰⁵ In this method, CTAB and sodium metasilicate are diluted in water, and by adding ethyl acetate, its hydrolysis to acetic acid ensures a highly homogeneous acidification of the reaction mixture and

⁹³ G. A. Eimer, P. L.B., G. A. Monti, O. A. Anunziata, *Catalysis Letters* 78 (2002) 65.

⁹⁴ R. Ryoo, J. M. Kim, C. H. Ko, *Stud. Surf. Sci. Catal.* 117 (1998) 151.

⁹⁵ A. Sayari, C. Danumah, I. L.Moudrakovski, *Chem. Mater.* 7 (1995) 813.

⁹⁶ A. Sayari, I. L.Moudrakovski, C. Danumah, C. I. Ratcliffe, J. A. Ripmeester, K. F. Preston, *J. Phys. Chem.* 99 (1995) 16373.

⁹⁷ Z. Y. Yuan, S. Q. Liu, T. H. Chen, J. Z. Wang, H. X. Li, *Chem. Commun.* (1995) 973.

⁹⁸ D. Zhao, D. Goldfarb, *Chem. Commun.* (1995) 875.

⁹⁹ A. Corma, M. T. Navarro, P. J. Pariente, *Chem. Commun.* (1994) 147.

¹⁰⁰ A. Corma, Q. Kann, F. Rey, *Chem. Commun.* (1998) 579.

¹⁰¹ M. S. Morey, S. O'Brien, S. Schwarz, G. D. Stucky, *Chem. Mater.* 12 (2000) 898.

¹⁰² K. M. Reddy, I. L.Moudrakovski, A. Sayari, *Chem. Commun.* (1994) 1059.

¹⁰³ M. S. Morey, A. Davidson, H. Eckert, G. D. Stucky, *Chem. Mater.* 8 (1996) 486.

¹⁰⁴ M. S. Morey, G. D. Stucky, S. Schwarz, M. Fröba, *J. Phys. Chem. B* 103 (1999) 2037.

¹⁰⁵ J. Rathousky, M. Zukalova, A. Zukal, J. Had, *Collect. Czech. Chem. Comm.* 63 (1998) 1893.

consequently a uniform hydrolysis-condensation reaction of metasilicate. After a few minutes, a homogeneous precipitate can be observed. The result after calcination (to clear the pores of surfactant molecules) is Si-MCM-41 with narrower particle size distribution and uniform morphology.

Si-MCM-41 can be synthesized in several morphologies, not only μm -sized particles, but also as mesoporous nanoparticles. The first attempts to produce mesoporous nanoparticles go back to Park *et al.* who used ethylene glycol and microwave irradiation to produce particles of around 200 nm.¹⁰⁶ Also the use of mixtures of triblock-copolymer F127 and surfactant CTAB led to a drastically size reduction in the synthesis.¹⁰⁷ Working in high dilution results in mesoporous nanoparticles due to the reduction of the condensation velocity of the silicon source.^{108,109} Also a temperature influence^{108,109} and a pH control¹¹⁰ could be observed. By complexing TEOS with triethanolamine, the number of reactive seed crystal could be recently reduced and controlled, but the mesoporous pore structure is more star like.¹¹¹ In this work, we use a modified synthesis after Cai *et al.*¹⁰⁸ to produce mesoporous nanoparticles of Si-MCM-41 (chapter 3.2.1).

Besides the hexagonally ordered structures of Si-MCM-41, also cubic and lamellar mesoporous silica structure of the M41S family can be synthesized with the same procedure. Figure 29 shows two other silica composites of the M41S family.

Si-MCM-48 has a cubic structure, belongs to the space group $Ia\bar{3}d$ and is comparable to the lyotropic cubic phase. Si-MCM-48 consists of two independent but interpenetrative channel systems, acting like image and mirror image. The thickness of the walls and the pore diameters are comparable to Si-MCM-41. Si-MCM-50 is a lamellar composite material. The layered structure is only stable with incorporated surfactant molecules, after calcination the mesoporous structure collapses.

¹⁰⁶ S.E. Park, D.S. Kim, J.S. Chang, W.Y. Kim, *Catal. Today* 44 (1998) 301.

¹⁰⁷ K. Suzuki, K. Ikari, H. Imai, *J. Am. Chem. Soc.* 126 (2004) 462.

¹⁰⁸ Q. Cai, Z.-S. Luo, W.-Q. Pang, Y.-W. Fan, X.-H. Chen, F.-Z. Cui, *Chem. Mater.* 13 (2001) 258.

¹⁰⁹ J. Rathousky, M. Zukalova, P.J. Kooyman, A. Zukal, *Colloids Surf. A* 241 (2004) 81.

¹¹⁰ R. I. Nooney, D. Thirunavukkarasu, Y. Chen, R. Josephs, A. E. Ostafin, *Chem. Mater.* 14 (2002) 4721.

¹¹¹ K. Möller, J. Kobler, T. Bein, *Adv. Funct. Mater.* 17 (2007) 605.

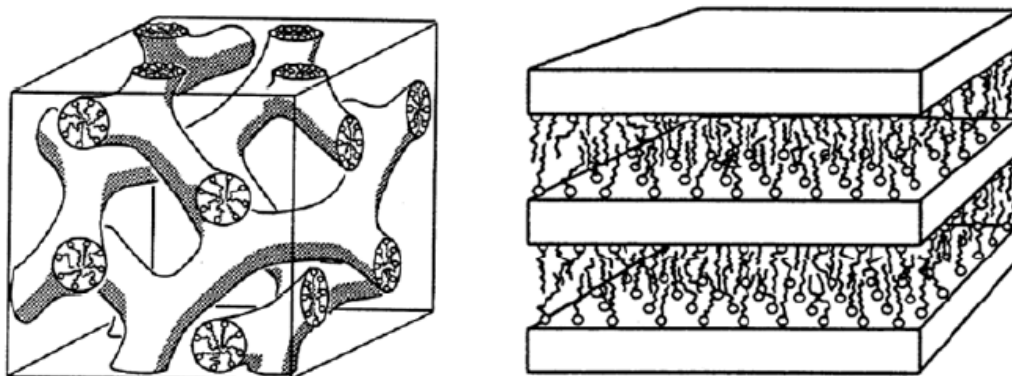


Figure 29. Si-MCM-48 and Si-MCM-50 structures as host-guest-composites with incorporated surfactant (taken from Ref. 89)

With the aim to synthesize mesoporous materials with larger pores and thicker pore walls, in 1998 Zhao *et al.* used triblock-copolymers as structure directing agents to synthesize ordered mesoporous silica materials of the SBA (University of Santa Barbara) family^{112,113} with pore diameters of up to 30 nm and wall thicknesses of 3 to 6 nm. One famous example is the Si-SBA-15, which has like Si-MCM-41 hexagonally ordered mesopores (space group $P6mm$), but with larger diameters than in Si-MCM-41. As porous structure is enabled via using P123 as structure directing agent, also the pore size of Si-SBA-15 can be tuned in a wide range changing the reaction conditions.¹¹⁴

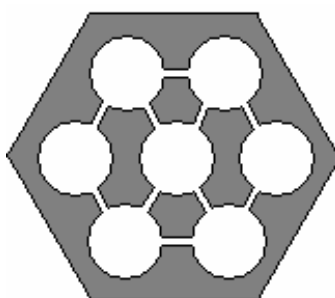


Figure 30. Hexagonal pore structure scheme of Si-SBA-15 with interconnecting micropores.¹¹⁵

¹¹² D. Zhao, J. Feng, Q. Huo, N. Melosh, G. H. Fredrickson, B. F. Chmelka, G. D. Stucky, *Science* 279 (1998) 548.

¹¹³ D. Zhao, Q. Huo, J. Feng, B. F. Chmelka, G. D. Stucky, *J. Am. Chem. Soc.* 120 (1998) 6024.

¹¹⁴ F. Zhang, Y. Yan, H. Yang, Y. Meng, C. Yu, B. Tu, D. Zhao, *J. Phys. Chem. B* 109 (2005) 8723.

One important structural difference between Si-MCM-41 and Si-SBA-15 is the existence of additional micropores in Si-SBA-15 connecting the mesopores, depicted in Figure 30. This structural property used Ryoo *et al.* in 1990 to synthesize a stable carbon replica by filling the pores with a carbon precursor followed by pyrolysis. This procedure is called “nano-casting”, a good overview gives Ref. 115.

Finally, another famous example of the SBA family is Si-SBA-16, synthesized with F127 as structure directing agent. Si-SBA-16 has a cubic pore structure, belonging to the space group $Im\bar{3}m$. Figure 31 shows a cut-out of its structure. The Si-SBA-16 pore system consists of small cages of around 8 nm in diameter, connected via narrow channels with each other forming a cubic structure.

Si-MCM-41 as well as Si-SBA-15 and Si-SBA-16 are synthesized in this work as host for organic moieties, preparing new solid proton conductors (chapter 3.2.1).

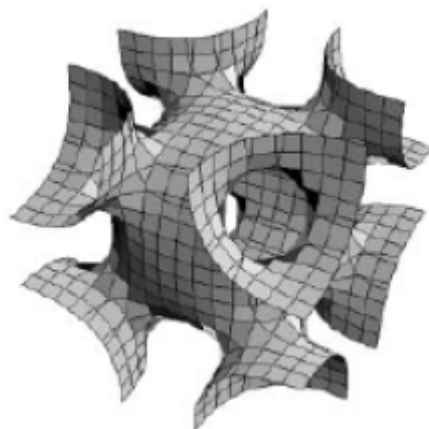


Figure 31. Structure model of cavities and their interconnection in Si-SBA-16.¹¹⁶

¹¹⁵ A.-H.Lu, F. Schüth, *Adv. Mater.* 18 (2006) 1793.

¹¹⁶ Y. Sakamoto, M. Kaneda, O. Terasaki, D. Zhao, J. M. Kim, G. D. Stucky, H. J. Shin, R. Ryoo, *Nature* 408 (2000) 449.

2.2.4 Formation processes of mesoporous materials

The true mechanism for the formation of mesoporous silica materials is unknown until now. Several mechanisms have been proposed since the discovery of the M41S family, and all of them depend on the interactions between the surfactants (and its lyotropic phases, see chapter 2.2.2) and the silica precursors. The most prominent and accepted mechanisms will be presented here, the true liquid crystal template mechanism (TLCT) and the mechanism of cooperative self-organization.

Already from the discovery, Beck *et al.* postulated the TLCT mechanism.²³ They proposed that, after the formation of the hexagonal lyotropic phase H_1 with CTAB, the spaces in between this arrangement are filled with the silica precursor forming the mesophase, shown in Figure 32.

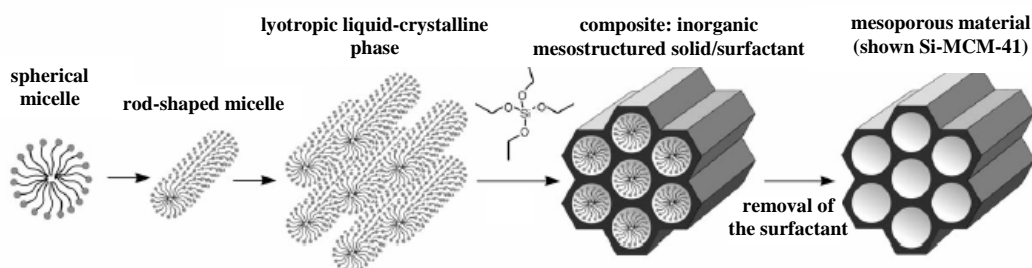


Figure 32. Formation of a mesoporous silica structure via TLCT mechanism.²⁴

However, this mechanism could not have been possible under the original reaction conditions under hydrothermal synthesis. The used surfactant concentration was far too low under the cmc of CTAB, and Davies *et al.* also found no evidence for this mechanism using ^{14}N -MAS-NMR, no hexagonally ordered cylindrical micelles could be observed.¹¹⁷ Anyway, under given circumstances the TLCT mechanisms is found and not completely withdrawn, e.g. when Attard *et al.* synthesized a hexagonal mesophase from polyethylene oxide solution.¹¹⁸ So, Davies proposed a cooperative

¹¹⁷ C.-Y. Chen, S. L. Burkett, H.-X. Li, M. E. Davies, *Microporous Mater.* 2 (1993) 27.

¹¹⁸ G. S. Attard, J. C. Glyde, C. G. Göltner, *Nature* 378 (1995) 366.

mechanism where the rod-shaped micelles were coated with few layers of silica, and the coated rods aggregate then to the hexagonal mesophase (Figure 33, way 2). This mechanism is called the cooperative self-organization process. Besides Davies' approach, Steel *et al.* postulated, instead of silica-coated rod-shaped micelles, the formation of silica layers with incorporated cylindrical micelles, which are then folded during the reaction forming the hexagonal Si-MCM-41 (Figure 33, way 1).¹¹⁹ If the surfactant concentration is too low, the folding can be hindered and the lamellar structures could be obtained. This mechanism was confirmed also by TEM observations, especially the transformation from lamellar to hexagonal structure.¹²⁰

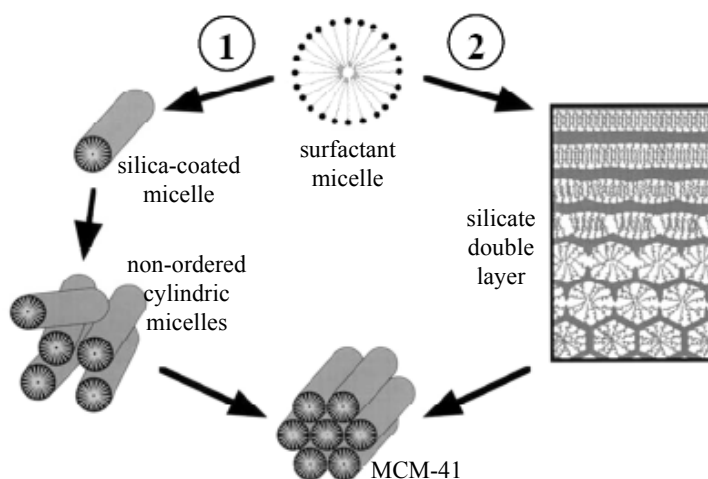


Figure 33. Two model for the cooperative self-organization process.¹²¹

As a modification of these mechanisms, taking into account the complicate ionic interactions between surfactant and silica-precursor, Firouzi *et al.* approved 1995, via *in-situ* $^1\text{H-NMR}$ and $^{29}\text{Si-NMR}$ and neutron scattering, the existence of a true cooperative self-organization process under silica condensation prohibiting

¹¹⁹ A. Steel, S. W. Carr, S. W. Anderson, *Chem. Commun.* (1994) 1571.

¹²⁰ V. Alfredsson, M. Keung, A. Monnier, G. D. Stucky, F. Schüth, *Chem. Commun.* (1994) 921.

¹²¹ J. Vartuli, W. Roth, J. Beck, S. McCullen, C. Kresge (Ed.), *The synthesis and properties of M41S and related mesoporous materials*, Springer, Heidelberg, 1st edition, 1998.

conditions.¹²² After adding a silica precursor to the solution of unordered CTAB micelles (Figure 34A), they observed the transformation into a hexagonal phase without condensation of the silica precursors forming an inorganic, non-condensed salt-like mesophases. The silica anions interact with the surfactant counter ions in an ion exchange mechanism forming a silicotropic liquid crystal (SLC) (Figure 34B). These SLCs aggregate then to SLC phases (Figure 34C) similar to the lyotropic phases (see chapter 2.2.2), but in contrast the surfactant concentrations are much lower, and the silica counter ions are reactive. By heating, the condensation took place forming Si-MCM-41.

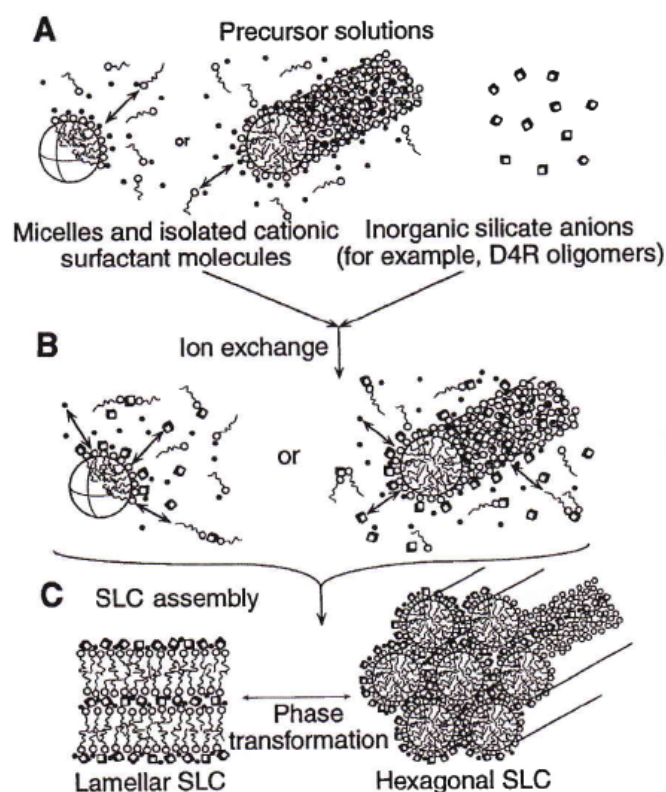


Figure 34. Formation of a silicotropic liquid crystal (SLC) phase.¹²²

¹²² A. Firouzi, D. Kumar, L. M. Bull, T. Besier, P. Sieger, Q. Huo, S. A. Walker, J. A. Zasadzinski, C. Glinka, J. Nicol, D. Margolese, G. D. Stucky, B. F. Chmelka, *Science* 267 (1995) 1138.

Firouzi *et al.* also showed later that the ion exchange between the surfactant counter ions and the silica anions is favorable with the existence of D4R (double-4-ring $[\text{Si}_8\text{O}_{20}]^{8-}$) under the reaction conditions,¹²³ due to the similarity in the calculated areas of D4R anions (0.098 nm^2) and the ammonium head group of CTAB (0.094 nm^2) resulting in an optimum charge distribution on the surface of the SLCs.

The interactions between the surfactant and the precursor play, as already seen, a fundamental role in the formation of the silica mesophases, so that a composite structure and no phase separation occur. Figure 35 illustrates the different interactions that can take place between the inorganic components and the head groups of the surfactants. According to the suggestion of Huo *et al.*^{124,125} these interactions are classified as follows: If the reaction takes place under basic conditions (when the silica species are present as anions) and cationic quaternary ammonium surfactants are used as the SDA, the synthetic pathway is termed S^+I^- (Figure 35a; S: surfactant; I: inorganic species). The preparation can also take place under acidic conditions (below the isoelectrical point of the Si-OH bearing inorganic species; $\text{pH} \sim 2$), whereby the silica species are positively charged. To produce an interaction with the cationic surfactant, it is necessary to add a mediator ion X^- (usually a halide) ($\text{S}^+\text{X}^-\text{I}^+$; Figure 35b) to attenuate repulsion forces via weak hydrogen bonds. In contrast, when negatively charged surfactants (e.g., long-chain alkyl sulfates) are used as the SDA, it is possible to work in basic media, whereby again a mediator ion M^+ must be added to ensure interaction between the equally negatively charged silica species ($\text{S}^-\text{M}^+\text{I}^-$; Figure 35c); a mediator ion is not required in acidic media (S^+I^- ; Figure 35d). Thus, the dominating interactions in pathways (a–d) are of electrostatic nature. Moreover, it is still possible to form attractive interactions via hydrogen bonds. This is the case when non-ionic surfactants are used (e.g., S^0 : a long chain amine, N^0 : polyethylene oxide), whereby uncharged silica species (S^0I^0 ; Figure 35e) or ion pairs ($\text{S}^0(\text{XI})^0$; Figure 35f) can be present.

¹²³ A. Firouzi, F. Atef, A. G. Oertli, G. D. Stucky, B. F. Chmelka, *J. Am. Chem. Soc.* 119 (1997) 3596.

¹²⁴ Q. Huo, D. I. Margolese, U. Ciesla, P. Feng, T. E. Gier, P. Sieger, R. Leon, P. M. Petroff, F. Schüth, G. D. Stucky, *Nature* 368 (1994) 317.

¹²⁵ Q. Huo, D. I. Margolese, U. Ciesla, D. G. Demuth, P. Feng, T. E. Gier, P. Sieger, A. Firouzi, B. F. Chmelka, F. Schüth, G. D. Stucky, *Chem. Mater.* 6 (1994) 1176.

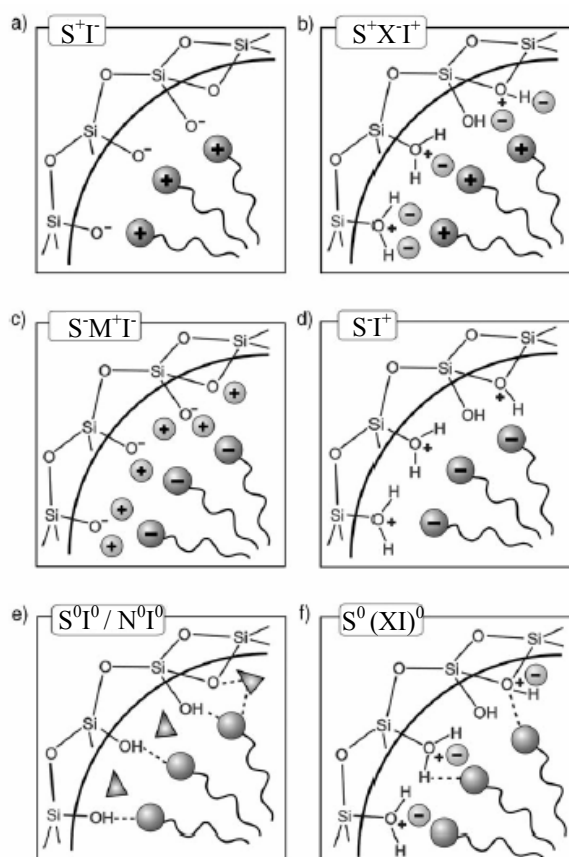


Figure 35. Possible synthetic routes with surfactant and inorganic species.²⁴

2.2.5 Detemplation and surface properties of amorphous silica

The detemplation of a template-silica composite is necessary to obtain the desired mesoporous silica material. To remove the template, different strategies are present in literature. The most prominent way is calcination, which is already used since the discovery of these materials.²³ All organic guests are hereby completely combusted in air at temperatures around 550 to 600 °C. One disadvantage of calcinations is the ongoing lattice change; in the calcination at too high temperatures, the pore diameter deteriorates and, due to condensation, the number of silanol-groups on the surface (see

below) decreases. Thus, scientists found new methods to extract the template SDA out of the silica host. Alternatives to calcinations are supercritical extraction¹²⁶ or treatment with ozone.^{127,128} In both cases, the pore radius remains constant, and all organic guests are removed.

But the mentioned methods have one big disadvantage: Intentionally incorporated organics, which should remain inside the pores (see chapter 2.2.6), are destroyed as well during these procedures. So, mild detemplation methods had to be found. One very selective method is the extraction with solvents, mostly with ethanol. Especially materials formed via $S^+X^-I^+$ or $S^{0}I^0$ mechanism can be completely extracted with pure ethanol under reflux for one day.^{125,129} In contrast, this method cannot be applied to e.g. Si-MCM-41 materials prepared in acidic media, in which strong electrostatic interactions (S^+I^-) between surfactant and the inorganic network exist. Thus, an additional cationic donor-ion is added to the solvent. Acidified ethanol (with low amounts of hydrochloric acid) is used to extract the template then.⁹¹

To reduce the extraction time, Lang *et al.* used a simple ion exchange method for the template removal, using NH_4NO_3 in ethanol.¹³⁰ The detemplation time could thereby be reduced to 45 minutes stirring the mixture at 60 °C due to the higher efficiency in exchange with NH_4NO_3 compared to HCl. In addition, the used template could be recovered. Finally, microwave treatment can be applied for template removal. Tian *et al.* presented this method for the extraction of either Si-MCM-41 or Si-SBA-15/16.¹³¹ The digestion times were only 2 - 5 minutes due to the efficient and fast heating via microwave radiation, using a mixture of HNO_3/H_2O_2 at 200 °C. The so extracted materials showed higher surface area, higher pore volumes and higher pore sizes than calcined materials, and additionally a higher number of surface silanol groups. Several detemplation results are presented in chapter 4.1.1.

¹²⁶ S. Kawi, M.W. Lai, *Chem. Commun.* (1998) 1407.

¹²⁷ M. T. J. Keene, R. Denoyel, P. L. Llewellyn, *Chem. Commun.* (1998) 2203.

¹²⁸ G. Büchel, R. Denoyel, P. L. Llewellyn, J. Rouquerol, *J. Mater. Chem.* 11 (2001) 589.

¹²⁹ P. T. Tanev, T. J. Pinnavaia, *Science* 271 (1996) 1267.

¹³⁰ N. Lang, A. Tuel, *Chem. Mater.* 16 (2004) 1961.

¹³¹ B. Tian, X. Liu, C. Yu, F. Gao, Q. Luo, S. Xie, B. Tu, D. Zhao, *Chem. Commun.* (2002) 1186.

The chemical reactivity of surfaces of amorphous silica depends strongly on the existence of these hydrophilic silanol groups. The pore walls of mesoporous materials locally show properties as amorphous silica¹³², and the existing surface silanol groups can be defined in groups (Figure 36):

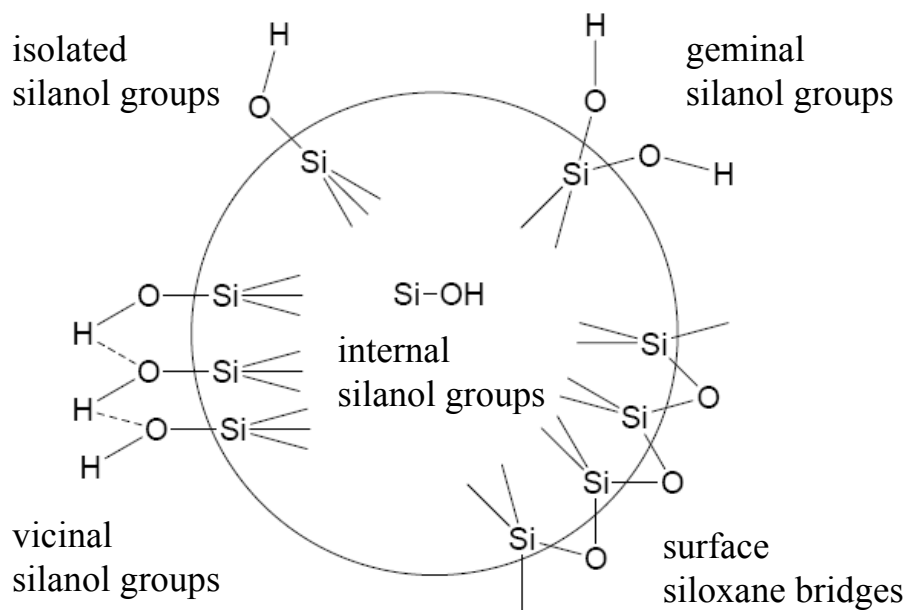


Figure 36. Types of silanol groups on a silica particle surface.¹³³

In isolated free silanol groups, geminal free silanol groups and vicinal (connected via hydrogen bonds) silanol groups. Geminal silanol group can not form hydrogen bonds in between.¹³⁴ Also siloxane groups exist on the silica surface, and internal silanol groups exist which are formed during the condensation processes. At a temperature of 25 °C under vacuum (all assumptions of the here presented Zhuravlev model are made for samples under vacuum), the silica surface is maximum hydrolyzed, means all type of silanol groups are existent, and the silanol groups are connected to adsorbed water via

¹³² M. Kruk, M. Jaroniec, A. Sayari, *Chem. Mater.* 11 (1999) 492.

¹³³ L. T. Zhuravlev, *Colloids Surf., A* 61 (2000) 1.

¹³⁴ P. L. Llewellyn, F. Schüth, Y. Grillet, F. Rouquerol, J. Rouquerol, K. K. Unger, *Langmuir* 11(1995) 574.

hydrogen bonds.¹³³ Above 25 °C, desorption of water begins, only a monolayer of water remains which is continuously desorbed with increasing temperature. At 190 °C, the density of silanol groups is maximized, resulting in a constant value of $\alpha_{\text{OH}} = 4.9 \text{ nm}^{-2}$, the Kiselev-Zhuravlev-constant.¹³³ However, at room temperature, an average number of around 3 silanol groups per nm^2 internal surface of Si-MCM-41 can be determined.^{135,136}

The degree and the profile of the surface curvature have also influence on the described surface silanol characteristics. In the pores of mesoporous materials, the distance between silanol groups depends on the pore diameter. With higher pore diameter, the surface curvature is lower, and the distance between the silanol groups is larger.

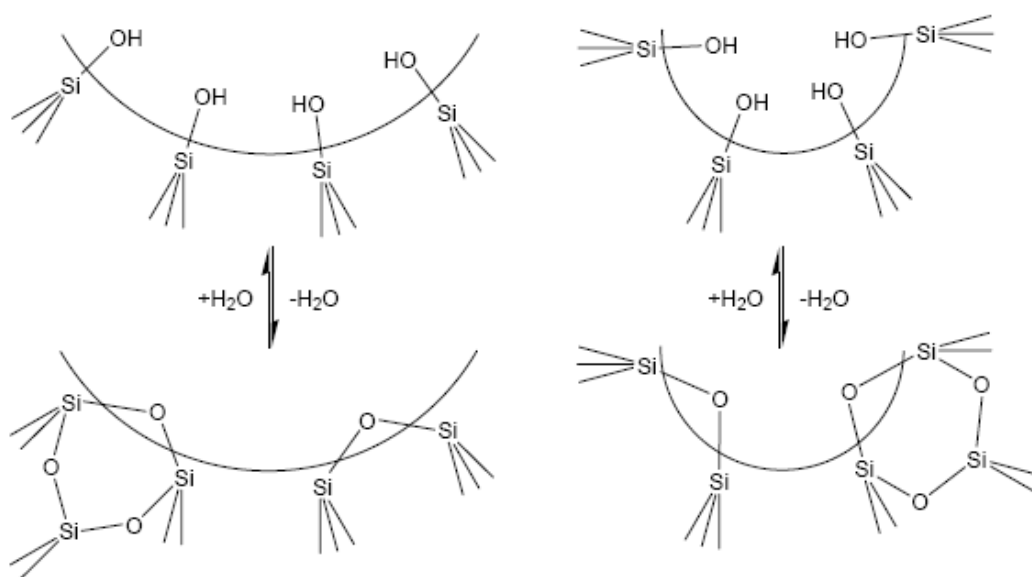


Figure 37. Two different pore diameters leading to different surface curvatures.¹³⁷

Figure 37 depicts this circumstance. This leads also to the assumption that silanol group condensation in smaller pores might start at lower temperatures than for larger pores.

¹³⁵ T. Ishikawa, M. Matsuda, A. Yasukawa, K. Kandori, S. Inagaki, T. Fukushima, S. Kondo, *J. Chem. Soc., Faraday Trans.* 92 (1996) 1985.

¹³⁶ X. Zhao, G. Lu, A. Whittaker, G. Millar, H. Zhu, *J. Phys. Chem. B* 101 (1997) 6525.

¹³⁷ Diplomarbeit Reimar Münnekhoff, Leibniz Universität Hannover, (2006).

Widenmeyer *et al.* reported, with an increase in pore diameter of Si-MCM-48 (and thereby a decrease in surface curvature), an increase of surface silanol groups from 1.4 to 1.9 groups per nm².¹³⁸ This result leads to the assumption that in the sample with smaller pore diameters already more silanol groups have been condensed, resulting in a lower number of silanol groups than in the sample with the larger pore diameter. Finally, the surface curvature depends also on the structure of pores. The spherical cages in Si-SBA-16 (see Figure 31) have a higher curvature than the cylindrical pores in Si-MCM-41 or Si-SBA-15, so more silanol groups might be already condensed.

2.2.6 Surface functionalization of mesoporous silica: grafting and co-condensation

The combination of the properties of organic and inorganic materials within one single material is very attractive for materials scientists because of the possibility to combine the enormous functional variation of organic chemistry with the advantages of a thermally stable and robust inorganic substrate. The symbiosis of organic and inorganic components can lead to materials whose properties can differ extremely from those of their individual, isolated components. Interesting modifications are for example organic functionalities such as C-C multiple bonds, alcohols, thiols, sulfonic and phosphonic acids, amines etc.

Four pathways are available for the synthesis of porous composite materials based on organosilica units²⁴:

- The post-synthetically modification of the pore surface of a purely inorganic silica material, called grafting.

¹³⁸ M. Widenmeyer, R. Anwender, *Chem. Mater.* 14 (2002) 1827.

- The simultaneous condensation of corresponding silica and organosilica precursors, called co-condensation.
- The incorporation of organic groups as bridging components directly and specifically into the pore walls by the use of bisilylated single-source organosilica precursors producing periodic mesoporous organosilicas (PMOs).
- The incorporation of functional groups via functionalized SDA⁸⁹ used for the synthesis of a mesoporous materials.

In this work, only the first two methods were used to synthesize organic-inorganic composites.

Grafting refers to the subsequent functionalization of the inner surfaces of mesoporous silica with organic groups. This process is carried out primarily by reaction of alkoxy-silanes of the type (R'O)₃SiR, or sometimes chlorosilanes ClSiR₃ or silazanes HN(SiR₃)₂, with the free silanol groups of the internal pore walls of powders or films (Figure 38).

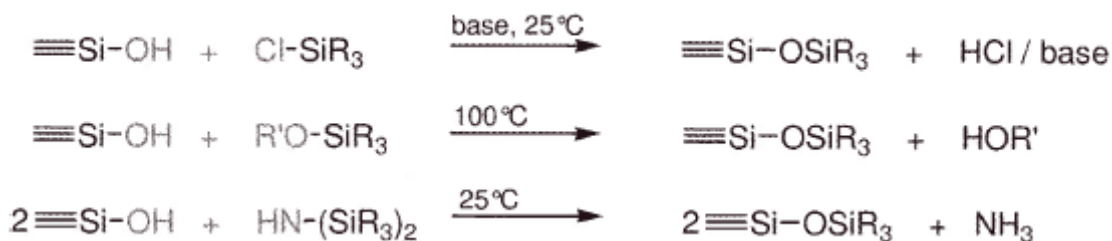


Figure 38. Possible surface silylation reactions.¹³⁹

In principle, functionalization with a high variety of organic moieties can be realized in this way by variation of the organic residue R, e.g. 1-allyl¹⁴⁰, aminopropyl^{141,142,143,144,145,146,147} groups, chloropropyl¹⁴⁸, diamino^{149,150}, triamino¹⁵⁰,

¹³⁹ N. Hüsing, G. Kickelbick (Ed.), *Hybrid Materials*, Wiley-VCH, Weinheim, 2007.

¹⁴⁰ V. Antochshuk, M. Jaroniec, *Chem. Commun.* (2002) 258.

¹⁴¹ A. Walcarius, M. Etienne, B. Lebeau, *Chem. Mater.* 15 (2003) 2161.

¹⁴² A. Matsumoto, K. Tsutsumi, K. Schumacher, K. K. Unger, *Langmuir* 18 (2002) 4014.

¹⁴³ K. Y. Ho, G. McKay, K. L. Yeung, *Langmuir* 19 (2003) 3019.

ethylenediamine¹⁵¹, malonamide¹⁵², carboxy^{143,146}, thiol^{141,145,153} (and after oxidation sulfonic acid^{154,155,156,157,158}), imidazole^{159,160,161}, perfluorosulfonic acid groups¹⁶² or even saccharides¹⁶³, for all kinds of application ranging from adsorption to heterogeneous catalysis. Surface silylation with alkoxy silanes (R'O)₃SiR are normally anchored in a reaction under toluene reflux. In this work, dichloromethane is used as solvent at 0 °C due to already earned knowledge.^{164,165}

Grafting has the advantage that the mesostructure of the starting silica phase is preformed and usually retained, whereas the functionalization of the walls is accompanied by a reduction in the pore diameter of the hybrid material (depending upon the size of the organic functionalization agent and the degree of occupation). If the organosilanes react preferentially at the pore openings during the initial stages of the synthetic process, the diffusion of further molecules into the center of the pores can be hindered, which can lead to a non-homogeneous distribution of the organic groups

¹⁴⁴ H. Yoshitake, T. Yokoi, T. Tatsumi, *Chem. Mater.* 14 (2002) 4603.

¹⁴⁵ A. M. Liu, K. Hidajat, S. Kawi, D. Y. Zhao, *Chem. Commun.* (2000) 1145.

¹⁴⁶ C. Lei, Y. Shin, J. Liu, E. J. Ackerman, *J. Am. Chem. Soc.* 124 (2002) 11242.

¹⁴⁷ H. Y. Huang, R. T. Yang, D. Chinn, C. L. Munson, *Ind. Eng. Chem. Res.* 42 (2003) 2427.

¹⁴⁸ G. S. Armatas, C. E. Salmas, M. Louloudi, G. P. Androutsopoulos, P. J. Pomonis, *Langmuir* 19 (2003) 3128.

¹⁴⁹ R. A. Khatri, S. S. C. Chuang, Y. Soong, M. Gray, *Ind. Eng. Chem. Res.* 44 (2005) 3702.

¹⁵⁰ T. Yokoi, H. Yoshitake, T. Tatsumi, *J. Mater. Chem.* 14 (2004) 951.

¹⁵¹ F. Zheng, D. N. Tran, B. J. Busche, G. E. Fryxell, R. S. Addleman, T. S. Zemanian, C. L. Aardahl, *Ind. Eng. Chem. Res.* 44 (2005) 3099.

¹⁵² P. Trens, M. L. Russell, L. Spjuth, M. J. Hudson, J.-O. Liljenzin, *Ind. Eng. Chem. Res.* 41 (2002) 5220.

¹⁵³ L. Mercier, T. J. Pinnavaia, *Environ. Sci. Technol.* 32 (1998) 2749.

¹⁵⁴ D. Das, J.-F. Lee, S. Cheng, *Chem. Commun.* (2001) 2178.

¹⁵⁵ D. Das, J.-F. Lee, S. Cheng, *J. Catal.* 223 (2004) 152.

¹⁵⁶ B. Sow, S. Hamoudi, M. H. Zahedi-Niaki, S. Kaliaguine, *Microporous Mesoporous Mater.* 79 (2005) 129.

¹⁵⁷ V. Dufaud, M. E. Davis, *J. Am. Chem. Soc.* 125 (2003) 9403.

¹⁵⁸ L. M. Yang, Y. J. Wang, G. S. Luo, Y. Y. Dai, *Microporous Mesoporous Mater.* 84 (2005) 275.

¹⁵⁹ T. Kang, Y. Park, K. Choi, J. S. Lee, J. Yi, *J. Mater. Chem.* 14 (2004) 1043.

¹⁶⁰ T. Kang, Y. Park, J. Yi, *Ind. Eng. Chem. Res.* 43 (2004) 1478.

¹⁶¹ G. S. Armatas, C. E. Salmas, M. Louloudi, G. P. Androutsopoulos, P. J. Pomonis, *Langmuir* 19 (2003) 3128.

¹⁶² M. Alvaro, A. Corma, D. Das, V. Fornés, H. García, *Chem. Commun.* (2004) 956.

¹⁶³ G. Rodríguez-López, M. D. Marcos, R. Martínez-Máñez, F. Sancenón, J. Soto, L. A. Villaescusa, D. Beltran, P. Amorós, *Chem. Commun.* (2004) 2198.

¹⁶⁴ Y. Rohlfiing, PhD thesis, University of Bremen, January 2004.

¹⁶⁵ D. Fattakhova-Rohlfiing, J. Rathousky, Y. Rohlfiing, O. Bartels, M. Wark, *Langmuir* 21 (2005) 11320.

within the pores, and a thereby lower degree of functionalization. In some cases, with very bulky compounds like coumarin¹⁶⁶, this can lead to complete closure of the pores (pore blocking).

An alternative method to synthesize functionalized mesoporous silica phases is the co-condensation method (*in-situ* synthesis). In this synthesis for mesostructured silica phases, tetraalkoxysilanes (e.g. TEOS) react with terminal alkoxysilanes of the type (R'O)₃SiR in the presence of SDAs leading to materials with organic moieties covalently anchored to the pore walls. The SDAs are hereby the same as for the synthesis of pristine mesoporous silica. A number of successful syntheses via co-condensation are reported until now, including functionalization with alkyl^{167,168}, alkoxy¹⁶⁹, amino^{150,169,170,171,172,173,174,175,176}, aromatic^{167,169,177,178,179}, cyano/isocyano^{170,172,177,180}, diamino¹⁸¹, phosphonic esters¹⁸², organophosphine^{177,183}, thiol^{168,169,184,185,186} or vinyl/allyl groups^{168,169,172,187,188,189,190,191}. As further reactions,

¹⁶⁶ N. K. Mal, M. Fujiwara, Y. Tanaka, *Nature* 421 (2003) 350.

¹⁶⁷ S. L. Burkett, S. D. Sims, S. Mann, *Chem. Commun.* (1996) 1367.

¹⁶⁸ L. Mercier, T. J. Pinnavaia, *Chem. Mater.* 12 (2000) 188.

¹⁶⁹ C. E. Fowler, S. L. Burkett, S. Mann, *Chem. Commun.* (1997) 1769.

¹⁷⁰ D. J. Macquarrie, *Chem. Commun.* (1996) 1961.

¹⁷¹ A. S. M. Chong, X. S. Zhao, *J. Phys. Chem. B* 107 (2003) 12 650.

¹⁷² S. Huh, J. W. Wiench, J.-C. Yoo, M. Pruski, V. S.-Y. Lin, *Chem. Mater.* 15 (2003) 4247.

¹⁷³ D. J. Macquarrie, D. B. Jackson, J. E. G. Mdoe, J. H. Clark, *New J. Chem.* 23 (1999) 539.

¹⁷⁴ T. Yokoi, H. Yoshitake, T. Tatsumi, *Chem. Mater.* 15 (2003) 4536.

¹⁷⁵ S. Che, A. E. Garcia-Bennett, T. Yokoi, K. Sakamoto, H. Kunieda, O. Terasaki, T. Tatsumi, *Nat. Mater.* 2 (2003) 801.

¹⁷⁶ N. Liu, R. A. Assink, B. Smarsly, C. J. Brinker, *Chem. Commun.* (2003) 1146.

¹⁷⁷ F. Cagnol, D. Grosso, C. Sanchez, *Chem. Commun.* (2004) 1742.

¹⁷⁸ C. M. Bambrrough, R. C. T. Slade, R. T. Williams, *J. Mater. Chem.* 8 (1998) 569.

¹⁷⁹ R. C. T. Slade, C. M. Bambrrough, R. T. Williams, *Phys. Chem. Chem. Phys.* 4 (2002) 5394.

¹⁸⁰ C. Yang, B. Zibrowius, F. Schüth, *Chem. Commun.* (2003) 1772.

¹⁸¹ X. Wang, J. C. C. Chan, Y.-H. Tseng, S. Cheng, *Microporous Mesoporous Mater.* 95 (2006) 57.

¹⁸² R. J. P. Corriu, L. Datas, Y. Guari, A. Mehdi, C. ReyL, C. Thieuleux, *Chem. Commun.* (2001) 763.

¹⁸³ R. J. P. Corriu, C. Hoarau, A. Mehdi, C. Reyé, *Chem. Commun.* (2000) 71.

¹⁸⁴ R. Richer, L. Mercier, *Chem. Commun.* (1998) 1775.

¹⁸⁵ A. Walcarius, C. Delacôte, *Chem. Mater.* 15 (2003) 4181.

¹⁸⁶ Q. Wei, Z. Nie, Y. Hao, Z. Chen, J. Xou, W. Wang, *Mater. Lett.* 59 (2005) 3611.

¹⁸⁷ M. H. Lim, C. F. Blanford, A. Stein, *J. Am. Chem. Soc.* 119 (1997) 4090.

¹⁸⁸ S. R. Hall, C. E. Fowler, B. Lebeau, S. Mann, *Chem. Commun.* (1999) 201.

¹⁸⁹ M. H. Lim, A. Stein, *Chem. Mater.* 11 (1999) 3285.

¹⁹⁰ Y. Q. Wang, C. M. Yang, B. Zibrowius, B. Spliethoff, M. Lindén, F. Schüth, *Chem. Mater.* 15 (2003) 5029.

¹⁹¹ Y. Wang, B. Zibrowius, C. M. Yang, B. Spliethoff, F. Schüth, *Chem. Commun.* (2004) 46.

thiol groups are oxidized to SO₃H groups^{192,193,194,195,196,197}, phosphonate esters to phosphonic acid groups¹⁸², and cyano groups to carboxylic acid groups¹⁸⁰.

Besides the typical application for SO₃H functionalized materials in heterogeneous catalysis¹⁹⁸, Kaliaguine *et al.* investigated SO₃H functionalized mesoporous non-ordered silica materials concerning their proton conductivity properties¹⁹⁹, being the most closely related study to the here presented work.

In comparison to grafting, the distribution of functionalized group in the silica mesostructure is much better, due to the fact that the organic units are already homogeneously dispersed in the starting mixtures. Therefore, a pore blocking is obviously no problem. But co-condensation procedure has also some disadvantages: The addition of extra molecules can influence the micelle formation and the network formation mechanisms, leading to a decreasing order with increasing concentration of (R'O)₃SiR. In general, the quality of the mesoporous structure is worse. Furthermore, the degree of loading does normally not exceed 40 %. It can also be observed that lower loadings are achieved than (R'O)₃SiR units are offered in the synthesis mixture, indicating the reaction mixtures favor homocondensation reactions, at the cost of cross-linking co-condensation reactions with the silica precursors. This is also caused by the different hydrolysis and condensation rates of the structurally different precursors.

Of course, by incorporating organic moieties, the surface areas, pore volumes and pore diameters of the ordered mesoporous composite materials are decreased. And for the template removal, only mild procedures like extraction methods can be used to avoid the destruction of the organic functionalities on the pore walls.

¹⁹² M. H. Lim, C. F. Blanford, A. Stein, *Chem. Mater.* 10 (1998) 467.

¹⁹³ W. M. Van Rhijn, D. E. De Vos, B. F. Sels, W. D. Bossaert, P. A. Jacobs, *Chem. Commun.* (1998) 317.

¹⁹⁴ I. Diaz, C. Marquez-Alvarez, F. Mohino, J. Pérez-Pariente, E. Sastre, *J. Catal.* 193 (2000) 283.

¹⁹⁵ V. Ganesan, A. Walcarius, *Langmuir* 20 (2004) 3632.

¹⁹⁶ Y.-F. Feng, X.-Y. Yang, Y. Di, Y.-C. Du, Y.-L. Zhang, F.-S. Xiao, *J. Phys. Chem. B* 110 (2006) 14142.

¹⁹⁷ D. Margolese, J. A. Melero, S. C. Christiansen, B. F. Chmelka, G. D. Stucky, *Chem. Mater.* 12 (2000) 2448.

¹⁹⁸ J. A. Melero, R. van Grieken, G. Morales, *Chem. Rev.* 106 (2006) 3790.

¹⁹⁹ S. Mikhailenko, D. Desplandier-Giscard, C. Danumah, S. Kaliaguine, *Microporous Mesoporous Mater.* 52 (2002) 29.

2 Fundamentals

In this work, highly ordered silica materials containing proton conductive groups like e.g. SO_3H , phosphonic acid (PO_3H_2) and imidazole groups are prepared, either by grafting or co-condensation synthesis.

3 Experimental

In this section, either the applied syntheses of mesoporous silica materials functionalized with organic moieties for proton conductivity are explained as well as the used measurement techniques for characterization of the synthesized materials.

3.1 Analytical methods

In the following chapters, the analytical methods for sample characterization used in this work are presented, including the measurement assemblies. The central analytical method is here the impedance spectroscopy, which is used to determine proton conductivity of the solid proton conductors and composite membranes. Besides standard methods like X-ray powder diffractometry or nitrogen adsorption techniques, also theoretical calculations are introduced, which were performed in collaboration with the University of Bremen to confirm experimental measured results of proton conductivity.

3.1.1 Impedance spectroscopy

From the requirements for membrane materials in fuel cells (see chapter 2.1.4), a total electronic insulator behavior for membrane materials with simultaneous maximum proton conductivity is demanded. Direct current measurements are therefore not applicable for measuring the resistance and accordingly the proton conductivity of membranes. A protonic current is not measurable, typical instruments only measure the electric current, but the membrane materials are blocking the electrons. So, the principle of charge separation must be used, as the detecting charge carriers, here protons, have to be brought in direct relation to measurable electric variables. In our case, hydrogen atoms are oxidized at the positive electrode ($\text{H} \rightarrow \text{H}^+ + \text{e}^-$), and for charge neutrality, back reaction at the negative electrode occurs ($\text{H}^+ + \text{e}^- \rightarrow \text{H}$), enabling a coupling between the charge carriers inside the membrane materials and measurable electrical current. In direct current, the charge carriers would aggregate at the interfaces between electrodes and membrane causing polarization. This leads to an exponential decrease in current over time, so that no time independent value for the conductivity can be obtained. Thus, the resistance of membranes or conductivity is determined under alternating current conditions, where no interface polarizations are occurring, due to time-periodical change of the electric field vector. No charge carrier accumulation is produced, and no time-dependent decrease in current observed.

In direct current circuits, the ohmic resistance is defined by the ohmic law, where R is the resistance, and U and I are the applied voltage or current, respectively.²⁰⁰

$$R = \frac{U}{I} \quad (\text{Eq. 3.1})$$

In contrast, the voltage and current in alternating current circuits pass a time dependent change of the actual values of voltage and current, described in a sine function, while an angular frequency $\omega = 2\pi f$ ($f = \text{frequency}$) introduces the periodicity.²⁰⁰

²⁰⁰ J. Grehn, J. Krause (Eds.), *Metzler Physik*, 3rd Edition, Schroedel Verlag, Hannover, 1998.

$$u(t) = |u| \sin(\omega t) \quad (\text{Eq. 3.2})$$

$$i(t) = |i| \sin(\omega t) \quad (\text{Eq. 3.3})$$

Similar to direct current circuits, the alternating current resistance Z , called impedance, is defined over the quotient of the actual voltage and current at a given time t , resulting in the given equation:

$$Z = \frac{u(t)}{i(t)} = \frac{|u|}{|i|} e^{i\varphi} = |Z| e^{i\varphi} \quad (\text{Eq. 3.4})$$

The impedance is frequency dependent, and defined by its absolute value $|Z|$ and the phase shift φ .

In alternating current circuits, three kinds of resistance are possible, namely ohmic, inductive and capacitive resistances. Z is thereby the sum of the ohmic resistance R , the inductive resistance X_L , and the capacitive resistance X_C .²⁰⁰

Every component, a resistor, an inductor or a capacitor, causes additionally a typical phase shift.

Pure ideal ohmic components in an alternating current circuit are similar as in direct current circuits. The impedance of an ideal ohmic component is therefore the same as the direct current resistance, the phase shift is zero:

$$Z = |Z| = R \quad (\text{Eq. 3.5})$$

A pure ideal inductive component acts direct proportional to the frequency of the excitation signal, the phase shift is $+90^\circ$, the current follows the voltage.

$$Z = X_L = i\omega L \quad (\text{Eq. 3.6})$$

3 Experimental

For pure capacitive components, an inverse proportional relation between the excitation frequency and the capacitive resistance exist. The phase shift is -90° , the voltage follows the current.

$$Z = X_C = -i \frac{1}{\omega C} \quad (\text{Eq. 3.7})$$

By using the Euler equation²⁰¹

$$e^{i\varphi} = \cos(\varphi) + i \sin(\varphi) \quad (\text{Eq. 3.8}),$$

Eq 3.4 can be transformed into the rectangular form

$$Z(\omega) = |Z| \cos(\varphi) + i |Z| \sin(\varphi) = Z' + Z'' \quad (\text{Eq. 3.9})$$

The first summand is called “real part” $\text{Re}(Z)$ of the impedance Z , while the second summand is called the “imaginary part” $\text{Im}(Z)$. Figure 39 shows the impedance Z plotted in the complex plane as a vector.

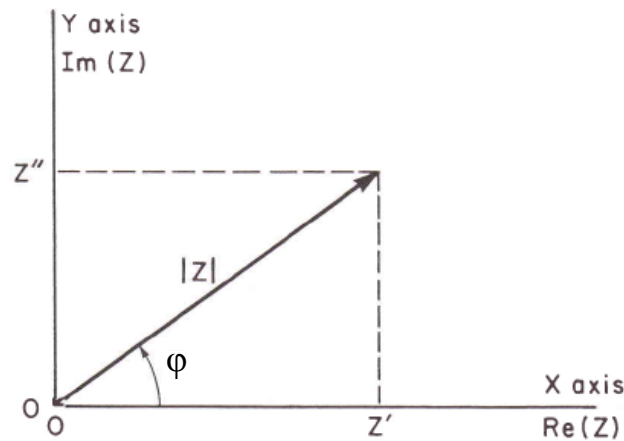


Figure 39. The impedance plotted as a planar vector, with polar or rectangular coordinates.²⁰¹

²⁰¹ E. Barsoukov, J. R. MacDonald (Edt.), *Impedance spectroscopy*, 2nd edition, Wiley&Sons, Hoboken, New Jersey, 2005.

In impedance spectroscopy (IS), all these relations are used to investigate the electric properties of a given component. In general, a sinusoidal excitation voltage signal with low amplitude is applied on a sample to be measured, measuring the answering signal and calculating the complex impedance. As the impedance is frequency dependent, the measurement is repeated over a wide frequency range, typical from 1 Hz to 1 MHz. The results can be plotted in several types of diagrams to analyze the data. One example is the Nyquist plot, Figure 40 depicts an ideal Nyquist plot for the shown equivalent circuit, and the arrows indicate the increasing frequency.

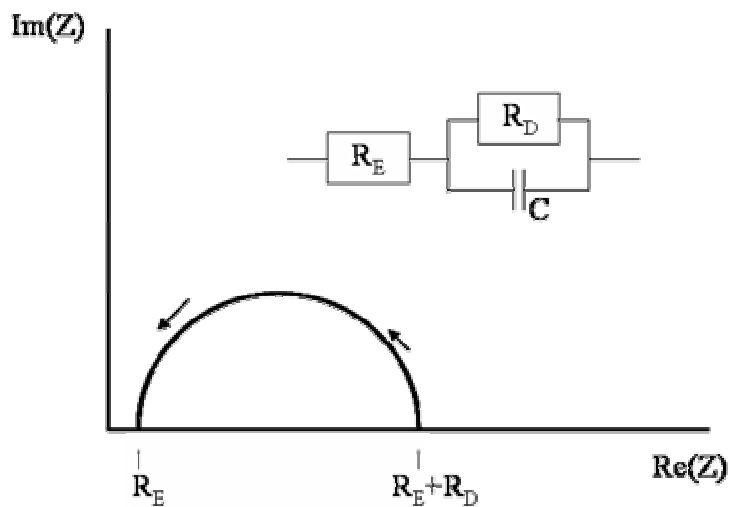


Figure 40. Ideal Nyquist plot with corresponding equivalent circuit.²⁰¹

At high frequencies, the intersection of the semicircle with the x-axis corresponds to the electrolyte (or membrane) resistance R_E to be measured. The semicircle ends in another intersection with the x-axis. This resistance corresponds to the electrolyte resistance plus the transfer resistance R_D due to the charged barrier layer at the interface electrode-membrane, which the charge carriers have to overcome. Both resistances are also shown in the equivalent circuit. The drawn capacity C describes the electrical properties of the charged barrier layer, because charge carriers can be stored in this layer, which is a similar behavior like a capacitor.

3 Experimental

If diffusion processes are taking place in the measured membrane, the appearance of a Warburg-straight can be observed, corresponding to an additional element Z_W in the equivalent circuit (Figure 41).

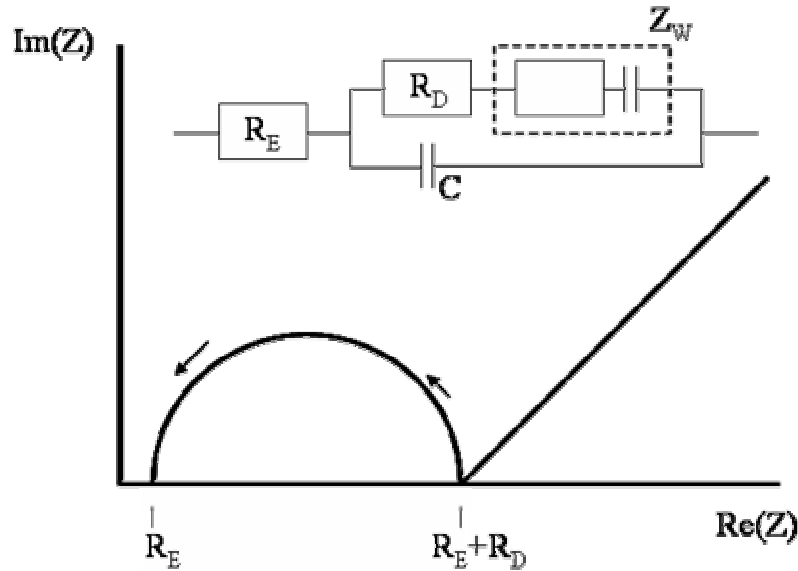


Figure 41. Ideal Nyquist plot with Warburg-straight.²⁰¹

A deeper analysis of the Warburg behavior was not done, the focus was on determination of the electrolyte resistance. Most of the time, the diagrams are not as ideal, e.g. the Warburg-straight directly passes into the semicircle, or nearly no semicircle is visible.

A second and easier way to analyze impedance spectra are Bode diagrams. In a Bode diagram, the overall impedance is plotted against the frequency. Additionally, the phase shift between applied voltage and answering current signal is also plotted against the frequency. When the phase angle is zero (or close to zero), the impedance is, following equation 3.5, fully ohmic. In fact, the resistance of the membrane can at this point be directly observed, and used to calculate the proton conductivity σ of the membrane following

$$\sigma = \frac{1}{R} \cdot \frac{l}{A} \quad (\text{Eq. 3.10})$$

where R is the resistance corresponding to the phase angle closest to zero in the Bode diagram, l is the height of the sample between the electrodes, and A the cross-sectional contact area of the measured sample with the electrodes.²⁰⁰

Figure 42 shows a typical measured Bode diagram. This type of diagram was always used for the impedance analysis.

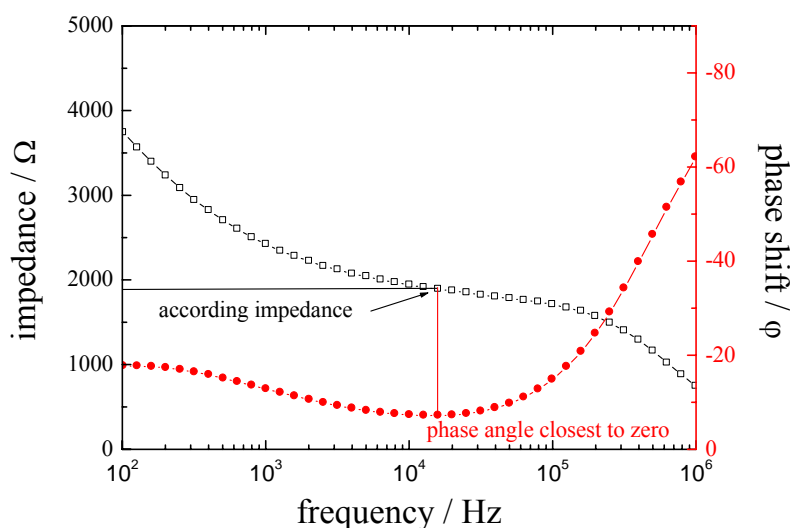


Figure 42. Typical measured Bode diagram, impedance (\square) and phase shift (\bullet).

IS measurements on functionalized mesoporous powders were performed with a Zahner electrochemical workstation IM6e in a frequency range from 1 - 10^6 Hz with an oscillating voltage of 100 mV, using the software THALES 2.48 LPTLINK for controlling and analysis. For sample preparation, the functionalized powders were pressed with 40 kN to small pellets of 8 mm in diameter ($A = 0.503 \text{ cm}^2$) and 0.5 to 1 mm in thickness, which is hardly influencing the mesoporous structure. Only a slight decrease in intensity is observed in the XRD after pressing (Figure 43). This is caused by the hardened particle agglomerates after pressing, which could not be efficiently

3 Experimental

mortared to very fine powders for sample preparation for XRD like the calcined Si-MCM-41 powders. However, the porous structure of the samples is still given.

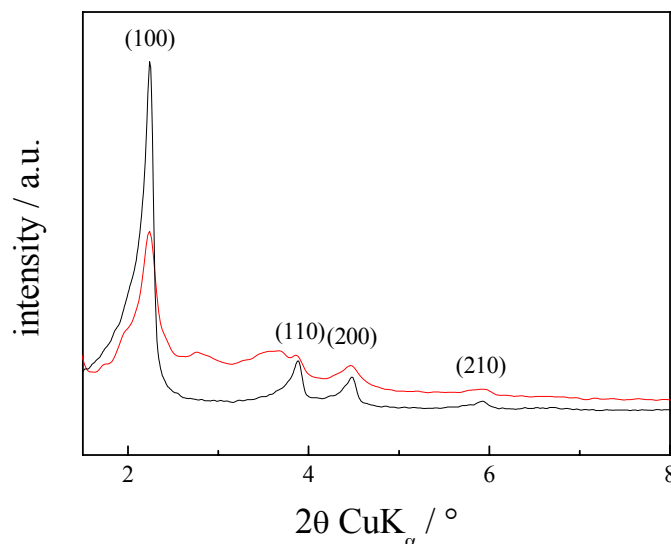


Figure 43. XRD patterns of Si-MCM-41 (compare chapter 4.1.1) before (black) and after (red) pressing to pellets.

The pellets were placed between two thin graphite slices (8 mm \varnothing) as GDLs and then put into a Teflon specimen holder where the pellet is clamped between two sintered metal electrodes (stainless steel, 8 mm \varnothing). The PTFE holder is then put into a gas-tight stainless steel body with thermocouple access to the holder. This body is connected via a stainless steel tube to a stainless steel water reservoir.

This type of cell is called water vapor conductivity cell, and was invented by Alberti *et al.* in 2001.²⁰² This cell is ideal for measuring samples under different RH. The RH depends generally on the ratio between the actual pressure and the saturation vapor pressure of water. With increasing temperature, the necessary amount of water vapor for saturation increases, resulting in a deteriorating RH of a given volume with heating. Moreover, every RH has a belonging temperature. The error of RH is around 5 %.

²⁰² G. Alberti, M. Casciola, L. Massinelli, B. Bauer, *J. Membr. Sci.* 185 (2001) 73.

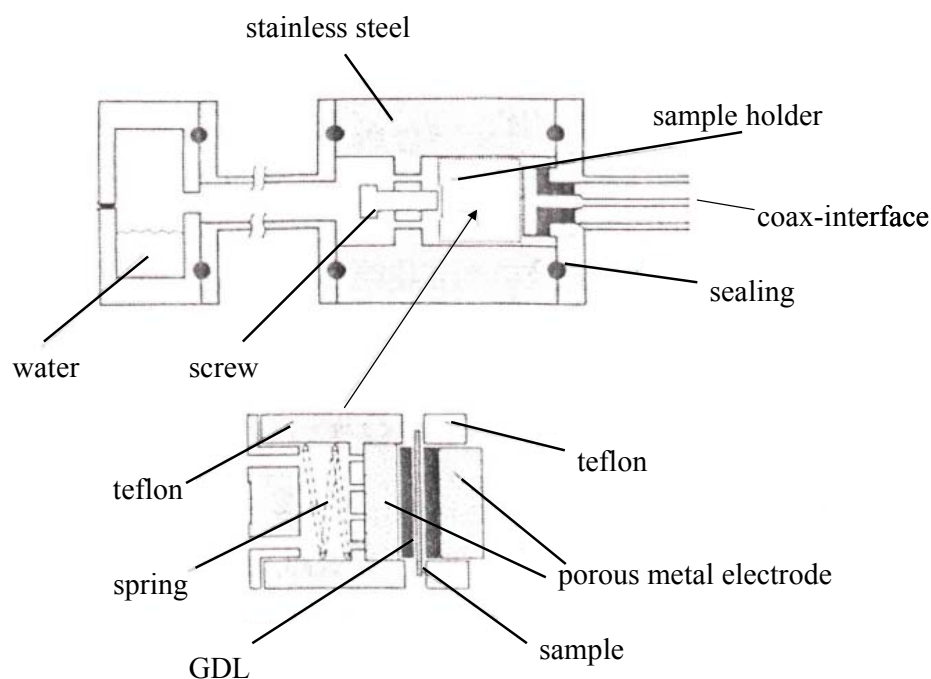


Figure 44. Scheme of the water vapor conductivity cell.²⁰²

The degree of RH in the cell and at the sample can be controlled by adjusting the temperature at the sample and of the water tank. For example, for 50 % RH at 120 °C, the water tank must have a temperature of 99 °C; for 100% RH, the water tank is heated to a temperature of 120 °C, respectively. Reliable data can be determined between 60 °C and 140 °C with equilibrium times of maximum 30 minutes. Temperatures are controlled inside the cell at the water tank and at the sample with thermocouples.

The proton conductivity values of these measurements are very accurate concerning the order of magnitude, but no further decimal places are interpreted in the following, as the accuracy decreases strongly, and literature also only compares values up to the first decimal place in scientific notation.

Composite membranes made of polysiloxanes and inorganic particles were measured using also a Zahner electrochemical workstation IM6 eX in combination with the measuring cell HTZ 200 in the group of Prof. Grathwohl at University of Bremen, as the membrane casting was performed in the same group. The principle of the HTZ 200

3 Experimental

is similar to the water vapor cell in Figure 44, but higher temperatures and lower relative humidities can be set, reaching aimed fuel cell membrane conditions like 180 °C with 5 % RH. The assembly can be seen in Figure 45.

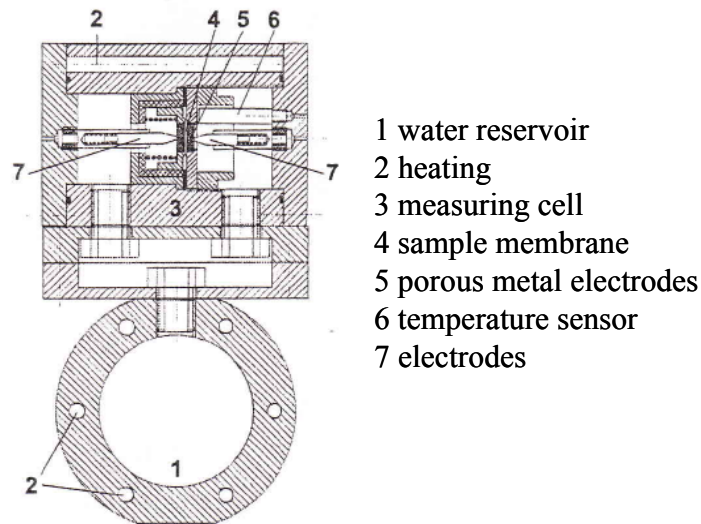


Figure 45. HTZ200 conductivity cell from University of Bremen.²⁰³

For the measurement of the MEAs, the samples were fixed between two GDL 24 BC of a 25/125-HT fuel cell test bench (HIAT GmbH, Germany) and pressurized to 1 bar. Both sides of these membranes were coated with a mixture of carbon black containing 40 wt% Pt (Elyst A 40) and pre-polymerized sulfonated diphenyldimethoxysilane (sDPDMS) in ethanol. The use of functionalized polysiloxane as the proton conducting component within the electro catalyst system suits the concept to reach a better transition phase between the electrocatalyst and the membrane, caused by a covalent bonding between the polysiloxane components. Cross-linking of MEAs was accomplished at a temperature of 150 °C. The feed was 8 mL/min H₂ and 4 mL/min O₂. The single cell fuel cell measurements were performed at temperatures of 22, 30, 40 and 50 °C applying a RH of 95 % in each case.

²⁰³ M. Jeske, *Entwicklung bifunktionaler Membranen für HT-PEMFCs*, Dissertation, Universität Bremen, 2007.

Composite membranes made with polyoxadiazole were measured in the frequency range 1-10⁶ Hz at signal amplitude 100 mV and obtained from the impedance modulus at zero phase shift (high frequency side) with 20-100% RH. Measurements were performed with a flow cell purged with wet nitrogen; relative humidity was controlled by bubbling nitrogen gas in water heated at a suitable temperature between 30 and 80 °C. The impedance measurements were carried out on stacks containing up to five membranes (cumulative thickness around 500 µm). The spectrometer used was a Zahner IM6 electrochemical workstation.

3.1.2 X-ray diffractometry

X-ray diffractometry is an important tool for the structural characterization of crystalline solids. In general, X-rays have the same diffraction properties like all electromagnetic waves. As the wavelength of X-rays exhibits around 100 pm, it is in the same order of magnitude like bond distances between atoms in crystals. Thus, the diffraction of X-rays on periodically changing electron density contrasts is used for structural investigations of solids.

Due to their three-dimensional periodic structure, crystals can act like a three-dimensional diffraction grating. In case of a crystalline sample, the electron density contrast is caused by the position of atoms, and thereby position of electrons. When X-rays hit a crystal, the diffraction is understood as reflection at the lattice planes of the crystalline structure, which has a constant distance d . A reflection can only be obtained, if the crystal has a specific orientation towards the X-ray source and the detector, and can only be detected if constructive interference between several reflected X-ray beams from different lattice layers occurs. For constructive inference, the path difference

3 Experimental

between two X-ray beams must be an integer multiple of the wavelength. These requirements are concluded in the Bragg-equation.²⁰⁴

$$2d \cdot \sin\theta = n \cdot \lambda \quad (\text{Eq. 3.11})$$

θ is here the diffraction angle, λ is the wavelength of the incident X-ray beam, n is the order of interference (an integer number). So, θ depends only on the distance between the lattice layers d . In X-ray powder diffractometry, finely ground powders were measured with a high number of statistically oriented crystals.

Mesostructured materials exhibit, in contrast to crystals, no long range ordering, but the ordered porous structures also lead to periodical electron density contrasts, at which X-ray diffraction is caused. If the porous structure is somehow filled, the electron density contrast changes, resulting in changed intensities of the diffraction reflections (see chapter 4.2.1). As this ordering has much larger “lattice” distances d caused by the porous structure, the reflection signals occur at very low angles, between 0.5 and 10° 2θ depending on the pore structure.

For a hexagonal pore structure, the lattice constant a_0 (see Figure 28) can then be calculated via

$$a_0 = \frac{2 \cdot d_{100}}{\sqrt{3}} \quad (\text{Eq. 3.12})$$

where d_{100} is the first reflection in such a diffractogram and can be calculated with the Bragg equation, with $n = 1$.²⁰⁵ For cubic pore structures, the lattice constant a can be determined via

$$a = d_{hkl} \sqrt{h^2 + k^2 + l^2} \quad (\text{Eq. 3.13})$$

²⁰⁴ P. W. Atkins, *Physikalische Chemie*, 2nd Edition, Wiley-VCH, Weinheim, 1999.

²⁰⁵ W. Kleber, H.-J. Bautsch, J. Bohm, *Einführung in die Kristallographie*, 18th Edition, Verlag Technik, Berlin, 1998.

if (hkl) are the Miller-Indices, which describe the set of lattice layers, and d_{hkl} is the lattice layer distance corresponding one X-ray reflection.²⁰⁵

In this work, the synthesized powders were characterized with a Philips X'pert MPD diffractometer, working in a Bragg-Brentano-geometry with copper K_{α} radiation ($\lambda = 1.5406 \text{ \AA}$) at 40 kV and 40 mA. A curved graphite crystal as monochromator is used to eliminate undesired radiation (fluorescence, K_{β} radiation). The powders are prepared in a powder sample holder after fine mortaring, and measured between 0.5 and $10^{\circ} 2\theta$ with a step size of 0.02° and 5 s measuring time at every step.

3.1.3 Infrared spectroscopy

If infrared (IR) radiation is absorbed by a molecule or crystal, discrete vibrations states between atoms or groups in molecules or crystals are stimulated. The excitation from a lower vibration state into a higher vibration state occurs with the absorption of energy of a wavelength characteristic for the bond energy between two atoms or atom groups. The stronger the bond and the higher the force constant k of the bond, the higher is the vibration frequency, which is proportional to the energy of the vibration state. Moreover, the IR spectrometer detects the amount of absorbed energy at this wavelength.²⁰⁴

Vibration states are only IR-active if, during the corresponding vibration, the dipole moment changes. Due to this rule, the number of observed vibrations is usually smaller than the number of possible normal vibrations. The number of possible normal vibration is $3N-6$ ($3N-5$ for linear molecules), when N is the number of atoms in a molecule.

The absorption bands used for structural investigations in the IR spectrum, whose wavelengths are at the high end of the visible light spectrum, are between 2.5 and $25 \mu\text{m}$. Usually, the position of absorption bands in the IR spectra are denoted in

3 Experimental

wavenumber $\bar{\nu}$, which is the reciprocal value of the wavelength. IR spectra are therefore in between 4000 and 400 cm^{-1} .²⁰⁴

Fourier-Transform-IR (FTIR) spectroscopy measures simultaneously all frequencies of the IR spectrum. Multi-frequent IR radiation, which has the same intensity at all time, is transformed via an interferometer into an interferogram, being now a function of time and not of the frequency. After passing through the sample, the interferogram is Fourier-transformed back into to frequency domain. Thereby, the measuring time is much shorter compared to single frequency measurements.

The IR measurements in this work are performed on a FTIR spectrometer Bruker Tensor 27 (resolution: 2 cm^{-1} , 200 scans) in the range of 400-4000 cm^{-1} in ATR (attenuated total reflectance) mode in the Institute for Inorganic Chemistry at the Leibniz University of Hannover. The powders are densely fixed on a diamond crystal, and IR radiation is passed through this crystal reflecting at the internal surface in contact to the sample. This total reflection produces an evanescent wave which extends into the sample. Although this technique needs slightly more sample for measurement, it can be performed faster without additional chemicals like KBr for pellet preparation for IR transmission measurements. As the to detecting organic moieties are already only hardly detectable due to very low loading compared to the silica framework of the measured samples, influences of impurities on the spectra can be therefore avoided.

For the analysis, the software OPUS 5.0 was used. For comparison, the spectra of silica materials are normalized on the silica network band at $\sim 1060 \text{ cm}^{-1}$. However, quantitative information of functionalization are hardly meaningful via IR, due to the fact that the loading with organic groups is very low, resulting in only very weak signals compared to the intense Si-O-Si signals.

3.1.4 Sorption measurements

Via adsorption measurements, information about the internal/external surface, pore size distribution and pore volumes of porous materials can be determined. Using nitrogen as adsorbate, the adsorption isotherms are measured at a constant temperature of 77 K. The adsorbed amount of gas on a sample is hereby detected depending on the equilibrium pressure p . Drawing the adsorbed amount of gas against the relative pressure p/p_0 , where p_0 is the saturation vapor pressure of the measurement gas, one gets the adsorption isotherm.

Via the method after Brunauer, Emmett und Teller (BET)²⁰⁶, the specific BET surface can be calculated from the estimated nitrogen adsorption isotherms. This theory describes multilayer adsorption, where one layer of adsorbed gas can act as adsorbent for additional adsorption layers. The observed adsorption isotherms can be classified in different types of isotherms. Figure 46 shows the six after IUPAC classified isotherm types.

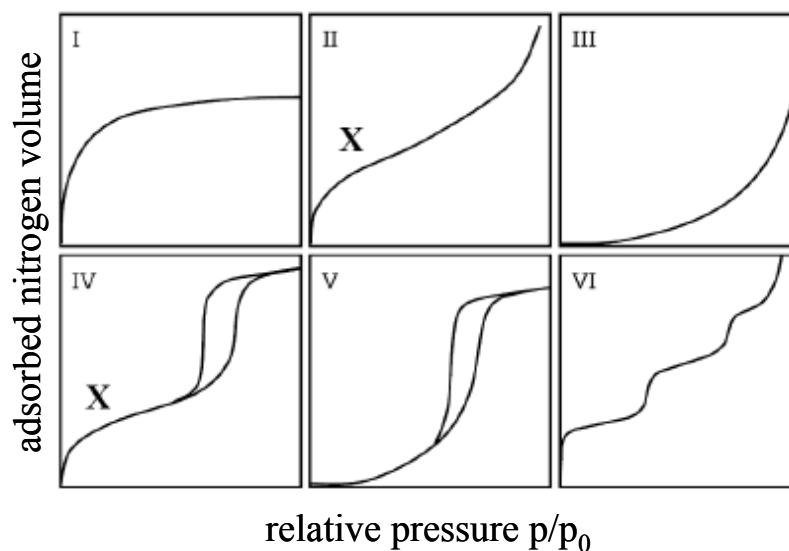


Figure 46. Classes of adsorption isotherms.²⁰⁷

²⁰⁶ S. Brunauer, P. Emmett, E. Teller, *J. Am. Chem. Soc.* 60 (1938) 306.

²⁰⁷ B. Lindlar, *Synthese und Modifizierung großporiger M41S-Materialien*; Eidgenössische Technische Hochschule Zürich, 2001.

3 Experimental

- type I isotherm: microporous substances with small external surface, e.g. activated carbon or zeolites
- type II isotherm: non-porous materials or macropores, at X a complete monolayer is reached
- type III isotherm: rare, no monolayer is formed, e.g. adsorption of water on hydrophobic non-porous substances
- type IV isotherm: mesoporous adsorbents with hysteresis loop caused by capillary condensation in the mesopores, at X a complete monolayer is reached
- type V isotherm: like type III isotherm, here for porous materials, adsorption of polar components on hydrophobic substances
- type VI isotherm: stepwise multilayer adsorption on a non-porous surface.²⁰⁷

Mesoporous materials of the M41S or SBA family are characterized by a small external surface ($< 10 \text{ m}^2/\text{g}$) and large internal surface ($\sim 1000 \text{ m}^2/\text{g}$), resulting normally in type IV isotherms. Until the point X (see Figure 46) the monolayer adsorption in the pores takes place at small relative pressures. The following steep increase with increasing relative pressures belongs to the multilayer adsorption, ending in adsorption at the external particle surface. In the desorption branch, the occurring sorption hysteresis loop is typical for mesoporous materials, caused by capillary condensation of the adsorbate inside the mesoporous material.

With the method of Barrett, Joyner und Halenda (BJH) the pore size distribution and pore volumes can be calculated.²⁰⁸ Here, the pore radius is estimated via the Kelvin radius which is proportional to p/p_0 . From their ratio, the pore diameter can be calculated. Although this method shows pore size dependent errors when used on mesoporous materials with pores smaller than 3 nm, the method is anyway used for pore diameter estimation, because, as reported, the method is still very good for relative

²⁰⁸ E. P. Barrett, L. G. Joyner, P. P. Halenda, *J. Am. Chem. Soc.* 73 (1951) 373.

comparison of pore sizes, and applicable on the structure types used in this work.^{138,209} Alternative methods are developed recently for the interpretation of sorption data, namely nonlocal density functional theory (NLDFT)²¹⁰, which were verified by suitable silica materials with well-defined pore hierarchy and connectivity.²¹¹ This method is quite new and not evaluated on the here presented materials, therefore it was not used, but might be applicable in the future, especially for materials showing pore blocking effects.

Nitrogen adsorption measurements in this work were performed on a Quantachrome Autosorb 3B analyzer. Prior to each adsorption measurement, approx. 0.1 g sample were outgassed at 200 °C for 24 hours. The Autosorb1 software was used for analysis. Some additional adsorption measurements were also performed on a Micromeritics ASAP 2010 machine by Dr. Jiří Rathouský from the J. Heyrovský Institute of Physical Chemistry of AS CR in Prague.

Water adsorption measurements have also been performed to investigate the hydrophilicity of samples. The isotherms were obtained by volumetric vapor adsorption using a BELSORP 18-3 (Bel Japan Inc.) at 22 °C with an equilibration time of 500 s. Water adsorption measurement need, due to the larger water molecule and the stronger interactions to interfaces due to its dipolar behavior, longer measurements time, especially for desorption. The isotherms are classified as for nitrogen adsorption, and pore diameters can be derived via Kelvin-equation.²¹² These measurements were performed by Dr. Michaela Wilhelm at the University of Bremen.

²⁰⁹ M. Thommes, R. Köhn, M. Fröba, *J. Phys. Chem. B* 104 (2000) 7932.

²¹⁰ A. V. Neimark, P. I. Ravikovitch, *Microporous Mesoporous Mater.* 44 (2001) 697.

²¹¹ M. Thommes, B. Smarsly, M. Groenewolt, P. I. Ravikovitch, A. V. Neimark, *Langmuir* 22 (2006) 756.

²¹² S. Komarneni, R. Pidugu, V. C. Menon, *J. Porous Mater.* 2 (1996) 99.

3.1.5 Electron microscopy

In an optical light microscope, the maximum resolution of the microscope is restricted by the wavelength of incident light. Good optical light microscopes can therefore reach resolution of down to micrometers.

In electron microscopy, instead of photons electrons are used for creating images of samples with high magnification. As the wavelength of an incident electron is normally much smaller than that of photons, accelerated electron beams give maximum resolutions in the nanometer range.

For accelerating an electron, it has to be brought into an electric field. The potential energy E_{pot} of an electron depends on its charge e and the applied voltage U .²⁰⁰

$$E_{\text{pot}} = eU \quad (\text{Eq. 3.14})$$

$$E_{\text{kin}} = \frac{1}{2}mv^2 \quad (\text{Eq. 3.15})$$

All the potential energy is transformed into kinetic energy E_{kin} , and energy conservation gives the following relation.

$$\begin{aligned} E_{\text{pot}} &= E_{\text{kin}} \\ eU &= \frac{1}{2}mv^2 \\ v &= \sqrt{2\frac{e}{m_e}U} \end{aligned} \quad (\text{Eq. 3.16})$$

So, the velocity v of an electron in an electric field can be calculated from its charge e ($e = 1.60 \times 10^{-19}$ C), its mass m_e ($m_e = 9.11 \times 10^{-31}$ kg) and the voltage of the applied field.²⁰⁰ For example, with $U = 1$ V, an electron gets the velocity of 590 km/s.

Using the relation of de Broglie, the wavelength λ of an electron can be calculated, together with the Planck's constant h ($h = 6.626 \times 10^{-34}$ Js).²⁰⁴

$$\lambda = \frac{h}{p} = \frac{h}{mv} \quad (\text{Eq. 3.17})$$

As can be seen, the higher the velocity of the electron, the smaller is the wavelength of the electron.

The maximum resolution d can then be calculated following the equation after Ernst Abbe.²¹³

$$d = 0.61 \frac{\lambda}{n \cdot \sin \alpha} \quad (\text{Eq. 3.18})$$

In this equation, $n \cdot \sin \alpha$ is called numeric aperture, a device dependent constant. With smaller wavelengths, the point resolution of the electron microscope decreases. In conclusion, the applied acceleration voltage in an electron microscope strongly defines its point resolution.

For creating an image, the accelerated electrons have to be focused on the sample in the electron microscope. Compared to lenses in optical light microscopes, here magnetic coils focus the accelerated electrons, like lenses focus a light beam. If the electron beam, also called the primary beam, hits the sample surface, different interactions between the primary beam and the sample can take place, shown in Figure 47.

Secondary electrons arise from inelastic scattering of the primary beam via interactions with the shell electrons or the atomic nuclei of the sample.

Back scattering electrons arise from elastic scattering of the primary beam with the positively charged atomic nuclei. The electrons are deflected changing their movement direction, but not their energy. Via single or multiple scattering, these electrons can leave the sample.

²¹³ D. B. Williams, C. B. Carter, *Transmission Electron Microscopy, Spectrometry*, Springer Science and Business Media, New York, 1996.

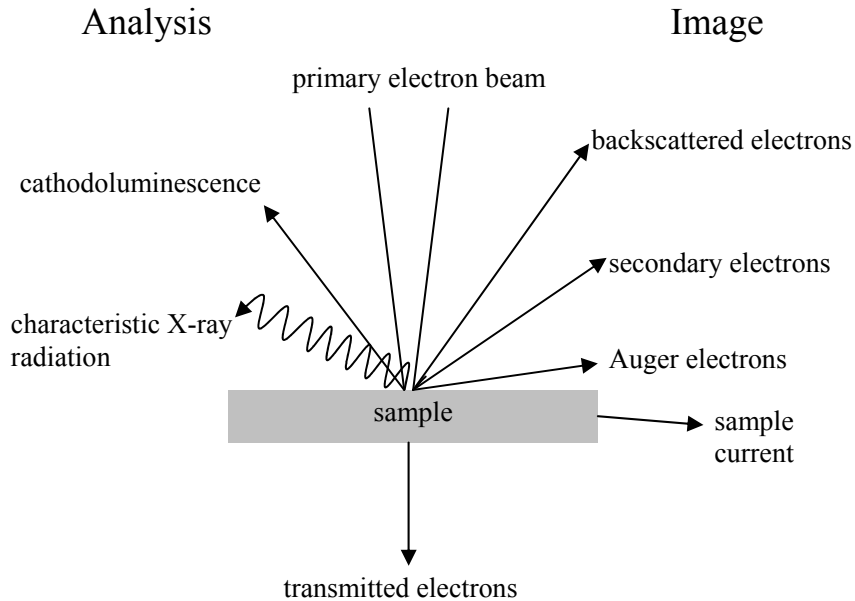


Figure 47. Possible interactions between the incident beam and the sample.²¹³

Characteristic X-ray radiation arises from inelastic scattering of the primary beam with core-near electrons, which can result in the release of an electron leaving a core-near electron hole. Electrons from higher energy levels can now fall into these holes emitting element characteristic X-ray radiation for the energy difference of these levels leaving the sample, also called X-ray fluorescence.

Auger electrons arise when the inelastic scattering of the primary beam with the core-near electrons results in the emission of radiation after recombination of higher-shell electrons with the hole, but this radiation excites a surface-near electron to leave the sample, called the Auger-electron.

Cathodoluminescence is the emission of light in the region of visible or infrared wavelengths from the sample caused by the primary beam.

The sample current occurring from absorbed electrons can also be used for imaging like the secondary or back-scattered electrons in the scanning electron microscope (SEM). The transmitted electrons are used in transmission electron microscopy (TEM) for imaging.

SEM and TEM have several differences explained in the following and depicted in Figure 48.

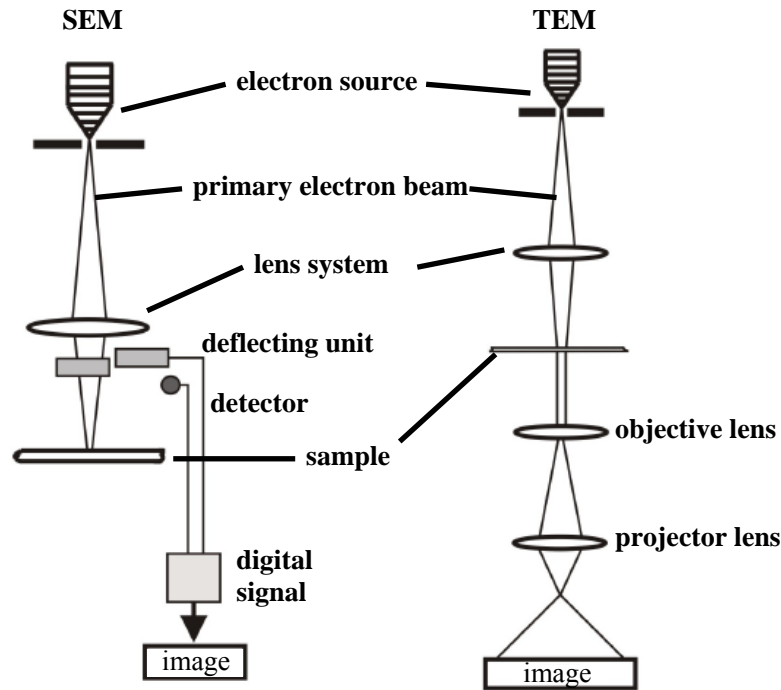


Figure 48. Course of beam in SEM and TEM.²¹³

SEMs only create indirect images. Between sample and image, no course of beam exists; the signal producing and the signal processing units are separated. The incident electrons are focused via lens systems, consisting of a condenser and an objective lens, on the sample. A deflecting unit controls via magnetic coils the electron beam scanning line-by-line over a certain area. The resulting signals are detected and sent to the digital signal processing unit, which forms an image from the detected secondary or back-scattered electron signals. Magnification can be realized by reducing the area of scanning of the electron beam via setting the coil current. The whole system, including sample and detector, is under vacuum, that no interactions between the primary beam and air/gas molecules can disturb the imaging process.

In contrast, TEM creates real images like an optical light microscope. The primary beam is focused on the sample. After passing through the sample, the electrons form the

3 Experimental

first image behind the objective lens. Via an intermediate lens (not shown in Figure 48) a second image is formed in front of the projector lens. The resulting image is acquired via imaging the second image via the projector lens.

In this work, the morphologies of the silica materials were determined with a JEOL JSM-6700 field emission SEM. The electron source is a field emission canon, a thin tungsten tip, from which electrons can tunnel in an electric field. The JEOL JSM-6700 has four detectors, one for secondary electrons, one for back-scattered electrons, a semi-in-lens detector for small working distances, and a detector for energy-dispersive X-ray spectroscopy (EDXS, see chapter 3.1.6). Acceleration voltages from 0.5 to 30 kV are possible, resulting in a maximum point resolution of ~1 nm. Powder samples for SEM were prepared on a graphite slice, which was gluing on a brass sample holder.

For higher resolutions and analysis of the pore structure of the synthesis mesoporous materials, in this work a JEOL JEM-2100F UHR field emission TEM was used. The primary beam was produced using a Schottky-field emitter made of zirconium oxide/tungsten, where moderate heating already generates electrons at low electric field strengths. High-resolution TEM (HRTEM) and scanning TEM (STEM, the electron beam scans through the sample like in a SEM) is also possible with the used TEM, as well as EDXS with better accuracy than in the SEM. Sample preparation was performed via powder dispersion in ethanol in ultrasonic bath, giving afterward a small drop of dispersion on a copper grid. After drying, the samples can be analyzed.

3.1.6 Electron-dispersive X-ray spectroscopy and electron energy-loss spectroscopy

Energy-dispersive X-ray spectroscopy (EDXS) is used in combination with SEM or TEM for the surface analysis of solids. EDXS analyzes the characteristic X-ray radiation emitted from a sample after interaction with a primary electron beam of high energy. So, EDXS is a qualitative and quantitative, non-destructing method for the determination of the local element composition of a sample.

A high energy electron beam can, via inelastic scattering, strike out a core-near electron out of an atom. Electrons from higher shells can now recombine with the resulting electron hole by falling into the lower energy shell. Meanwhile, a characteristic radiation is emitted, characteristic for the energy difference between both shells and therefore element specific. Several recombination paths are possible, while electrons from different energy levels can fall into the electron hole.²¹³

The detected result is a spectrum containing several spectral lines for every detected element. The spectral lines are denoted as K_{α} , K_{β} , ..., L_{α} , L_{β} ,... The big letters name the electron shell in which an electron fell down, and the index indicates from which shell this electron fell down (α = one level higher, β = two level higher).

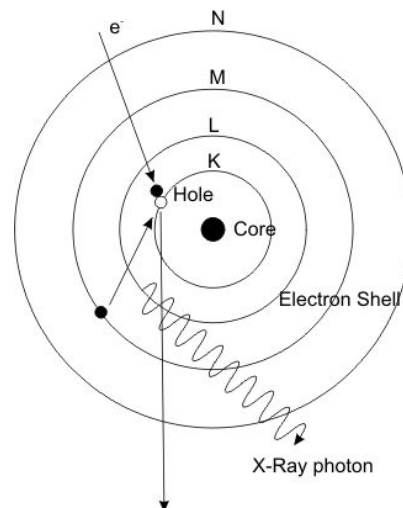


Figure 49. Principle of EDXS.²¹³

3 Experimental

The X-ray photon produced in Figure 49 should for example be denoted as K_{β} , as the stroke-out electron came from the K shell, and the recombined electron fell down from the M shell, which is two levels higher than the K shell.²¹³

The used SEM in this work is equipped with an Oxford Instruments INCA 300 energy-dispersive X-ray spectrometer, and the used TEM with an Oxford Instruments INCA 200 TEM spectrometer. In both cases, an UTW detector (ultra thin window) is used for the detection of elements with atomic numbers larger than 4 (=Beryllium).

Regular detectors with Beryllium windows allow the detection only beginning with atomic number 11, due to the strong absorption of radiation of the beryllium window for radiation of low energy (< 1 eV), which means also the main K_{α} radiation of all elements with atomic number < 11 would be absorbed. Carbon has an exceptional position, because surface contaminations and carbonization caused by the electron beam always result in a carbon EDXS signal, especially in SEM.

For quantitative analysis, the area under the estimated signals is analyzed with INCA software. However, the quantitative analysis has, especially at smaller signals, a relative big error, which can be up to 20 % due to surface roughness or varying penetration depths. In contrast, the qualitative analysis is nearly error-free.

With the INCA software, also the determination of EDX spectra of selected points (spot analysis), lines (line scans) or areas (mapping) for the elemental distribution in the sample are possible.

Electron energy-loss spectroscopy (EELS) is another analysis method combined with TEM. In general, the inelastic scattering of an incident electron beam with a thin sample is observed. The interactions between the high energy electrons of the primary beam and the inner shell or “core” electrons of the specimen lead to an energy loss of the transmitted high energy electrons, the resulting energy difference is due to the ionization of the sample atoms. A large number of electrons shows no energy loss and cross the sample without any interaction (zero loss), but as the ionization energies are characteristic for elements and their oxidation state, the energy loss of inelastic scattered electrons can be used to receive qualitative information about elemental composition in

a probed specimen, their oxidation states, bonding and nearest neighbor distribution. Differences in the energy onsets of the ionization signals (called *edges*) distinguish between the different elements, whereas the fine structure of the edges themselves give the information about the element bonding and neighboring information. In contrast to EDXS, any solid bond element can be detected, but the specimen has to be very thin.²¹³

3.1.7 Thermal analysis

Thermogravimetric analysis (TGA) and differential thermoanalysis (DTA) are thermal analysis procedures to investigate the thermal stability and composition of solids, including the determination of melting or boiling points. By applying a temperature program on a heating device containing a sample, the thermal dependent changes of the sample in a sweep gas stream can be detected, including phase transitions and structural breakdowns.²¹⁴

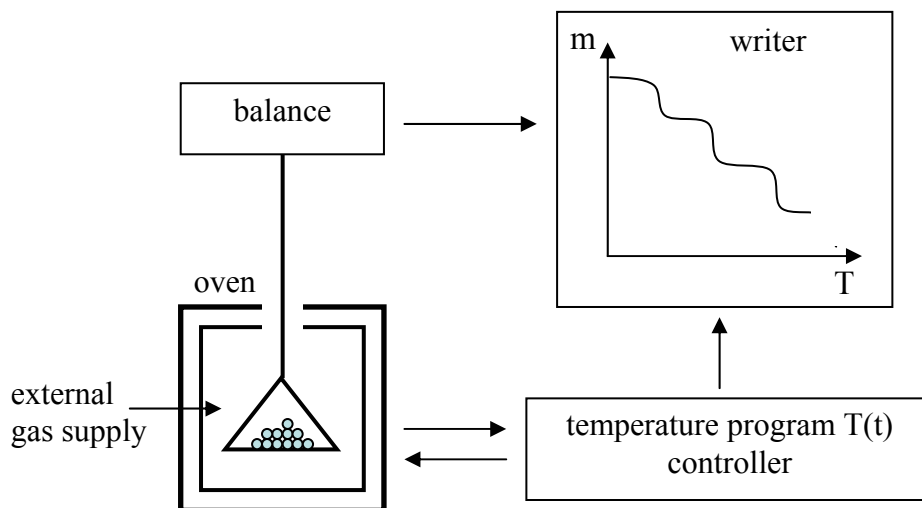


Figure 50. Principle of thermogravimetric analysis TGA.²¹⁴

²¹⁴ D. A. Skoog, J. J. Leary, *Instrumentelle Analytik*, Springer-Verlag, Berlin, 1996.

3 Experimental

Figure 50 shows schematically the working principle of a TGA. A small amount of sample (some mg) is put on a sensitive balance into an oven under gas stream (usually air). A temperature program increases the temperature of the oven with a constant heating rate (usually 5 °C/min), and the change in weight is detected by the balance and analyzed in a measuring curve, plotting the mass loss against the temperature.

For the exact determination of transition temperatures, a DTA is performed simultaneously. In this technique, the temperature difference between the sample and a reference material is measured, while both undergo the same temperature program. At specific temperatures, a temperature difference between sample and reference material can be detected, and the exact temperature determined. Also the value of temperature difference gives information about endo- or exothermic processes. These techniques are very suitable for getting an idea about the composition of a material. Functional groups, e.g. organic moieties, have specific combustion temperatures in TGA.

In this work, thermal analyses have been performed by Birgit Beiße and Falk Heinroth in the Institute of Inorganic Chemistry at the Leibniz University of Hannover. In a corundum crucible, the samples were analyzed with a Netzsch Simultaneous Thermal Analyzer 429 with a heating rate of 5 °C/min in air between 20 and 1000 °C.

3.1.8 Computational modeling

Simulations of proton transport in immobilized imidazole and immobilized sulfonic acid systems were performed in collaboration with the University of Bremen at the Bremen Center for Computational Materials Science (BCCMS). The simulations study was developed using classical molecular dynamics (MD) simulations, and the density-functional based tight-binding method (DFTB) to calculate the energy barriers for the transition of an excess proton between donor-acceptor groups.

Classical MD simulation is a computational method where the intermolecular and intramolecular interactions between molecules are provided via force-fields and then by solving equations of motion the trajectories of the atoms are known. The dynamical properties of the system can be calculated, for instance, transport coefficients, and also static properties. One advantage over the ab-initial methods is that a larger number of atoms can be handled. In the systems presented in this work, after system equilibration, production runs of several nanoseconds were performed analyzing the trajectories of atoms every picosecond. The simulations were run in a canonical ensemble (NVT), where the number of particles (N), volume (V) and temperature (T) are kept constant.

In this work, for the classical MD simulations the GROMACS program²¹⁵ and its OPLS force field are employed, the charges are obtained via Gaussian 03 (B3LYP/6-31G(d)).²¹⁶ In total the simulation box contains 144 molecules arranged in a two-dimensional grid equally spaced by the restraining of the terminal carbon atoms of the carbon spacer chain: 1 charged molecule (donor) and 143 neutral molecules (acceptors). From the trajectories, radial distribution functions were calculated, giving an insight into the dynamics between proton donor and acceptor molecules. The radial distribution function (RDF) analysis is important in order to describe the arrangement of atoms or molecules in the volume available to the system. The RDFs provide an insight of how close a donor can be to an acceptor and one can estimate at which closest distances they approach. The dynamics of the systems is studied via the MD simulations; however, this method does not allow chemical reactions, what avoids obtaining the proton jump event between the donor-acceptor molecules. To study the proton jump event a quantum

²¹⁵ E. Lindahl, B. Hess, D. van der Spoel, *J. Mol Model.* 7 (2001) 306.

²¹⁶ M. J. Frisch, G. W. Trucks, H. B. Schlegel, G. E. Scuseria, M. A. Robb, J. R. Cheeseman, J. A. Montgomery, Jr., T. Vreven, K. N. Kudin, J. C. Burant, J. M. Millam, S. S. Iyengar, J. Tomasi, V. Barone, B. Mennucci, M. Cossi, G. Scalmani, N. Rega, G. A. Petersson, H. Nakatsuji, M. Hada, M. Ehara, K. Toyota, R. Fukuda, J. Hasegawa, M. Ishida, T. Nakajima, Y. Honda, O. Kitao, H. Nakai, M. Klene, X. Li, J. E. Knox, H. P. Hratchian, J. B. Cross, V. Bakken, C. Adamo, J. Jaramillo, R. Gomperts, R. E. Stratmann, O. Yazyev, A. J. Austin, R. Cammi, C. Pomelli, J. W. Ochterski, P. Y. Ayala, K. Morokuma, G. A. Voth, P. Salvador, J. J. Dannenberg, V. G. Zakrzewski, S. Dapprich, A. D. Daniels, M. C. Strain, O. Farkas, D. K. Malick, A. D. Rabuck, K. Raghavachari, J. B. Foresman, J. V. Ortiz, Q. Cui, A. G. Baboul, S. Clifford, J. Cioslowski, B. B. Stefanov, G. Liu, A. Liashenko, P. Piskorz, I. Komaromi, R. L. Martin, D. J. Fox, T. Keith, M. A. Al-Laham, C. Y. Peng, A. Nanayakkara, M. Challacombe, P. M. W. Gill, B. Johnson, W. Chen, M. W. Wong, C. Gonzalez, J. A. Pople, *Gaussian 03, Revision C.02*, Gaussian, Inc., Wallingford CT (2004).

3 Experimental

method was applied, in this work the DFTB quantum mechanical modeling method was used.

The DFTB method is applied in order to calculate the energy barriers for the transition of an excess proton between two groups. During an energy minimization the positions of the atoms that participate in the transport, i.e. proton donor and acceptor, are fixed keeping them within a defined distance from each other. In order to avoid rotations of the molecule also two other heavy atoms of each molecule are kept fixed. The position of the proton is chosen via an additional potential and it is defined by the reaction coordinate mCEC²¹⁷ implemented in the RXNCOR module of CHARMM.²¹⁸ The proton is moved in several steps from one group to the other to obtain an approximated minimal energy path for the proton transfer. To validate the DFTB parameters used in this context, single point energy density functional theory (DFT) calculations for the identical configurations are done using Gaussian 03 program via B3LYP/6-31G(d).²¹⁶ This calculation provides the values for the proton transfer energy barrier as a function of the distance between donor and acceptor groups. Via the energy barrier calculations one can estimate at which distance the donor-acceptor atoms would have a low energy barrier for a proton jump to occur.

The calculations are performed by Dr. Welch L. Cavalcanti and Dipl.-Phys. Pia Tölle at the BCCMS.

3.1.9 Ion exchange capacities

Ion exchange capacities (IEC) are measured by titration to determine the number of protogenic groups anchored on the synthesized host materials. For SO₃H group

²¹⁷ P. H. König, N. Ghosh, M. Hoffmann, M. Elstner, E. Tajkhorshid, Th. Frauenheim, Q. Cui, *J. Phys. Chem. A* 110 (2006) 548.

²¹⁸ B. R. Brooks, R. E. Bruccoleri, B. D. Olafson, D. J. States, S. Swaminathan, M. Karplus, *J. Comp. Chem.* 4 (1983) 187.

determinations, approx. 0.1 g of functionalized powder was suspended in a 0.01 M sodium hydroxide solution for 48 hours. Hereby, the protons of the SO₃H groups are exchanged against sodium cations, and the exchanged protons form water with the hydroxide ions. The non-reacted sodium hydroxide is titrated after centrifuging with 0.01 M hydrochloric acid under use of Tashiro pH indicator, changing its color at the pH of distilled water. The IECs are then calculated via

$$x = \frac{0.01 \text{ mol} \cdot V \cdot 1000}{1000 \text{ mL} \cdot m} \quad \text{in mmol/g} \quad (\text{Eq. 3.19})$$

where V is the reacted volume of sodium hydroxide solution ($V = 50 \text{ mL} - V_{\text{titr}}$) and m is the weighted amount of powder.

For basic groups like imidazole, the solutions are the opposite; the powder was suspended in hydrochloric acid and titrated with sodium hydroxide solution.

This method is very sensitive with an error of max. 5 %, but the result depends strongly on accurate weighing and analysis preparation.

3.2 Syntheses

In the following chapters, the different syntheses performed in this work are presented, beginning with the syntheses of the pristine mesoporous silica hosts. The used grafting and co-condensation reactions are presented in principle, where alkoxy silanes (R'O)₃SiR are used for functionalization. Subsequent reactions like oxidations, peptide bond formations or others are presented separately.

3.2.1 Synthesis of pristine mesoporous silica hosts

Si-MCM-41 powders were prepared following the procedure called “homogeneous precipitation” proposed by Rathousky *et al.*¹⁰⁵ 2.61 g of cetyltrimethylammonium bromide (CTAB) were dissolved in 400 mL water at 30 °C. Then 2.67 g sodium metasilicate (NaSiO₃) were added. The molar ratio of the individual components of the reaction mixture was 1 CTAB : 3103 H₂O : 3.05 Na-silicate. After complete dilution, 4 mL of ethyl acetate were added under vigorous stirring, whose hydrolysis to acetic acid ensures highly homogeneous acidification of the reaction mixture and consequently a uniform hydrolysis-condensation reaction of the NaSiO₃. After 15 s, the stirring was stopped and the solution was kept still for 24 hours at room temperature in a closed polyethylene (PE) bottle. The final pH was around 10 for a typical synthesis. Hydrothermal treatment was carried out for additional 48 hours at 100 °C. The white precipitate was recovered by hot filtration and washed with ethanol and water. The resulting white powder was dried at 80 °C over night. The product was usually calcined at 600 °C for 20 hours (heating rate: 1 °C/min), resulting in a complete removal of the surfactant.

In a typical synthesis for pure Si-MCM-41 nanoparticles inspired by Cai *et al.*¹⁰⁸, 0.7 mL NaOH solution (2M) and 96 mL water were mixed and heated upon 80 °C following the addition of 0.2 g of CTAB. After dissolving, 1 mL TEOS was added to the solution. The final molar composition of the solution was 1200 H₂O : 0.31 NaOH : 0.125 CTAB : 1 TEOS. Stirring was continued for 2 hours followed by filtration and subsequent washing with water and ethanol. The template was extracted via ethanol/HCl extraction.

Si-SBA-15 powders were prepared following the procedure applied by Zhang *et al.*¹¹⁴ using the triblock-copolymer P123 (EO₂₀PO₇₀EO₂₀) and TEOS as silicon source. Typically, 1 g of P123 was dissolved in 30 g of 2M HCl solution and 7.5 g of water at 40 °C. Then 2.08 g of TEOS were added and the mixture was stirred for 16 hours. The resulting slurry was then hydrothermally treated at 100 °C for 48 hours. The product

was filtered, washed with water and dried at 80 °C over night. Calcination was realized at 550 °C for 6 hours (heating rate: 1 °C/min).

Si-SBA-16 powders were prepared following the procedure of Kim *et al.*²¹⁹ using a mixture of the triblock co-polymers P123 and F127. 1 g of P123 and 5 g of F127 were dissolved in 46 g concentrated HCl solution (37 %) and 247 g water at 35 °C under stirring. After complete dissolving 23.91 mL TEOS were added and stirring was continued for another 15 minutes. The molar composition of the final mixture was 1 P123 : 2.3 F127 : 621 TEOS : 2727 HCl : 89182 H₂O. Then the mixture was kept at 35 °C for additional 24 hours without stirring in a closed PE bottle following a hydrothermal treatment at 100 °C for additional 24 hours. The product was filtered and the resulting white solid suspended in ethanol and filtered another time, following washing with ethanol and water. The product was dried at 100 °C and calcined at 550 °C for 5 hours (heating rate: 1 °C/min).

3.2.2 Functionalization of mesoporous silica hosts via grafting

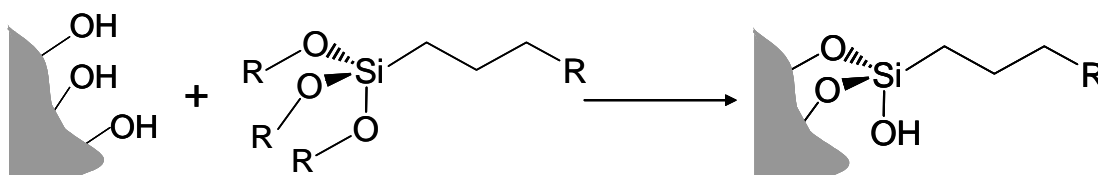


Figure 51. Grafting reaction with surface silanol groups.²⁴

For a typical grafting reaction¹⁶⁴ (Figure 51), 0.5 g mesoporous silica powder was put into a Schlenk flask and dried under vacuum for several hours. Then, the flask was filled with Argon, and the dried powder was suspended in 20 mL of dry dichloromethane (DCM). The water free conditions were needed to avoid the hydrolysis

²¹⁹ T.-W. Kim, R. Ryoo, K.P. Gierszal, M. Jaroniec, L.A. Solovyov, Y. Sakamoto, O. Terasaki, *J. Mater. Chem.* 15 (2005) 1560.

3 Experimental

of alkoxy silanes. Anyway, only two hours of drying the powder left some water inside the pores of the silica hosts, which helps to provide a high number of surface silanol groups. The suspension was cooled down to a value between -10 and 0 °C with an ice/NaCl mixture, followed by the addition of a pre-cooled alkoxy silane to the suspension. The low reactions temperatures were used to ensure a slow reaction velocity, so that the alkoxy silanes have enough time to diffuse into the pores. The reaction mixture was stirred under Argon for 22 hours, and the cooling bath was not renewed after addition of the alkoxy silane. Afterwards, the mixture was filtered and the resulting white powder was washed with DCM and ethanol, and dried at 80 °C over night.

For different functionalizations, the following alkoxy silanes have been used (Table 3). All the grafting reactions were performed using different amounts of functionalization agent, namely 5 mmol, 10 mmol and 20 mmol alkoxy silane per gram mesoporous silica.

Table 3. Functionalization chemicals used for grafting.

alkoxy silane	abbreviation	resulting functionalization
(3-mercaptopropyl) trimethoxysilane	MPMS	propyl-SH (thiol)
Triethoxysilyl butyraldehyde	TESBA	propyl-CHO (aldehyde)
3-Aminopropyl triethoxysilane	APTES	propyl-NH ₂ (amine)
3-Chloropropyl trimethoxysilane	CITMS	propyl-Cl (chlorine)

The given silanes are used to anchor precursor groups for the subsequent forming of proton conductive groups on the silica surface, explained in the chapters 3.2.4 to 3.2.6.

3.2.3 Functionalization via co-condensation

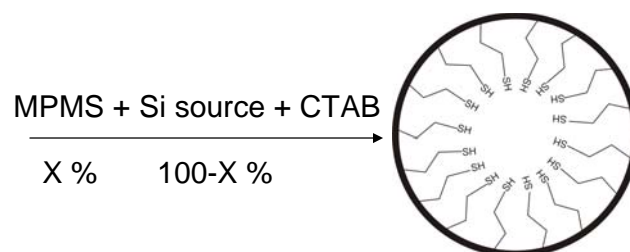


Figure 52. Principle of co-condensation, exemplarily with MPMS.

In this work, only Si-MCM-41 was functionalized via *in-situ* co-condensation method.²⁴ Functionalized Si-MCM-41 was synthesized following the homogeneous precipitation procedure already used for the synthesis of pristine Si-MCM-41, however, a certain percentage (10, 20, 30 and 40 mol. %) of the silica source NaSiO_3 was replaced by an alkoxy silane (Figure 52). In a typical synthesis, 2.61 g of CTAB was dissolved in 400 mL of deionized water at 30 °C. After the complete dissolution of the surfactant, NaSiO_3 and the alkoxy silane were added under stirring. The molar ratio of the individual components of the reaction mixture was 1 CTAB : 3103 H_2O : 3.05-x NaSiO_3 : x $(\text{R}'\text{O})_3\text{SiR}$, with x equaling either 0.30, 0.61, 0.92 or 1.22, respectively. Finally, 4 mL of ethyl acetate were added under vigorous stirring, whose hydrolysis to acetic acid ensures highly homogeneous acidification of the reaction mixture and consequently a uniform hydrolysis-condensation reaction of the metasilicate and the alkoxy silane. After 15 s, the stirring was stopped and the solution was kept still for 24 hours at room temperature in a closed PE bottle. Hydrothermal treatment was carried out for additional 48 hours at 100 °C. The white precipitate was recovered by filtration and washed with ethanol and water. Samples were dried at 80 °C over night. For template removal, 0.5 g of the as-synthesized powder was suspended in 100 mL ethanol, including 2 mL of concentrated HCl (37%), and boiled under reflux for 24 hours. The resulting extracted powder was filtrated and washed with water and

3 Experimental

ethanol, and dried at 80 °C over night. The following alkoxy silanes have been used to produce functionalized Si-MCM-41 via co-condensation (Table 4).

Table 4. Functionalization chemicals used for co-condensation.

alkoxy silane	abbreviation	resulting functionalization
(3-mercaptopropyl) trimethoxysilane	MPMS	propyl-SH (thiol)
Triethoxysilyl butyraldehyde	TESBA	propyl-CHO (aldehyde)
Diethylphosphatopropyl triethoxysilane	DPTES	propyl-PO(OEt) ₂

For the co-condensation of the mesoporous silica nanoparticles of Si-MCM-41 to SH-MCM-41, the reaction mixture in chapter 3.2.1 was modified as, compared to the standard reaction mixture 1200 H₂O : 0.31 NaOH : 0.125 CTAB : 1 TEOS, the molar amount of TEOS was set to 0.9 or 0.8, respectively, and after addition of TEOS stirring was performed for 15 minutes. Then, MPMS was added to the mixture, and stirring was continued for 105 minutes. The resulting reaction mixture was 1200 H₂O : 0.31 NaOH : 0.125 CTAB : 1-x TEOS : x MPMS, where x was 0.1 or 0.2 for 10 % or 20 % functionalization, respectively.

3.2.4 Thiol-oxidation to SO_3H

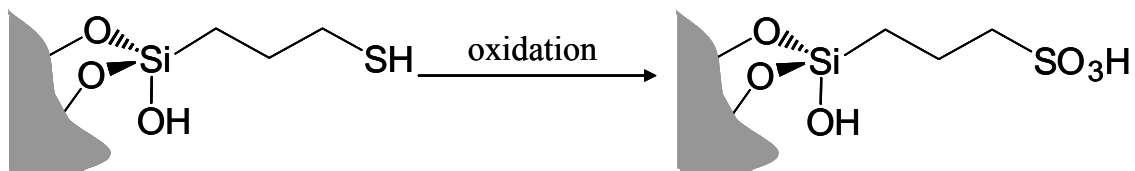


Figure 53. Oxidation of surface SH groups to SO_3H groups.¹⁹⁷

Oxidation of attached SH groups with hydrogen peroxide (H_2O_2) leads to SO_3H functionalized powders (Figure 53). In a typical reaction 0.3 g of SH functionalized powder are suspended in 10 mL of H_2O_2 solution (30 wt.-%) and stirred for 48 hours at room temperature. The product was filtered and washed with ethanol and water. The still wet solid is then suspended in 30 mL 2M H_2SO_4 and stirred for two hours at room temperature. Filtration and washing with ethanol and water were the final steps with subsequent drying at 80 °C over night.¹⁹⁷

As a second approach, microwave treatment was additionally used for powders synthesized via co-condensation for simultaneous template removal and SH oxidation. 0.1 g of non-extracted powder was suspended in a mixture of concentrated nitric acid (HNO_3 , 65 %) and H_2O_2 solution (30 wt.-%) in a Teflon reaction vessel, which is transparent for microwave radiation. The mixture was treated by continuous microwave irradiation (max. 600 W) for up to 5 minutes at 200 °C, the maximum internal pressure being 18 bars, in an MLS Ethos 1 microwave system.¹³¹

3.2.5 Imidazole anchorage/formation processes

Imidazole anchorage on different functionalized hybrid materials was performed in three different ways, to investigate experimentally the influence of the type of imidazole anchorage on the proton conductivity.

In one approach, with amino functionalized mesoporous silica, a peptide bonding between the functionalized powder and imidazole-2-carboxylic acid was formed.

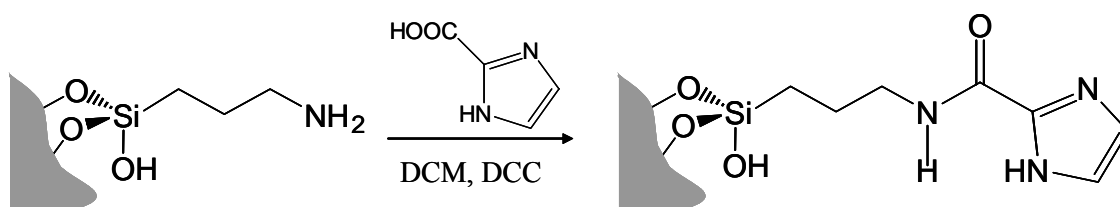


Figure 54. Peptide bond formation for imidazole anchorage.¹⁶⁴

In a typical synthesis (Figure 54), 0.2 g NH₂-MCM-41 was dried under vacuum for 2 hours. 5 mL DCM were added under Argon. Then, 1 mmol 2-imidazole-carboxylic acid (0.1 g) was added under stirring. As 10 mmol dicyclohexyl carbodiimide (DCC) were dissolved in 10 mL DCM, this solution is then added to the reaction mixture. The suspension is stirred for 24 hours.¹⁶⁴

DCC is used for the activation of the carboxylic acid function under mild conditions; it shows electrophilic reactivity like a ketene⁶³ and is often used in the synthesis of polypeptides using protection groups on amino acids.

In the reaction shown in Figure 55, DCC activates the carboxyl group of the imidazole carboxylic acid forming an intermediate O-acylisourea, which shows reactivity like an anhydride and reacts with the surface-bond amine to a peptide bond. As byproduct, N,N'-Dicyclohexylurea is formed.²²⁰

²²⁰ *Organikum*, 21st Edition, Wiley-VCH, Weinheim, 2001.

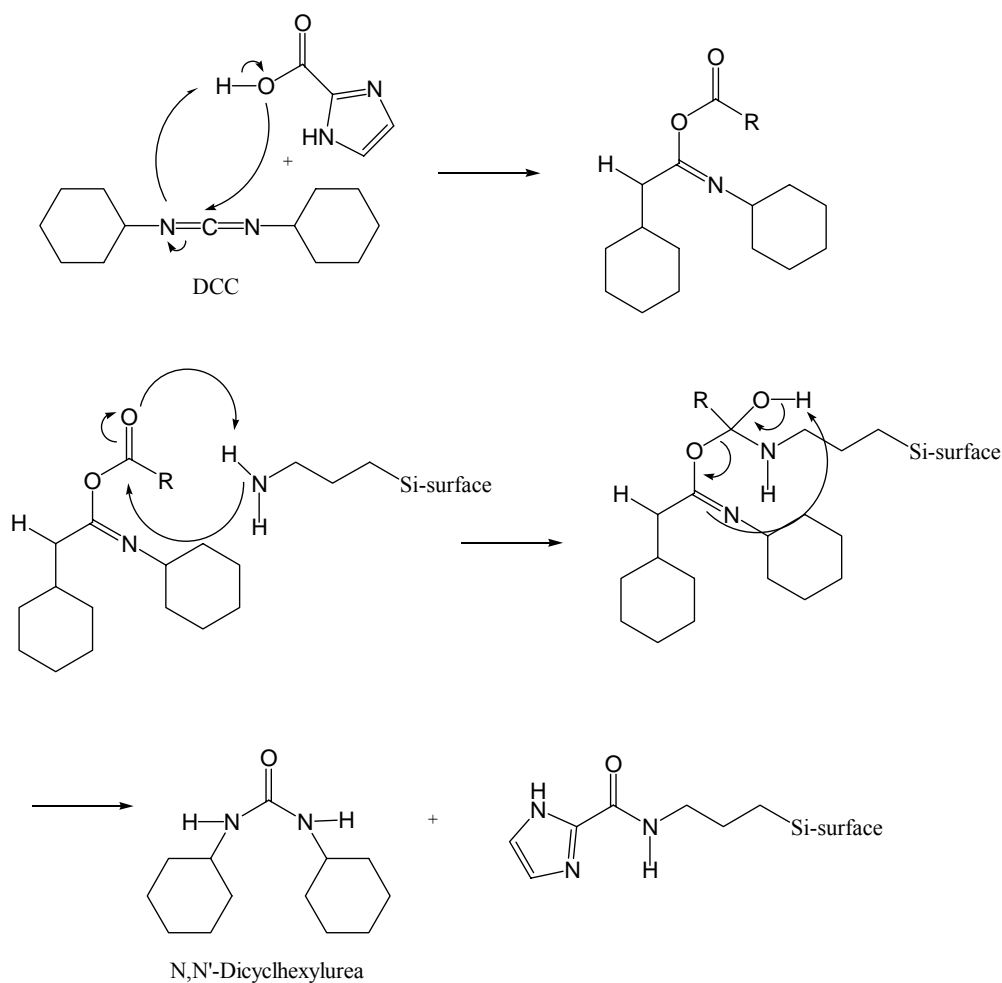


Figure 55. Mechanism forming a peptide bond between imidazole-2-carboxylic acid and surface-bound amine using DCC.²²⁰

The resulting powder is filtrated and washed with ethanol and DCM, and dried at 80 °C over night. Samples prepared via this way are denoted in section 4 as peptide-imidazole-MCM-41.

In a second approach for imidazole anchorage with aldehyde functionalized powders, an *in-situ* formation of imidazole was performed, following a procedure from Schuster *et al.*⁶²

3 Experimental

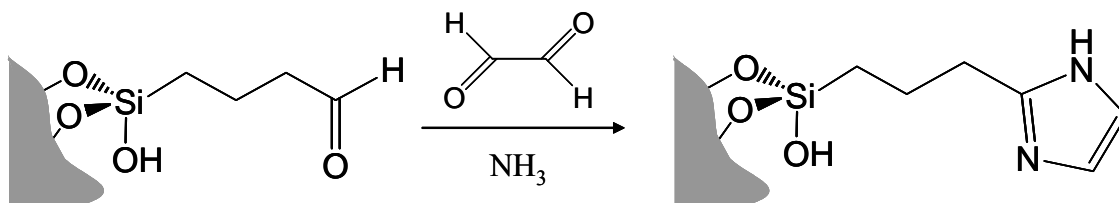


Figure 56. In-situ imidazole formation reaction.⁶²

In a typical synthesis (Figure 56), 0.3 g of aldehyde functionalized powder were suspended in 6 mL methanol at 0 °C, and 0.69 mL of glyoxal were added. Then, 2.58 mL of ammonia solution (7M in methanol) were added to the suspension, kept stirring for 6 hours at 0 °C and kept still without stirring 3 days at approx. 4 °C.

The reaction takes place in two steps; the first is shown in Figure 57 when ammonia as a nucleophile can attack the carbonyl group of an aldehyde. Under release of an OH⁻, an immonium-ion is formed as intermediate, which is stabilized as the resulting N,N-acetale.²²¹

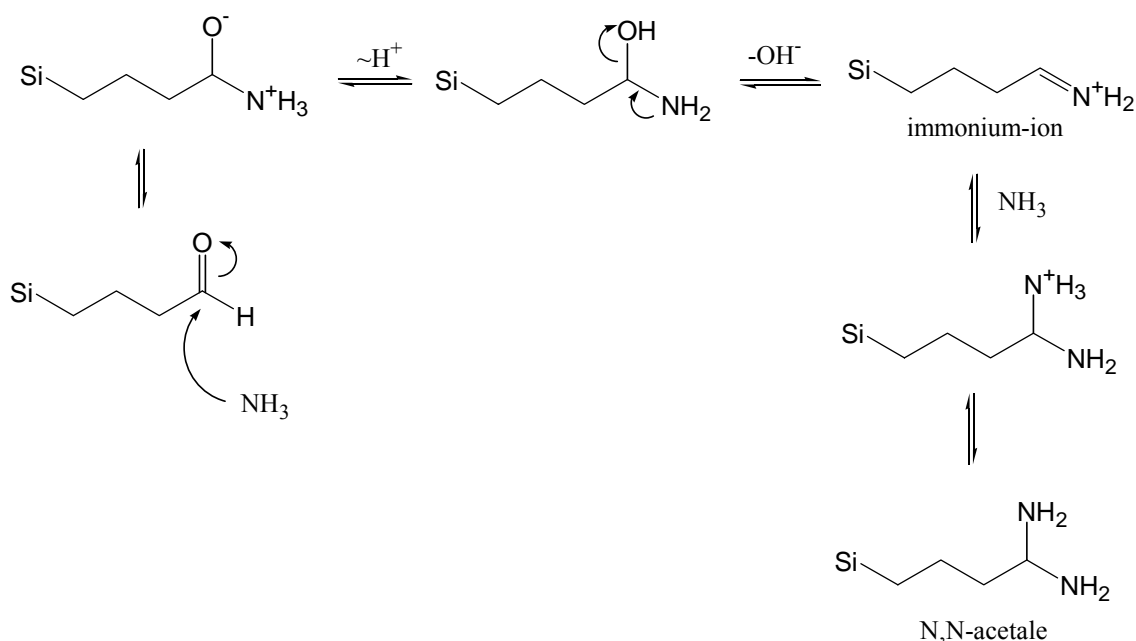


Figure 57. Formation of an N,N-acetale of a surface-bond aldehyde with ammonia.²²¹

²²¹ R. Brückner, Reaktionsmechanismen, 2nd Edition, Spektrum Verlag Heidelberg Berlin, 2003.

This N,N-acetale (or diamine in this case) can then react in a condensation reaction as a nitrogen-nucleophile two times with the carbonyl groups of the glyoxal via the following mechanism (Figure 58).²²¹

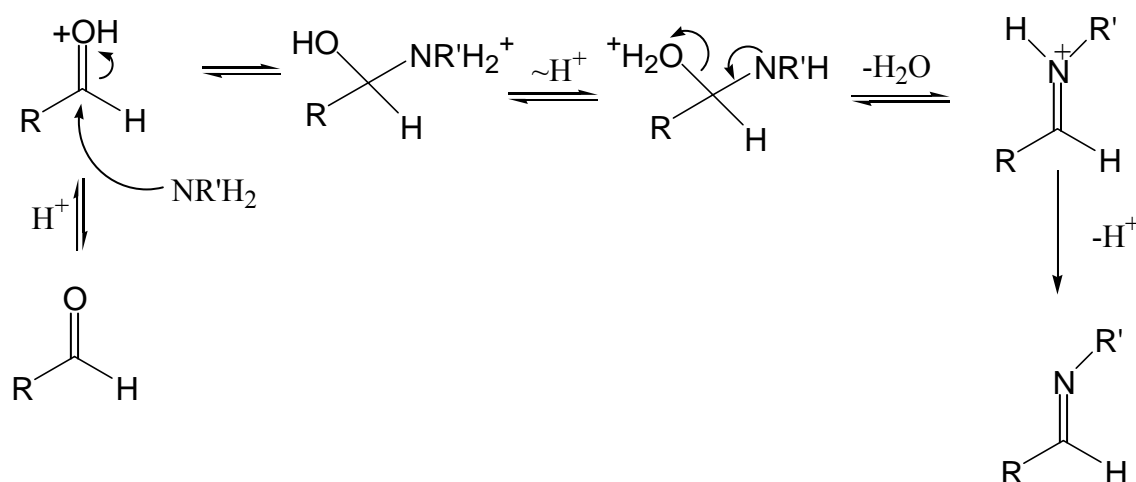


Figure 58. Condensation reaction of a nitrogen-nucleophile with a carbonyl resulting in an aldimine.²²¹

Following this reaction mechanism two times and in the second time as intramolecular condensation forming a stabilized aromatic ring compound, the imidazole heterocycle is formed (with several intermediate step including enamine formation and ring stabilization).²²¹

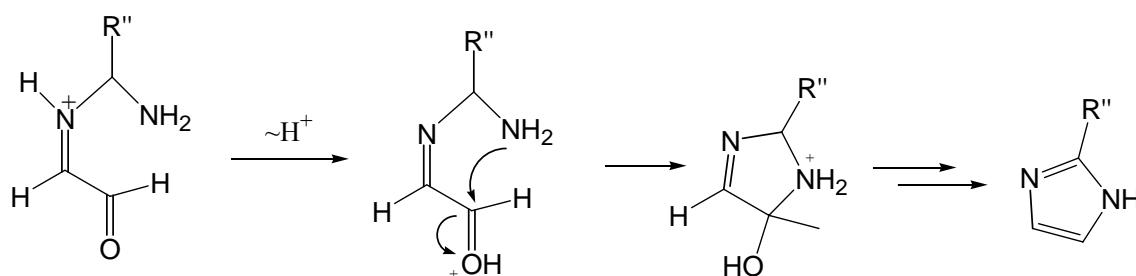


Figure 59. Imidazole ring formation.²²¹

Finally, 12 mL of water and 18 mL of ethyl acetate were added to the cold solution, stirring the mixture for 30 minutes. The resulting yellow powder was recovered with

3 Experimental

centrifuging, washed several times with ethanol, and dried at 80 °C over night. Samples prepared via this approach are denoted in section 4 as imidazole-MCM-41.

In the third approach using chlorine functionalized powders, N-imidazole anchorage was enabled in refluxing toluene, following a procedure of Armatas *et al.*¹⁴⁸

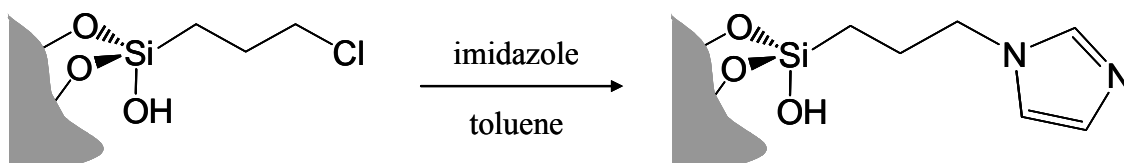


Figure 60. N-imidazole anchorage reaction.¹⁴⁸

In a typical synthesis (Figure 60), 0.5 g of functionalized powder was suspended in 20 mL of toluene and 0.3 g of solid imidazole were added to the suspension. The mixture was boiled under reflux at 125 °C for 24 hours. After reaction time, the resulting powder was filtrated and washed with toluene and ethanol, followed by drying at 80 °C over night. Sample prepared via this reaction are denoted in section 4 as N-imidazole-MCM-41.

3.2.6 Phosphonic acid formation

For the formation of phosphonic acid functionalized mesoporous samples (Figure 61), 0.5 g of $\text{PO}(\text{OEt})_2$ functionalized powder was suspended in 50 mL concentrated HCl solution (37 %) and boiled under reflux at 100 °C for 6 hours.²²²

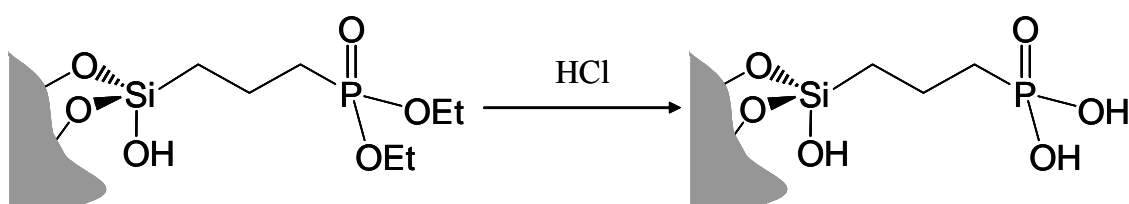


Figure 61. Phosphonic acid formation.²²²

The resulting sample was recovered by filtration and washed with high amounts of water. The solid was dried at 80 °C over night.

²²² Q. Yang, J. Yang, J. Liu, Y. Li, C. Li, *Chem. Mater.* 17 (2005) 3019.

4 Results

4.1 Pristine mesoporous silica

This chapter shows the results concerning the synthesized mesoporous silica materials, namely Si-MCM-41, Si-SBA-15 and Si-SBA-16.

Si-MCM-41 has also been synthesized in a modified synthesis procedure as mesoporous nanoparticles.

4.1.1 Si-MCM-41 via homogeneous precipitation

Powder XRD pattern of the calcined Si-MCM-41 material shows well resolved reflections in the small angle range. In the XRD pattern, the reflections can be indicated as (100), (110), (200) and (210) concerning d spacings of 3.92, 2.62, 1.96 and 1.48 nm, respectively (Figure 62). The high intensities of the peaks document the existence of a highly ordered hexagonal mesoporous structure. The hexagonal lattice constant $a_0 = 4.53$ nm was calculated.

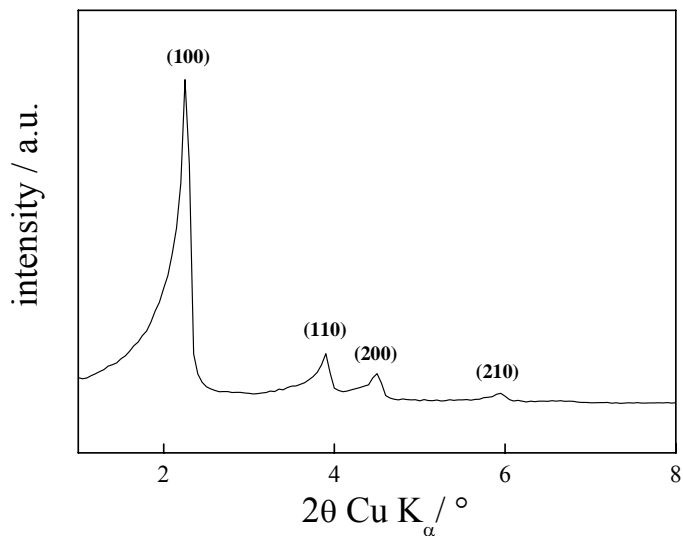


Figure 62. X-ray powder pattern of calcined Si-MCM-41.

The adsorption-desorption isotherm of the synthesized Si-MCM-41 is comparable to the literature data.²²³ At low relative pressure, monolayer adsorption occurs followed by multilayer adsorption and a strong increase in the adsorption at $p/p_0 = 0.32$ indicating the filling of the mesopores by capillary condensation (Figure 63).

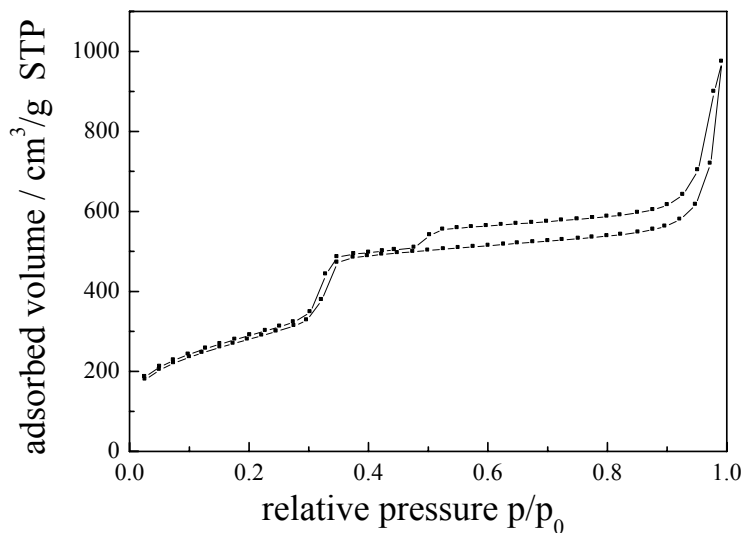


Figure 63. N₂ sorption isotherm for synthesized Si-MCM-41.

²²³ M. Kruk, M. Jaroniec, *Chem. Mater.* 15 (2003) 2942.

As typical for nitrogen adsorption measurements of CTAB-synthesized Si-MCM-41, the hysteresis behavior at a relative pressure of 0.32 caused by capillary condensation can only hardly be observed. The small hysteresis loop appearing at relative pressures > 0.5 , which is also an often observed phenomenon for Si-MCM-41, is caused by interparticular macropores present due to the small size of the Si-MCM-41 particles and by pore blocking or cavitation effects,^{223,224} where the capillary evaporation from a given pore is delayed when the pore has no access to the surrounding gas atmosphere. Si-MCM-41 exhibits the highest BET surface of the silica hosts and, estimated via the BJH method, a very narrow distribution of the pore diameters. The channel width lies in the range 2.7 ± 0.2 nm, with a very narrow pore size distribution (Figure 64), showing no additional larger pore size at higher values. Table 5 lists the obtained and calculated data compared to literature. From the pore diameter and lattice constant, an approximately wall thickness of around 1.8 nm can be calculated, a quite high value for Si-MCM-41 compared to literature.

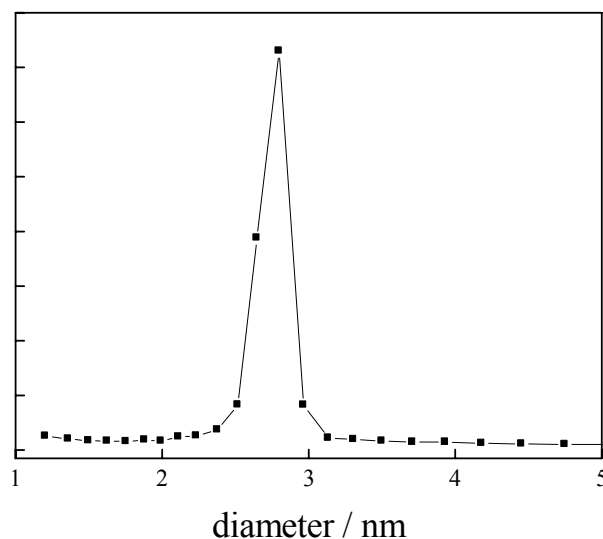


Figure 64. Pore size distribution of synthesized Si-MCM-41.

²²⁴ M. Thommes, B. Smarsly, M. Groenewolt, P. I. Ravikovitch, A. V. Neimark, *Langmuir* 22 (2006) 756.

4 Results

Table 5. Structural data of Si-MCM-41.

	S_{BET} (m^2/g)	Pore volume (cm^3/g)	Pore diameter (nm)	Lattice constant a_0 (nm)	Wall thickness (approx. nm)
Si-MCM41	1181	1.128	2.7	4.53	1.8
literature ¹⁰⁵	1086	0.866	3.3	4.38	1.1

Si-MCM-41 consists of small particles of 1–2 μm in size with a rough surface (Figure 65). The rough surface is generated during the precipitation process, and has nothing to do with the porous structure of the material.

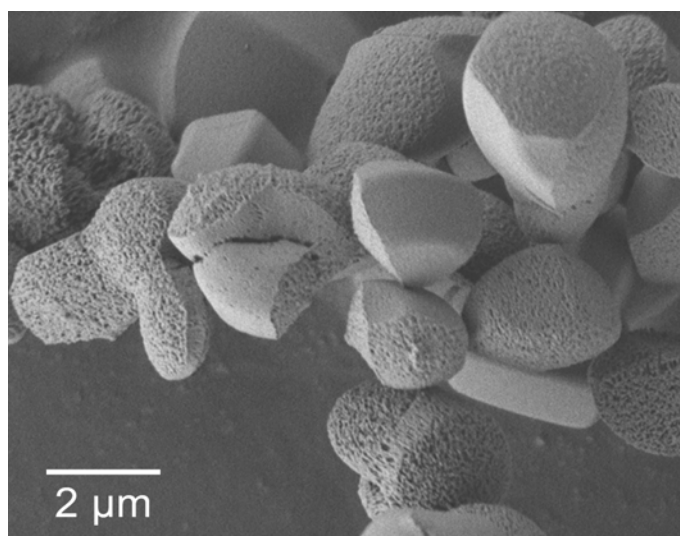


Figure 65. SEM image of synthesized Si-MCM-41.

The data for the pore diameter and lattice constants are confirmed by additional TEM measurements for the host material (Figure 66). In this figure, several particles are lying above each other. The dark lines are the amorphous silica walls of Si-MCM-41, the bright lines are the pores, due to different thicknesses for the electron beam. The picture shows in a cross-section only a thin region at the surface of a Si-MCM-41 particle, where the sample is thin enough for the electron beam. The rough surface of the

particle, already observed in SEM, is also denoted by the fluctuating contrast in the image at the surface region (lower part).

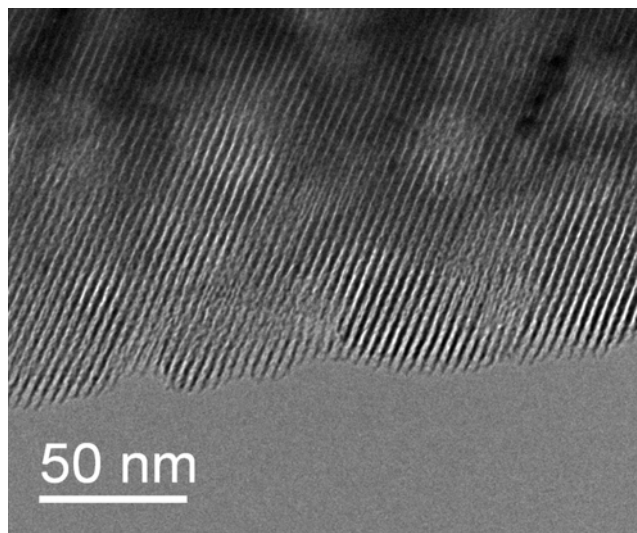


Figure 66. TEM micrograph showing the pores of synthesized Si-MCM-41.

Very interesting is the influence of the detemplation of the silica host via different methods. As synthesized Si-MCM-41 shows already the hexagonal pore structure, although the template is still inside (Figure 67, black line).

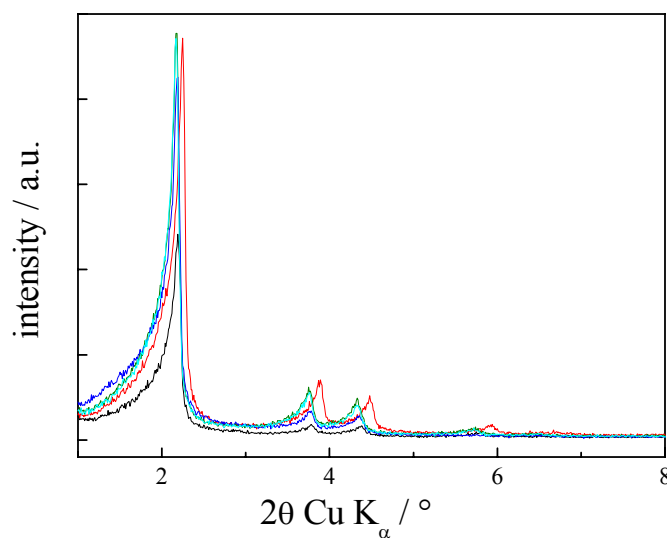


Figure 67. XRDs showing the effect of the detemplation method on Si-MCM-41. Template containing Si-MCM-41 (black), after calcination (red), after ethanol/HCl extraction (green), after ion exchange with NH_4NO_3 (bright blue), after microwave extraction (dark blue).

After calcination, the intensity of the reflections increases (Figure 67, red line). This is caused by the contrast matching between the incorporated organic groups (here: surfactant molecules) in the pores and the silica walls, resulting in lowered reflection intensities due to pore filling.²²⁵ After calcination, the reflections are shifted to higher 2θ values corresponding to a decrease in the pore size. During calcination, the template surfactant is removed, but the amorphous structure condensates further to a thermodynamically more stable state, more suitable to SiO_2 , leading to a decrease in pore size. If the template surfactant CTAB is extracted via ethanol/HCl extraction (green line), ion exchange with NH_4NO_3 (bright blue line) or microwave treatment (dark blue line) (compare chapter 2.2.5), nearly no shift in the reflection maxima is observed. Table 6 shows the change in lattice constants for the different detemplation methods, indicating the shrinking of the lattice by calcination. Nitrogen adsorption measurements showed however no difference in surface area between a calcined sample and an extracted sample. As via calcination a higher amount of powder can be detemplated, this method was still used to prepare mesoporous Si-MCM-41.

Table 6. Lattice values of Si-MCM-41 after detemplation.

	a_0
MCM as-syn	4.65
MCM calcined	4.53
MCM ethanol/HCl extracted	4.69
MCM microwave extracted	4.67
MCM NH_4NO_3 ion exchange	4.70

But especially for organically modified Si-MCM-41, the ethanol/HCl extraction method is one method of choice, as, due to the mild conditions at around 80 °C, no covalently bonded functionalities are destroyed, and only the template is removed out of the porous structure. However, if extracted sample are further calcined, the functionalities are again removed, and the porous host materials remain.

²²⁵ B. Marler, U. Oberhagemann, S. Vortmann, H. Gies, *Microporous Mater.* 6 (1996) 375.

During microwave template extraction, anchored surface functionalities also remain stable, and this method has another interesting effect presented later in chapter 4.3.1. The ion exchange method is not applied during this work, but is also a fast alternative for template removal. However, it can only be applied for template-containing silica structures synthesized via ionic interaction procedures (compare Figure 35).

4.1.2 *Si-SBA-15*

In agreement with literature data¹¹², the here synthesized Si-SBA-15 consists of 1–2 μm long worm-like particles aggregating to bigger structures, which can be seen in SEM images (Figure 68).

Its XRD pattern also indicates a highly ordered hexagonal mesoporous structure (Figure 69); the three most prominent (100), (110) and (200) peaks have d spacings of 9.92, 5.77 and 4.99 nm, respectively. As expected, the calculated hexagonal lattice constant is with $a_0 = 11.45$ nm much higher than for Si-MCM-41 with typical values around 4.5 nm.

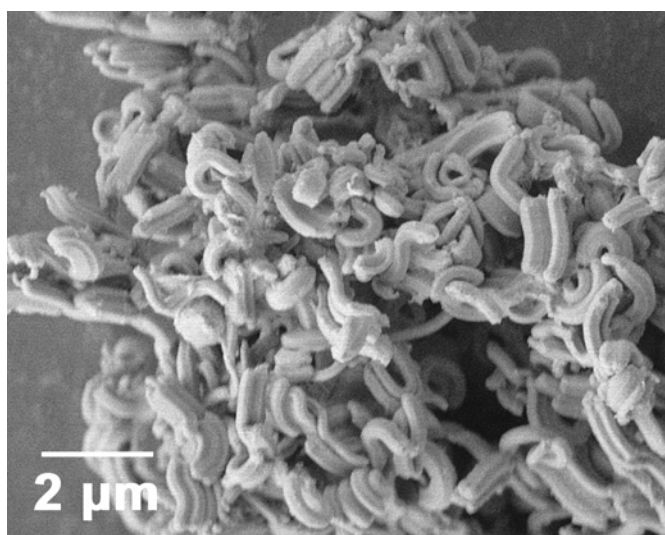


Figure 68. SEM image of Si-SBA-15.

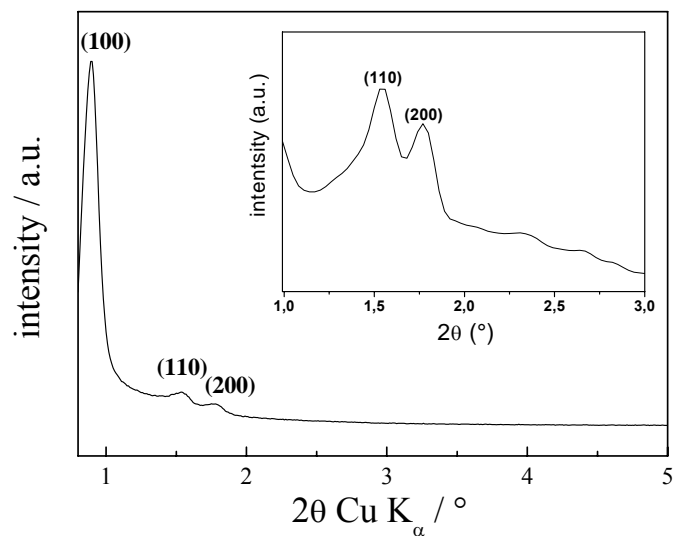


Figure 69. X-ray powder pattern of calcined Si-SBA-15.

The pores of Si-SBA-15 are much bigger with the 7.0 ± 0.2 nm than those of Si-MCM-41, and Si-SBA-15 shows the highest nitrogen uptake of the mesoporous silica hosts corresponding to the highest pore volume of $1.157 \text{ cm}^3/\text{g}$.

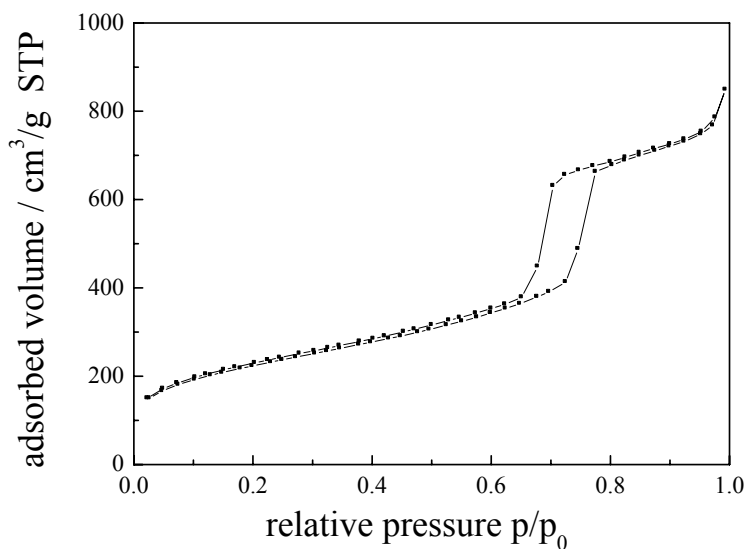


Figure 70. N_2 sorption isotherm for synthesized Si-SBA-15.

The shape of its hysteresis loop in nitrogen adsorption (Figure 70) also indicates a larger pore size than for the other silica materials, it occurs at much higher relative pressures around 0.7. At low relative pressures, an increase for a small amount of micropores is observable, due to a micropore volume of $0.151 \text{ cm}^3/\text{g}$. From literature, only a micropore volume of $0.03 \text{ cm}^3/\text{g}$ is reported. Table 7 summarizes the structural data of the synthesized Si-SBA-15 compared to literature, showing that a smaller pore diameter and thereby larger wall thickness could be achieved. Especially the pore diameter of 7 nm is of big interest for the later observed proton conductivity in the functionalized pores (chapter 4.2.1).

The pore size distribution (Figure 71) shows, as for Si-MCM-41, a narrow peak. The observed and calculated data for Si-SBA-15 are summarized in Table 7, showing a much higher wall thickness of Si-SBA-15 than for Si-MCM-41.

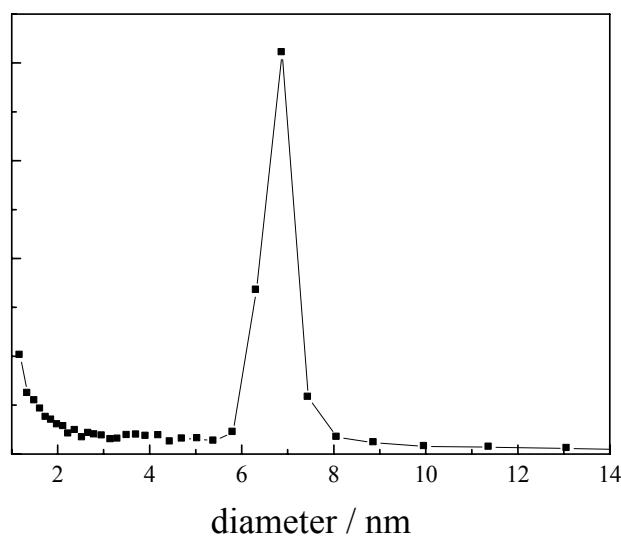


Figure 71. Pore size distribution of synthesized Si-SBA-15.

4 Results

Table 7. Structural data of Si-SBA-15.

	S_{BET} (m^2/g)	Pore volume (cm^3/g)	Pore diameter (nm)	Lattice constant a_0 (nm)	Wall thickness (approx. nm)
Si-SBA15	769	1.157	7.0	11.45	4.5
literature ¹¹⁴	690	1.170	9.0	11.30	2.3

The porous structure is of course additionally confirmed via TEM images, which make visible the highly hexagonally ordered pore structure (Figure 72). Three particles can be seen in this figure overlapping, the dark lines are again the pore walls, while the bright lines are the pores themselves.

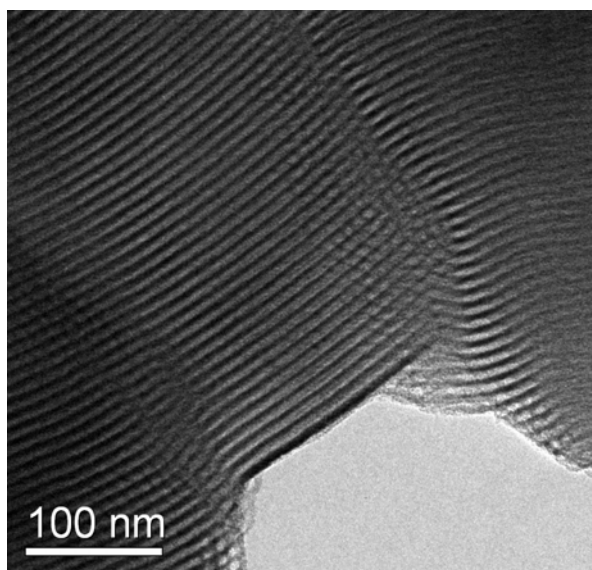


Figure 72. TEM micrograph of synthesized Si-SBA-15.

4.1.3 Si-SBA-16

Si-SBA-16 exhibits particles of different sizes in a regime of 1-3 μm with rhombododecahedron shape, which is typically found for this material (Figure 73).²¹⁹

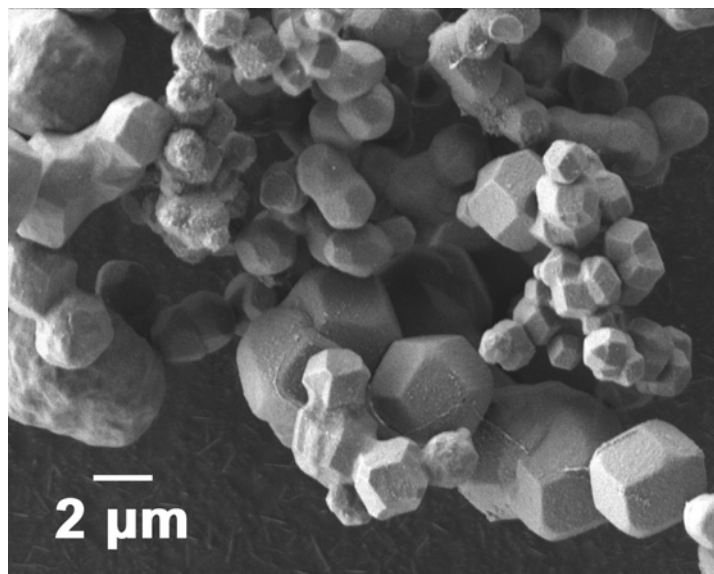


Figure 73. SEM image of synthesized Si-SBA-16.

Because of the cubic pore structure, the XRD pattern (Figure 74) differs slightly from those of Si-MCM-41 and Si-SBA-15 with hexagonal pore structure. Four peaks could be indicated as (200), (220), (310) and (222) with d spacings of 7.88, 6.56, 5.58 and 5.11 nm, proving a highly ordered cubic pore arrangement. The signals are quite weak, but this is typical for this material.²¹⁹ A lattice constant a was calculated to 15.76 nm. Due to the large lattice constant the peaks with lower (hkl) indices could not be resolved with the used instrument.

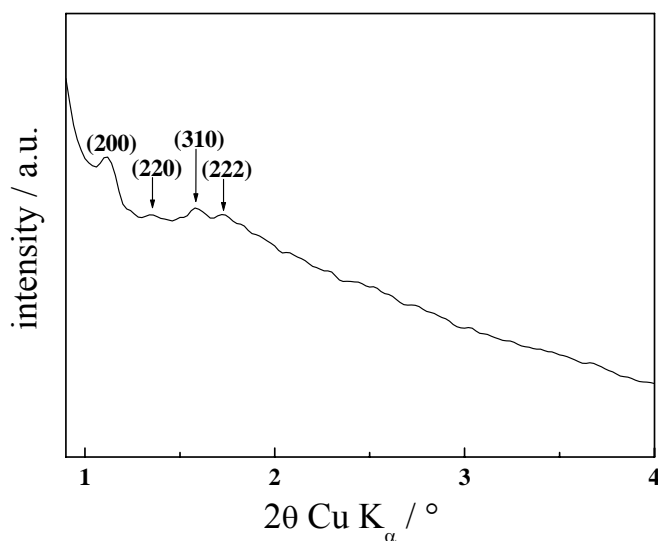


Figure 74. XRD pattern of Si-SBA-16.

Si-SBA-16 with its cage-like structure shows a cavitation effect²²⁴ in the desorption branch at around $p/p_0 \sim 0.5$, because the adsorbed gas in the cages of Si-SBA-16 has to be released via channels whose diameter are smaller than the cages diameter. The cage diameter is therefore estimated via pore size distribution from the adsorption branch to approx. 6.2 nm, while from the desorption branch only the pore channel widths could be calculated due to the cavitation effect. The adsorption branch shows the increase for the multilayer adsorption at similar relative pressures like Si-SBA-15 (Figure 75).

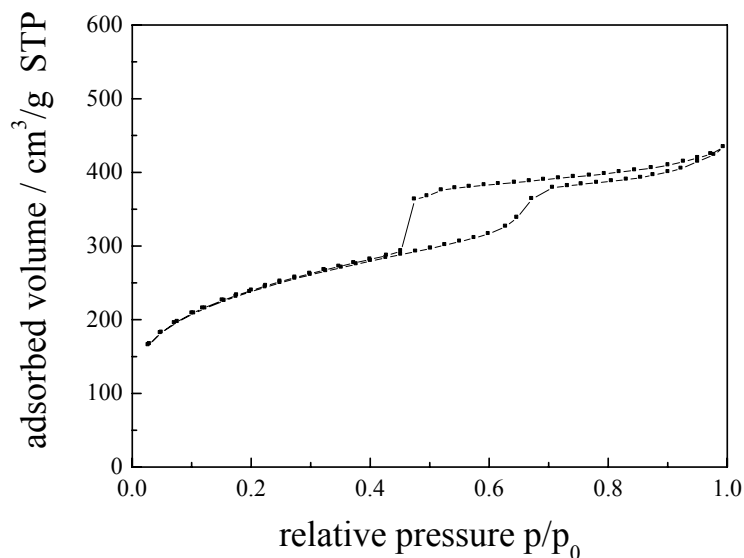


Figure 75. N₂ sorption isotherm of synthesized Si-SBA-16.

Si-SBA-16 pore structure has the smallest pore volume 0.642 cm³/g of all silica materials, but the walls thickness is the highest of all host silica materials with about 11 nm. And also the BET surface is the smallest with 792 m²/g, but comparable to the typical literature data. Table 8 summarized the data for Si-SBA-16, indicating that, unlike the pore volume, the synthesized materials are similar to literature example. Figure 76 shows the cage diameter of Si-SBA-16 estimated from the adsorption branch of the measured nitrogen isotherm.

Table 8. Structural data of Si-SBA-16.

	S _{BET} (m ² /g)	Pore volume (cm ³ /g)	cage diameter (nm)	Lattice constant a (nm)	Wall thickness (approx. nm)
Si-SBA16	792	0.642	6.2	15.76	9
literature ²²⁶	790	0.470	7.6	14.00	7

²²⁶ T.-W. Kim, R. Ryoo, M. Kruk, K. P. Gierszal, M. Jaroniec, S. Kamiya, O. Terasaki, *J. Phys. Chem. B* 108 (2004) 11480.

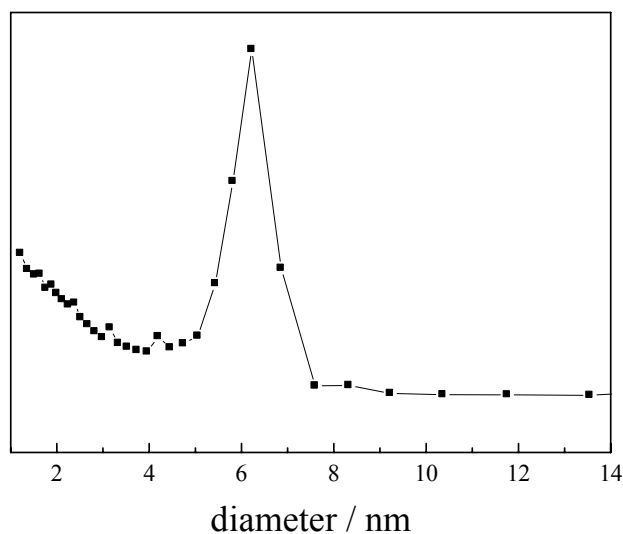


Figure 76. Cage diameter of Si-SBA-16 estimated from nitrogen adsorption.

4.1.4 Si-MCM-41 nanoparticles

The applied synthesis of nanosized Si-MCM-41 with highly ordered hexagonal pore structure was successfully performed and confirmed via four well resolved reflections in the small angle range in the XRD pattern. The reflections can be indicated as (100), (110), (200) and (210) concerning d spacings of 4.07, 2.35, 2.04 and 1.54 nm, respectively (Figure 77), and show thereby the same high order as the μm -sized Si-MCM-41 materials synthesized by “homogeneous precipitation”.

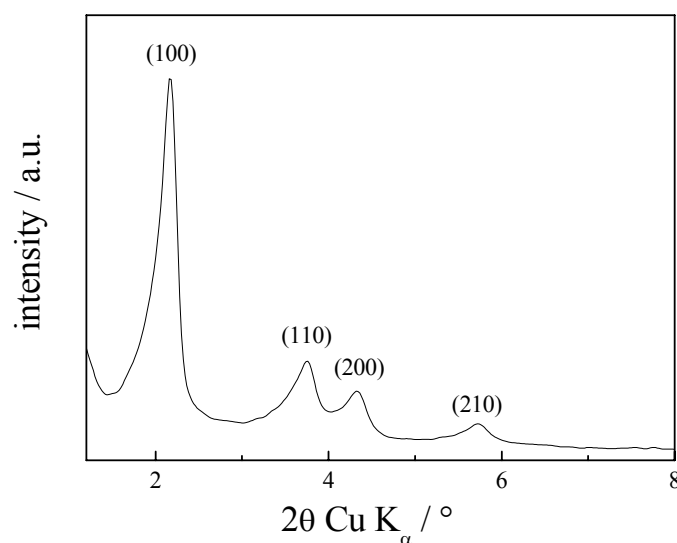


Figure 77. XRD pattern of synthesized nano-Si-MCM-41.

Nano-Si-MCM-41 has a BET surface area of about 1459 m²/g, a pore volume of 1.344 cm³/g and a pore diameter of approx. 2.8 nm (Table 9). Compared to the μm-sized Si-MCM-41 data in Table 5, pore diameter, lattice constant and wall thickness are very alike, although the synthesis method is very different. The values for surface area and pore volume of the nanomaterials are much higher per gram. However, compared to the literature, the here synthesized materials have strongly improved texture properties like drastically increased surface area and pore volume, including much thicker and more stable pore walls. Important for a successful synthesis is a strict control of the reaction temperature of 80 °C. Also a template removal via ethanol/HCl extraction conserves the high ordering of the nanoparticles better than the calcination applied in literature.¹⁰⁸

Table 9. Structural data of nano-Si-MCM-41.

	BET surface area (m ² /g)	Pore volume (cm ³ /g)	Pore diameter (nm)	Lattice constant a ₀ (nm)	Wall thickness (approx. nm)
nano-Si-MCM-41	1459	1.344	2.8	4.70	1.7
literature ¹⁰⁸	965	0.840	3.0	3.46	0.5

4 Results

The nitrogen sorption isotherm for nano-Si-MCM-41 in Figure 78 looks very similar to the one of $\mu\text{m-Si-MCM-41}$ seen in Figure 63, with the steep increase in adsorption at relative pressure 0.32 caused by capillary condensation. At relative pressures > 0.98 , a strong increase in the adsorption is observed due to interparticular porosity. From a slight increase in the isotherm at very low relative pressures < 0.1 , a small amount of micropores could be assumed, but these were not detectable via simple nitrogen adsorption. Small angle neutron scattering (SANS) coupled with *in-situ* nitrogen adsorption could give insight into a possible pore connectivity between the mesopores of the nanoparticles via micropores, as this method was applied and evaluated already for other hierarchical porous silica materials with 14 nm spherical mesopores connected via 3 nm worm-line pores.²²⁷ This is part of further investigations.

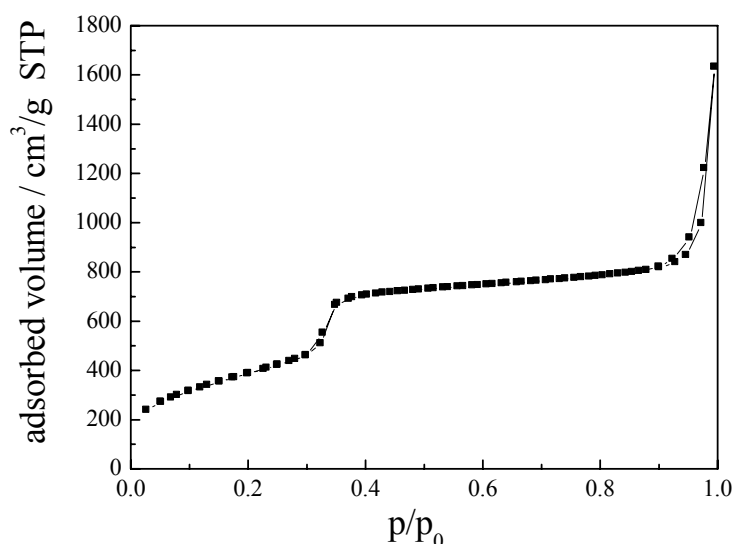


Figure 78. N_2 sorption isotherm for synthesized nano-Si-MCM-41.

The pore size distribution (Figure 79) is also very narrow, like for $\mu\text{m-Si-MCM-41}$, showing a pore diameter of 2.8 nm, and no larger pores at higher values. In the SEM and (HR)TEM images, the particles sizes of around 100 nm and the highly ordered pore structures can be seen (Figure 80), confirming the XRD and sorption results.

²²⁷ O. Sel, A. Brandt, D. Wallacher, M. Thommes, B. Smarsly, *Langmuir* 23 (2007) 4724.

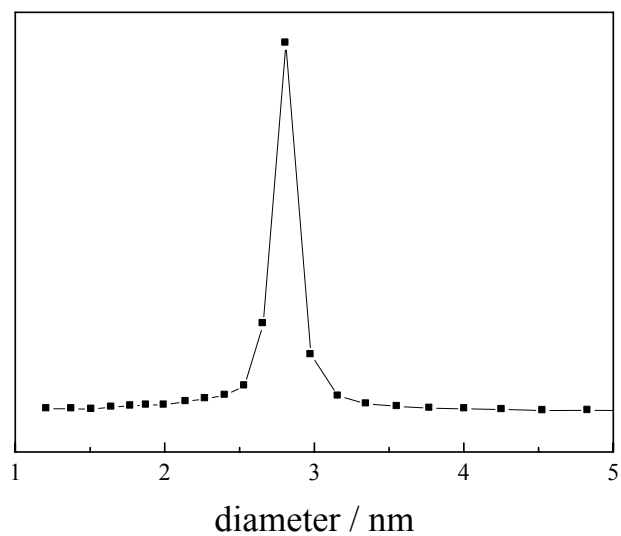


Figure 79. Pore size distribution of synthesized nano-Si-MCM-41.

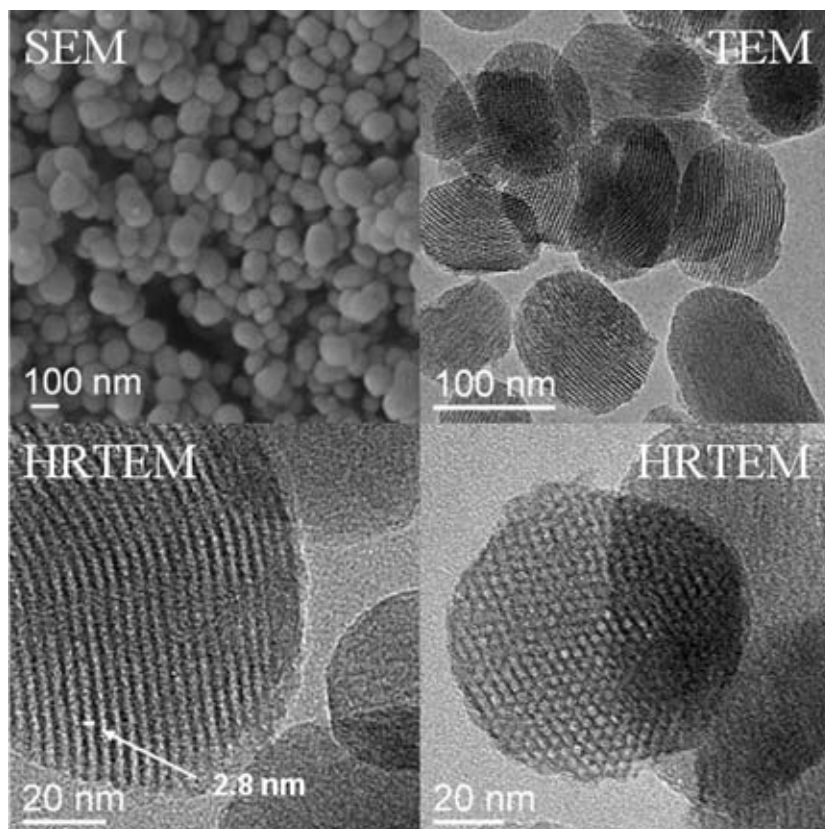


Figure 80. SEM and (HR)TEM images of synthesized nano-Si-MCM-41.

Especially in the lower right TEM image, the hexagonal honeycomb structure is visible in the 100 nm particle. The black lines are in the TEM images the pore walls and the white dots/lines are the pores.

The high dilution technique in high amounts of water, together with the high reaction temperature of 80 °C and the short reaction time (two hours) are responsible for the small particle size. Especially the high temperature slows down the particle growth. Increasing the reaction temperature further leads to a slightly decrease of the particle size, but with low reasonable extend.²²⁸

4.1.5 Silica host summary

Different silica host materials have been successfully synthesized according to the introduced reactions in section 3, namely Si-MCM-41, Si-SBA-15, and Si-SBA-16. They all show highly ordered porous structures with high surface areas for binding organic groups in nitrogen adsorption measurements, while the pore size has a narrow distribution for all materials. XRD and TEM proof the high ordering of the materials, while SEM showed particles of several micrometers.

The successful synthesis of mesoporous nanoparticles, nano-Si-MCM-41, with very good hexagonally pore order and particles size of 100 nm is a highlight of this work, showing that the properties of μm -Si-MCM-41 could also be transferred into the nanometer range, and even improved e.g. with higher surface area for bonding of functional groups. The different types of pore systems and particles sizes will play a role in proton conductivity measurements of functionalized hosts presented later, when either smaller pore diameters (chapter 4.2.1) or small particles (chapter 4.3.5) will show the best proton conductivity properties.

²²⁸ Y. G. Jin, R. Marschall, unpublished results.

4.2 Functionalization via grafting

The surfaces of the synthesized mesoporous materials presented in chapter 4.1 are functionalized with different organic groups to enable proton conductivity in the materials. The focus lies here on the functionalization with SO_3H groups, being the most promising groups for proton conductivity in solid proton conductors. But also other functionalities via grafting are established and compared to the SO_3H materials in the following chapters. As host material, the Si-MCM-41 is mostly used due to the results presented in chapter 4.2.1.

4.2.1 Functionalization of mesoporous silica with SO_3H groups via grafting

Si-MCM-41, Si-SBA-15 and Si-SBA-16 are functionalized first with SH groups following the procedure presented in chapter 3.2.2. As the alkoxy silane MPMS reacts with the surface silanol groups, the only by-product is methanol from the silane rests. The successful functionalization can be seen in IR spectroscopy. After silylation of the mesoporous materials with MPMS, the FT-IR spectra of all the composites show absorption bands in two regions. Between 2850 and 3000 cm^{-1} the typical bands for C-H stretching vibrations of aliphatic CH_2 groups appear²²⁹, indicating the successful functionalization of the host material with the silane compound. At 2580 cm^{-1} , the band for the S-H stretching vibration should become visible; this band, however, is typically rather weak and hardly observable, especially due to the low amount of sulfur incorporated into the silica materials (maximum 1.16 mmol/g calculated from TG

²²⁹ M. Hesse, H. Meier, B. Zeeh, *Spektroskopische Methoden in der organischen Chemie*, 6th Ed., Thieme, Stuttgart (2002).

weight loss, Figure 85). As typical, not all the offered silanes react with the silica surface. But with increasing the amount offered, the bonding amount can be increased.

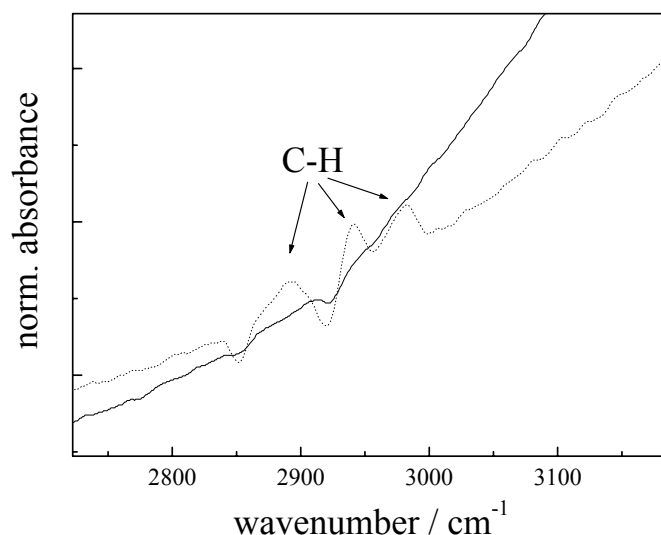


Figure 81. IR spectra of mesoporous silica (black line) and SH functionalized silica (dotted line).

In Figure 81, the aliphatic signals for the successful silylation are shown, compared to non-functionalized silica showing no peaks. Both spectra show a strong increase in absorption to higher wavenumbers, which corresponds to a broad signal of adsorbed water in the pores at higher wavenumber around 3300 cm⁻¹.

IR spectroscopy gives qualitative information about the silylation, but quantitative results are normally not reliable. To observe a trend in ongoing and increasing functionalization, XRD can be used making visible the ongoing pore filling. As mentioned in chapter 3.2.2, the silica functionalizations have been performed with different amount of MPMS offered in the reaction. In XRD, the reflection intensities decrease with an increasing loading of the silica with propyl-SH groups due to contrast matching in XRD of the silica walls with the carbon chains (compare chapter 3.1.2). Figure 82 shows this effect exemplarily for SH functionalized Si-MCM-41.

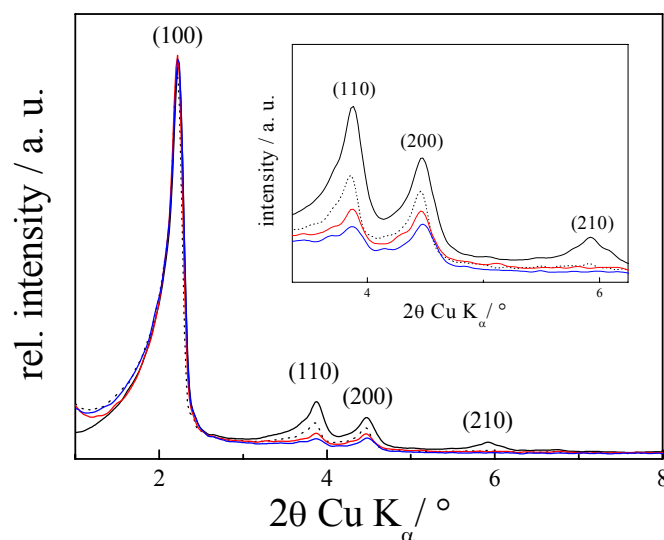


Figure 82. XRDs for SH-MCM-41 with decreasing intensities for pristine Si-MCM-41 (black) and SH functionalized Si-MCM-41 after 5 mmol (dotted), 10 mmol (red) and 20 mmol (blue) grafting.

The black line indicates the XRD of pristine Si-MCM-41 already introduced in chapter 4.1.1, the dotted line corresponds to 5 mmol/g MPMS in the grafting reaction, the red line to 10 mmol/g, and the blue line to 20 mmol/g. The XRD patterns are normalized on the (100) reflection for better comparison. Especially in the inset, it can clearly be seen that, with increasing offer of MPMS in the functionalization reaction, the intensity of the reflections is decreasing indicating the trend of higher surface functionalization with organic moieties by higher alkoxy silane offer, due to the mentioned contrast matching between silica host and the carbon chains in the pores.²²⁵ With increasing pore filling, the electron density contrast becomes more similar between walls and pores, and the reflection intensity decreases.

Nitrogen adsorption measurements confirm these observations. Pure Si-MCM-41 has a large BET surface area and pore volume (compare Table 5). After functionalization, the surface areas and especially pore volumes decrease due to the incorporation of organic moieties onto the pore surface. The measurements presented in Figure 83 are exceptionally performed on a Micromeritics Gemini 2375 apparatus, but nevertheless showing clearly the influence of functionalization.

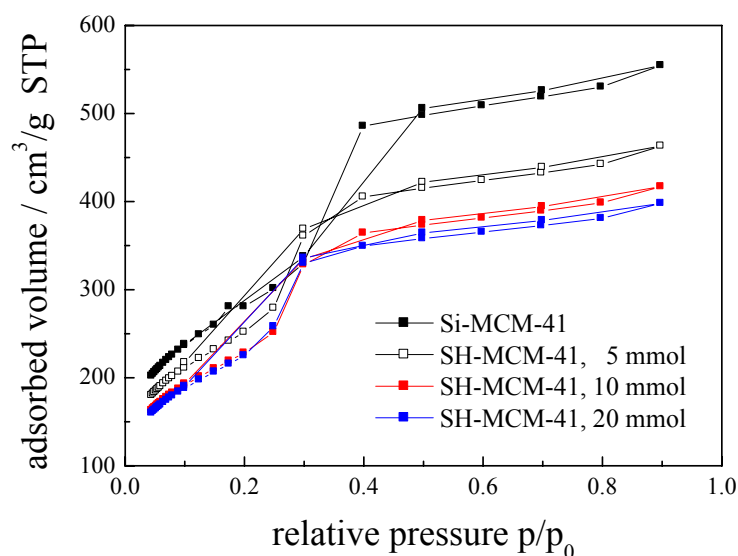


Figure 83. N₂ adsorption isotherms for pristine Si-MCM-41 (■) and SH functionalized Si-MCM-41 after 5 mmol (□), 10 mmol (■) and 20 mmol (■) grafting.

Like in the XRDs the reflection intensities decreased with pore filling, here the adsorbed volume deteriorates with increasing amount of MPMS in the grafting reaction. The estimated pore volumes decrease continuously down from 1.128 cm³/g for the pristine host to 0.615 cm³/g, and the surface areas down from 1181 to 817 m²/g.

To enable SO₃H functionalities on the silica surface, the different SH functionalized silica were treated in H₂O₂ (chapter 3.2.4). The best way to confirm the successful oxidation is again IR spectroscopy.

After successful oxidation of the anchored SH groups with H₂O₂, two bands for sulfonate groups appear in the range from 1100 cm⁻¹ to 1300 cm⁻¹.²²⁹ Figure 84 shows exemplarily a cut-out of the FT-IR spectrum of SO₃H functionalized Si-MCM-41 (dashed line). In this cut-out the strong asymmetric Si-O-Si stretching vibration at approx. 1058 cm⁻¹ dominates all the three shown curves; in order to better visualize the S-O bands, all the spectra are normalized to this vibration. The spectrum shown with a solid black line represents the host material Si-MCM-41. An additional small band at 1240 cm⁻¹ results from a second asymmetric Si-O-Si stretching vibration. After thiol-grafting, no change in the spectrum is observed, as no bands for C-H or S-H vibrations

lie in the shown region. In contrast to the hardly visible S-H vibration, the C-H stretching vibrations between 2850 and 3000 cm^{-1} are observable either after SH grafting or after SH oxidation.

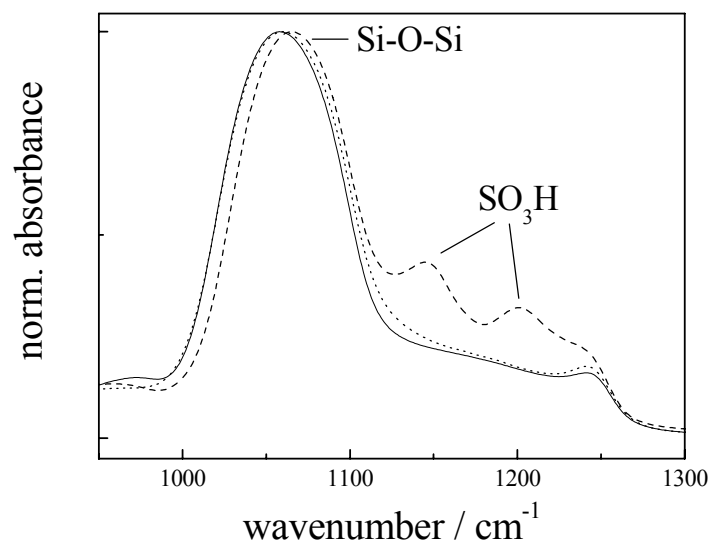


Figure 84. IR spectra of pure Si-MCM-41 (black line), SH-MCM-41 (dotted line) and SO₃H-MCM-41 (dashed line).

As the S-H vibration is hardly visible in the IR spectrum, IR gives no information about a complete oxidation of all SH groups to SO₃H groups. This information can be provided via thermal analysis.

Important steps to achieve a high degree of functionalization with SO₃H groups are an efficient grafting step as well as a complete oxidation of the thiol groups. TGA and DTA analyses of a SO₃H functionalized Si-MCM-41 sample after 20 mmol/g grafting reaction and subsequent oxidation reaction clearly show an incomplete oxidation under the conditions used (Figure 85). Following the desorption of water at around 100 °C, the peak at 343 °C in the DTA indicates the decomposition of non-reacted alkylthiol groups, the following second peak at 430 °C corresponds to the decomposition of alkylsulfonic acid groups¹⁹⁷. The slight differences in the temperatures of the peak minima with respect to the study of Margolese *et al.*¹⁹⁷ (343 °C instead of 350 °C and 430 °C instead of 460 °C) are probably caused by the different measurement assembly

and different heating rates (10 °C/min instead of 5 °C/min). Concerning the mass loss from the TGA, a functionalization with SH of 1.16 mmol/g is calculated. The extent of oxidation is about 86 % due to ionic exchange capacity (IEC) of 1.0 mmol/g, being in the range of reported post-synthesis oxidation methods¹⁹⁷ (77 % for 48 hours reaction time). Theoretically, a maximum IECs of 1.67 mmol/g might be possible, but blocking effects and hindrance of MPMS diffusion into the pores restrict the loading. IECs are further discussed in chapter 4.2.2 in comparison to proton conductivity values. Other oxidation methods are reported¹⁵⁸ giving no values about oxidation extend, but another new approach will be presented in this work later (chapter 4.3.1).

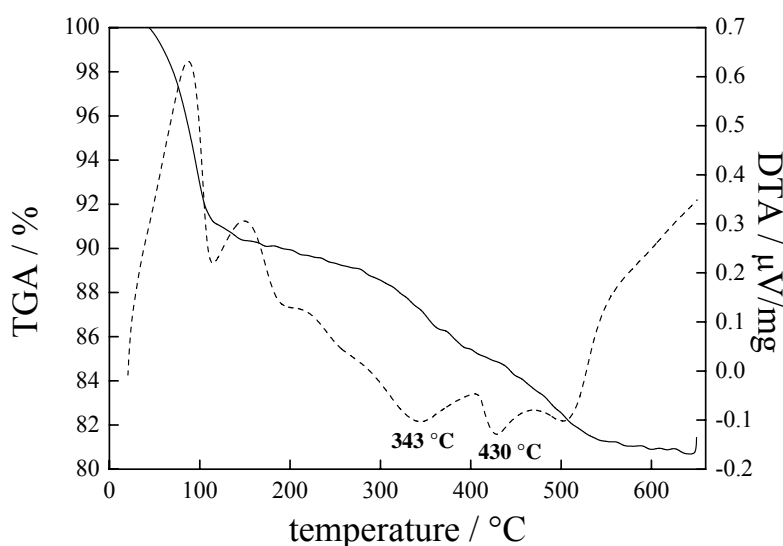


Figure 85. TGA (black line) and DTA (dashed line) of SO₃H-MCM-41 after 20 mmol/g grafting with MPMS and subsequent oxidation.

With the oxidation of SH groups to SO₃H groups, another property of the functionalized powders changes extremely, namely the water adsorption. The water uptake of inorganic particles was examined by volumetric vapor sorption at 22 °C in the relative pressure range of p/p_0 0.0–0.98. The resulting isotherms are presented in Figure 86. The isotherms on the pristine Si-MCM-41 and grafted SO₃H-MCM-41 are of type V,^{87,207} the pore filling and emptying occurring within a narrow range of relative pressure at approx. 0.4 and 0.5, respectively. This values of relative pressure correspond to the pore

diameters of about 2-3 nm as calculated from the Kelvin's equation.²¹² The shift in the location of the sharp step in both adsorption and desorption isotherms towards lower relative pressures is due to a slight narrowing of the average pore width caused by the grafting (Figure 83).²³⁰

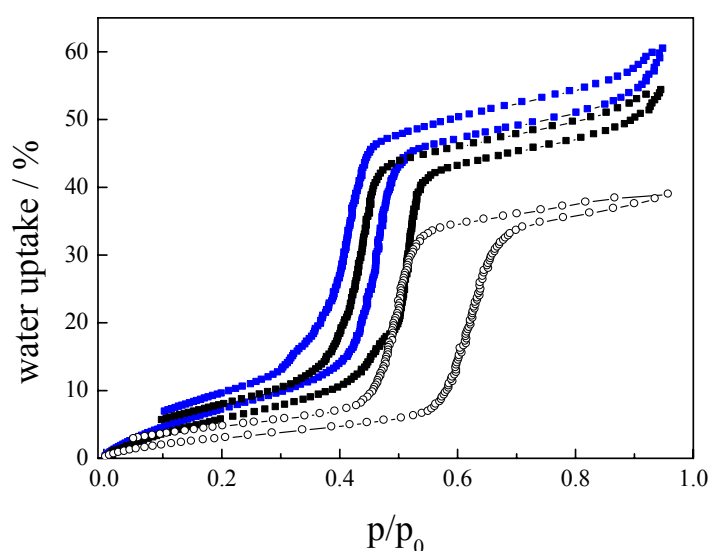


Figure 86. Water uptake of pristine Si-MCM-41 (■), SH-MCM-41 (○) and SO₃H-MCM-41 (■) after 20 mmol/g grafting and oxidation.

Pure Si-MCM-41 shows a very high water uptake up to 50 wt.-% at $p/p_0 = 0.95$. This can be explained by the very hydrophilic surface of the material, bearing many silanol groups, 2.8 to 3.2 per nm^2 .^{135,136} When these silanol groups are used to bind organic moieties, the functionalization silanes need at least 1-2 silanol groups to attach to the Si-MCM-41 surface, decreasing drastically the pore wall hydrophilicity. In addition, functionalization with MPMS implicates the addition of the hydrophobic propyl chain ending in a low hydrophilic thiol group. These facts result in a drastic decrease of water uptake for SH functionalized Si-MCM-41 indicating the increasing hydrophobicity of the sample. When the SH groups are subsequently oxidized, the low hydrophilic thiol-group is converted into the very acidic and hydrophilic SO₃H group. The high hydrophilicity of this end group overcompensates even the hydrophobicity of the spacer

²³⁰ S. J. Gregg, K. S. W. Sing, *Adsorption, Surface Area, and Porosity*, Academic Press Inc., London, (1982).

propyl chain and the decreased number of surface silanol groups, resulting in a water uptake even higher than the pure material of 60 wt.-%. Especially at low relative pressures up to 0.2, which area is more interesting for application (low RH), the SO₃H functionalized sample already shows a steeper increase in water uptake, and the SH-MCM-41 a weaker increase compared to the pristine Si-MCM-41.

However, the adsorption of water is at low relative pressure somehow irreversible, as the desorption branch does not close to the adsorption branch of the isotherms of SH and SO₃H functionalized Si-MCM-41, indicating irreversible water adsorption in the pores. In fact, the observed high water storage capability and hydrophilicity makes SO₃H functionalized MCM-41 suitable as efficient solid proton conductors.

4.2.2 Proton conductivity of grafted SO₃H functionalized silica materials

For determining the proton conductivity of the synthesized samples, pellets of the samples were tested in impedance spectroscopy (IS). The measured samples were referred with different abbreviations like x mmol y, where x mmol gives is the amount of MPMS used in the functionalization reaction per gram solid materials, and y represents the degree of RH in the cell and at the sample during the impedance measurement. For example, 5 mmol 100 refers to a sample where 5 mmol MPMS per gram host material were added in the grafting reaction and impedance spectroscopy of the sample was performed at 100 % RH.

Figure 87 compares the results of impedance measurements for the three host materials functionalized with SO₃H groups, after grafting with 5 mmol/g of MPMS and oxidation, at 100 % RH. The proton conductivity clearly increases with temperature for all the samples because of the higher diffusivity of water and the higher flexibility in the chains of the organic moieties. Proton conductivity with water currently occurs via the

so-called Grotthuss mechanism.³ In this mechanism the proton transport is mainly based on hopping of the protons from one water molecule to the next (chapter 2.1.5). To a smaller extent, also the diffusion of H_9O_4^+ complex-ions (Eigen-ion) enhances the proton transport.

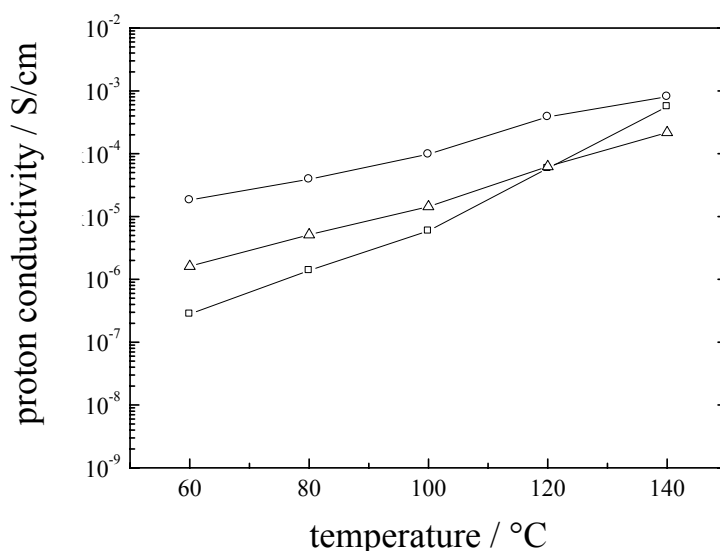


Figure 87. Proton conductivities at 100 % RH of $\text{SO}_3\text{H-MCM-41}$ (□), $\text{SO}_3\text{H-SBA-15}$ (○) and $\text{SO}_3\text{H-SBA-16}$ (Δ) after 5 mmol/g grafting and oxidation. The lines are only to guide the eyes and have no physical meaning.

A temperature increase strongly affects both mechanisms. The diffusion in water is faster, and since the movement of the anchored SO_3H modified propyl chains is affected also the proton hopping between the groups is enhanced, because the spacer propyl chains rotate and vibrate more easily, and the SO_3H groups at the end of the chains can easier encounter each other, and thus the direct proton transport is facilitated. This is confirmed in MD simulations, when direct counting of the total amount of donor-acceptor pairs (protonated and deprotonated SO_3H groups) available at 0.28 nm (a preferred distance for proton transfer⁵⁸, see also chapter 4.3.1, Figure 123) was performed during simulation. For a group density of 1 group/nm² (the maximum value for grafted materials, see below), this value exhibits 9 pairs. For each possible donor-acceptor pair the total time that this pair is within the 0.28 nm is a variable called

4 Results

collision number, and it is counted every 1 ps. In order to estimate a probability of having the collision of an specific donor-acceptor pair in the total time, for each pair the collision number is divided by the total time (total number of frames) obtaining a quantity called collision ratio of the specified donor-acceptor pair. For the density of 1 group/nm² the pair that has the highest number of collisions has a collision ratio of 0.42 at 177 °C, this value decreases to only 0.32 at 127 °C. This means that, at higher temperatures, the protogenic groups encounter each other more easily and more often.

The channel geometry of the pores in which the sulfonic acid groups are fixed helps to attach and keep water and supports the guidance of the protons through the tested pellets. The three materials show different increase of their conductivity with temperature indicating a water storage effect. At elevated temperatures above 100 °C the functionalized Si-MCM-41 with its narrower 3 nm pores keeps the water molecules better than the wider (~7 nm pore diameter) Si-SBA-15 and Si-SBA-16 materials. In all measurements Si-SBA-16 shows the lowest proton conductivities; the cubic pore arrangement cannot guide the protons and water molecules as good as the hexagonal 1D channel pore arrangement in the other materials. At higher loadings (20 mmol/g, Figure 88) functionalized Si-MCM-41 shows conductivities almost one order of magnitude higher than for the Si-SBA-15 and Si-SBA-16 composites.

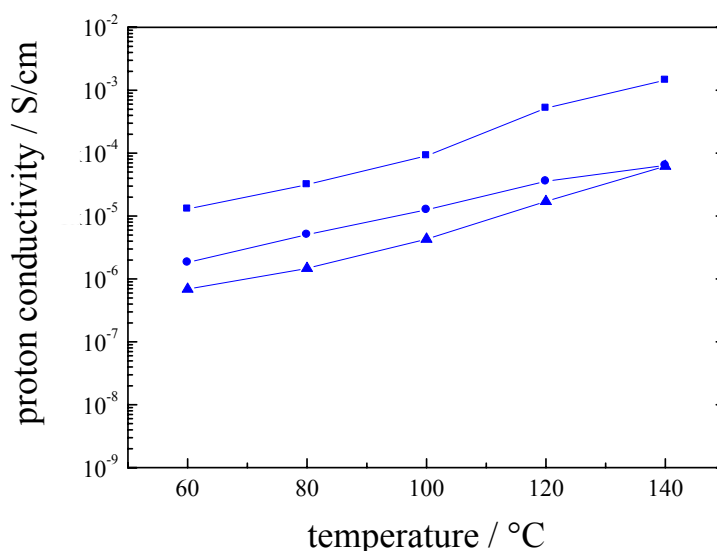


Figure 88. Proton conductivities at 100 % RH of SO₃H-MCM-41 (■), SO₃H-SBA-15 (●) and SO₃H-SBA-16 (▲) after 20 mmol/g grafting. The lines are only to guide the eyes and have no physical meaning.

The reason is given by the much higher surface area of Si-MCM-41 providing more silanol groups at which the MPMS can bind. Thus, more SO₃H groups on the surface can attach water for guiding the protons through the pores. In addition, in the narrower pores of Si-MCM-41, the SO₃H groups stand closer to each other than in Si-SBA-15 or Si-SBA-16 facilitating the proton hopping between the SO₃H groups. Si-MCM-41 materials possess around 2.8-3.2 silanol groups per nm² inner surface.^{135,136} For estimating the average distance between the SO₃H groups in Si-MCM-41 and Si-SBA-15, the degree of functionalization is related to the pore volumes and pore diameters. Assuming that mostly the silane reagents attach to one or two silanol groups, minimum distances between the grafted moieties of 0.33 nm for Si-MCM-41 and 0.5 nm for Si-SBA-15 result, and a maximum density of 1 group per nm² can be achieved. By rotating around the C-bonds, the SO₃H moieties have to reach the 0.28 nm distance for proton transfer, which is much easier at higher loadings. This rough calculation supports the assumption that in smaller pores the proton transfer proceeds easier because of the shorter distance between SO₃H groups supporting the proton hopping.

Figure 89 shows schematically the situation inside a pore of Si-MCM-41 after functionalization with SO_3H groups via grafting and oxidation, indicating the movement of the grafted moieties for surface proton transfer.

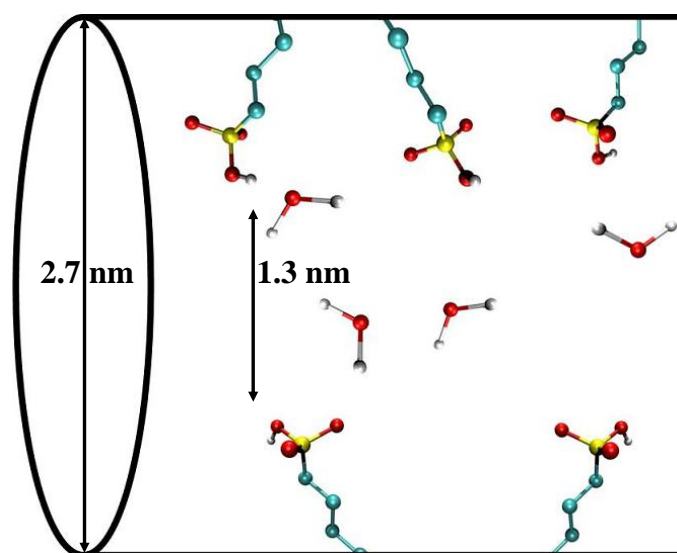


Figure 89. Model of the situation inside a pore of Si-MCM-41 after grafting and oxidation. carbon (blue), oxygen (red), hydrogen (white), sulfur (yellow). Pore diameter and chains sizes are in the correct relation.

The hexagonal pore arrangement seems to be advantage for good proton conductivity in mesoporous silica based solid proton conductors, but grafting still leads to an inhomogeneous distribution of SO_3H groups in the pores, with only 1.0 mmol/g. Water is still needed for the proton transport to overcome the remaining gaps between the SO_3H moieties, which can not be closed via chain movement. Besides of providing more internal surface, the narrower channels of the Si-MCM-41 host have the additional advantage that the SO_3H groups point more into the centre of the channels enabling easier proton hopping between groups anchored on opposite sides of the channels. However, it gives only a trend since 100 % oxidation (see chapter 4.2.1) as well as uniform distribution of the anchored species in the pores due to the grafting process is not very likely.

As mentioned before, theoretically, IECs of 1.67 mmol/g might be possible, but blocking effects and hindrance of MPMS diffusion into the pores in the grafting reaction restrict the loading. A 5 mmol SO_3H -MCM-41 sample exhibits an IEC of 0.8 mmol/g, this value continuously increase to 0.9 and 1.0 mmol/g for 10 mmol and 20 mmol (compare chapter 4.2.1). Figure 90 presents the conductivities of Si-MCM-41 functionalized with different amounts of MPMS in the grafting reaction at 100% RH.

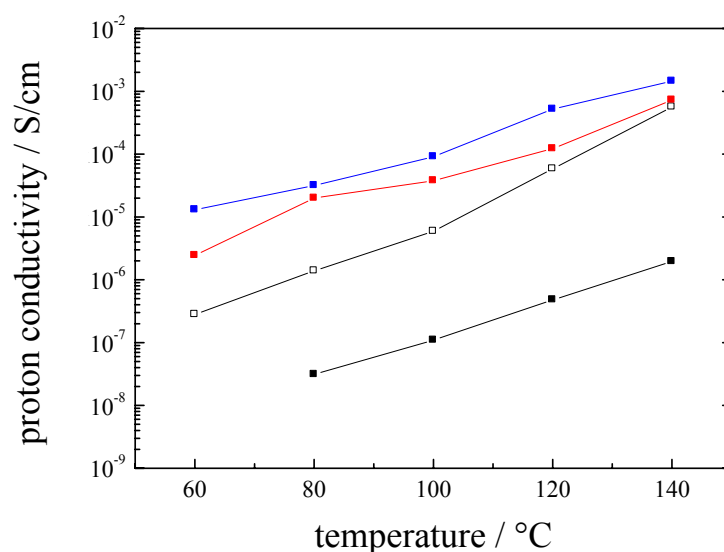


Figure 90. Proton conductivities for SO_3H -MCM-41 0mmol100 (■), 5mmol100 (□), 10mmol100 (■) and 20mmol100 (■). The lines are only to guide the eyes and have no physical meaning.

The conductivity increases continuously, demonstrating that the degree of functionalization of the samples increases with the offer of grafting reagent. Additionally, the already presented IECs confirm this trend. But it shows that via grafting no linear increase in conductivity and IEC can be reached due to the very strong pore blocking effects in the grafting process.

Anyway, the sample 20 mmol 100 has the highest conductivity of the samples with proton conductivity up to 10^{-3} S/cm. For that reason, Si-MCM-41 was chosen as main host material for further proton conductivity research as solid proton conductor, due to its promising properties in conductivity and group density.

4 Results

Surprisingly, a non-sulfonated sample (0 mmol 100) also shows a negligible proton conductivity of about 10^{-6} S/cm and also an increase in the conductivity with increasing temperature. The values, however, are at least two orders of magnitude lower than for the acid-functionalized sample 5 mmol 100. The weak proton conductivity of pristine Si-MCM-41 is related to a partial dissociation of water molecules in the presence of silanol groups, leading to an increased charge carrier concentration close to the inner surface.¹⁹⁹

The Arrhenius plots for the temperature dependence of the proton conductivity for three different grafted SO₃H-MCM-41 samples are given in Figure 91, and the activation energies have been calculated from the slopes of the fitting lines.

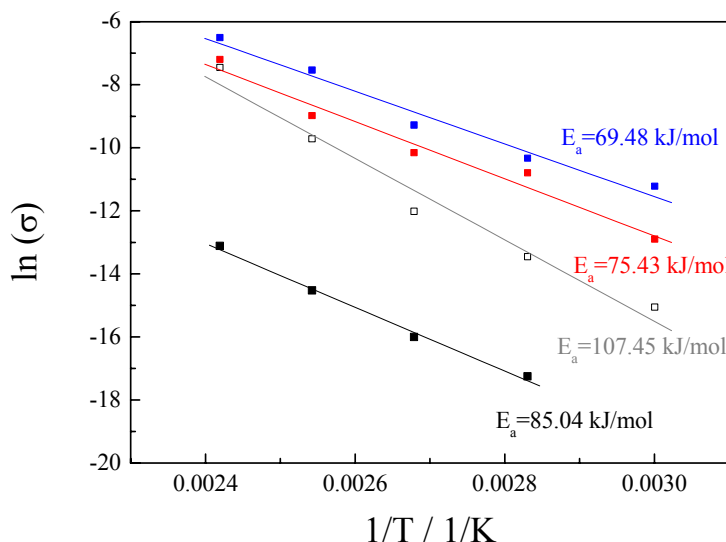


Figure 91. Arrhenius plots for SO₃H-MCM-41 0mmol100 (■), 5mmol100 (□), 10mmol100 (■) and 20mmol100 (■) with additional fitting line for calculation of the given activation energies.

The activation energies decrease from 107.45 kJ/mol to 69.48 kJ/mol with increasing loading, assuming that with more proton conductive SO₃H groups, the proton transport through the solid proton conductors is facilitated. Especially the high value for the 5 mmol sample indicates the low loading with SO₃H groups. It is even higher than for pristine Si-MCM-41.

Via grafting, 1-2 surface silanol groups of the Si-MCM-41 were used to anchor MPMS, and a third one is hindered by the anchored MPMS and can not take part in a proton transfer mechanism anymore. Since these surface silanol groups have however been responsible for proton conductivity in the pristine system, the connection between the surface silanol groups for proton conductivity is disturbed after grafting with MPMS and subsequent oxidation to SO_3H groups.

In the SO_3H functionalized Si-MCM-41, the proton transport occurs via hopping between the SO_3H , and the activation energy for this hopping is much higher than for the pure Grotthuss mechanism⁵⁶ (13.5 and 38.5 kJ/mol). If the distance between the SO_3H groups is too large for fast proton transfer (especially in lowly loaded materials), the activation energies increase.

An important finding of this study is the strong influence of RH and the water storage capability of SO_3H functionalized Si-MCM-41. In order to prove this, the measurement progression of the sample SO_3H -Si-MCM-41 20 mmol under different RH is shown in Figure 92.

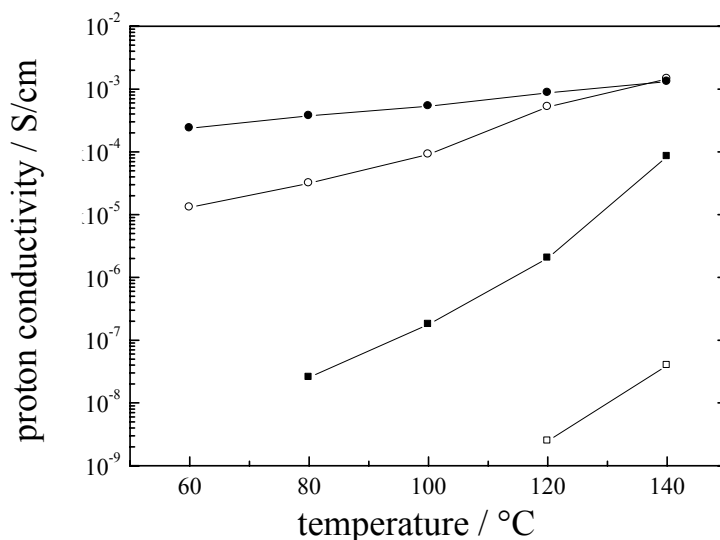


Figure 92. Proton conductivities for 20mmol0 SO_3H -MCM-41 (□), 20mmol50 (■), 20mmol100 (○) and 20mmol100 2nd (●). The lines are only to guide the eyes and have no physical meaning.

4 Results

First, IS was performed without gaseous water atmosphere. The proton conductivity was found lower than in non-modified samples at 100 % RH ($\sim 10^{-9}$ S/cm), due to less surface silanol groups for water dissociation. By increasing the humidity continuously in the measurement cell to 100 % RH, the proton conductivity of the powder also increases continuously by five orders of magnitude. This indicates again that the density of SO_3H groups after post synthetically grafting is not high enough to enable a water-free proton transport through the material, proving the presence of a water-assisted proton transport between the SO_3H groups in the sample. Finally, the sample was tested twice at 100 % RH successively (20 mmol 100 and 20 mmol 100 2nd). In the second 100 % RH run, the conductivity shows higher values in the low temperature regime; at 140 °C both curves fall together to an almost identical value. After the first measurement period the sample had stored the water inside the pores, as gaseous water condensed during cooling down of the specimen holder, and the enrichment of water supports the proton conductivity in the second measurement.

The high dependence of the proton conductivity on water is confirmed and underlined by energy barrier calculations for proton transfer between two SO_3H groups. The proton jump is limited by the energy barrier the proton has to overcome on one hand, and the availability of SO_3H groups in the vicinity on the other. Only next neighbor groups are assumed to be involved in the transfer leading to a pair interaction model. In a simple model description, neglecting the dynamic effects determined via collision counting earlier, the proton transfer depends on the distance the proton has to bridge during hopping. The energy barrier for a proton jump as a function of the O-O distance is shown in Figure 93.

This DFTB data for the barrier have been validated against more accurate ab-initio density functional theory (DFT) calculations. The results calculated via DFTB and DFT are in very good agreement for small distances up to 3.0 Å, and the deviation for larger distances is on average smaller than 2 kcal/mol. At an oxygen-oxygen distance of 2.5 Å the barrier is vanished corresponding to the region where the proton can be delocalized between the oxygen atoms as in a Zündel complex.⁵⁸ If one single water molecule is included in between a donor-acceptor pair, the energy barrier is strongly lowered. For

instance, for the interval from 5.0 Å to 7.0 Å the barrier raises to an order of 20 kcal/mol; while under dry conditions, from 2.5 Å to 4.5 Å the barrier goes up to 80 kcal/mol.

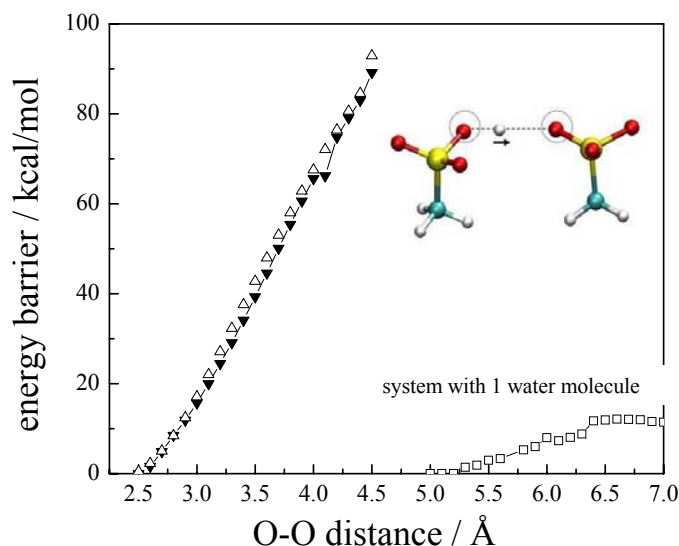


Figure 93. Energy barrier plot for the proton transfer between oxygen atoms belonging to two methyl SO_3H molecules (inset). ▼ (DFTB), △ (DFT), □ represent the curve for the case with 1 water molecule in between the two methyl SO_3H molecules calculated via DFTB.

In the Figure 90, it was observed that proton conductivities always continuously increase with temperature. This is a complete contrast to the behavior of Nafion[®], where at temperatures above 80 °C the proton conductivity decreases drastically due to desorption of water from the polymer pores (Figure 94). In the case of Si-MCM-41 the strong adsorption of water at the large number of remaining non-functionalized silanol groups and on the SO_3H groups formed enhances the conductivity.

As recently found for composites consisting of Nafion[®] and SO_3H functionalized zeolite mordenite²³¹, the proton conductivity at elevated temperatures (140 °C) of a Nafion[®]- SO_3H -zeolite composite membrane is improved.

An addition of SO_3H functionalized Si-MCM-41 to Nafion[®] membranes should therefore also improve the proton conductivity of Nafion[®], and the high-temperature

²³¹ R. Scheffler, A. Huth, G. Hübner, R. Marschall, J. Caro, M. Wark, *Chem. Ing. Tech.* 79 (2007) 2035.

water management of PEM fuel cells, when the presented water storage capability of the mesoporous additives can adsorb the cathode product water and store for an enhanced proton conductivity of the composite membranes. Results on fabricated composite membranes with SO_3H functionalized Si-MCM-41 are presented in chapter 4.4.

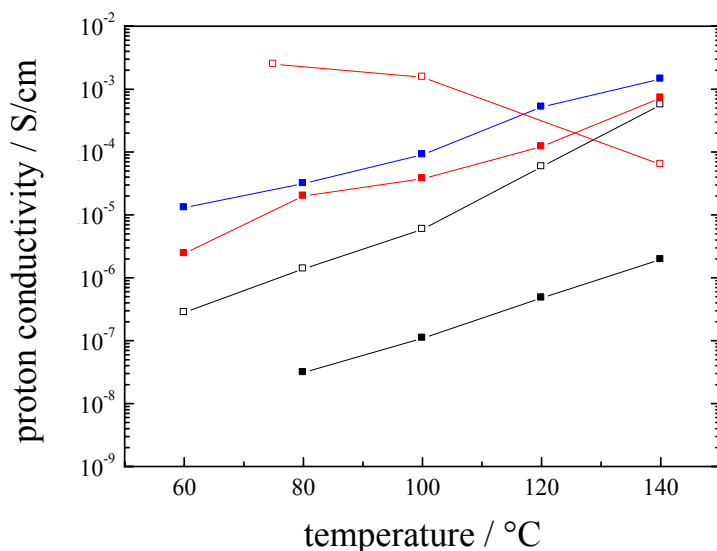


Figure 94. Proton conductivities for SO_3H -MCM-41 0mmol/100 (■), 5mmol/100 (□), 10mmol/100 (■) and 20mmol/100 (■) compared to Nafion (□) running dry. The lines are only to guide the eyes and have no physical meaning.

The disadvantages of the grafting process have already been described. Mainly caused by pore blocking in the grafting reaction, a non-linear increase in the loading of mesoporous silica with SO_3H groups compared to the amount of offered MPMS in the grafting reaction is observed. By further increasing the amount of MPMS offered up to 40 mmol/g, the loading of Si-MCM-41 can still be slightly increased.

After grafting Si-MCM-41 with 30 mmol/g or 40 mmol/g MPMS and following oxidation, the IEC increased to 1.1 and 1.2 mmol/g. Also the proton conductivities increased from 10^{-3} to 10^{-2} S/cm (Figure 95). In general, in SO_3H functionalized Si-MCM-41 materials, the proton conductivities depend on the IEC and increase with increasing IECs.

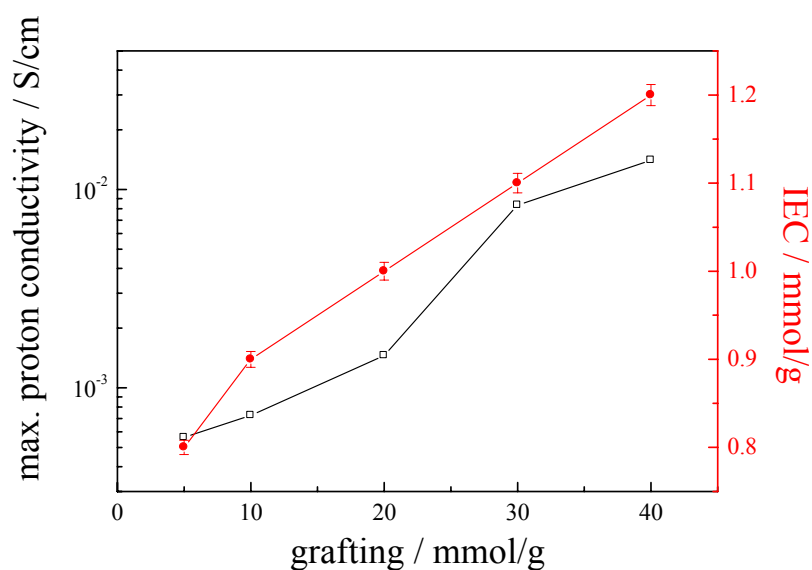


Figure 95. Enhancement of proton conductivity of SO₃H-MCM-41 by more offered MPMS (□). Increasing IECs are shown additionally (●). The lines are only to guide the eyes and have no physical meaning.

However, this procedure is still quite inefficient. For increasing the proton conductivity one order of magnitude, 80 times more MPMS has to be used in the grafting process, while still only one thirtieth (from IEC) anchors to the silica surface as SO₃H groups. For comparison with other protogenic groups, a typical grafting reaction with 20 mmol/g is applied in further investigations.

4.2.3 *N*-Imidazole functionalization of Si-MCM-41 via grafting

As presented in chapter 3.2.5, imidazole functionalities can be enabled on mesoporous silica via three different methods. The surface functionalization with imidazole via nitrogen atom (*N*-imidazole anchorage) is reached via grafting with CITMS and following reaction with liquid imidazole to *N*-imidazole functionalized Si-MCM-41.

The successful anchorage of propyl-chlorine groups can be investigated via IR spectroscopy and the ongoing functionalization in XRD and nitrogen adsorption.

Figure 96 shows a cut-out of IR spectra measured after grafting with CITMS. The best way to confirm the successful grafting in the IR spectra is here also the observation of C-H stretching vibrations between 2800 and 3000 cm^{-1} of aliphatic CH_2 -groups clearly visible in the IR shown. The Cl-C vibration around 900 cm^{-1} is too weak and additionally covered by the Si-O-Si lattice vibration.

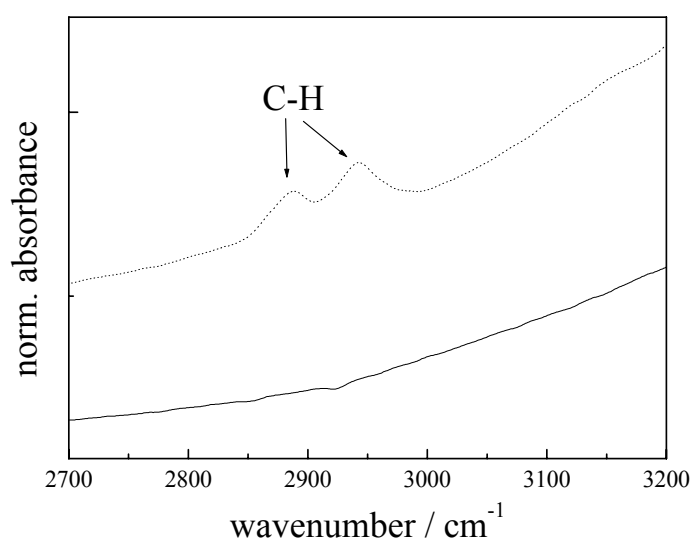


Figure 96. IR spectra of pure Si-MCM-41 (black line) and Cl functionalized Si-MCM-41 (dotted line).

Figure 97 shows the same effects in the XRD patterns of Cl-MCM-41 as shown for SH-functionalized Si-MCM-41 in chapter 4.2.1. The black line indicates the XRD of pristine Si-MCM-41 already introduced in chapter 4.1.1, the dotted line corresponds to 5 mmol/g CITMS in the grafting reaction, the red line to 10 mmol/g , and the blue line to 20 mmol/g . Like for the other grafting samples already shown, the reflection intensities decrease with increasing loading, that even the (110) and (200) reflections nearly disappear. Also nearly no big difference between a 10 mmol and a 20 mmol sample can be seen.

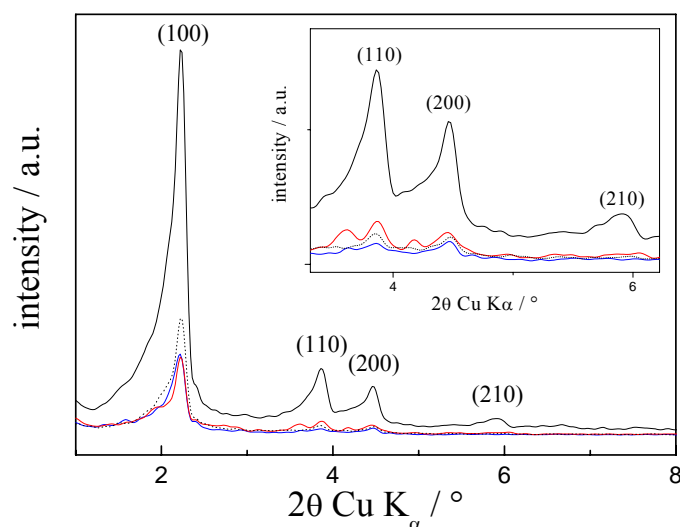


Figure 97. XRDs for Cl-MCM-41 with decreasing intensities. Pure Si-MCM-41 (black), 5 mmol (dotted), 10 mmol (red), 20 mmol (blue).

This is also the case in the nitrogen adsorption measurements shown in Figure 98. After 5 mmol grafting reaction, just a slight difference in the adsorption isotherm compared to pristine Si-MCM-41 can be seen. The capillary condensation step occurs at lower pressures around 0.25 indicating a pore size reduction after grafting. The pore size was roughly calculated to 2.2 nm. But with increasing loading, the pore volumes and surface area decrease more drastic. As the 5 mmol sample has still a BET surface of 1300 m²/g (which is larger than for pure Si-MCM-41, possibly due to stronger interactions between N₂ and the chlorine function), the 10 and 20 mmol sample have only around 1100 m²/g surface area. The same trend is determined for the pore volumes decreasing from 0.966 to 0.795 and 0.754 cm³/g, respectively. The 10 and 20 mmol samples have even a smaller pore diameter of 2.1, the increase for capillary condensation is hardly visible in the same region as for the 5 mmol sample. The strong pore blocking during grafting reaction seems to be even more drastic here, because nearly no difference between 10 mmol and 20 mmol grafting reaction can be seen.

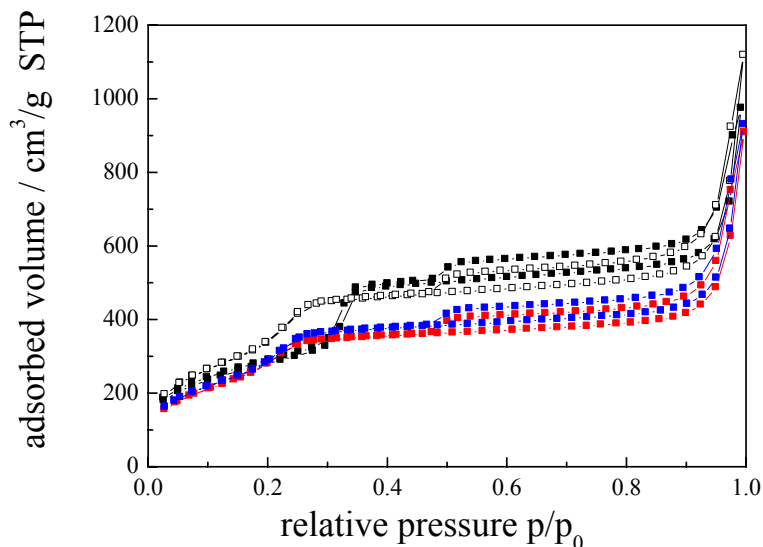


Figure 98. N₂ adsorption isotherms for pristine Si-MCM-41 (■) and Cl functionalized Si-MCM-41 with 5 mmol (□), 10 mmol (■) and 20 mmol (■) CITMS.

The N-imidazole anchorage then can only be seen in IR spectroscopy, the structural changes are too weak to observe in nitrogen adsorption and XRD.

Two C-N vibrations between 1500 and 1600 cm⁻¹ become visible after N-imidazole anchorage. An N-H stretching vibration around 3400 cm⁻¹ could not be observed, as the imidazole anchorage is enabled via the only free nitrogen atom. Of course the C-H vibrations remain visible. The shown peak at 1638 cm⁻¹ belongs to the O-H deformation vibration of adsorbed water.²³²

²³² IR reference spectra H₂O, www.nist.gov, April 2008.

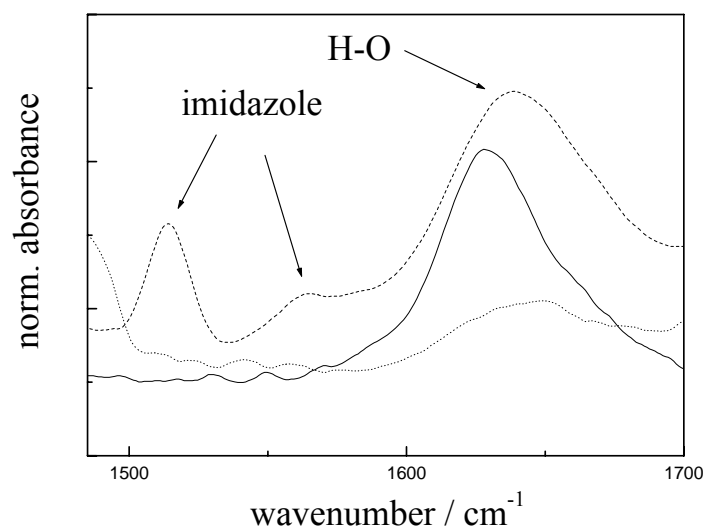


Figure 99 IR spectra of pure Si-MCM-41 (black line), Cl-MCM-41 (dotted) and N-imidazole-MCM-41 (dashed).

The proton conductivities at 100 % RH of the N-imidazole functionalized Si-MCM-41 are shown in Figure 100.

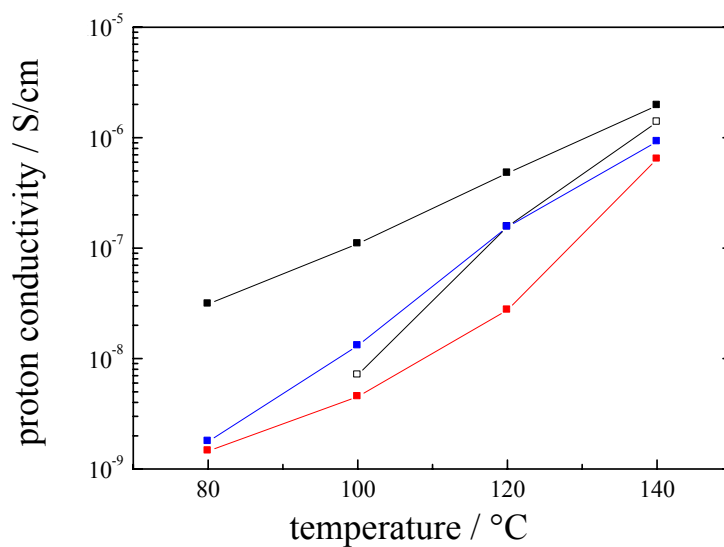


Figure 100. Proton conductivities for different N-imidazole-MCM-41 at 100 % RH. 5 mmol (□), 10 mmol (■), 20 mmol (■) compared to pristine Si-MCM-41 (■) 0 mmol. The lines are only to guide the eyes and have no physical meaning.

For all degrees of functionalization, the proton conductivities are in the same region, but all very low compared to SO₃H-MCM-41 (Figure 90). N-imidazole-MCM-41 shows maximum conductivities of up to 10⁻⁶ S/cm, which are three orders of magnitude lower than for the best and comparable SO₃H-MCM-41, and even lower than the pristine silica material Si-MCM-41. There are several reasons for this behavior: One problem of imidazole as protogenic group is that imidazole brings no mobile charge carrier into the system, whereas SO₃H groups easily give their protons away for proton conductivity. In imidazole systems, excess protons must be provided externally, e.g. via additional acid functionalization in the pores, or via much more water content (bringing more protons via self-dissociation). The second reason is the imidazole-anchorage via nitrogen atom. For a proton transport, the free nitrogen in the imidazole ring has to pick a proton, the group has to rotate and collide with free nitrogen from another imidazole group (Figure 101).

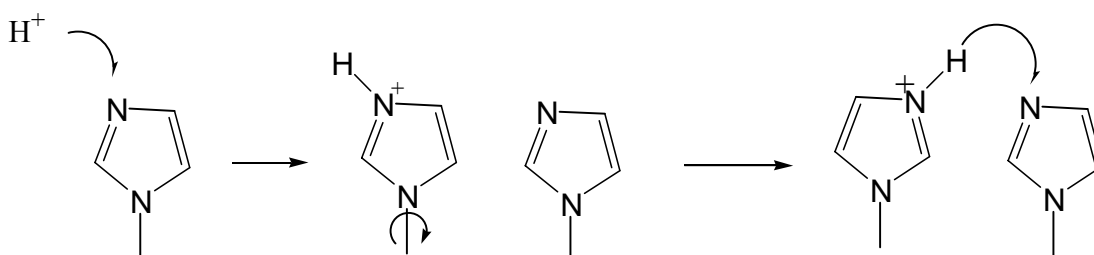


Figure 101. Proton hopping in N-imidazole systems.

An imidazole anchorage via the carbon atom in between the nitrogen atoms (C1) should be of advantage for proton conductivity²³³, due to the imidazole resonance presented in Figure 19. Two more types of imidazole functionalized Si-MCM-41 for proton conductivity are presented in the following chapters.

²³³ S. J. Paddison, K.-D. Kreuer, J. Maier, *Phys. Chem. Chem. Phys.* 8 (2006) 4530.

4.2.4 Imidazole functionalization of Si-MCM-41 via grafting and peptide bonding

As a second way to enable imidazole functionalities on the mesoporous silica pore surface, grafting can be performed with APTES to functionalize the surface of Si-MCM-41 with amine groups (see chapter 3.2.2). In a second step, a peptide bond with imidazole-2-carboxylic acid can be formed (see chapter 3.2.5).

The successful functionalization with amine groups and the successful peptide-bond formation can be seen by IR spectroscopy.

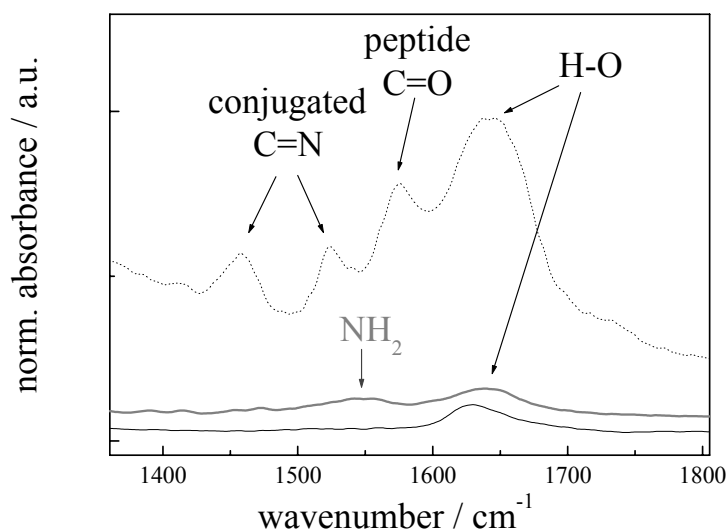


Figure 102. IR spectra of pristine Si-MCM-41 (black line) compared to NH₂-MCM-41 (grey) and peptide-imidazole-MCM-41 (dotted line) after 20 mmol grafting and peptide bond formation. The imidazole-spectrum is enlarged for better signal observation.

Besides the H-O deformation vibration around 1630 cm⁻¹ (varies slightly in the three spectra), a weak signal for amine-groups can be seen in the cut-out of the three IR spectra (Figure 102) after functionalization with APTES at 1540 and 1555 cm⁻¹. Also detectable are the bands for the C-H stretching vibrations around 2900 cm⁻¹ for the successful functionalization. After peptide bond formation, the number of bands

increases, indicating the carbonyl-band of a solid peptide at 1575 cm^{-1} and the two bands for C=N valence vibration for conjugated cyclic systems (imidazole) between 1400 cm^{-1} and 1550 cm^{-1} , proving the successful imidazole anchorage.²²⁹

The increasing functionalization is again visible in the XRD patterns of the peptide-imidazole functionalized mesoporous Si-MCM-41 materials.

Figure 103 shows the same effects in the XRD patterns of peptide-imidazole-MCM-41 as already observed for SH-functionalized Si-MCM-41 in chapter 4.2.1. The black line indicates the XRD of pristine Si-MCM-41 already introduced in chapter 4.1.1, the dotted line corresponds to 5 mmol/g APTES in the grafting reaction, the red line for 10 mmol/g, and the blue line to 20 mmol/g with subsequent peptide bond formation. Like for the other grafting samples already shown, the reflection intensities decrease with increasing loading, that even the (110) and (200) reflections nearly disappear.

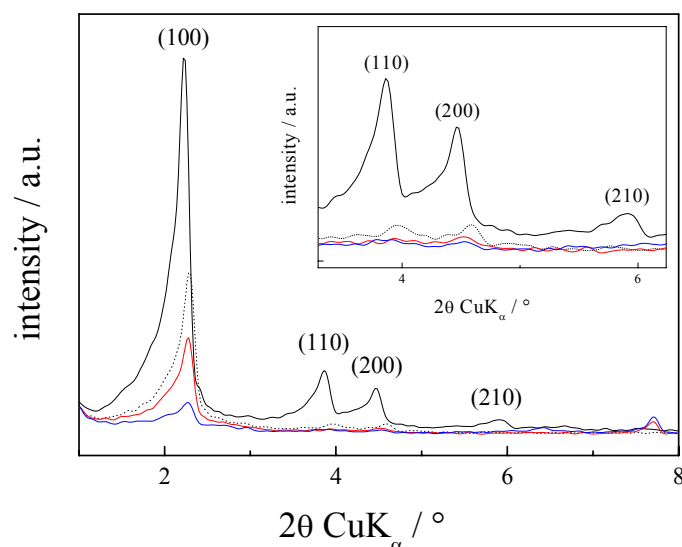


Figure 103. XRDs for peptide-imidazole-MCM-41 with decreasing intensities. Pure Si-MCM-41 (black), 5 mmol (dotted), 10 mmol (red), 20 mmol (blue).

In the nitrogen adsorption isotherms, this trend is obviously confirmed. Figure 104 shows clearly the decreasing volume of nitrogen adsorbed in the adsorption measurement. Also the adsorption step for capillary condensation in the isotherms of functionalized materials is strongly shifted to lower relative pressures compared to

pristine Si-MCM-41, indicating a smaller pore diameter. Table 10 depicts the deteriorating structural data with increasing pore filling with more imidazole groups. For example, the surface areas decrease from 704 to 349 m²/g with increasing loading, and the pore volumes decrease strongly down to 0.260 cm³/g.

Table 10. Structural data of peptide-imidazole functionalized Si-MCM-41 determined from nitrogen adsorption measurements.

	S_{BET} m ² /g	pore volume / cm ³ /g	pore size / nm
Pristine Si-MCM-41	1181	1.128	2.7
Pep-imidazole-MCM-41 5 mmol	704	0.624	2.1
Pep-imidazole-MCM-41 10 mmol	464	0.354	2.0
Pep-imidazole-MCM-41 20 mmol	349	0.260	2.0

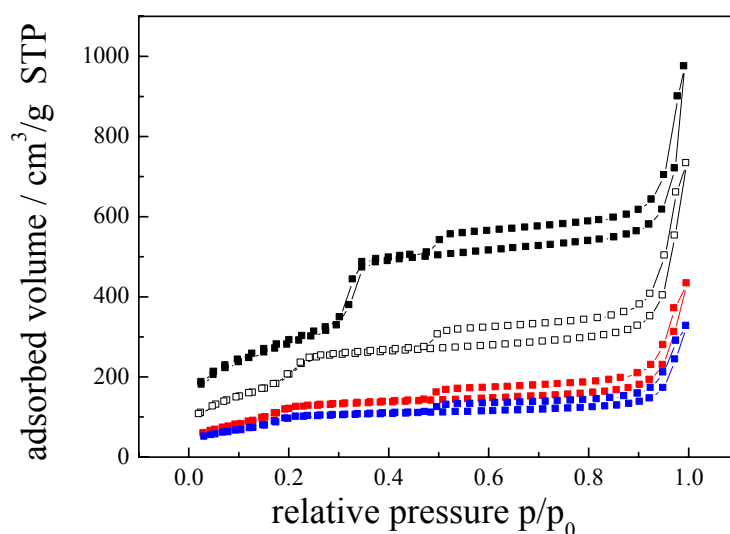


Figure 104. N₂ adsorption isotherms for pristine Si-MCM-41 (■) compared to peptide-imidazole functionalized Si-MCM-41 after 5 mmol (□), 10 mmol (■) and 20 mmol (■) grafting with APTES followed by peptide bond formation.

The proton conductivities at 100 % RH are for the peptide-imidazole anchored Si-MCM-41 materials (Figure 105) at least two orders of magnitude higher than for N-imidazole Si-MCM-41 (Figure 100), reaching 4x10⁻⁴ S/cm, and is therefore clearly

improved compared to the unfunctionalized Si-MCM-41. In addition, an increase in proton conductivity with loading is also observed for these materials as for the already described systems.

The reason for a better proton transport is the existence of both a donor and an acceptor function in the immobilized imidazole group. The hydrogen bond network formed between imidazole and water is very similar to pure water, and the mechanism of proton transport is similar to that in water.²³⁴ So, the proton transport of immobilized imidazole anchored via peptide bond is facilitated by the amphoteric behavior of such anchored imidazole. However, an asymmetric anchorage of the imidazole heterocycle is disadvantageous, as Paddison *et al.* showed that an asymmetric immobilization of imidazole, e.g. in the C₄ position, has a higher energy difference between the protonated and the non-protonated imidazole system, which results in a higher energy barrier for a proton transfer for proton conductivity.²³³

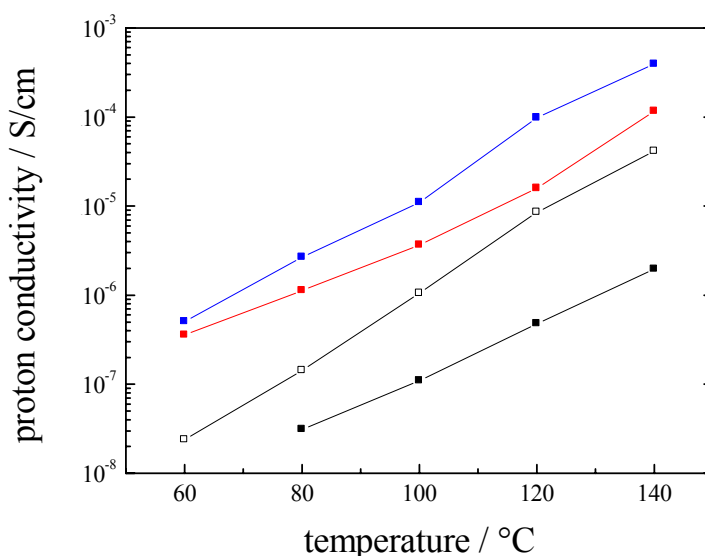


Figure 105. Proton conductivities for different peptide-imidazole-MCM-41 at 100 % RH. 5 mmol (□), 10 mmol (■), 20 mmol (■) compared to pristine Si-MCM-41 (■) 0 mmol. The lines are only to guide the eyes and have no physical meaning.

²³⁴ W. Münch, K. D. Kreuer, W. Silverstri, J. Maier, G. Seifert, *Solid State Ionics* 145 (2001) 295.

The anchorage of imidazole via nitrogen atom is an asymmetric anchorage and has an unfavorable conductivity mechanism, and is therefore much worse than the C₁-anchorage. Anyway the comparison is not very meaningful, as the spacer length between the N-imidazole and the peptide-imidazole differs by two atoms, and a peptide bond introducing a partially double bond character is introduced, which can decrease the mobility of the whole spacer chain. For comparison with SO₃H systems, the next chapter presents the results for symmetric anchored imidazole via 3C-chain spacer, established via *in-situ* imidazole formation.

4.2.5 Imidazole functionalization of Si-MCM-41 via grafting and in-situ formation

The third possibility to synthesize imidazole-functionalized Si-MCM-41 can be reached via functionalizing Si-MCM-41 with TESBA and following *in-situ* imidazole formation using glyoxal and ammonia (chapter 3.2.5).

The successful functionalization with aldehyde-groups and the successful formation of imidazole can be seen in IR spectroscopy.

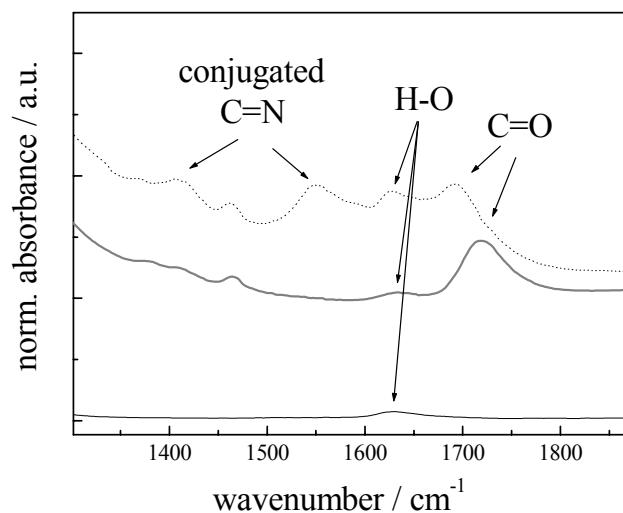


Figure 106. IR spectra of pristine Si-MCM-41 (black line) compared to CHO-MCM-41 (grey) and imidazole-MCM-41 (dotted line) after 20 mmol TESBA grafting and in-situ imidazole formation.

Again the H-O deformation vibration around 1630 cm^{-1} can be seen in the three cut-out of the IR spectra (Figure 106). The intensity of this signal is very weak and differs slightly, but is still detectable. A strong signal for the aldehyde C=O vibration appears after grafting with TESBA above 1700 cm^{-1} , and still remains after imidazole formation, indicating a non-quantitatively reaction of all aldehyde groups to imidazole. A reason for that can be the hindered diffusion of all the reagents into the pores of the aldehyde functionalized Si-MCM-41. After imidazole formation reaction, the number of bands increases, indicating the two bands for C=N valence vibration for conjugated cyclic systems (imidazole) between 1400 cm^{-1} and 1550 cm^{-1} , proving the successful imidazole anchorage.²²⁹

Once again, the successful and continuous grafting can be observed in XRD measurements and nitrogen adsorption.

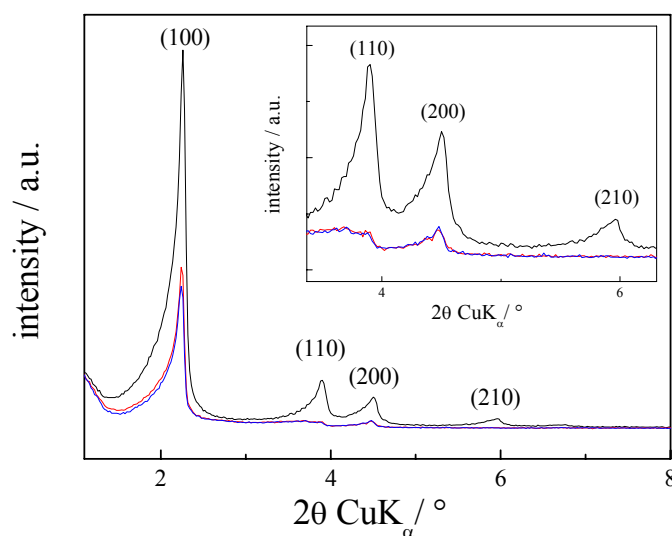


Figure 107. XRDs for imidazole-MCM-41 with decreasing intensities. Pure Si-MCM-41 (black), 10 mmol (red), 20 mmol (blue).

Figure 107 shows the XRD patterns of imidazole-MCM-41 compared to pristine Si-MCM-41. The black line indicates the XRD of pristine Si-MCM-41 already introduced in chapter 4.1.1, the red line depicts the XRD of 10 mmol/g imidazole grafted Si-MCM-41, and the blue line belongs to the 20 mmol/g sample with subsequent imidazole formation. Like for the other grafting samples already shown, the reflection intensities decrease with increasing loading, that even the (110) and (200) reflections nearly disappear.

In the nitrogen adsorption isotherms, this observation is again confirmed. Figure 108 shows clearly the decreasing volume of nitrogen adsorbed in the adsorption measurement. The adsorption step for capillary condensation in the isotherms of functionalized materials is again shifted to lower relative pressures compared to pristine Si-MCM-41, indicating a smaller pore diameter of the grafted samples due to attached organic moieties. Table 11 shows the deteriorating structural data with increasing pore filling with more imidazole groups. For example, the pore volumes decrease from 1.128 to 0.825 cm^3/g with increasing loading. Surprisingly, the surface areas are higher than for pristine Si-MCM-41, due to stronger interactions between N_2 and the aldehyde

functions on the walls compared to non functionalized Si-MCM-41, but the 20 mmol sample has as a trend the lowest surface area.

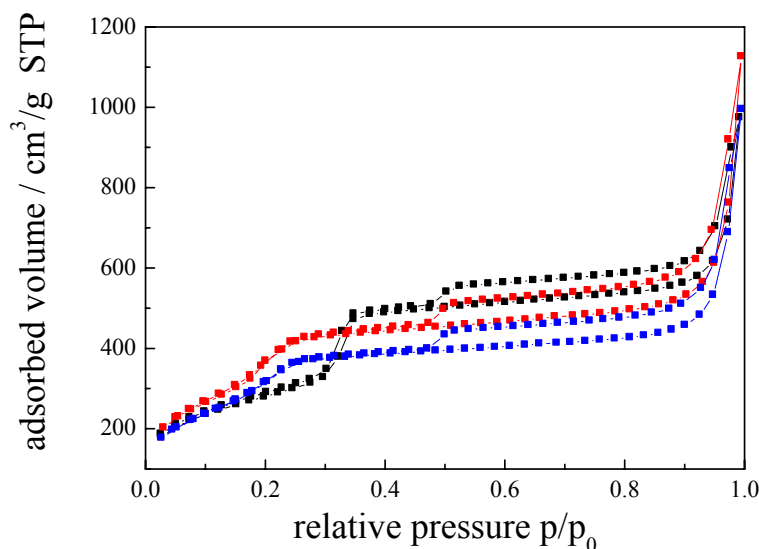


Figure 108. N₂ adsorption isotherms for pristine Si-MCM-41 (■) compared to aldehyde functionalized Si-MCM-41 after 10 mmol (■) and 20 mmol (■) grafting with TESBA.

Table 11. Structural data of imidazole functionalized Si-MCM-41 determined from nitrogen adsorption measurements.

	S _{BET} m ² /g	pore volume / cm ³ /g	pore size / nm
pristine Si-MCM-41	1181	1.128	2.7
CHO-MCM-41 10 mmol	1460	0.948	2.1
CHO-MCM-41 20 mmol	1259	0.825	2.1

Figure 109 shows the proton conductivities for the imidazole functionalized Si-MCM-41 powders, reaching values for the 20 mmol sample of 10⁻⁴ S/cm. The values are slightly lower than for the peptide-imidazole functionalized Si-MCM-41 samples (chapter 4.2.4). This is caused by the shorter 3C spacer length of the imidazole Si-MCM-41 powders, whereas the peptide-imidazole samples have a 5 atom spacer between the silica host and the protogenic groups. Although the peptide bond is,

compared to a single bond, quite constrained, the longer spacers allow the imidazole groups to reach each others more easily.

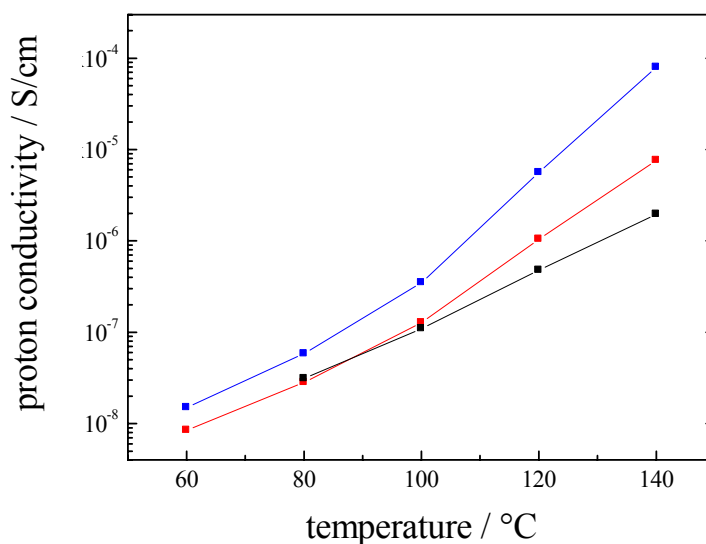


Figure 109. Proton conductivities for different imidazole-MCM-41 at 100 % RH, 10 mmol (■), 20 mmol (■) compared to pristine Si-MCM-41 (■) 0 mmol. The lines are only to guide the eyes and have no physical meaning.

Compared to the SO₃H functionalized Si-MCM-41 materials (chapter 4.2.2), the proton conductivities are at least one order of magnitude lower. This is caused by the lower loading with imidazole groups determined by measuring the IEC, being 0.48 mmol/g for the 20 mmol sample compared to 1.0 mmol/g for SO₃H. As already mentioned at the IR (Figure 106), no complete transformation from all aldehyde groups into imidazole groups could be achieved. Also by increasing the amount of TESBA offered in the grafting step up to 40 mmol/g and equivalent imidazole reaction, no significant increase in the IEC (0.56 mmol/g) and proton conductivities could be achieved (Figure 110). The reason for that is a stronger pronounced pore blocking effect than for SH functionalized MCM-41 samples, due to a size effect: The molecules for the formation of the imidazole, glyoxal and ammonia, exhibit a hindered diffusion into the pores of the aldehyde functionalized Si-MCM-41 due to their molecule size. Like in a pore blocking during grafting reaction, the anchored aldehyde functionalities hinder the glyoxal to diffuse into the porous structure for imidazole formation. The molecules for thiol

oxidation (compare chapter 3.2.4) are much smaller and can easily reach their reaction centers.

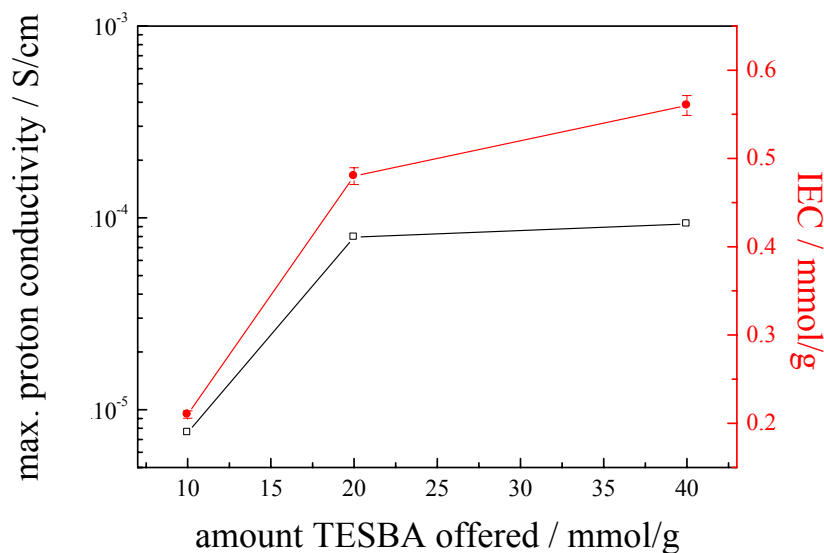


Figure 110. Maximum proton conductivities (\square) and IECs (\bullet) of imidazole functionalized Si-MCM-41 depending on the amount of TESBA offered in the grafting step.

On the other hand, the slope of the increasing proton conductivities with temperature of the imidazole functionalized materials (Figure 109) is much higher than for the SO_3H functionalized materials, indicating a higher temperature dependence of the proton conductivity in the imidazole functionalized samples. Calculating the activation energies proved this assumption, imidazole-MCM-41 sample showed activation energies at least 20 kJ/mol higher than SO_3H -MCM-41.

The stronger dependence of the imidazole functionalized Si-MCM-41 sample on the water content can be seen in the proton conductivities at 50 % RH of these samples presented in Figure 111. Compared to the SO_3H functionalized Si-MCM-41 at 50 % RH, the proton conductivities are three orders of magnitude lower at 140 °C, reaching only 10^{-7} S/cm. The lower conductivity values are due to the fact that oxo-acids better retain water and water molecules are better constrained around oxo-acids than around imidazole.²³³ It was also shown by minimum energy calculations that the binding between imidazoles during proton transfer is worse than in sulfonic acids, underlining

the worse proton conductivities for imidazole groups.²³³ The results underlined also the worse amphoteric character of imidazole groups compared to sulfonic acids, making them less suitable for an efficient proton transfer mechanism. In contrast to SO₃H groups on Si-MCM-41, the imidazole functionalized samples have also no charge carriers inside the system. These materials always need excess charge carriers (excess protons) for a reasonable proton conductivity, and are therefore more dependent on temperature and RH in the system, resulting in higher charge carrier concentration (water dissociation).

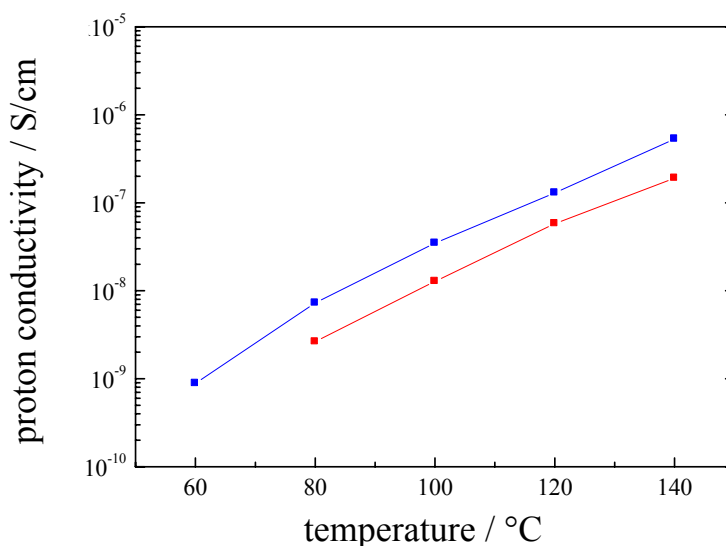


Figure 111. Proton conductivities for different imidazole-MCM-41 at 50 % RH, 10 mmol (■), 20 mmol (■). The lines are only to guide the eyes and have no physical meaning.

4.2.6 Summary of grafting results

From proton conductivity measurements of different SO₃H functionalized mesoporous silica hosts, the Si-MCM-41 as host material turned out to be the best mesoporous material for functionalization with protogenic moieties, due to its narrow pores (2.7 nm), its hexagonal ordered, proton guiding pore system, and its water storage

capability. Proton conductivity in the pores of functionalized Si-MCM-41 takes place via proton transfer between functional groups, supported by water molecules resulting in a Grotthuss-like mechanism (Figure 112).

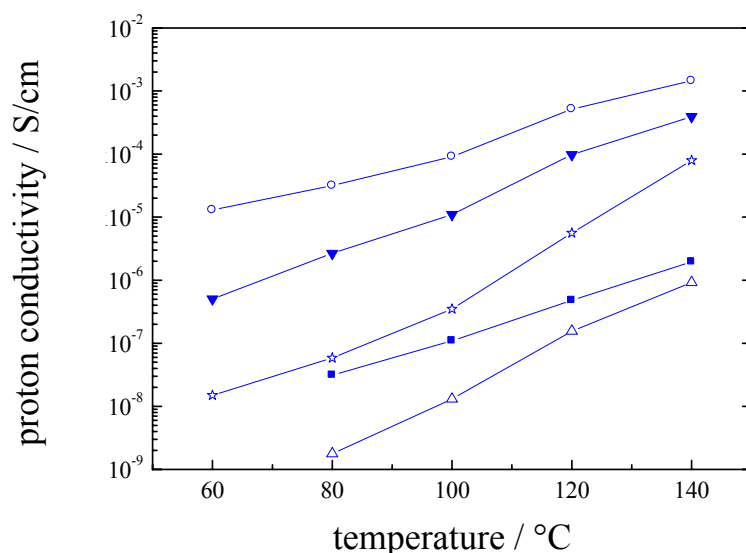


Figure 112. Proton conductivities of functionalized Si-MCM-41 at 100 % RH and 20 mmol grafting with (Δ) N-imidazole, (\blacktriangledown) peptide-imidazole, (*) imidazole and (\circ) SO₃H groups, compared to pristine Si-MCM-41 (\blacksquare). The lines are only to guide the eyes and have no physical meaning.

In contrast to Nafion[®], the proton conductivities of all grafted materials increase with temperature up to 140 °C. Although the same reaction conditions are used for the entire prepared samples, different degrees of loading with protogenic groups were achieved due to the mentioned problems of the grafting process itself (chapter 2.2.6) and related diffusion problems of reagents into the pores of the functionalized materials for the subsequent reactions.

The gaseous water atmosphere has different influences on the proton conductivities of the protogenic systems, while the SO₃H functionalized Si-MCM-41 systems turned out to be the best solid proton conductors synthesized via grafting. The second best is the peptide-imidazole function, but it has to be mentioned that the peptide-imidazole Si-MCM-41 has a longer spacer chain between the silica host wall and the protogenic group than all the other grafted materials. However, the IECs are comparable to SO₃H,

reaching 0.7, 0.8 and 1.1 mmol/g for 5, 10 and 20 mmol grafting, respectively. But also these values are not good enough to reach the proton conductivities of SO₃H, due to the absence of efficient amounts of intrinsic charge carriers. The imidazole-grafted samples only take the third place, due to the inefficient *in-situ* imidazole formation inside the pores of Si-MCM-41, confirmed by very low IECs compared to the presented SO₃H functionalized materials. This leads to the assumption that the spacer length is more important for proton conductivity than the type of anchorage, if the imidazole is anchored via C₁. N-imidazole grafted samples even show lower proton conductivities than the host materials itself, due to the inefficient proton transport mechanism between the N-imidazole anchored moieties. Additionally, the number of surface silanol groups, which enabled small proton conductivity in the pristine Si-MCM-41, decreased due to grafting with CITMS on the surface of Si-MCM-41. Together with the unfavorable proton conduction mechanism, this explains the low proton conductivity values for N-imidazole-MCM-41 samples.

4.3 Functionalization via co-condensation

In contrast to chapter 4.2, the now presented functionalized mesoporous silica materials are synthesized in a one-pot synthesis, called *in-situ* co-condensation, where the functionalizing alkoxy silane is already added to the mixture forming the silica materials (chapter 3.2.3). Due to the observed pore size dependence of proton conductivity results presented in chapter 4.2, only Si-MCM-41 is functionalized in co-condensation method, using the same protogenic groups presented in the grafting results. The influence of the higher and more homogeneous loading of the silica material after co-condensation exhibits a strong influence on the proton conductivities of the presented solid proton conductors.

4.3.1 Functionalization of mesoporous silica with SO₃H groups via co-condensation

Si-MCM-41 is functionalized with SH groups following the co-condensation procedure presented in chapter 3.2.3, using different amounts of MPMS substituting the silicon source (20 %, 30 %, 40 %). As the alkylrests condensate together with TEOS, a homogeneous and statistical distribution of SH groups is expected. Different methods were used to extract the used surfactant CTAB, namely ethanol/HCl extraction and microwave digestion with HNO₃/H₂O₂. The samples are designated as x % SO₃H-MCM-41-y, where x represents the amount of MPMS-substitution in the co-condensation reaction, and y gives the abbreviation for the extraction process; extr for ethanol/HCl extraction, mw for microwave digestion, and calc for additional calcination.

FT-IR spectroscopy evidences the template removal in the microwave oven simultaneously with the oxidation of the SH groups to SO₃H ones. After microwave treatment two peaks corresponding to sulfonate stretching vibrations appear in the region from 1100 cm⁻¹ to 1300 cm⁻¹, as already shown for the grafted samples (Figure 84).

Thermogravimetric measurements of the oxidized samples also confirm these results. The extent of SH group oxidation was estimated from the change in the decomposition temperatures. SH group decomposition starts at about 330 °C, whereas side chains with SO₃H groups start to decompose at temperature as high as about 375 °C, as determined for samples containing exclusively SH or SO₃H groups (Figure 113).

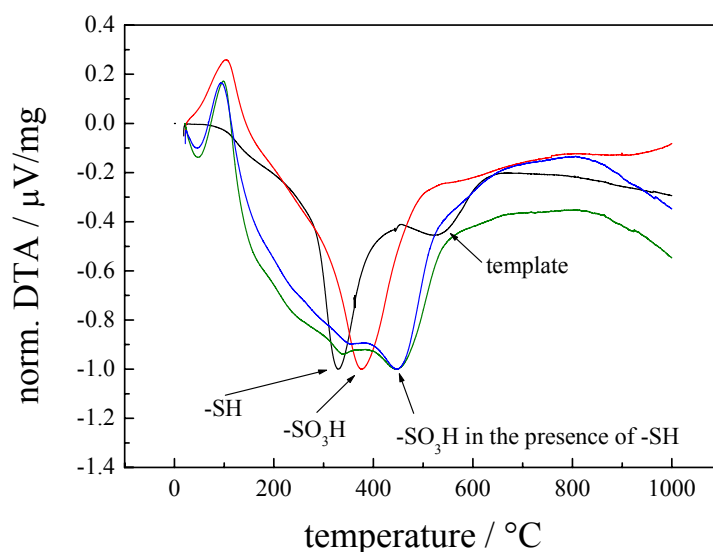


Figure 113. DTA curves, normalized by the largest signal. 20% SH-MCM-41-extr (black); 20% SO₃H-MCM-41-mw (red); 30% SO₃H-MCM-41-mw (green); 40% SO₃H-MCM-41-mw (blue).

As both groups are present in a sample due to incomplete oxidation, the decomposition temperatures were found shifted towards higher values, as already shown in chapter 4.2.1 (Figure 85). While for 20 % SO₃H-MCM-41-mw full oxidation is achieved by the given procedure, the 30 and 40 % SO₃H-MCM-41-mw still contain very small amounts of thiol groups. Compared to the extracted 20 % SH-MCM-41-extr, the microwave treated 20 % SO₃H-MCM-41-mw shows no more template signal indicating a complete template removal by microwave irradiation unlike the ethanol extraction.

The texture properties of the prepared samples were determined by the analysis of the adsorption isotherms of N₂ at the boiling point of liquid nitrogen compared to the pure Si-MCM-41.

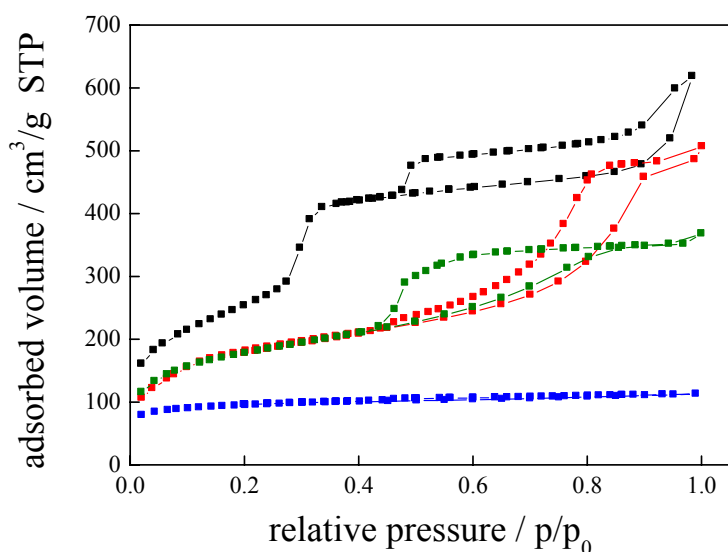


Figure 114. Nitrogen adsorption isotherms on the pristine Si-MCM-41 (■) and on functionalized samples 20 (■), 30 (■) and 40 % (■) SO₃H-MCM-41-mw.

The addition of MPMS to the reaction mixture for the preparation of the functionalized Si-MCM-41 had a profound effect on the texture properties (Figure 114). The isotherms for the 20 % and 30 % SO₃H-MCM-41-mw exhibit variously shaped hysteresis loops corresponding to differently sized mesopores. On the contrary, the isotherm for the 40 % SO₃H-MCM-41-mw shows more or less horizontal plateau after a steep increase in adsorption at very low relative pressures. The BET surface areas for 20 and 30 % SO₃H-MCM-41-mw samples equal 645 and 625 m²/g, respectively. For the 40 % SO₃H-MCM-41-mw sample the BET equation does not hold, which indicates the microporous nature of this sample without capillary condensation in mesopores.

Using the comparative plot method, it could be shown that all the samples contain some proportion of micropores, that for the 40 % SO₃H-MCM-41-mw being the largest, practically exclusive presence of micropores, and the presence of pores larger than micropores, such as small mesopores, for the 20 and 30 % SO₃H-MCM-41-mw samples.²³⁵ The clear reason for that is narrowing of the mesopores corresponding to the Si-MCM-41 structure and their transformation to micropores or small mesopores

²³⁵ R. Marschall, J. Rathouský, M. Wark, *Chem. Mater.* 19 (2007) 6401.

approx. 2 nm in diameter. This phenomenon is especially prominent for the 40 % SO₃H-MCM-41-mw. The pore size calculated from the pore volume and the Langmuir surface area is about 1.5 nm. Assuming a chain length of around 0.7 nm for the (CH₂)₃-SO₃H chain, then by subtracting twice the chain length from the diameter of the pores of the pure MCM-41 (2.7 nm ± 0.2), the size of the micropores should be roughly 1.3 to 1.5 nm, which is illustrated in Figure 115, confirming the nitrogen adsorption data.

This conclusion is also in agreement with Lim *et al.* who established a high pore filling of the Si-MCM-41 with MPMS which results in a pore diameter of about 1.4 nm.²³⁶

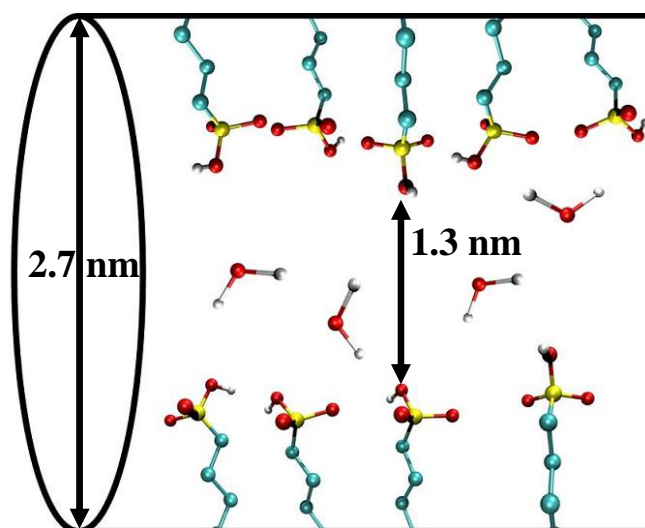


Figure 115. Schematic picture of a pore of 40 % SO₃H-MCM-41-mw, atoms: carbon (blue), oxygen (red), hydrogen (white), sulfur (yellow). Pore diameter and chain sizes are shown in the correct relation.

Figure 116 shows the XRD patterns for functionalized 20 % and 40 % SO₃H-MCM-41-mw samples. The diffractogram for 20 % SO₃H-MCM-41-mw exhibits a drastically diminished (100) reflection and a complete absence of the (110) and (200) reflections.

²³⁶ H. Lim, C. F. Blanford, A. Stein, *Chem. Mater.* 10 (1998) 467.

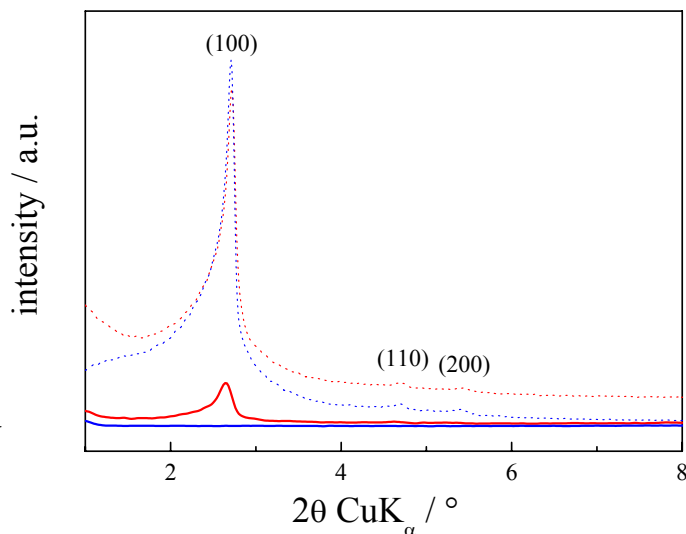


Figure 116. XRDs for 20 % (red) and (blue) 40 % SO₃H-MCM-41-mw samples, and for calcined 20 % (red dotted) and 40 % (blue dotted) SO₃H-MCM-41-calc samples.

Finally, no reflections for the 40 % SO₃H-MCM-41-mw have been observed at all. This confirms the substantial (for 20 % SO₃H-MCM-41-mw) or practically complete (for 40 % SO₃H-MCM-41-mw) filling of the Si-MCM-41 pores in the functionalized and microwave treated mesoporous materials. As the presence of organic groups in the pores matches in electron density to the silica walls, the reflection intensity is decreased, as observed for the grafting materials.²²⁵ The XRD patterns measured after the complete removal of the organic matter by additional calcination show the expected three well-resolved reflections for the Si-MCM-41, but shifted to higher values compared to pure Si-MCM-41, indicating a slightly lower pore diameter caused by the influence of MPMS on the formation of the SLC phase.

The high regularity of the pore ordering for the functionalized SO₃H-MCM-41-mw samples is also confirmed by TEM. The TEM micrographs in Figure 117 clearly show the pore arrangement characteristic for the Si-MCM-41 structure obtained for the 40 % SO₃H-MCM-41-mw sample.

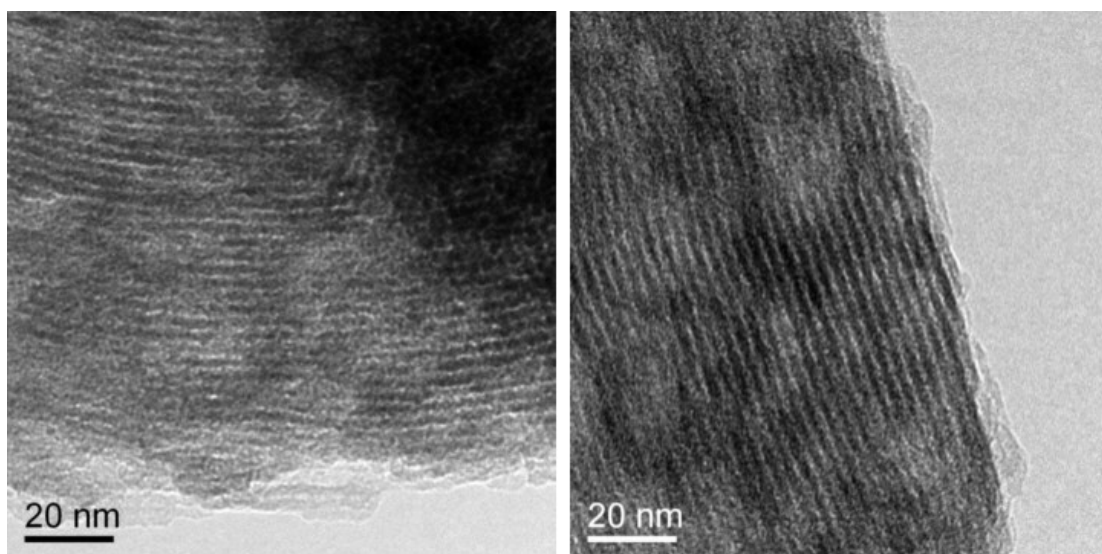


Figure 117. TEM images of 40 % SO₃H-MCM-41-mw.

Sometimes, co-condensation reactions have a trend to perform homocondensation, that the alkoxy silanes and the silicon source condensate apart from each other. This is in the presented synthesis totally not the case.

An EDXS mapping was performed in SEM at several areas of the synthesized samples, showing the incorporation of sulfur in all the particles. Figure 118 summarized exemplarily the EDXS analysis performed on the co-condensed materials functionalized with SO₃H groups for the 20 % SO₃H-MCM-41-mw. It can be clearly seen from the mapping pictures that the sulfur is incorporated homogeneously in all the silica particles, and the EDX spectra also confirms the incorporation of sulfur into the mesoporous silica to a ration of 1:4, which is slightly lower as expected for the 20 % co-condensation reaction. This error is small and due to the calculation software, since for determination of the atomic percentages it assumes a dense and even sample, which is not the case in the observed samples.

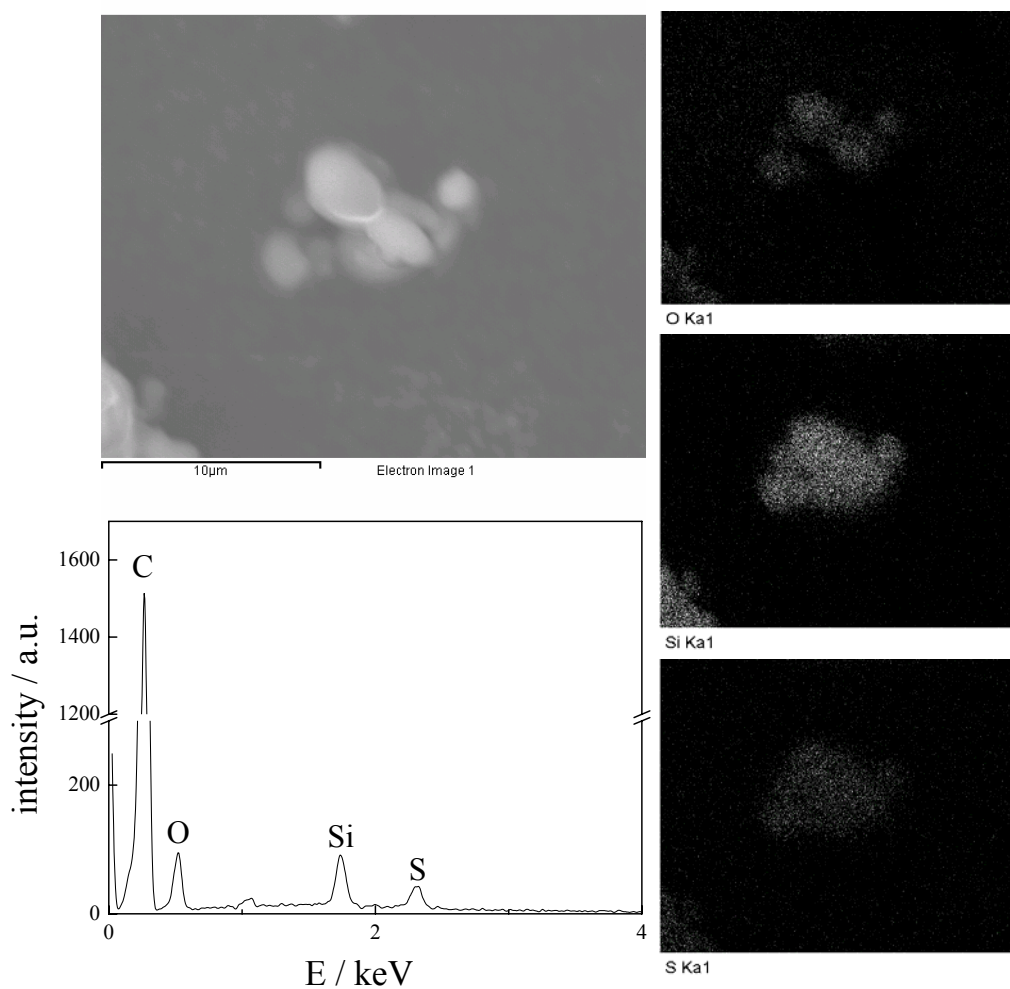


Figure 118. SEM picture of 20 % SO_3H -MCM-41-mw (upper left) and EDX mapping for oxygen (upper right), silicon (middle right) and sulfur (lower right). The EDX spectrum (lower left) was performed over the whole sample, the carbon signal results from the graphite slice from sample preparation.

Figure 119 shows that the proton conductivity of all the microwave treated samples increases continuously with temperature and also increases with the extent of substitution of metasilicate by MPMS in the co-condensation synthesis.

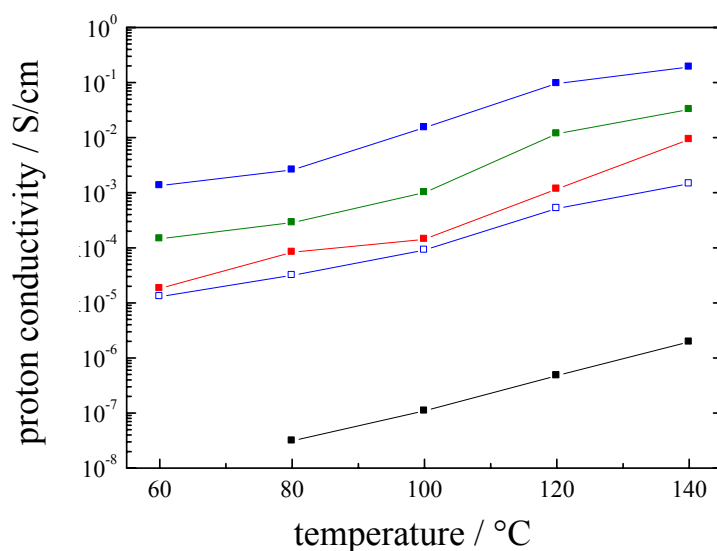


Figure 119. Proton conductivity measured at 100 % RH for 0 % (■), 20 % (■), 30 % (■) and 40 % (■) SO₃H-MCM-41-mw compared to 20 mmol grafted SO₃H-MCM-41(□). The lines are only to guide the eyes and have no physical meaning.

The highest proton conductivity of 0.2 S/cm is achieved with the 40 % SO₃H-MCM-41-mw sample due to the very high pore filling with SO₃H groups. The channel geometry of the pores observed in TEM (Figure 117), in which the sulfonic acid groups are fixed, does not only help to keep water but also supports the guidance of the protons through the tested pellets.

Compared to materials functionalized by grafting with MPMS, the loading of samples prepared by co-condensation is much higher and therefore the proton conductivity is increased by two orders of magnitude. While the IEC does not exceed 1 mmol/g for the SO₃H-MCM-41 hybrid materials prepared by grafting with 20 mmol MPMS, for those synthesized by co-condensation it exhibits up to 2.30 mmol/g of SO₃H groups accessible for ion exchange in 40 % SO₃H-MCM-41-mw (2.10 mmol/g for 30 % and 1.61 mmol/g for 20 %). This value is much higher than that found by Lim *et al.*²³⁶ with 1.76 mmol/g, although these authors report a sulfur content of 4.7 mmol/g. In contrast to our material, in their work most of the sulfur seems to be buried in the walls due to thicker pore walls.

Assuming that Si-MCM-41 exhibits a surface area of approx. $1000 \text{ m}^2/\text{g}$, the average density of OH groups on its surface is about 3 per square nanometer. In a grafting process, every MPMS is attached by reacting with one to two OH groups, and roughly a maximal loading of SO_3H groups of 1.67 mmol/g results. The fact that the loading, which has been really achieved by grafting, is lower indicates that blocking effects and hindrance of MPMS diffusion in the pores impede the grafting process. As in a co-condensation process the limitations of a grafting process are removed, loadings of up to $1.6 \text{ SO}_3\text{H}$ groups per nm^2 can be realized documenting that the MPMS in average binds with less than 3 groups. It is noteworthy that the IEC does not follow linearly the amount of MPMS offered in the co-condensation synthesis. This indicates that with a higher offer of MPMS increasing amounts of SH groups are buried inaccessibly within the pore walls and explains why in the 30 % and 40 % samples also SH groups were detected by DTA measurements (Figure 113). Figure 120 illustrates the situation inside the pores of functionalized MCM-41; the higher pore filling in samples synthesized by co-condensation being helpful for a better guidance of protons through the narrowed pore channels.

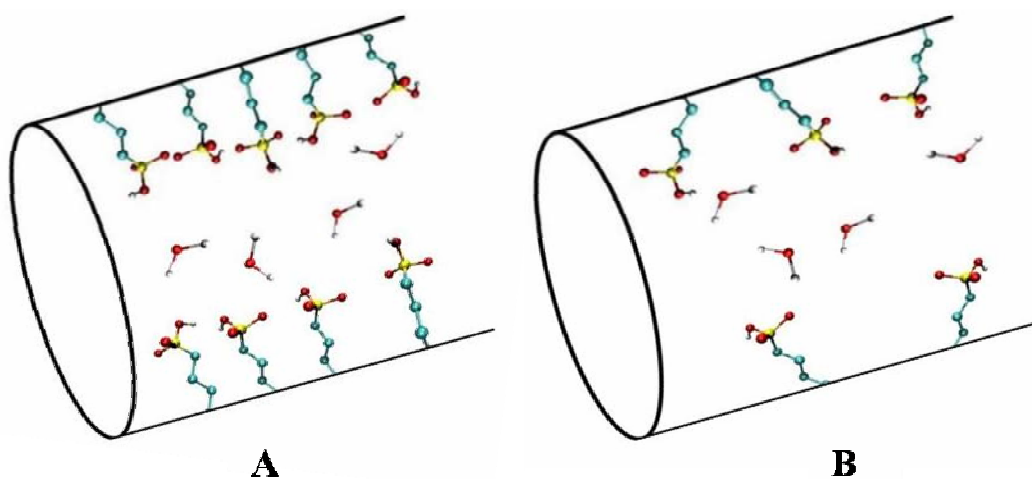


Figure 120. Illustration of the environment inside the pores of Si-MCM-41 after functionalization with SO_3H groups. A: after co-condensation, B: after grafting. Atoms: carbon (blue), oxygen (red), hydrogen (white), sulfur (yellow). Pore diameters and chain sizes are shown in the correct relation.

The activation energies for the overall proton transport mechanism have been calculated from the Arrhenius plots of the different SO₃H-MCM-41-mw samples and the slopes of the fitting lines (Figure 121).

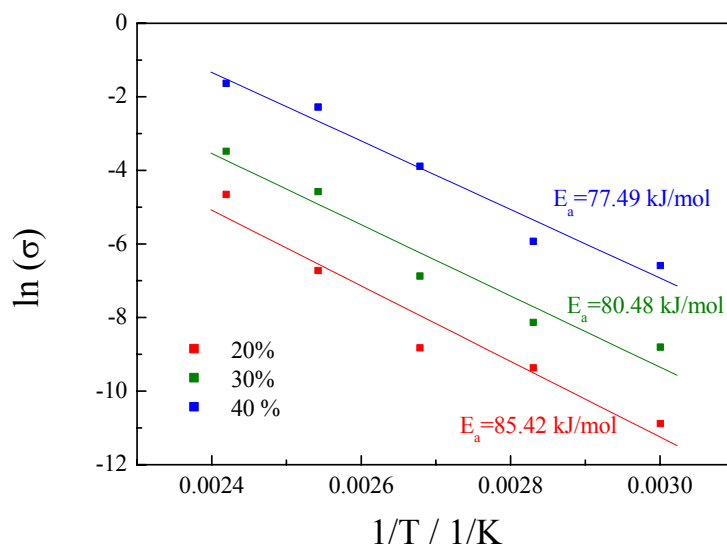


Figure 121. Arrhenius plots for 20 % (■), 30 % (■) and 40 % (■) SO₃H-MCM-41-mw with additional fitting line for calculation of the given activation energies.

The values of activation energy are again decreasing with increasing loading like in the grafted samples since the SO₃H groups can reach each other easily for proton transfer. The values are all in between an interval of 10 kJ/mol and much higher than for a pure Grotthuss mechanism⁵⁶ (13.5 and 38.5 kJ/mol), and also higher than in the grafted samples (compare chapter 4.2.2, Figure 91).

Since in the co-condensed samples the SO₃H groups are much closer together and can reach each other for proton transfer more easily, less additional water molecules are needed for proton transfer than in the grafted samples. Proton transfer only via SO₃H groups has a higher activation energy than water assisted proton transfer (Grotthuss mechanism), and this is the reason that the co-condensed samples have higher activation energies than the grafted samples, where more water molecule have been incorporated in the proton transfer mechanism, making the overall proton transfer mechanism of the

grafted samples more Grotthuss-like than in the co-condensed samples, resulting in lower activation energies for grafted samples.

As already mentioned, less water is sufficient to achieve a similar extent of proton transport like in grafted samples, because the SO_3H groups are closer together (compare Figure 115). If the materials are synthesized by *in-situ* co-condensation, the water-free proton conductivity is much higher than for the grafted samples. This can be seen in Figure 122.

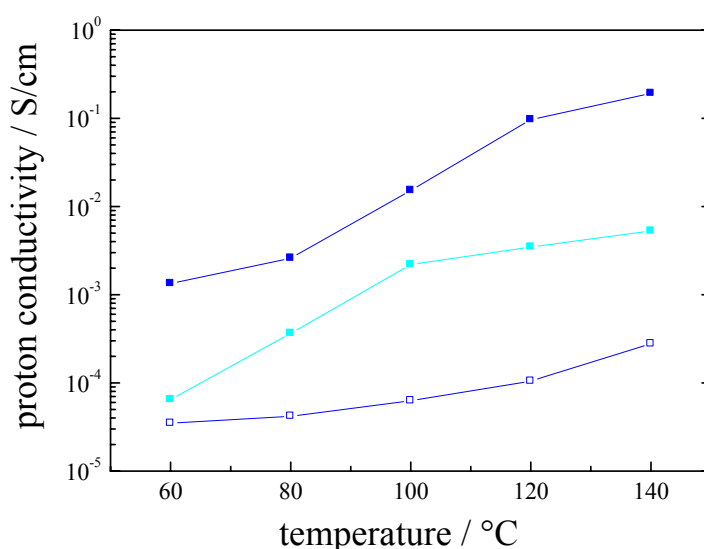


Figure 122. Dependence of proton conductivity for 40% SO_3H -MCM-41 on the relative humidity (0% (□), 50% (■), 100% (■)) in the measurement cell. The lines are only to guide the eyes and have no physical meaning.

Compared to the grafted sample (Figure 92), the water-free proton conductivity of the 40 % co-condensed sample is three orders of magnitude higher, and reaches 10^{-4} S/cm at 140 °C. The reason for that is the increase of SO_3H -group density inside the pore system, and less water is needed/used for the proton transport mechanism through the solid proton conductors.

Computational results clearly confirm the trend of the experimentally found proton conductivities and activation energies for increasingly loaded SO_3H -MCM-41 materials. From MD trajectories collected each 1 ps the RDFs are calculated and their dependence on increasing the conducting groups per area is shown in Figure 123 (compare chapter

3.1.8). As presented the first RDF peak is found at 2.8 Å, at this point the energy barrier for a proton jump is 8.5 kcal/mol, which is an ideal value for proton transfer. The area under the first peak is related to the total amount of pairs that can be found at this distance and grows with increasing of the density of conducting groups per area.

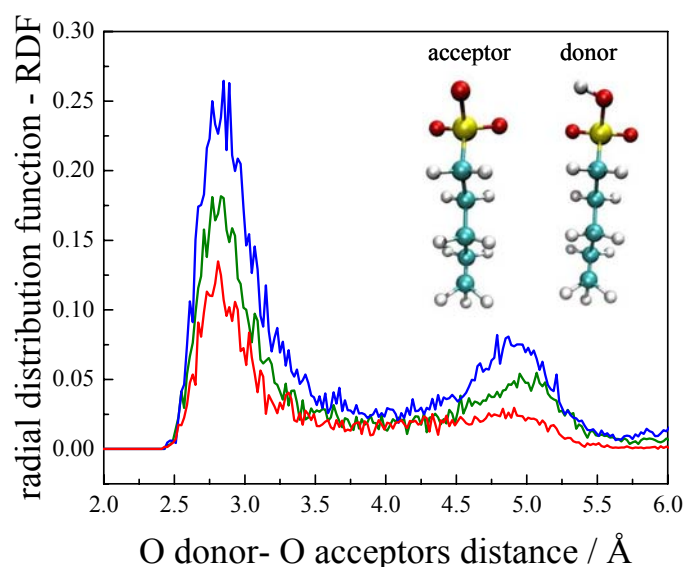


Figure 123. Radial distribution functions for the distances between oxygen donor atom and oxygen acceptor atoms for different densities of conducting groups per area at $T = 400$ K. Red line (1 group/nm^2), green line (2.04 groups/nm^2) and blue line (4 group/nm^2).

Again like in chapter 4.2.2, a direct counting of the total amount of donor-acceptor pairs available at 2.8 Å was performed for the total number of frames. For 4 groups/nm^2 a total of 21 donor-acceptor available pairs can be found, while for 2.04 groups/nm^2 this amount goes down to 18 pairs, and at 1 group/nm^2 this value strongly decreases to only 9 pairs as shown earlier. For each possible donor-acceptor pair the total time that this pair is within the maximum 2.8 Å (first RDF peak) is a variable called collision number, and it is counted every 1 ps. In order to estimate a probability of having the collision of an specific donor-acceptor pair in the total time, for each pair the collision number is divided by the total time (total number of frames) obtaining a quantity called collision ratio of the specified donor-acceptor pair.

For instance, for 4 groups/nm^2 and 2 groups/nm^2 the donor-acceptor pairs that lead to the highest collision number have a collision ratio in order of 0.54 at 450 K, which

means that this specific pair is present within these 2.8 Å for at least 50 % of the total frames. While for the density of 1 group/nm² the pair that has the highest number of collisions has an order of 0.42 collision ratio at 450 K. These results indicate that densities of 4 groups/nm² and 2 groups/nm² have a considerable higher probability of proton transfers compared to the 1 group/nm² case. Due to these RDF and collision ratio determinations, a high density of SO₃H groups turned out to be very important for proton transfer, in agreement to the increasing proton conductivities measured for the continuously enhanced SO₃H loadings in these hybrid materials.

4.3.2 Functionalization of mesoporous silica with PO₃H₂ groups via co-condensation

Another acidic group for enabling proton conductivity in mesoporous silica materials is the phosphonic acid group PO₃H₂. As an alkoxy silane with an acidic end group would react with itself forming esters, PO₃H₂ moieties have to be synthesized using precursors with protected acid function, e.g. phosphonic acid alkylester alkoxy silanes. The alkylester groups can after co-condensation be transformed into PO₃H₂ groups via reaction with concentrated HCl (chapter 3.2.6).

Figure 124 shows the successful functionalization of Si-MCM-41 with phosphonic acid diethyl ester and successful transformation to PO₃H₂ groups. The P-O-alkyl vibrations of the esters are too weak and hidden (1030-1050 cm⁻¹)²²⁹ under the very strong Si-O-Si lattice vibrations to be determined. The best observable peaks are again the aliphatic C-H stretching vibrations of the spacer chain and the ester groups containing CH₃ groups. After transformation into PO₃H₂ moieties, the signals for the C-H vibrations of CH₃ groups disappear, and only the C-H vibrations for CH₂ groups remain.

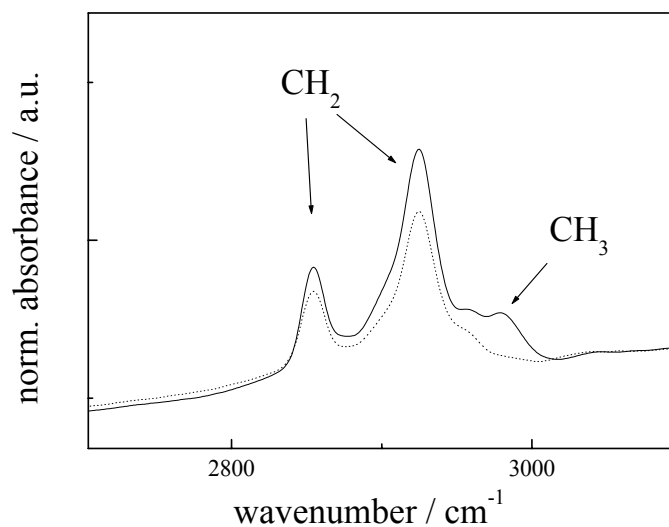


Figure 124. IR spectra of phosphonic acid diethyl ester (black line) and phosphonic acid functionalized Si-MCM-41 (dotted) prepared via co-condensation, extraction and HCl transformation.

In the XRD patterns after template extraction, a strong decrease in the (100) reflection for the 20 % PO₃H₂-MCM-41 and 30 % PO₃H₂-MCM-41 can be detected, due to increasing incorporation of organic moieties (Figure 125).

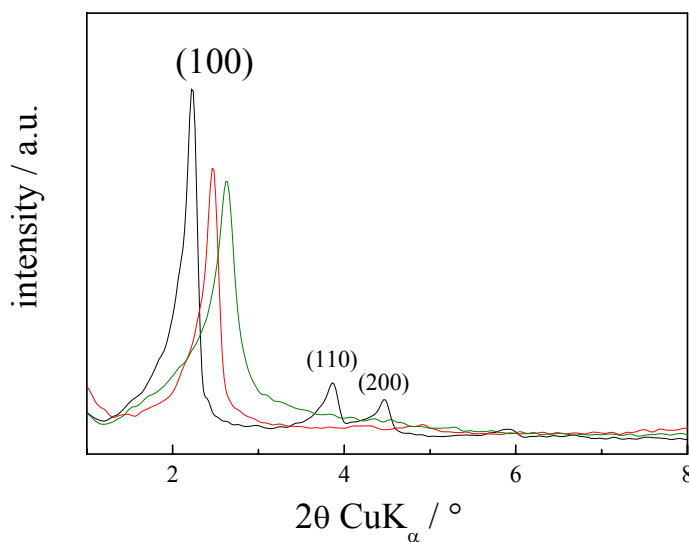


Figure 125. XRD patterns of 20 % (red) and 30 % (green) PO₃H₂-MCM-41 compared to pure Si-MCM-41.

A complete absence of the (110) and (200) reflections is determined like already shown for the grafted materials, indicating an increased pore filling with the functionalizing agents via co-condensation leading to contrast matching between filled pore and silica wall.²²⁵ Additionally, a shift in the (100) reflections is observed for the co-condensation samples compared to pure Si-MCM-41 to higher angles 2θ , indicating a lattice constant decrease. When alkoxy silanes are introduced in the synthesis of the silica framework, these additional reagents can influence the formation of the SLCs and the cooperative self-assembly mechanism for the silica condensation, leading to a decreased lattice constant. Some alkoxy silanes even hinder the formation of a mesoscopic phase in the homogeneous precipitation method, e.g. aminopropyl triethoxysilane (APTES), so no mesoporous silica material is formed.²³⁷

The proton conductivities for the PO_3H_2 functionalized Si-MCM-41 powders are presented in Figure 126.

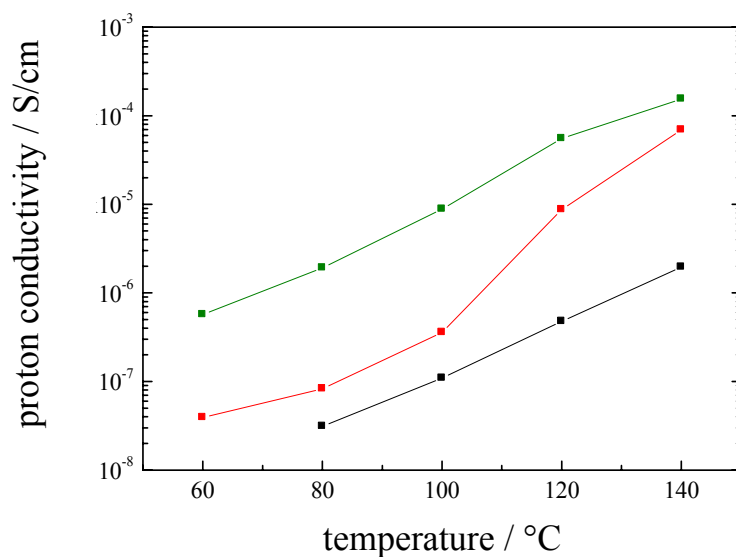


Figure 126. Proton conductivity measured at 100 % RH for 20 % (■) and 30 % (■) PO_3H_2 -MCM-41 compared to pure Si-MCM-41 (■). The lines are only to guide the eyes and have no physical meaning.

²³⁷ R. Marschall, unpublished results.

The 20 % PO₃H₂-MCM-41 sample exhibits proton conductivities under 100 % RH, continuously increasing with temperature, of up to 6x10⁻⁵ S/cm. The 30 % PO₃H₂-MCM-41 sample shows slightly higher proton conductivities due to an increased loading with PO₃H₂ groups, exhibiting values up to 10⁻⁴ S/cm. Both samples have better proton conductivity properties than the pure Si-MCM-41.

Compared to the SO₃H functionalized Si-MCM-41 samples prepared via co-condensation, the values for proton conductivities of the similar prepared PO₃H₂-MCM-41 samples are around two orders of magnitude lower. In contrast to SO₃H groups, which have a lower pK_s value (~ -3.0) and deprotonate more easily for proton conductivity, the PO₃H₂ group is less acidic (pK_s ~ 2.1) and gives less mobile charge carriers. Another reason are the lower IEC values: 20 % PO₃H₂-MCM-41 has only an IEC of 1 mmol/g, increasing to 1.55 mmol/g for the 30 % sample. Additionally, if less PO₃H₂ are deprotonated, also less oxygen atoms are free for accepting protons in the group-supported Grotthuss-like mechanism. In conclusion, less protogenic groups support the Grotthuss-like mechanism in PO₃H₂-MCM-41 samples than in SO₃H-MCM-41 samples.

4.3.3 Functionalization of mesoporous silica with imidazole groups via co-condensation

Co-condensation of TESBA with sodium metasilicate leads to aldehyde functionalized mesoporous silica. As presented in chapter 3.2.5, subsequent *in-situ* imidazole formation leads to imidazole functionalized mesoporous silica.

The successful formation of imidazole in the pores can be detected in IR spectroscopy. The IR spectrum looks like the one from the grafting process (Figure 106), with some remaining aldehyde signals. A strong signal for the aldehyde C=O vibration appears after co-condensation with TESBA above 1700 cm⁻¹, and still remains after imidazole

4 Results

formation, indicating again a non-quantitatively reaction of all aldehyde groups to imidazole. After imidazole formation reaction, the number of bands increases, indicating the two bands for C=N valence vibration for conjugated cyclic systems (imidazole) between 1400 cm^{-1} and 1550 cm^{-1} , proving the successful imidazole anchorage.²²⁹

XRD measurement presented in Figure 127 show the increasing functionalization with imidazole groups by reflection intensity decrease²²⁵ compared to pure Si-MCM-41.

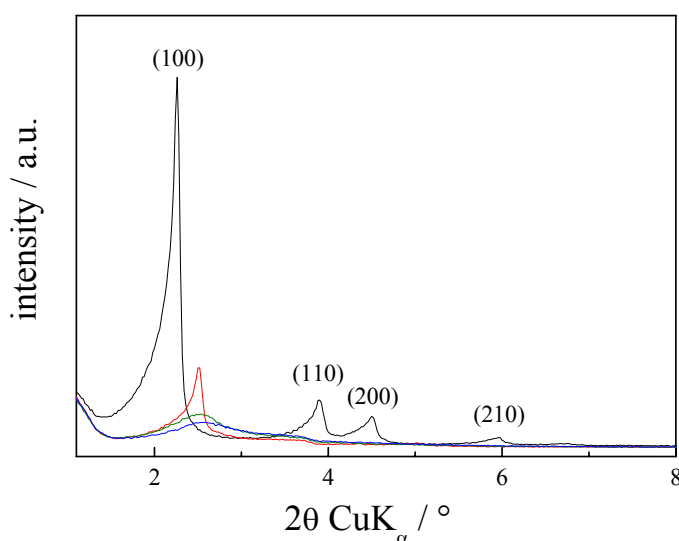


Figure 127. XRD patterns of 20 % (red), 30 % (green) and 40 % (blue) imidazole-MCM-41 compared to pristine Si-MCM-41.

No higher reflections than the (100) reflection can be detected in the functionalized materials, and the (100) reflection is shifted to higher 2θ values as expected for the co-condensation materials.

The addition of TESBA to the reaction mixture for the preparation of the functionalized Si-MCM-41 has again a profound effect on the texture properties (Figure 128). The isotherms for the 20 % to 40 % CHO-MCM-41 exhibit variously shaped hysteresis loops corresponding to differently sized mesopores, and look quite similar to those of $\text{SO}_3\text{H-MCM-41}$ (Figure 114). The BET surface areas for 20, 30 and 40 % CHO-MCM-41 samples equal 1251 , 953 and $854\text{ m}^2/\text{g}$, respectively. The formation of small

mesopores is therefore measured, reaching 2.1 nm pores for the 40 % sample. The shape of the isotherms exhibit also an increasing pore blocking effect with loading, especially visible in the desorption branch of the isotherm of the 40 % CHO-MCM-41.

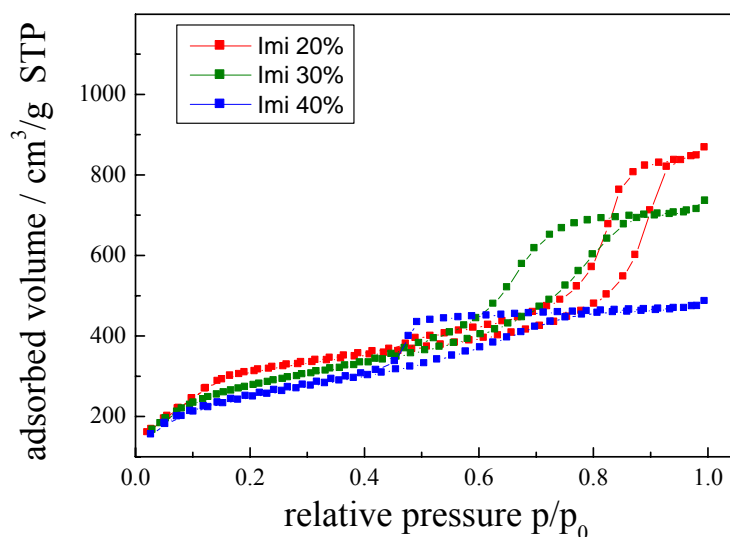


Figure 128. Nitrogen adsorption isotherms of functionalized samples 20 (■), 30 (■) and 40 % (■) CHO-MCM-41.

The resulting proton conductivities of the imidazole functionalized Si-MCM-41 are shown in Figure 129 for the 20, 30 and 40 % samples. Due to the observed pore blocking effect by the introduced aldehyde moieties, the *in-situ* reaction to imidazole is even more hindered than in the grafted materials (see chapter 4.2.5). The measured IEC values for the 20 to 40 % sample are only 0.27, 0.31, 0.36 mmol/g, compared to SO₃H materials with up to 2.3 mmol/g. These values explain the relative low conductivity values after co-condensation, exhibiting up to 5×10^{-5} S/cm. The conductivity values also do not differ very much due to the very similar IECs.

Although the high loading with organic groups via co-condensation is mostly of advantage, this example shows the disadvantage of the applied synthesis. If the following reaction to form the protogenic group involves too many or bulky molecules, a prior co-condensation with alkoxysilanes might be even of disadvantage due to the pore diameter reduction by the incorporated moieties. In the here presented imidazole

case, this led to even worse conductivity results than for the grafted materials (compare chapter 4.2.5). The IEC values of the imidazole functionalized Si-MCM-41 after grafting are higher up to 0.56 mmol/g, leading to higher proton conductivities (up to 10^{-4} S/cm) than for the co-condensation materials.

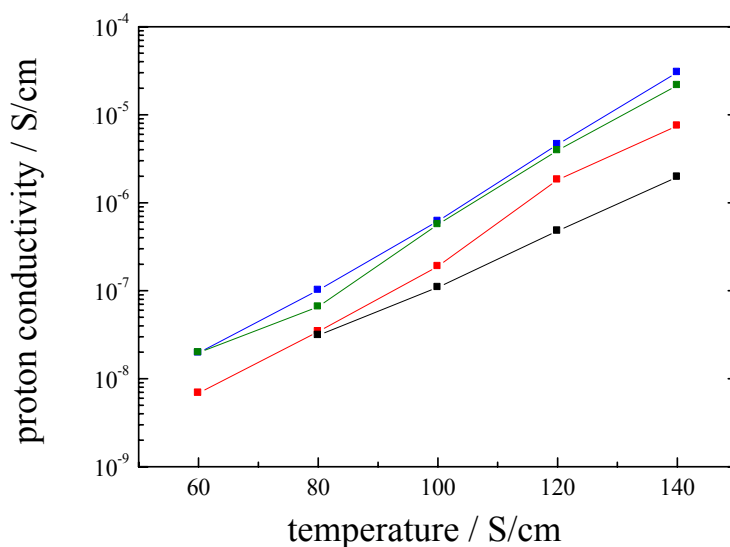


Figure 129. Proton conductivity measured at 100 % RH for 20 % (■), 30 (■) and 40 % (■) imidazole-MCM-41 compared to pure Si-MCM-41 (■). The lines are only to guide the eyes and have no physical meaning.

4.3.4 Summary on proton conductivities of functionalized Si-MCM-41 materials synthesized via co-condensation

Functionalization of Si-MCM-41 via co-condensation leads to an increased loading with functional groups compared to grafting reactions. As in a co-condensation only near pH-neutral alkoxy silane can be used, only precursors of the needed protogenic groups are incorporated into the silica framework. After template removal via ethanol/HCl extraction, the precursor groups are transformed into the protogenic groups. An exception is the transformation of SH into SO_3H groups, where the transformation can

be performed simultaneously with the template removal in a microwave oven (see chapter 4.3.1). If the group transformation reaction contains too many or too bulky reactants, the transformation can be hindered due to an inhibited diffusion into the pores (see chapter 4.3.3., *in-situ* imidazole formation).

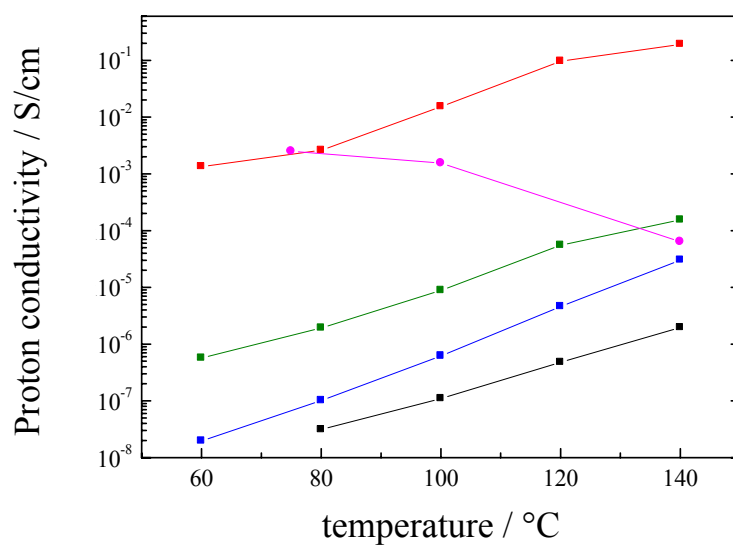


Figure 130. Proton conductivity measured at 100 % RH for pure Si-MCM-41 (■), 40 % Imi-MCM-41 (■), 30 % PO₃H₂-MCM-41 (■) and 40 % SO₃H-MCM-41 (■) compared to Nafion measured under the same conditions (●) running dry. The lines are only to guide the eyes and have no physical meaning.

Figure 130 shows the summary of the best proton conductivities of all prepared samples via co-condensation under 100 % RH compared to Nafion[®]. Resulting in a hindered imidazole formation, the imidazole-MCM-41 shows only slightly higher proton conductivities than the pure Si-MCM-41. PO₃H₂ functionalized Si-MCM-41 shows even higher proton conductivities, but still not reaching the very high values for SO₃H-MCM-41 prepared via 40 % co-condensation. This material exhibits the highest IECs (2.3 mmol/g) and the highest proton conductivities up to 0.2 S/cm. The values of the pressed powders of these materials even exceed the values for Nafion[®] membranes under the same condition, showing the typical conductivity drop above 100 °C due to water loss and structural degradation.

In general, the acidic head groups seem to be more suitable for proton conductivity in solid proton conductors, due to their intrinsic charge carriers. Imidazole-functionalized solid proton conductors need excess charge carriers for high proton conductivities. By solving the problem of pore blocking for the imidazole formation reaction, the conductivity values of these systems should be enhanced drastically. Also the synthesis of mixed systems like SO₃H-imidazole-MCM-41 (with different SO₃H/imidazole ratios) could lead to enhanced proton conductivity; however, the use of two alkoxysilanes in the co-condensation reaction can influence the formation of the silica framework in the homogeneous precipitation process even more than single alkoxysilanes already do.

4.3.5 Mesoporous Si-MCM-41 nanoparticles functionalized with SO₃H groups via co-condensation

In chapter 4.1.4, the results on synthesized mesoporous Si-MCM-41 nanoparticles have been described. As these materials exhibit outstanding texture properties, and concerning the very good results for SO₃H functionalized Si-MCM-41 via co-condensation (chapter 4.3.1 and chapter 4.3.4), the co-condensation approach was used to functionalize also the pure Si-MCM-41 nanoparticles with SO₃H moieties.

In the first approaches, the SH functionalizing alkoxysilane MPMS (in 10 and 20 % amount) was added directly to the synthesis mixture described in chapter 3.2.1, resulting in a synthesis mixture molar composition of 1200 H₂O : 0.31 NaOH : 0.125 CTAB : 1-x TEOS : x MPMS (x = 0.1, 0.2). Unfortunately, this approach did not lead to a desired result, as the particle morphologies and pore structures changed drastically due to a strong influence of MPMS on the SLC formation.

As for a TEOS substitution of 10 % some ordered porosity is still observable in the TEM, the shape of the particles changed drastically to more worm-like particles (Figure 131 a and b). By adding even more MPMS, the ordered porosity breaks down

completely, while the particle shape changed again to small spheres (Figure 131 c and d).

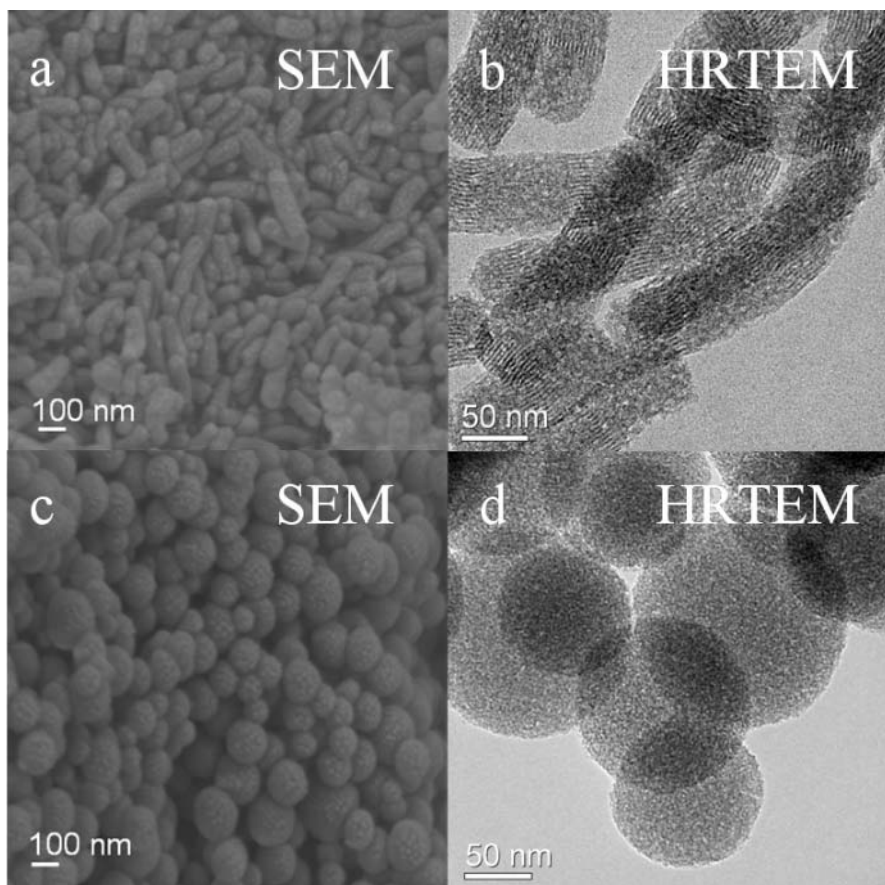


Figure 131. SEM and HRTEM images of Si-MCM-41 nanoparticles after 10 % (a and b) and 20 % (c and d) co-condensation.

For establishing a uniform particles shape and an ordered hexagonal pore structure, pre-hydrolysis experiments were performed, where the synthesis mixture $1200 \text{ H}_2\text{O} : 0.31 \text{ NaOH} : 0.125 \text{ CTAB} : 1-x \text{ TEOS}$ was stirred, adding the MPMS ($x = 0.1$ or 0.2) after a certain reaction time. 15 minutes pre-hydrolysis turned out to be the best time for reaching a uniform sphere-like particle shape with additional hexagonally ordered pore structure, including propyl-SH groups. During pre-hydrolysis time, the first seed crystals were formed with an already preformed hexagonal porous structure, acting as template for further particle growth. During the particle growth, the MPMS is added and incorporated into the already preformed structure, which is only growing further. Figure

132 shows two SEM images of 10 % SH functionalized nano-Si-MCM-41, using the pre-hydrolysis strategy.

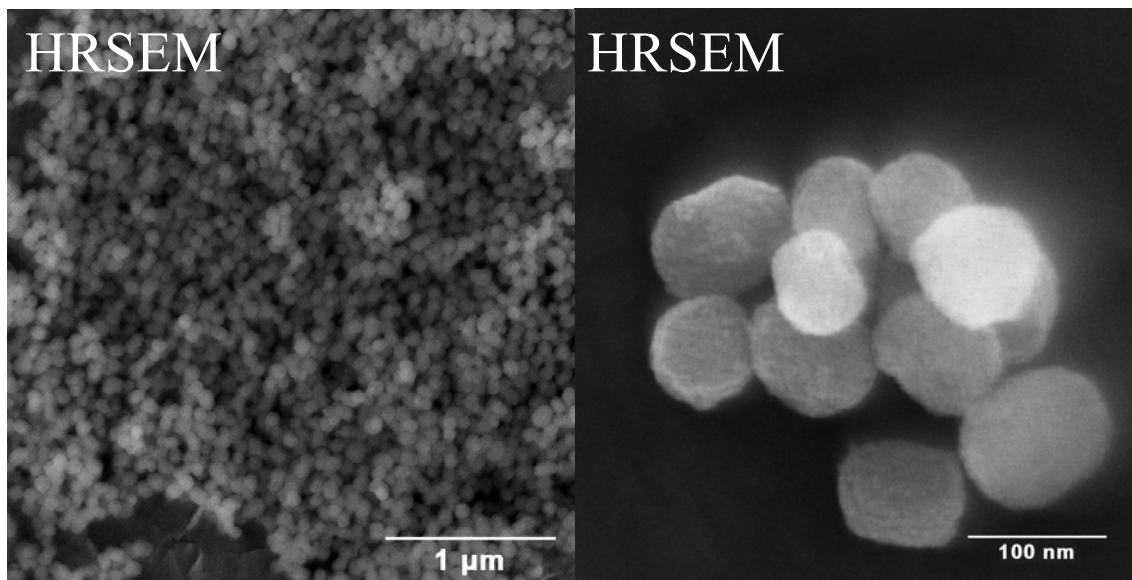


Figure 132. High-resolution SEM (HRSEM) images of SH functionalized mesoporous Si-MCM-41 nanoparticles by pre-hydrolysis strategy after template extraction.

It can be clearly seen that the particle size exhibits around 100 nm like for the pure nano-Si-MCM-41, and also the morphology is similar. The particles show a rough surface (right), and tend to form aggregates of large amounts of particles in dry powders.

XRD patterns and nitrogen adsorption measurements of the SO_3H functionalized mesoporous nanoparticles (after template extraction and oxidation via fast microwave treatment, see chapters 3.2.4 and 4.2.1) show the ordered hexagonal pore structure of the nanoparticles after pre-hydrolysis synthesis.

XRD data in Figure 133 compare the reflections of the pure material with the co-condensed samples. Pure nano-Si-MCM-41 shows four well resolved reflections typical for Si-MCM-41, as shown in chapter 4.1.4. With high pore filling occurring from the co-condensation, like for the grafting samples already shown, the reflection intensities decrease with increasing loading due to contrast matching between the filled pores and the silica walls, that even the (110) and (200) reflections nearly disappear²²⁵ for the

10 % nano-SO₃H-MCM-41 sample, while complete absence of more than the (100) reflection is observed for 20 % nano-SO₃H-MCM-41.

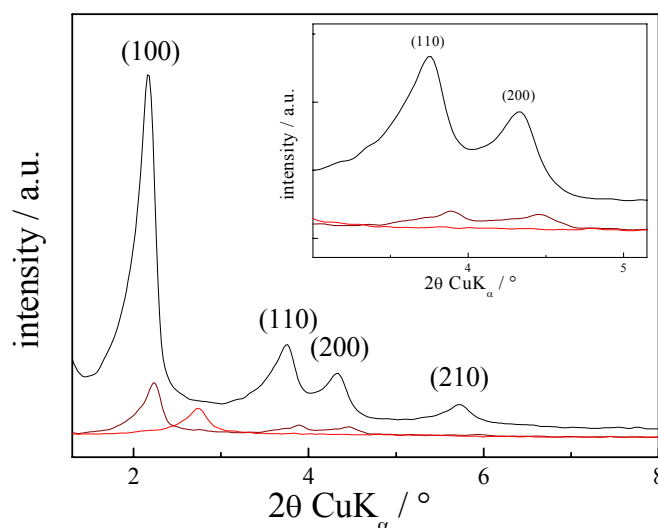


Figure 133. XRD patterns for pure nano-Si-MCM-41 (black) compared to 10 % (brown) and 20 % (red) nano-SO₃H-MCM-41.

Also the lattice changes slightly with adding of MPMS in the synthesis: The (100) reflections move to higher 2θ values, indicating decreasing lattice constants a_0 (calculated via $a_0 = 2d_{100}/\sqrt{3}$)²⁰⁵ with increasing amount of MPMS in the synthesis from 4.70 over 4.55 down to 3.72 nm. These trends were already reported for μm -sized SO₃H-functionalized Si-MCM-41, in the same behavior reflections shifted and intensities deteriorated (chapter 4.3.1).

Figure 134 shows the nitrogen adsorption isotherms of the two functionalized nanomaterials after microwave treatment compared to the pure nano-Si-MCM-41 material. As already shown, nano-Si-MCM-41 exhibits no hysteresis loop, but a steep increase for capillary condensation in mesopores at relative pressure around 0.3. 10 % nano-SO₃H-MCM-41 shows surface areas, pore volumes and average pore diameters of 1418 m² g⁻¹, 1.31 cm³ g⁻¹ and 2.5 nm, respectively, as the increase for capillary condensation occurs at slightly lower relative pressures. With higher extent of silicon source substitution, the influence of MPMS becomes stronger, and the values decrease

4 Results

more drastically to 1135 m²/g, 0.74 cm³/g and 2.1 nm (Table 12), and nearly no capillary condensation for mesoporosity can be observed.

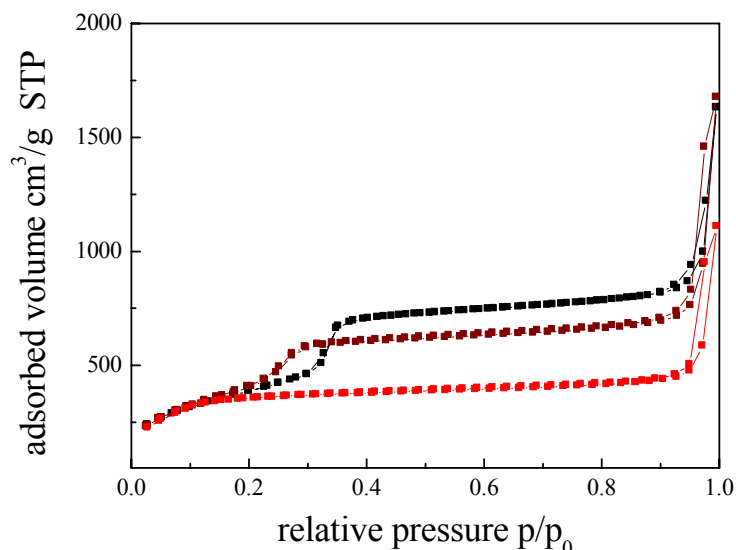


Figure 134. Nitrogen adsorption isotherms for pure nano-Si-MCM-41 (black) compared to 10 % (brown) and 20 % (red) nano-SO₃H-MCM-41.

Table 12. Structural properties of nanosized functionalized silica materials.

	BET surface	pore	measurable pore	lattice
	area	volume	diameter	constant
	m ² /g	cm ³ /g	nm	nm
nano-Si-MCM-41	1459	1.344	2.8	4.7
10 % MPMS	1418	1.31	2.5	4.55
20 % MPMS	1135	0.74	2.1	3.72

The existing pore geometry of the microwave treated materials can be confirmed by transmission electron microscopy. The TEM micrographs in Figure 135 clearly show the pore channels of the Si-MCM-41 host material besides the filled pores with a remaining distance between the pore walls of 2.9 ± 0.1 nm in FFT calculation.

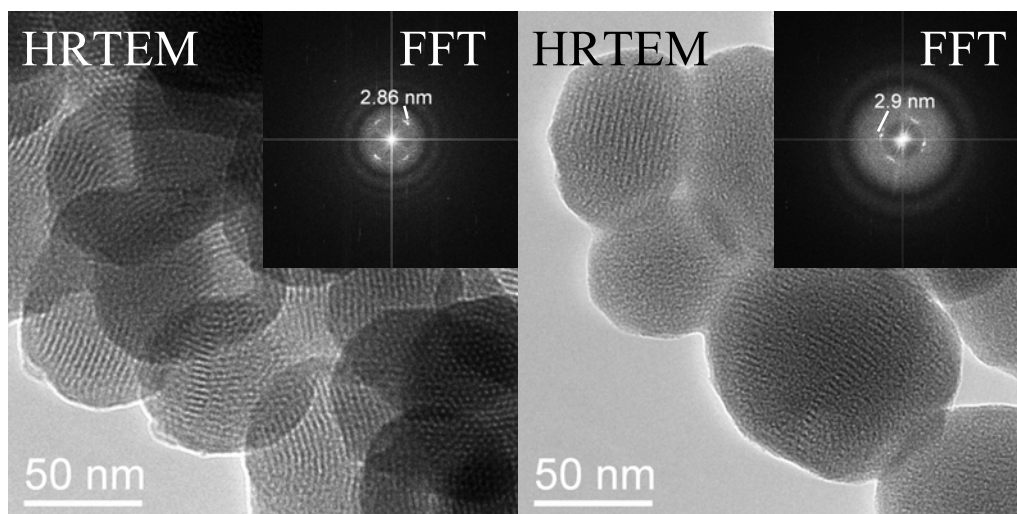


Figure 135. TEM images and FFT calculation for 20 % nano-SO₃H-MCM-41.

EDXS and EELS performed in the TEM confirm also the incorporation of the MPMS in the silica matrix. The successful incorporation of the sulfur-containing side chains can be controlled by EDXS. From calculation the atomic percentage of silicon and sulfur, a sulfur-silicon ratio of 1:5 was estimated, confirming the co-condensation reaction and substitution of 20 % of silicon source by MPMS forming the mesoporous matrix. Figure 136 shows the result of the EDXS measurement with well resolved signals for silicon, oxygen and sulfur. The carbon signal results from the sample preparation for TEM analysis and the carbon spacer chains.

Figure 137 shows the EELS analysis of the same sample. The presented cut-out shows the signal for amorphous carbon, belonging to the spacer-chain of the MPMS, and is not a result of the TEM preparation. For EELS, the pure powder was measured on a special Mg grid, containing no carbon, which could not be used for EDXS, as it would be destroyed during EDXS.

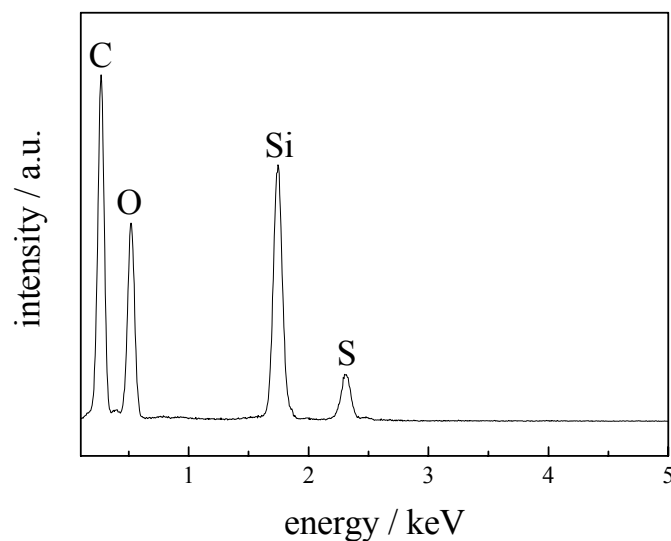


Figure 136. EDX spectrum of 20 % nano-SO₃H-MCM-41.

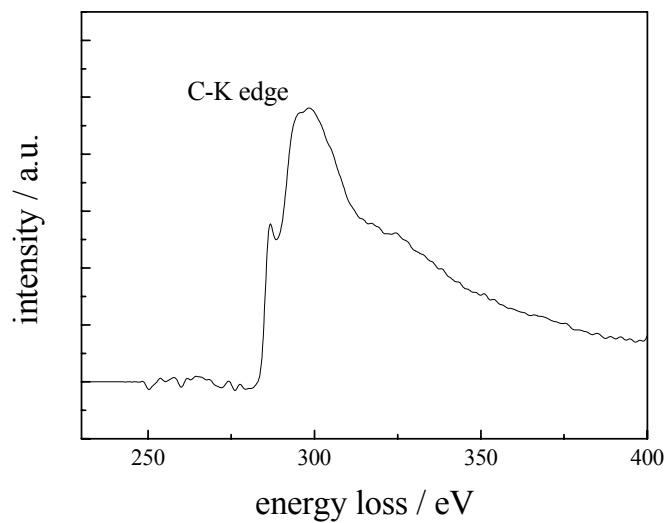


Figure 137. EEL spectrum of 20 % nano-SO₃H-MCM-41.

Figure 138 shows the results for the proton conductivities for the nanoparticular samples under 100 % RH. Similar to the already presented results of variously functionalized μm -sized Si-MCM-41 samples, the proton conductivities increase with temperature and loading, here up to 5×10^{-2} S/cm.

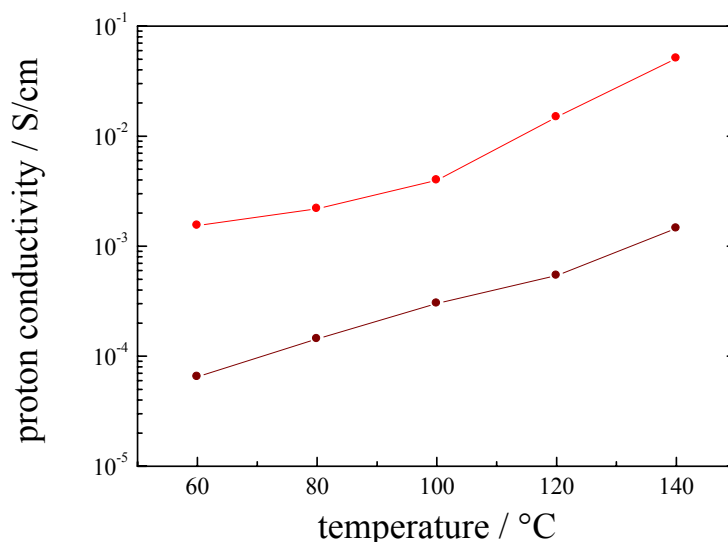


Figure 138. Proton conductivities under 100 % RH for 10 % (●) and 20 % (●) nano-SO₃H-MCM-41. The lines are only to guide the eyes and have no physical meaning.

Much more interesting is the comparison between the nanoparticulate and the μm -sized Si-MCM-41 particles functionalized with SO₃H groups.

In every case, at low loadings (Figure 139a, 10 %) or at higher loadings (Figure 139b), the nanoparticulate samples show higher proton conductivities than the comparable co-condensed μm -sized particles.

The proton conductivity of the hybrid nanoparticles increases with SO₃H loading. The loadings increase from 0.84 mmol/g for 10 % nano-SO₃H-MCM-41 to 1.78 mmol/g for 20 % nano-SO₃H-MCM-41, resulting in proton conductivities up to 5×10^{-2} S/cm. The particle size seems to have a very strong influence on the proton conductivity; a nanoparticulate 20 % sample shows even higher proton conductivities than a μm -sized sample of higher loading (30 %, IEC = 2.1 mmol/g). This might be caused by the higher external surface of small nanoparticles compared to larger μm -sized particles, facilitating the pore access and the surface proton conductivity. The higher external surface, and after sample preparation to pellets, the higher number of grain boundaries seem to be responsible for the strong increase in proton conductivity in mesoporous SO₃H functionalized nanoparticles of Si-MCM-41.

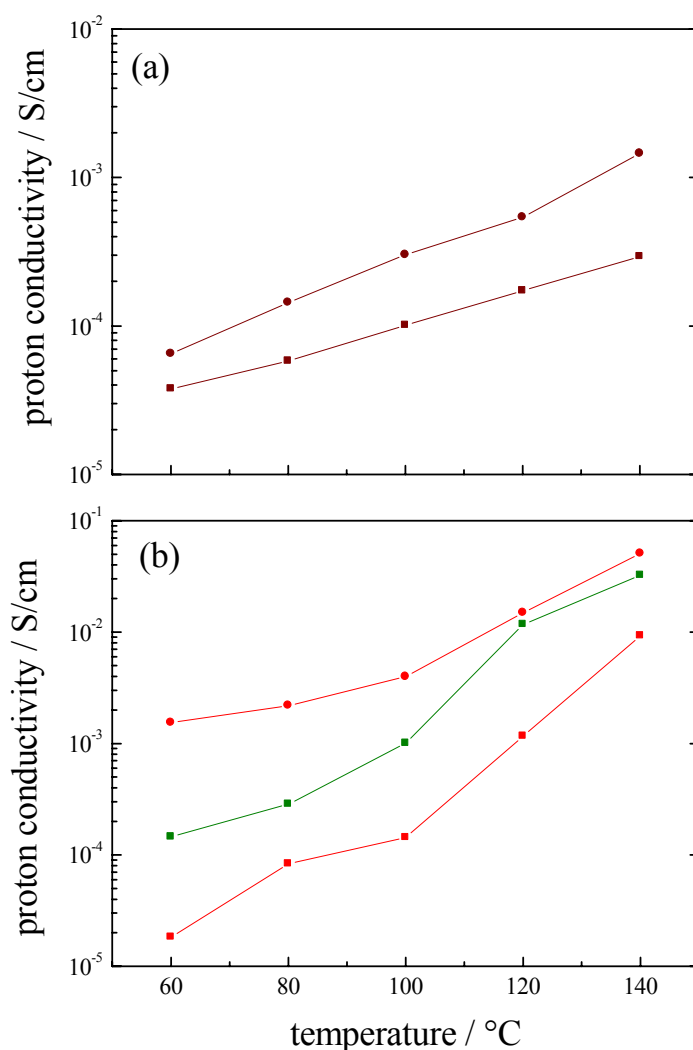


Figure 139. Comparison of the proton conductivities under 100 % RH after (a) 10 % co-condensation for 10 % nano-SO₃H-MCM-41 (●) and μm-SO₃H-MCM-41 (■); and after (b) 20 % co-condensation for 20 % nano-SO₃H-MCM-41 (●) and μm-SO₃H-MCM-41 (■) also compared to 30 % μm-SO₃H-MCM-41 (■). The lines are only to guide the eyes and have no physical meaning.

Only the 40 % SO₃H-MCM-41 materials exhibit higher proton conductivities (not shown in this picture, see chapter 4.3.1, Figure 119) with loading of 2.3 mmol/g. But also using the pre-hydrolysis strategy, an ordered hexagonal mesoporosity of higher loaded SO₃H functionalized nanoparticles could not be achieved up to now. Mesoporous SO₃H functionalized Si-MCM-41 nanoparticles with higher loadings might

even exceed the already very high proton conductivities of the μm -sized SO_3H -Si-MCM-41 material (0.2 S/cm).

Compared to SO_3H functionalized non-porous silica nanoparticles (we used Aerosil[®] 380 with average primary particle sizes of 7 nm, aggregating to at least 25 nm agglomerates) with comparable IEC (1.45 mmol/g), the mesoporous structure turned out to be crucial for high proton conductivity (Figure 140), especially at low temperatures.

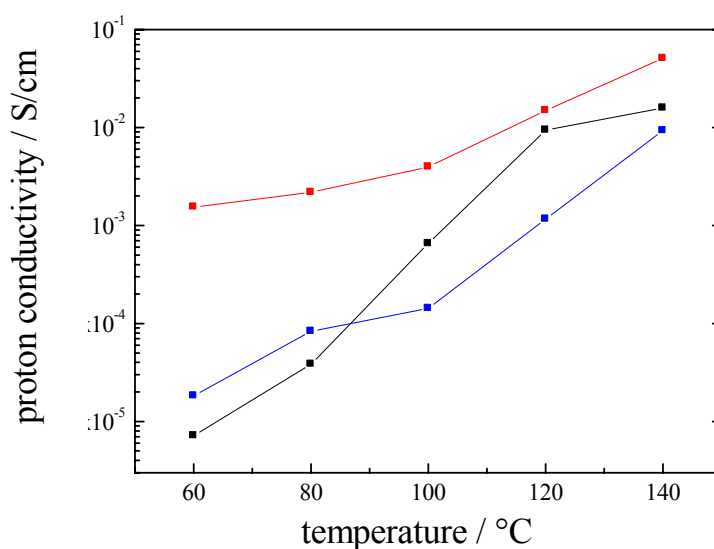


Figure 140. Comparison of the proton conductivities under 100 % RH of 20 % nano-SO₃H-MCM-41 (■, IEC 1.78 mmol/g) to SO₃H functionalized Aerosil[®] (■, IEC 1.45 mmol/g) and 20 % μm -SO₃H-MCM-41 (■, IEC 1.6 mmol/g). The lines are only to guide the eyes and have no physical meaning.

Between 60 and 100 °C, the mesoporous structure incorporates and stores the applied water for a good proton transfer. In this region, even the μm -sized SO₃H-MCM-41 particles have higher proton conductivities than the dense sample. At higher temperatures above 100 °C, the proton conductivity via the higher external surface of the nanoparticles comes into fore, and the dense silica nanoparticles show higher conductivity values than the μm -sized SO₃H-MCM-41 particles. Nevertheless, the functionalized mesoporous nanoparticles still show higher proton conductivities due to the guidance of protons through the well accessible mesoporous structure of the nanoparticles and the water storage capability.

The calculated activation energies also confirm the observation that the mesoporous samples are much favorable for good proton transport than the dense silica. Figure 141 shows the Arrhenius plots for the sulfonated Aerosil[®] nanoparticles compare to the co-condensed SO₃H-MCM-41 sample and the nanoparticular SO₃H-MCM-41 sample.

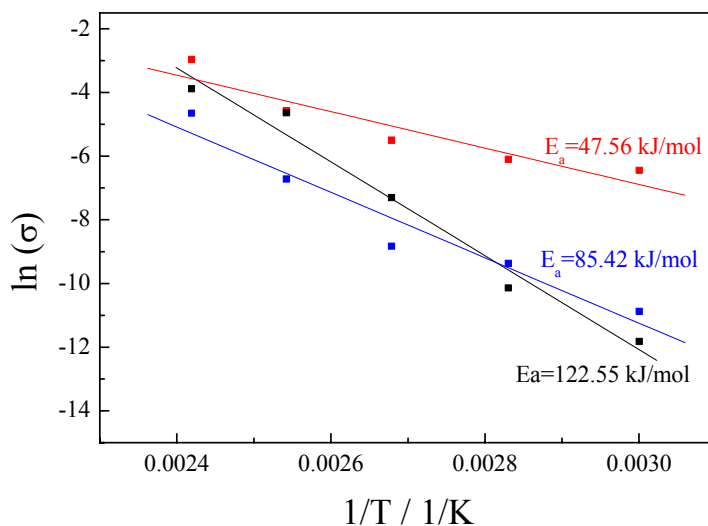


Figure 141. Comparison of activation energies of 20 % nano-SO₃H-MCM-41 (■, IEC 1.78 mmol/g) to SO₃H functionalized Aerosil[®] (■, IEC 1.45 mmol/g) and 20 % μm-SO₃H-MCM-41 (■, IEC 1.6 mmol/g).

The sulfonated Aerosil[®] nanoparticles exhibit much higher activation energy than the mesoporous samples, finally indicating that the mesoporous structure of the silica samples is crucial for good proton conductivity. The proton transport in the Aerosil[®] only occurs via surface conductivity on the external surface of the particles.

The SO₃H functionalized mesoporous silica nanoparticles have also much lower activation energy than their μm-sized counterparts, due to the well accessible pore entrances of the particles caused by the higher external surface, leading to a better and easier proton transfer via grain boundaries between the single particles.

4.4 Composite membranes containing SO₃H functionalized Si-MCM-41 particles

In the last chapters, the success in preparing new solid proton conductors with very high proton conductivities was reported. For a use in a high temperature PEMFC, these materials are not directly useful, as the pressed powders are too brittle and not thin enough to fabricate efficient stacks. Therefore, these new solid proton conductors were used in combination with different kinds of polymers, namely polysiloxanes, polyoxadiazoles and Nafion[®], to synthesize composite membranes. The results are presented in the following chapters. While the polymers are changed, the solid proton conductor is in all the composite membranes the same, the SO₃H functionalized Si-MCM-41 prepared via 20 mmol grafting, although it is not the optimum solid proton conductor presented in this work.

4.4.1 Composite membranes and MEAs with polysiloxanes

The approach described in the following is based on the development of bifunctional membranes consisting of siloxanes which are modified with different groups for the improvement of intrinsic proton conductivity (see chapter 2.1.4). Further, composite membranes with incorporated SO₃H functionalized Si-MCM-41 particles were prepared. The water uptake, the proton conductivity and other properties which are relevant for their use as membrane in a HT-PEMFC are measured and evaluated. The resulting microstructure is also described in detail, and for the first time it was possible to manufacture and characterize membrane electrode assemblies (MEAs) of these composites.

Composite membranes made of a proton conducting polysiloxane and embedded inorganic particles were prepared from a precursor solution of different acidic silanes with proton conducting SO₃H groups (sulfonated diphenyl-dimethoxysilane, sDPDMS, and sulfonated 2-phenylethyl trimethoxysilane sPETMS) and a basic silane containing the N-heterocycle benzimidazole (triethoxysilylpropylbenzimidazole-5-amide, TEOSPBA), which were additionally mixed with sulfonated polysiloxanes like vinyl-terminated diphenylsiloxane-dimethylsiloxane block-copolymer (sDPS-DMS-V(t)). While the ionic interaction of acid and basic groups densifies the polymer structure due to additional ionic cross-linking, the use of block-copolymers with linear chains expands the polysiloxane network and enhances the elasticity of the resulting membranes. 9.6 wt.-% or 17.1 wt.-% of the unmodified or SO₃H functionalized Si-MCM-41 particles were given to this solution and the suspension was homogenized by intense mechanical stirring. For membrane preparation, the suspension was cast on Teflon foils. During previous drying at room temperature and increasing the temperature up to 150 °C, respectively, cross-linking took place resulting in self-supporting composite membranes. In the same way the particle-free polysiloxane membranes were synthesized for comparison. The SEM images taken from the cross-section of a particle-free membrane and a composite membrane are shown in Figure 142. The thickness of crack-free membranes is about 500-600 μm. The particle free membrane displays a uniform microstructure with a smooth surface of the cross-section of the fractured membrane (Figure 142a). From the polished cross-section of the 17.1 wt.-% composite membrane (Figure 142b), a homogenous distribution of SO₃H functionalized Si-MCM-41 particles (1-2 μm) throughout the dense polysiloxane matrix can be seen. The rough surface structure results from a pull-out of particles during preparation of SEM samples and does not represent continuous pores. In spite of the high particle content, the composite membrane possesses a sufficient elasticity, but it should be mentioned that somewhat higher particle contents (more than about 20 wt.-%) lead to membranes showing unfavorable brittleness.

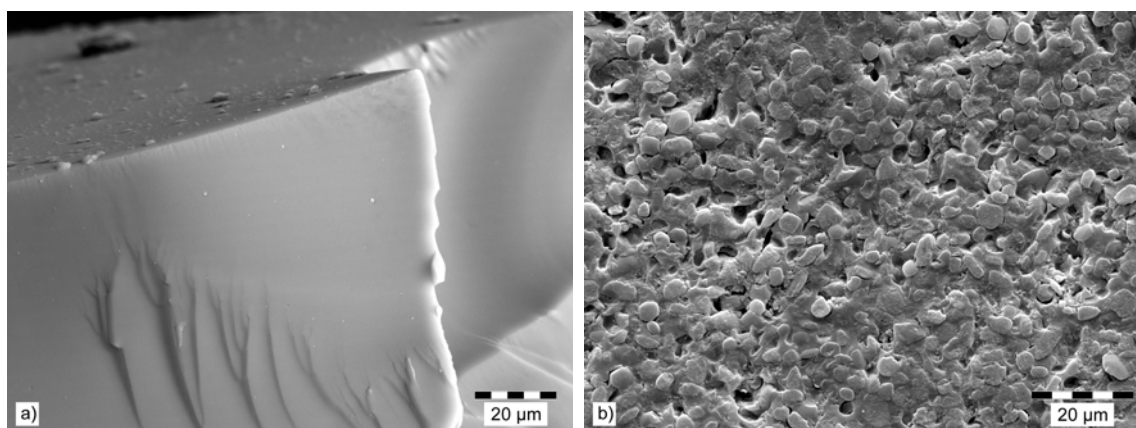


Figure 142. SEM micrographs of particle free polysiloxane membrane (a) and 17.1 wt.-% SO₃H-MCM-41 particle containing polysiloxane composite membrane (b).

Embedded particle increased the water uptake of the membranes significantly. The water adsorption behavior of composite membranes with 17.1 wt.-% particle content is shown in Figure 143 compared to pure polysiloxane membranes, and refers to an expanded network with enhanced water diffusion. Consequently, the isotherms of 17.1 wt.-% Si-MCM-41 and 17.1 wt.-% SO₃H-MCM-41 composite membranes exhibit some hysteresis, which can be attributed to capillary condensation of water vapor in the mesopores of embedded particles. Due to the improved water adsorption in functionalized pores (see chapter 4.2.1, Figure 86), the final water uptake of the SO₃H-MCM-41 composite is higher (14.1 wt.-%) than that of the Si-MCM-41 composite membrane (12.5 wt.-%). The non-closure of the water adsorption/desorption isotherms is an additional indication of small diffusion rates and irreversible water desorption.

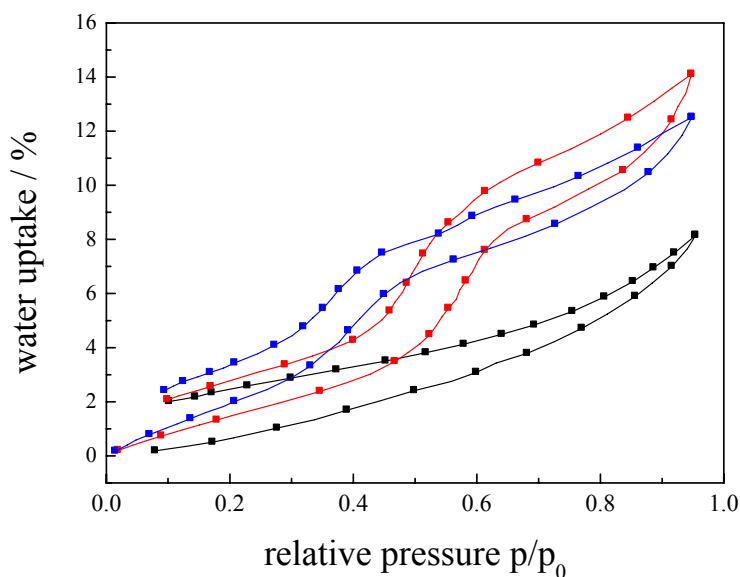


Figure 143. Water adsorption isotherms of polysiloxane composite membranes containing 17.1 wt.-% Si-MCM-41 (■) or SO₃H-MCM-41 (■), compared to pure polysiloxane membrane (■).

The thermal stability of the composite membranes was investigated by TGA up to 600 °C in an air flow (Figure 144). Beside membranes containing Si-MCM-41 particles, the particle-free polysiloxane and a Nafion[®] 117 membrane were examined. All membranes retain at least 95 % of their weight up to 260 °C; the lost weight can be attributed to residual water. The thermal degradation of the Nafion[®] membrane already starts at temperature of 300 °C due to the decomposition of SO₃H groups followed by pyrolysis of the CF₂ backbone of the polymer at temperatures around 500 °C.²³⁸ The onset of the decomposition temperature of polysiloxane-based membranes is comparable to that of Nafion[®], but the extent of weight loss with increasing temperature is much smaller. This enhanced thermal stability of the polysiloxane, and especially of the composite membranes, can be attributed to the temperature tolerance of the cross-linked polysiloxane network that protects the organic matrix to some extent. The composite membranes thereby have a slightly higher stability at 200 °C and above, and show less weight loss up to 500 °C than the pure polysiloxane membrane.

²³⁸ Q. Deng, C.-A. Wilkie, R.-B. Moore, K.-A. Mauritz, *Polymer* 39 (1998) 5961.

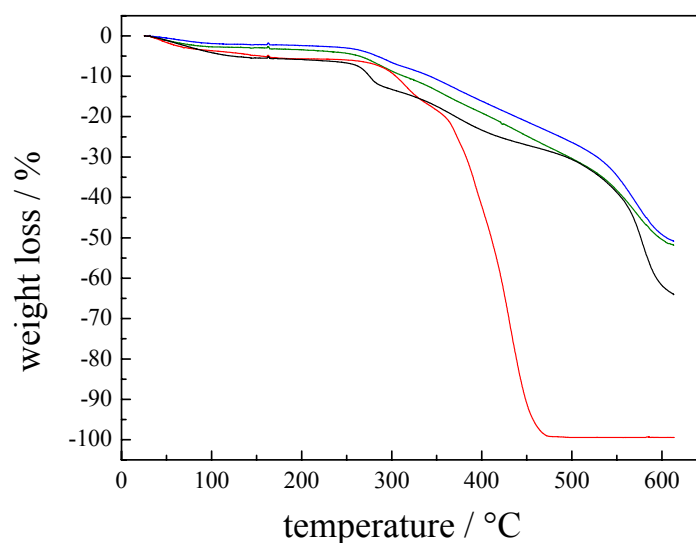


Figure 144. TG analysis of composite membranes of polysiloxanes containing unfunctionalized Si-MCM-41 (green), SO₃H functionalized Si-MCM-41 (blue) compared to pure polysiloxane membranes (black) and Nafion[®] 117 (red).

At 600 °C the decomposition of the entire polysiloxane and its conversion to SiO₂ is almost completed, what can be deduced from the obtained residual mass of 35 wt.-% for unmodified polysiloxane membrane and about 50 wt.-% for particle containing composite membranes, respectively. These values are in good agreement with the calculated amount of SiO₂ after complete oxidation.

The proton conductivity of polysiloxane-based membranes was measured in comparison to Nafion[®] 117 in the temperature range from RT to 190 °C simulating the working conditions of HT-PEMFCs (Figure 145). During the measurement cycles, the RH (curve with blue circles) decreases from 95 % RH in the low temperature range (20 - 80 °C) to below 10 % RH in the high temperature range (150 - 180 °C). The standard membrane material Nafion[®] 117 shows the typical continuous decrease of the proton conductivity with increasing temperature caused by the loss of water. At around 30 °C (95 % RH) the proton conductivity of Nafion[®] 117 is in the range of 2×10^{-3} S/cm and decreases to 2×10^{-5} S/cm at 180 °C (7 % RH). The pure polysiloxane membrane exhibits a slightly lower proton conductivity of 10^{-3} S/cm, which drops to the value of 10^{-8} S/cm at 110 °C

indicating a massive loss of water at higher temperatures. A further increase of the temperature results in a slight increase of conductivity up to 10^{-6} S/cm at 180 °C (7 % RH), which is the typical behavior of the bifunctional polysiloxane membranes.⁴⁹

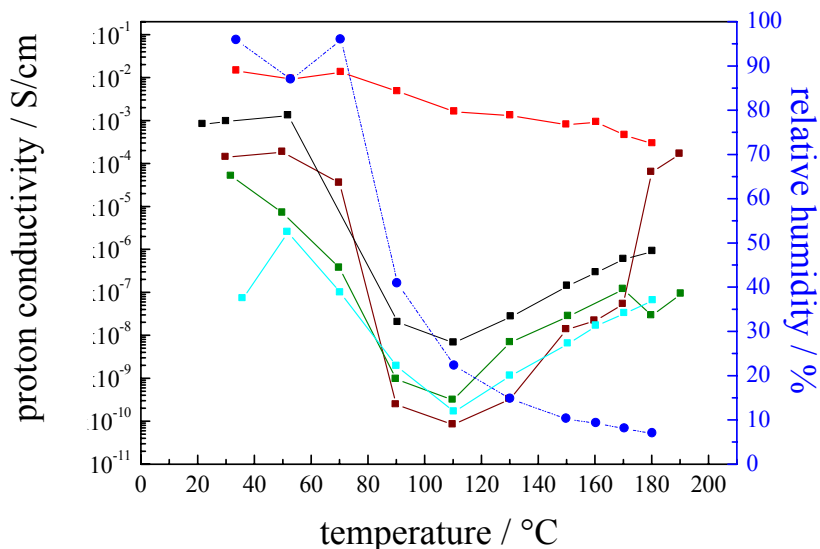


Figure 145. Proton conductivities measured under decreasing RH (●) of composite membranes of polysiloxanes with 9.6 wt.-% Si-MCM-41 (■), 9.6 wt.-% SO₃H-MCM-41 (■), 17.1 wt.-% SO₃H-MCM-41 (■) compared to pure polysiloxane membrane (■) and Nafion[®] (■). The lines are only to guide the eyes and have no physical meaning.

This increase in conductivity is probably induced by a water-free proton transport via heterocyclic proton conductors activated at higher temperatures. The composite membrane with 9.6 wt.-% SO₃H-MCM-41 shows a proton conductivity of 1.4×10^{-4} S/cm at 30 °C and 95 % RH, decreasing further with the continuous loss of water and poses a very low conductivity (10^{-11} to 10^{-10} S/cm) in the temperature range from 110 °C to 130 °C and 17 % RH. Interestingly, the conductivity of this membrane shows a remarkable increase at temperatures higher than 170 °C, reaching a value of 1.6×10^{-4} S/cm at 190 °C (7 % RH), being stable for several hours without any decrease. This high temperature conductivity exceeds the conductivity of particle-free polysiloxane membrane and is comparable to that of Nafion[®]. In contrast, the composite membranes containing 9.6 wt.-% Si-MCM-41 shows clearly lower proton conductivity particularly in this high temperature region. The results reveal two important findings:

(i) the water reservoir in the Si-MCM-41 pores can only be activated to facilitate proton transport if proton conducting SO_3H groups are additionally present, (ii) only at high temperatures the proton transfer from the functionalized Si-MCM-41 to the surrounding polysiloxane matrix leading to an increased overall proton conductivity is possible to a sufficient extent.

Surprisingly, the proton conductivity of a 17.1 wt.-% composite membrane is lower than that of particle-free polysiloxane membrane. Therefore, it can be suggested that the particles interrupt the proton conducting domains of the polysiloxane matrix to such an extent that the proton transfer through this membrane is hindered by a high energy barrier caused by the higher distance between the functional groups. Obviously the proton transfer through the functionalized channel pores can not compensate this barrier at low temperatures. However, at high temperatures, and thus under nearly dry conditions, two effects seem to support the proton transport: on one hand some few water molecules adsorbed in the SO_3H functionalized Si-MCM-41 particles seem to keep water-assisted proton transport working, and on the other hand, lower energy barriers for the proton movement in the Si-MCM-41 channels. The reason is the enhanced motion of the propyl chains in the anchored moieties in and at the pore entrances of the functionalized Si-MCM-41 particle as well as of the functional groups of the surrounding polysiloxane matrix. In general, the inorganic particles improved the thermal stability of the polysiloxane membranes, and the samples show a very high durability during the long measurement cycles under real conditions of an HT-PEMFC system.

In addition, it was for the first time possible to prepare and measure MEAs based on the composite membrane system polysiloxane with Si-MCM-41 particles. For the MEA preparation, supported membranes were used, which were prepared by casting the polymer precursor solution containing 9.6 wt.-% Si-MCM-41 and SO_3H -MCM-41, respectively, on a polyetheretherketone fleece and cross-linking the precursors at room temperature. Both sides of these membranes were coated with a mixture of carbon black containing 40 wt.-% Pt (Elyst A 40) and pre-polymerized sDPDMS in ethanol. Cross-linking of MEAs was accomplished at a temperature of 150 °C. A scheme of the

resulting MEA is shown in Figure 146, and the results of MEA measurements, which were performed using H₂ and O₂ as feed at 95 % RH at different temperatures, are presented in Figure 147.

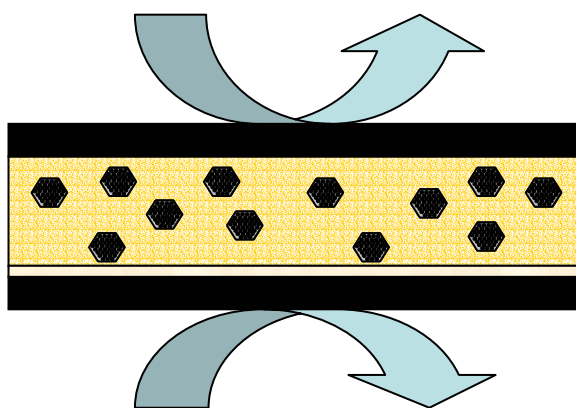


Figure 146. Scheme of a MEA prepared with polysiloxane-MCM-41 composite membrane. The black layers represent the electrocatalyst, and the thin beige layer depicts the polyetheretherketone fleece. In between, the composite membrane is shown.

In accordance with the values of the proton conductivity measurement, the current density of the new MEA system containing SO₃H functionalized Si-MCM-41 particles gain a higher current density in comparison with the MEA containing unmodified inorganic particles. Both systems show the expected increase of the current density with increasing temperature up to 40 or 50 °C, respectively.

The MEA of polysiloxane containing 9.6 wt.-% Si-MCM-41 poses an increase of current density from 0.4 mA/cm² (22 °C) to 0.9 mA/cm² (50 °C), while the current densities of MEA of polysiloxane containing 9.6 wt.-% SO₃H-MCM-41 increase from 3.5 mA/cm² (23 °C) to 4.4 mA/cm² (40 °C). The cell voltage of the MEA containing 9.6 wt.-% Si-MCM-41 was in the range of 870 mV to 900 mV, and in case of the MEA containing 9.6 wt.-% SO₃H-MCM-41 in the range of 670 mV to 800 mV, in dependence of the operation temperature.

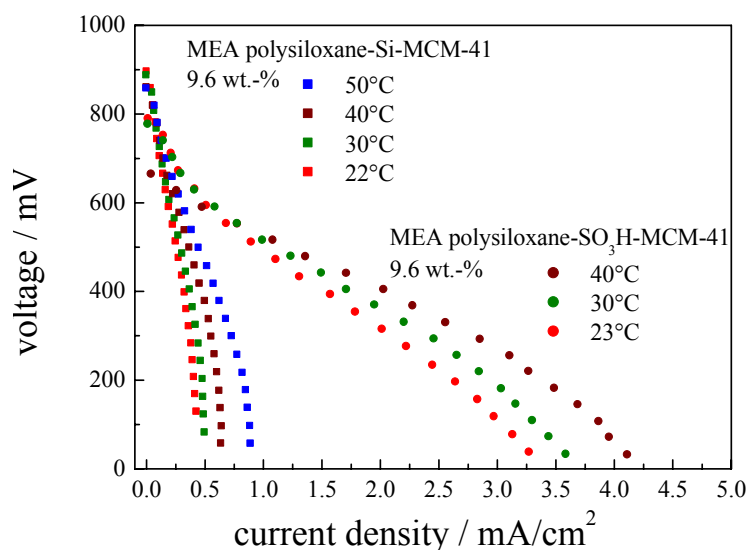


Figure 147. Polarization curves of prepared MEAs of Si-MCM-41 containing polysiloxane composite membranes.

These results clearly indicate the influence of the sulfonated Si-MCM-41 particles, which enhance the MEA performance due to an advanced proton transport in functionalized pore channels. Although MEAs based on particle-free polysiloxane membranes described elsewhere²³⁹ show a higher current density and a higher runtime, the embedding of smaller inorganic particles (like functionalized nanoparticles of Si-MCM-41, chapter 4.3.5) or particles with higher degree of conducting groups (made by co-condensation method, chapter 4.3.1) with an improved covalently attachment to the polysiloxane matrix will probably enhance the efficiency of new MEAs based on composite membranes further.

²³⁹ M. Jeske, C. Ellenberg, C. Soltmann, M. Wilhelm, D. Koch, G. Grathwohl, J. New Mater. Electrochem. Syst., special issue (2008) in press.

4.4.2 Composite membranes with polyoxadiazole

In a second approach for fabricating composite membranes with SO₃H functionalized Si-MCM-41, sulfonated polyoxadiazole was selected based on its excellent thermal and mechanical stability as well as good proton conductivity values.^{51,240}

The typical polymerization of the polyoxadiazole polymer had the following steps: initially poly(phosphoric acid) PPA was added to a flask and heated up to 100 °C under dry argon atmosphere. Then, hydrazine sulfate (HS) was added to the PPA and homogenized through stirring and heating of the reaction medium. After reaching the reaction temperature (160 °C), dicarboxylic acid 4,4'-diphenylether (DPE) was added to the flask. The molar dilution rate (PPA/HS) and the molar monomer rate (HS/DPE) were kept constant and equal to 10 and 1.2, respectively. After reaction time of 5 hours, the reaction medium was poured into tepid water (containing 5 % of sodium hydroxide), for precipitation of the polymer. The pH of this precipitation bath was controlled by addition of extra amounts of 5 % NaOH aqueous solutions.

Homogeneous membranes were cast from solutions with a polymer concentration of 4 wt.-% in Dimethyl sulfoxide (DMSO). After casting, the DMSO was evaporated in a vacuum oven at 60 °C for 24 hours. For further residual solvent removal, the membranes were immersed in water bath at 60 °C for 48 hours and dried in a vacuum oven at 60°C for 24h. The final thickness of the membranes was about 50 µm. Composite membranes were prepared by adding 2.5-10 wt.-% of functionalized Si-MCM-41 (based on polymer content) into the 4 wt.-% polymeric solution. The solution was stirred for 6 hours and cast on a glass plate at 60 °C for solvent evaporation and dried following the same protocol described for the membranes prepared only with the polymer.⁵¹ The final thickness of the membranes was in the range 30 µm. The particle distribution in the polymer can be seen in the SEM images in Figure 148. A well dispersed particle phase and no segregation were observed.

²⁴⁰ D. Gomes, J. Roeder, M. L. Ponce, S. P. Nunes, *J. Membr. Sci.* 295 (2007) 121.

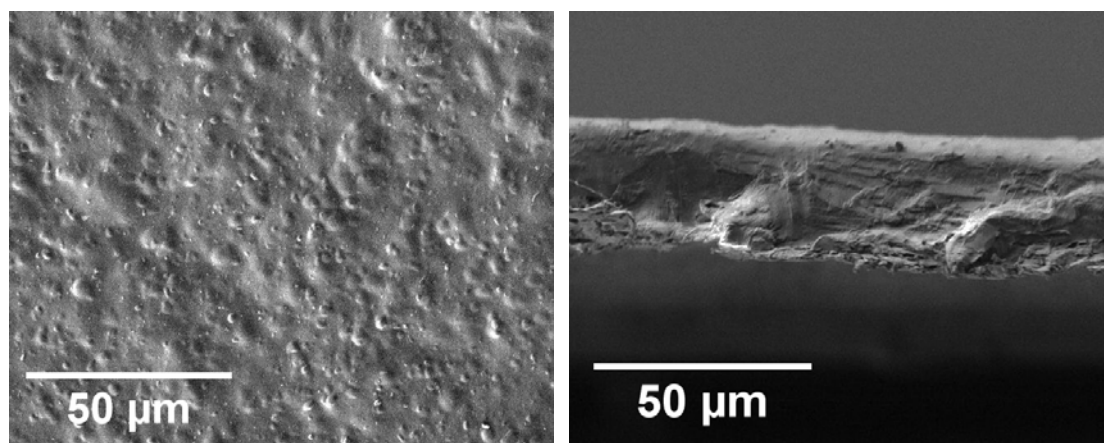


Figure 148. SEM images of polyoxadiazole-SO₃H-MCM-41 composite membrane with cross-section (right).

The ionic conductivity data at 120 °C and under 5-25 % RH of the composite membranes containing 5 wt.-% of filler are shown in Figure 149. To analyze the effect of the filler without the influence of eventual residual phosphoric acid used for converting the sulfonated membrane into its acid form, the conductivity of the membranes in sodium salt form was measured.

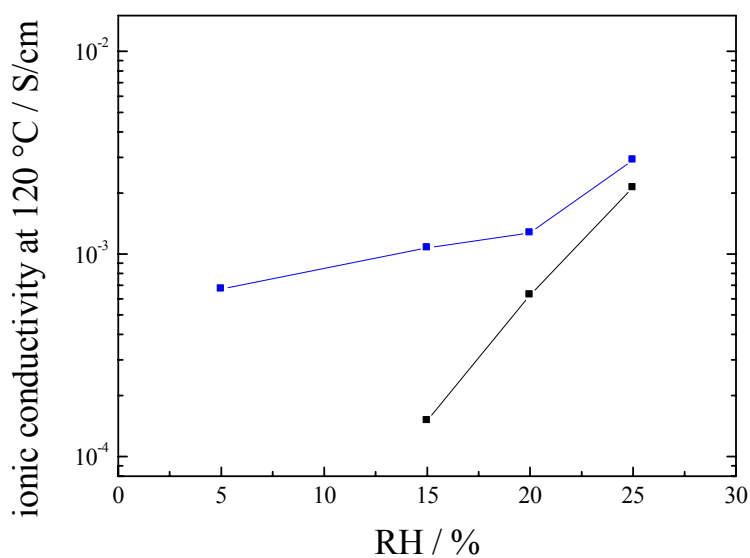


Figure 149. Ionic conductivity of pristine polyoxadiazole membrane (■) and composite membrane with SO₃H-MCM-41 (■) as a function of relative humidity measured at 120°C. The lines are only to guide the eyes and have no physical meaning.

4 Results

The composite membrane clearly has higher proton conductivity than the pristine polymer membrane in all range of RH. The significant difference between conductivity data of composite membranes and the pristine polymer membrane at low RH (e.g. 15 % RH) is a consequence of the better water retention capacity of the composite membranes due to the sulfonated mesoporous silica incorporated.

Although porous particles were incorporated into the polymer, only negligible gas permeation through the silica-polyoxadiazole composite membrane could be measured, indicating a gas tight membrane for fuel cell application also at 140 °C. This is depicted in Figure 150 in hydrogen permeation measurements. The results show that the silica particles are very good incorporated into the dense polymer matrix since the permeation values would be much higher through mesoporous particles. Thus, they support proton conductivity, but do not disturb the gas tight behavior.

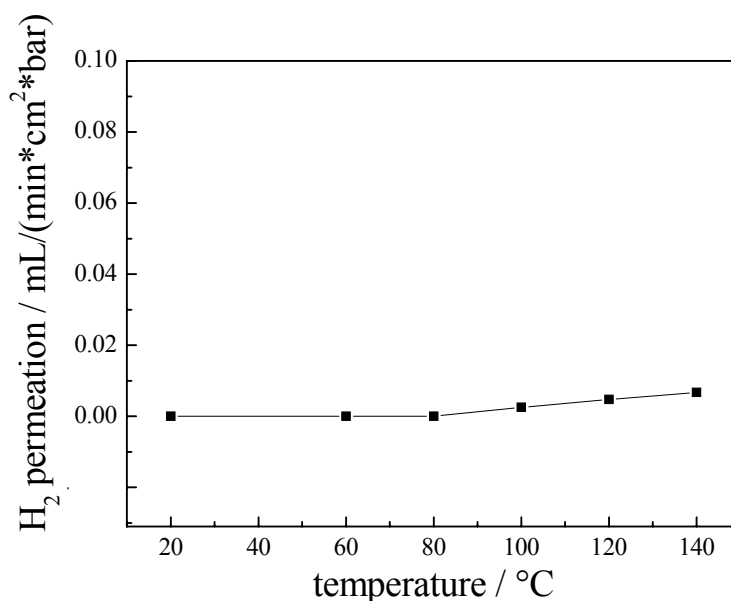


Figure 150. H₂ permeation through a functionalized silica polyoxadiazole composite membrane (5 wt.-%).

Dynamic mechanical thermal analysis (DMTA) was used for determination of glass transition temperature (T_g) and loss tangent ($\tan \delta$). $\tan \delta$, as the ratio of the dynamic loss modulus to the dynamic storage modulus, is related to the molecular motions and phase transitions. It is therefore sensitive to all molecular movement occurring in

polymers. For composites, the molecular movements at the interface contribute to the value of $\tan \delta$ that enables to determine the bonding between the interface of the matrix and the particles.²⁴¹

The T_g values of the composite membranes slightly increase with addition of sulfonated silica (Table 13), which might be caused by the hydrogen bonding between the SO_3H groups of the silica and the polyoxadiazole.

Table 13. Results of dynamic mechanical thermal analysis of polyoxadiazole-nanocomposite containing SO_3H -MCM-41.

polymer sample		
+ filler	T_g (°C)	temp. maximum of $\tan \delta$ (°C)
polymer	416	430
+2.5 wt.-%	430	450
+5 wt.-%	435	450
+10 wt.-%	420	440

Interaction between the sulfonated silica and the polyoxadiazole results in constrained polymer chains in the vicinity of the inorganic particles. The depression in $\tan \delta$ indicates the reduction of mobile chains during the glass transition,^{242,243} where the relative peak height is proportional to the volume of the constrained chains.

²⁴¹ S. Hamdan, D. M. A. Hashim, M. Yusop, *A. J. Sci. Tech. Develop.* 21 (2004) 69.

²⁴² S.-W. Chuang, S. L.-C. Hsu, Y.-H. Liu, *J. Membr. Sci.* 305 (2007) 353.

²⁴³ Y. Rao, J. M. Pochan, *Macromolecules* 40 (2007) 290.

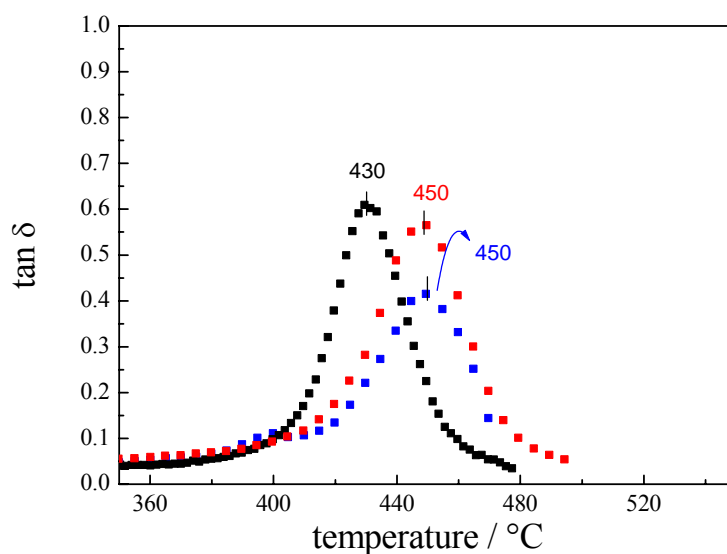


Figure 151. Trace of $\tan \delta$ vs. temperature as measured by DMTA at 1 Hz for the nanocomposite containing 2.5 wt.-% (■) or 5 wt.-% (■) sulfonated mesoporous silica, compared to the pure polymer (■).

Figure 151 clearly shows the reduction of the relative peak height of $\tan \delta$ and the increase of the T_g values with increasing amount of sulfonated Si-MCM-41. This result supports once more the very well dispersed silica particles within the polymeric matrix. On the other hand, for 10 wt.-% SO_3H -MCM-41 aggregation of the large μm -size particles leads to a decrease of mechanical properties as well as insignificant change in the T_g value.

Thermal stability of composite membranes prepared with 2.5-10 wt.-% of SO_3H -MCM-41 particles was analyzed by TGA. As shown in Figure 152, the pristine polyoxadiazole membrane shows two distinct regions of weight loss. The first loss occurs between 250 and 370 °C with an approximate weight loss of 4 % due to decomposition of SO_3H groups. The second region starting at 469 °C is associated with the loss of volatiles caused by the degradation of the polyoxadiazole.

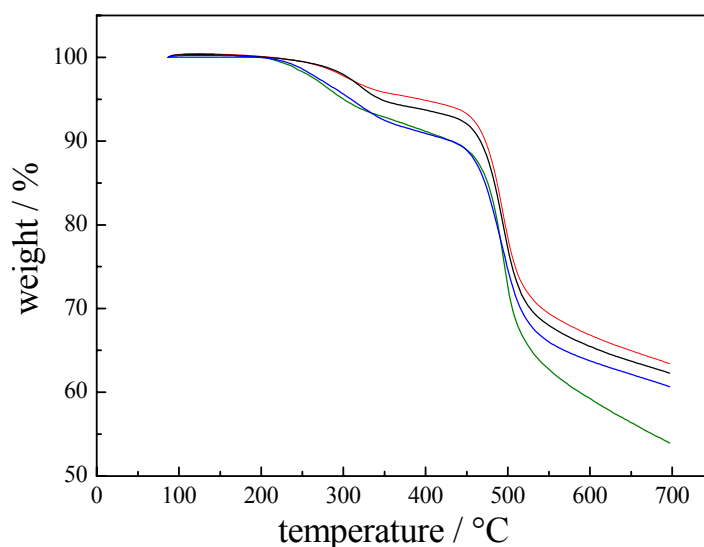


Figure 152. TGA curve for the polyoxadiazole nanocomposite membranes containing 2.5 wt.-% (red), 5 wt.-% (green) and 10 wt.-% (blue) SO₃H-MCM-41 compared to the pure polyoxadiazole (black).

The addition of 2.5 wt.-% of SO₃H-MCM-41 did not alter the degradation pattern of the pure polyoxadiazole membrane. On the other hand, from a 5 wt.-% loading of SO₃H-MCM-41 the first region of weight loss shifted toward lower temperature probably because of the weaker interaction between the sulfonic acid groups of the large mesoporous silica particles and of the polyoxadiazole chains. In conclusion, the inorganic particles improved the thermal and mechanical stability of the polyoxadiazole membranes up to 5 wt.-% incorporation, and improved the proton conductivities of pristine polymer membranes by one order of magnitude, especially at very low RHs.

4.4.3 Composite membranes with Nafion[®]

In a third approach for fabricating composite membranes with SO₃H functionalized Si-MCM-41, first experiments have been performed with Nafion[®] as proton conducting

4 Results

polymer. Pure polymer membranes and homogeneous composite membranes were cast on a glass plate having 125 °C, using a stainless steel pulling frame with defined casting slit (0.4 mm height). For composite membranes, 0.1 g of powder (pure Si-MCM-41 or SO₃H-MCM-41) were suspended in 20 mL of Nafion[®] polymer solution (DE 520, 5 wt.-% in water (~45 wt.-%)/1-propanol (~50 wt.-%)), and after 10 minutes stirring the suspension is transferred in a ZrO₂ grinding beaker. The suspension is 10 minutes treated in a ball mill for ideal particle distribution, and the resulting suspension is concentrated in a rotary evaporator to half volume before cast in the described way. After casting, the membranes were dried on the chilling glass plate, and remaining solvent was evaporated at 100 °C. For acidification of Nafion[®], the membranes were boiled one hour in H₂O₂ and H₂SO₄, respectively, followed by multiple washing with distilled water.

Figure 153 shows two SEM images of the fabricated composite membranes, using SO₃H-MCM-41 as additives. The well distributed particles in the Nafion[®] polymer can be seen in the left image (compare Si-MCM-41 particles in Figure 65). The right image clearly shows the absence of any particle segregation, which would result in an inhomogeneous proton transfer mechanism through the composite membrane, resulting in worse proton conductivity.

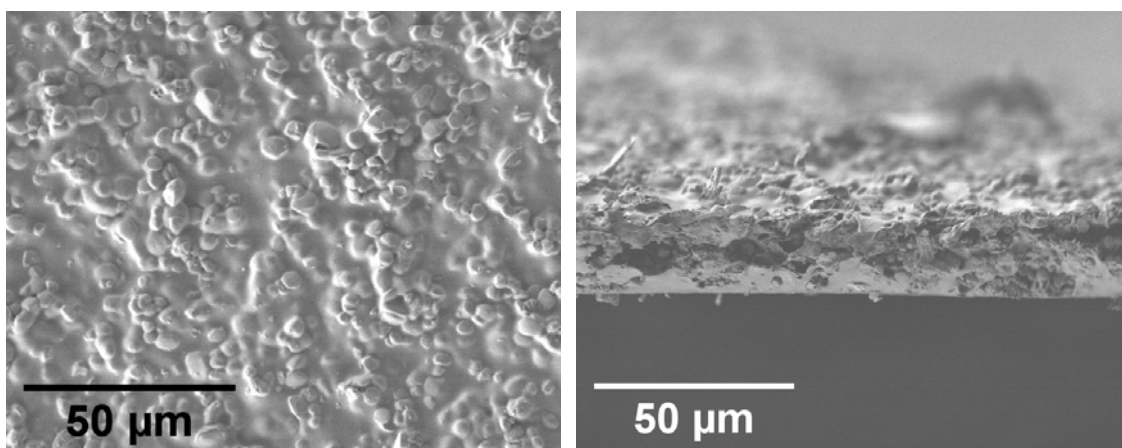


Figure 153. SEM images of composite membranes of Nafion[®] with SO₃H-MCM-41, right: cross-section of the approx. 20 μm thin composite membrane.

First proton conductivity measurements show the influence of incorporated silica particles into the Nafion[®] polymer (Figure 154). Surprisingly, a very thin (approx. 20 μm) pure Nafion[®] membrane shows a delayed conductivity drop under the given conditions of 100 % RH, due to an efficient gaseous humidification of the membrane sample in the sample holder (compare Figure 44).

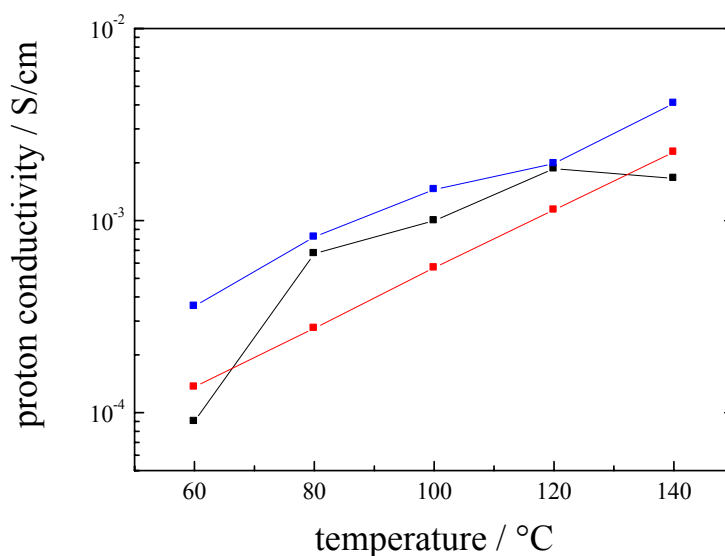


Figure 154. Proton conductivities of pure Nafion[®] (■) compared to composite membranes containing pristine Si-MCM-41 (■) and SO₃H-MCM-41 (■). The lines are only to guide the eyes and have no physical meaning.

After incorporation of pure Si-MCM-41 in the polymer matrix, the proton conductivity decreases. This leads to the assumption that the incorporation of “impurities” into Nafion[®] interrupts the polymer structure and the proton conductive domains, so the proton conductivity mechanism through the membrane is disturbed since the pure Si-MCM-41 particles are not strongly proton conductive. The unfunctionalized particles might also exhibit a worse contact between polymer and particles due to the absence of any functional moieties. This was also observed for the incorporation of the pure particles into polysiloxanes (chapter 4.4.1), and for the incorporation of TiO₂ and zeolite mordenite into Nafion[®].²³¹ The use of SO₃H functionalized Si-MCM-41 for fabrication of a composite membrane has surprisingly good influences on the proton conductivities. At low temperatures, the proton conductivity of the Nafion[®]-SO₃H-MCM-41 composite

membrane is significantly higher than for the pure Nafion[®] membrane. This is different to the effects observed with polysiloxanes (compare Figure 145), where the incorporation of the particles disturbed the intrinsic proton conductivity mechanism of the bifunctional membrane. The improved values here are possibly caused by the hydrophilic porous structure of the incorporated additives, taking up high amounts of water in their highly ordered pore structure which is necessary for good proton conductivity in Nafion[®]. Between 80 and 120 °C, the proton conductivities are quite similar, and differing again at 140 °C. For Nafion[®], the typical conductivity drop takes place, but to less extent than shown in Figure 94. The Nafion[®] membrane used here is much thinner (20 µm compared to 1 mm), and therefore the good humidification in the measurement cell ensures a lower water loss at elevated temperatures (120 °C). For the Nafion[®]-SO₃H-MCM-41 composite membrane the proton conductivity continuously increases, similar to the pure powders (compare chapter 4.2.2). The incorporated powder samples help to keep the water inside the composite membranes, so that the water loss of the Nafion[®] matrix has less effect on the overall proton conductivity. The retained water helps to ensure the proton transport through the fabricated composite membrane.

Changing the membrane thickness and particle content will give further insight into this composite system together with thermal analysis, H₂ permeation and water uptake measurements.

4.4.4 Summary of composite membranes containing SO₃H functionalized Si-MCM-41 particles

Incorporation of SO₃H-functionalized Si-MCM-41 particles into proton conductive polymers led in all three cases (polysiloxane, polyoxadiazole and Nafion[®]) to improved properties in the fabricated resulting composite membranes. A well dispersed particle phase is therefore very important for high conductivity and gas tightness, and the porous structure of the incorporated solid proton conductors turned out to be advantageous for water retention, facilitating the proton transport in the cast composite membranes. Together with bifunctional polysiloxane polymer, efficient composite membranes could be achieved working at temperatures of 180 °C and only 5 % RH. For the first time, MEAs with these new inorganic solid proton conductors as additives in polymers could be fabricated and tested.

Composite membranes with polyoxadiazoles also turned out to be improved in conductivity by incorporation of SO₃H functionalized Si-MCM-41 into the polymer. It was also shown that especially the mechanical stabilities of the composite membranes increased with incorporation of the additives, and no significant gas permeation could be observed.

First experiments on composite membranes with Nafion[®] also show improved properties if SO₃H-MCM-41 is incorporated into the polymer matrix.

However, incorporation of too many or unfunctionalized inorganic additives turned out to be disadvantageous for proton conductivity of the composite membranes, as the additives disturb the proton transport in the proton conductive polymer matrix. The imperfect proton transfer between particle and polymer matrix is an occurring problem which can only be prevented by homogeneous distribution of strongly interacting particles. Especially the use of functionalized solid proton conductors is therefore of significant advantage compared to unfunctionalized particles. But still there is always a need to find the perfect ratio between polymer and inorganic additive for every composite system.

5 Conclusion

In the present work, the synthesis of new solid proton conductors based on mesoporous silica materials and their use in composite membranes for HT-PEMFC membranes was discussed. To enable proton conductivity in the silica host systems, the powders were functionalized with proton conductive organic functionalities, namely SO_3H , PO_2H_3 and imidazole. This was fulfilled by two different synthesis methods, the post-synthetic grafting procedure or in-situ co-condensation procedure, to achieve different degrees of loading with the protogenic groups. The resulting solid proton conductors were tested concerning their solid proton conductivity properties, and subsequently incorporated into different proton conductive polymers (polysiloxane, polyoxadiazole and Nafion[®]) to fabricate composite membranes and, for the first time, MEAs with these novel solid proton conductors.

The focus of this work clearly lay on the synthesis of the mesoporous silica based proton conductors. Three types of mesoporous silica host materials have been used to synthesize the solid proton conductors. By using different amphiphilic molecules and their self-organization to supramolecular aggregates (micelles and liquid crystal phases) in aqueous media, different pore systems could be achieved in the mesoporous silica hosts. Mesoporous Si-MCM-41 was prepared using CTAB and sodium metasilicate, exhibiting hexagonally ordered mesopores in the range of 3 nm and particle sizes of 1-2 μm (chapter 4.1.1). Si-MCM-41 could also be synthesized in nanoparticles of 100 nm size (chapter 4.1.4).

5 Conclusion

Si-SBA-15 and Si-SBA-16 are mesoporous silica prepared using triblock-copolymers as amphiphilic molecule. Both exhibit larger pores than Si-MCM-41, Si-SBA-15 was synthesized with ~ 7 nm hexagonally ordered mesopores, and Si-SBA-16 had a cubic pore arrangement with ~ 6 nm cages connected via 4 nm pore channels. Both materials were synthesized in 1-2 μm particles sizes (chapter 4.1.2 and 4.1.3).

The different pore systems of the silica hosts turned out to be important for the proton conductivity properties of the solid proton conductors. When mesoporous silica hosts were functionalized with SO_3H groups via grafting reaction, it could be shown that the hexagonal pore arrangement of Si-MCM-41 and Si-SBA-15 showed higher proton conductivities, due to the better guidance of protons through the pore system compared to the cubic and non-directing pore system of Si-SBA-16. Additionally, the small pore diameter of Si-MCM-41 (~ 3 nm) turned out to be crucial for high proton conductivity, since the grafted SO_3H groups are closer to each other than in the 7 nm pores of Si-SBA-15, exhibiting higher proton conductivities. The proton transport occurs via the grafted SO_3H groups supported by additional water molecules in a Grotthuss-like mechanism, which is taking place in the pore system (chapter 4.2.2). Si-MCM-41 was then exclusively used for further investigations due to these results.

SO_3H groups have many properties making them very suitable for proton conductivity, especially their high capability for water storage (chapter 4.2.1). As these acidic systems provide a lot of intrinsic charge carriers, they showed much higher proton conductivities than the grafted imidazole systems (chapter 4.2.6), having no intrinsic charge carriers. Imidazole anchorage via grafting was performed in this work via three methods to compare the type of anchorage and the spacer length. It turned out that an imidazole binding via nitrogen atom is far too inefficient for proton conductivity as anchorage via C_1 atom (C-atom between the nitrogen atoms, chapter 4.2.3). Imidazole anchorage via peptide bond between imidazole-2-carboxylic acid and amine-grafted Si-MCM-41 was therefore more efficient, only being one order of magnitude lower in proton conductivity than SO_3H grafted Si-MCM-41. However, the spacer length between silica host and the imidazole groups was here 5 atoms (compared to propyl-chain for SO_3H grafting), having a strong influence on the proton conductivity due to better mobility in

the spacer chain. This could also clearly be seen when imidazole was in-situ formed with aldehyde grafted Si-MCM-41 using ammonia and glyoxal (chapter 4.2.5). Here, the chain length was identical with the SO₃H functionalized material, but the proton conductivity values for the imidazole grafted samples were much lower. This was also caused by lower loading due to a hindered diffusion of the reactants necessary for the imidazole formation into the pore system.

As Si-MCM-41 showed the best results of the silica hosts, co-condensation reactions were applied to synthesize Si-MCM-41 with higher loadings of e.g. SO₃H groups. This aim could be reached by co-condensation with MPMS, and subsequent treatment in a microwave oven, where template removal and SH oxidation to SO₃H groups could be performed simultaneously. The resulting materials still showed the porous structure with improved higher group loading (up to 2.3 mmol/g) and outstanding proton conductivity values up to 0.2 S/cm for 40 % co-condensed SO₃H-MCM-41 material (chapter 4.3.1). This is in accordance to performed theoretical simulations, showing that higher group density leads to higher proton conductivity values caused by more homogeneous distribution of the SO₃H groups via co-condensation. Co-condensation reactions performed to enable PO₃H₂ showed that these groups, due to the lower acidity of the system, exhibit much lower proton conductivity values than the SO₃H functionalized silica (chapter 4.3.2). Imidazole functionalization (via co-condensation with aldehyde functions and subsequent *in-situ* formation) exhibited even lower proton conductivities than the grafted imidazole-MCM-41 samples, due to pore blocking after co-condensation for the imidazole-forming reactants (chapter 4.3.3).

An outstanding result of this work is the synthesis of SO₃H functionalized Si-MCM-41 nanoparticles via co-condensation approach. Applying a pre-hydrolysis step in the synthesis, the highly ordered hexagonal pore structure could be retained during synthesis, incorporating the SO₃H groups during particle growth. Due to this ordering and better accessible pore structure due to higher external surface, the proton conductivities of these SO₃H-MCM-41 nanoparticles even exceeded their μm-sized counterparts.

5 Conclusion

It has to be mentioned that the proton conductivities of the synthesized powders were measured between 60 and 140 °C, and under 0, 50 and 100 % RH, and the proton conductivities increased for all prepared samples continuously with temperature, which in complete contrast to Nafion[®] membranes, which show a reported conductivity drop above 100 °C.

SO₃H functionalized Si-MCM-41 particles, since they showed the most promising values, were finally incorporated and well dispersed into three different polymers, where they improved clearly the properties of the pure proton conductive polymers. Together with polysiloxanes, composite membranes could be fabricated working at 180 °C and 5 % RH, showing proton conductivity values much higher than Nafion[®] at these industrial interesting working conditions. Also an increased water uptake and mechanical stability of the membranes was observed after particle incorporation. Non-functionalized Si-MCM-41 particles therefore showed worse properties. It was also possible to prepare for the first time MEAs with these systems (chapter 4.4.1), where the SO₃H functionalized composite again showed better results than composite membranes with unfunctionalized Si-MCM-41.

With polyoxadiazoles, composite membranes with SO₃H-MCM-41 could also be prepared and characterized. It was shown that the composite membranes have higher conductivity values than the pure polymers, and H₂ permeation tests proved the gas tightness of the composite membranes, although porous particles have been incorporated (chapter 4.4.2).

Finally, Nafion[®]-SO₃H-MCM-41 composite were prepared, indicating that thin Nafion[®] membranes shows smaller conductivity drop above 100 °C than pure Nafion[®], and that this material can also be improved by incorporation of solid proton conductor particles (chapter 4.4.3).

As up to now only grafted SO₃H-MCM-41 particles were used for composite membrane casting, the next steps would be the use of the co-condensed SO₃H-MCM-41 particles or nanoparticles, as these solid proton conductors showed even higher proton conductivity values. The detailed study of influences on the composite membrane properties (water uptake, thermal stability, gas permeation, proton conductivity) by

membrane thickness and particle content is of high importance for understanding these hybrid systems. Especially the water uptake is very relevant during fabrication of new MEAs with other polymers than polysiloxanes, since during MEA working conditions, the produced product water can be retained by the incorporated mesoporous solid proton conductors, using it for proton transport even at elevated temperatures.

Also the synthesis of silica (nano-) particles with imidazole functionalities is in the focus of research, as the incorporation of small amount of SO₃H groups to prepare mixed systems might overcome the problem of low charge carrier concentration in pure imidazole systems.

Finally, a variation of the host lattice to aluminum-incorporated Si-MCM-41 is interesting, as this incorporation of Al introduces acid sites and thereby even higher hydrophilicity of the host as pure Si-MCM-41, which might be favorable for higher proton conductivities after functionalization. First results showed an even higher water uptake of Al-MCM-41 than Si-MCM-41, up to 90 wt.-%, and higher proton conductivities than the pure Si-MCM-41. Functionalization of this material with proton conductive groups will be interesting and part of further investigations.

Appendix

A Abbreviations and Symbols

°	degree
μm	micrometer
A	Ampere
Å	Ångström (10^{-10} m)
a.u.	arbitrary units
a_0	lattice constant
AC	alternate current
AFC	Alkaline Fuel Cell
approx.	approximately
APTES	3-Aminopropyl triethoxysilane
APU	Auxiliary Power Unit
as-syn	as synthesized
BET	Brunauer-Emmet-Teller adsorption isotherm
BJH	Barret-Joyner-Halenda adsorption isotherm
C	capacity
C	Celsius
calc	calcined
CHO	aldehyde
CHP	Combined heat and power plant
CITMS	3-Chloropropyl triethoxysilane
c	centi (10^{-2})
cmc	critical micelle concentration
conc.	concentrated
cos	cosinus

Appendix

CTAB	cetyltrimethylammonium bromide
d	distance between lattice layers
DCC	dicyclohexyl carbdiamide
DCM	dichloromethane
DFT	density-functional theory
DFTB	density-functional tight-binding
DMFC	Direct Methanol Fuel Cell
DMSO	dimethyl sulfoxide
DMTA	dynamic mechanical thermal analysis
DPE	dicarboxylic acid 4,4'-diphenylether
DPTES	Diethylphosphatopropyl triethoxysilane
DTA	differential thermoanalysis
e ⁻	electron
E _a	activation energy
EDXS	energy-dispersive X-ray spectroscopy
EELS	electron energy-loss spectroscopy
E _{kin}	kinetic energy
EO	ethylene oxide
E _{pot}	potential energy
Eq	equation
et al.	et altera, lat: and others
eV	electron volt
extr	extracted
f	frequency
F127	a triblock copolymer
FFT	fast Fourier transformation
FT	Fourier-transform
g	gram
GDL	Gas Diffusion Layer
h	hour
<i>h</i>	Planck constant
hkl	Miller indices
HPA	heteropolyacid
HRTEM	high resolution TEM
HS	hydrazine sulfate
HT-PEMFC	High Temperature Polymer Electrolyte Membrane Fuel Cell
Hz	Hertz
I	current
IEC	ion exchange capacity
in-situ	lat.: local, in place
IR	infrared
IS	impedance spectroscopy
IUPAC	International Union of Pure and Applied Chemistry
J	Joule

K	kilo (10^3)
K	Kelvin
kcal	kilocalories
km	kilometer
L	induction
l	length
m	meter
m	milli (10^{-3})
M	molar, mol/L
M41S	class of mesoporous materials
MAS	magic angle spinning
MCFC	Molten Carbonate Fuel Cell
MCM	Mobile Composition of Matter
MD	molecular dynamics
m_e	mass of an electron
MEA	Membrane Electrode Assembly
MHz	megahertz
min	minute
mL	milliliter
mm	millimeter
mol	mole
MPMS	3-mercaptoproyl trimethoxysilane
mw	microwave
N	Newton
NASA	National Aeronautics and Space Administration
nm	nanometer
NMR	Nuclear Magnetic Resonance
p	momentum
P	power
p	saturation pressure
P123	a triblock copolymer
PAFC	Phosphoric Acid Fuel Cell
PEM	Polymer Electrolyte Membrane
PEMFC	Polymer Electrolyte Membrane Fuel Cell
Pep	peptide
pm	picometer
PMO	periodic mesoporous organosilica
PO	propylene oxide
PO_3H_2	phosphonic acid
PPA	polyphosphoric acid
ppm	parts per million
ps	picosecond
Pt	platinum
PTFE	polytetrafluorethylen (Teflon)

Appendix

R	resistance
RDF	radial distribution function
RH	relative humidity
RT	room temperature
s	second
S	Siemens
SBA	University of Santa Barbara
S _{BET}	surface area calculated via BET
SDA	structure directing agent
sDPDMS	sulfonated diphenyldimethoxysilane
sDPS-DMS	sulfonated diphenylsiloxane-dimethylsiloxane
SDS	sodium dodecylsulfate
SEM	scanning electron microscope
SH	thiol
sin	sinus
SLC	silicatropic liquid crystal
SO ₃ H	sulfonic acid
SOFC	Solid Oxide Fuel Cell
SPEEK	sulfonated polyetheretherketone
sPETMS	sulfonated 2-phenylethyl trimethoxysilane
SPSU	sulfonated polysulfone
T	temperature
t	time
tan δ	loss tangent
TEM	transmission electron microscope
TEOS	tetraethyl orthosilicate
TEOSPBA	triethoxysilylpropylbenzimidazole-5-amide
TESBA	triethoxysilyl butyraldehyde
T _g	glass transition temperature
TGA	thermogravimetric analysis
TLCT	True Liquid Crystal Template mechanism
U	voltage, potential
US	United States
v	velocity
V	volt
V	volume
W	Watt
wt.	weight
X _C	capacitive resistance
X _L	inductive resistance
XRD	X-ray diffraction
Y:ZrO ₂	yttrium-stabilized zirconium oxide
Z	impedance
$\Delta_f H^0$	standard formation enthalpy

$\Delta_R G^0$	free standard reaction enthalpy
$\Delta_R S^0$	standard reaction entropy
η	efficiency
φ	phase shift
λ	wavelength
ω	angular frequency
θ	diffraction angle

B Table of figures

Figure 1. Scheme of the first fuel cell developed by Sir William Grove. ²⁶	7
Figure 2. Different fuel cell types for comparison. ³¹	10
Figure 3. Working principle of a PEMFC single cell. ²⁸	13
Figure 4. Detailed cross section of a MEA. ³⁴	13
Figure 5. PEMFC stack with construction elements. ²⁸	15
Figure 6. Energy conversions in a Carnot or fuel cell process.	17
Figure 7. Ideal efficiencies of a hydrogen-oxygen fuel cell against the Carnot efficiency. ³⁸	18
Figure 8. Voltage losses in fuel cell operation due to electrode kinetics. Resulting polarization curve in red. ³⁹	19
Figure 9. Nafion and SPEEK membranes with their nanodomains. ⁴¹	22
Figure 10. Structural unit of sulfonated polysulfone (SPSU). ⁴⁷	23
Figure 11. Ideal structure of functionalized polysiloxane. ⁴⁹	24
Figure 12. Structural unit of sulfonated polyoxadiazole. ⁵¹	24
Figure 13. Polymer chains of sulfonated polyoxadiazoles including incorporated water. white: hydrogen, red: oxygen, dark blue: nitrogen, light blue: carbon, yellow: sulfur. ⁵¹	25
Figure 14. Random-cluster-network model. ⁴²	26
Figure 15. Surface conductivity mechanism in solid acid membranes. ⁵⁵ Water molecules are colored (oxygen: blue, hydrogen: red).	27
Figure 16. Grotthuss mechanism.	27
Figure 17. Zündel- and Eigen-ion. ⁵⁷	28
Figure 18. Proton transfer from Eigen-ion over Zündel-ion to Eigen-ion. Charged oxygen atoms are yellow. ⁶⁰	28
Figure 19. Imidazole resonance-stabilization. ⁶³	29
Figure 20. Proton transport in composite membranes. ⁵⁵ Additives are shown as green balls, water molecules colored in blue (oxygen) and red (hydrogen).	30
Figure 21. Micelle formation in different media. ⁷⁴	34

Figure 22. Surfactants with different chemical head groups. ⁷⁴	35
Figure 23. Triblock-copolymers P123 und F127. ⁷⁶	36
Figure 24. Phase diagram for the binary system CTAB in water. ⁷⁹	38
Figure 25. Pore widths and pore size distribution of nanoporous materials. ⁸⁸	41
Figure 26. Si-MCM-41 structure model with incorporated surfactants (taken from Ref. 89).	41
Figure 27. TEM-micrograph of Si-MCM-41. ²³	42
Figure 28. Scheme of hexagonally shaped pore in Si-MCM-41 with structural indices.	42
Figure 29. Si-MCM-48 and Si-MCM-50 structures as host-guest-composites with incorporated surfactant (taken from Ref. 89)	45
Figure 30. Hexagonal pore structure scheme of Si-SBA-15 with interconnecting micropores. ¹¹⁵	45
Figure 31. Structure model of cavities and their interconnection in Si-SBA-16. ¹¹⁶	46
Figure 32. Formation of a mesoporous silica structure via TLCT mechanism. ²⁴	47
Figure 33. Two model for the cooperative self-organization process. ¹²¹	48
Figure 34. Formation of a silicatropic liquid crystal (SLC) phase. ¹²²	49
Figure 35. Possible synthetic routes with surfactant and inorganic species. ²⁴	51
Figure 36. Types of silanol groups on a silica particle surface. ¹³³	53
Figure 37. Two different pore diameters leading to different surface curvatures. ¹³⁷ ...	54
Figure 38. Possible surface silylation reactions. ¹³⁹	56
Figure 39. The impedance plotted as a planar vector, with polar or rectangular coordinates. ²⁰¹	64
Figure 40. Ideal Nyquist plot with corresponding equivalent circuit. ²⁰¹	65
Figure 41. Ideal Nyquist plot with Warburg-straight. ²⁰¹	66
Figure 42. Typical measured Bode diagram, impedance (□) and phase shift (●).	67
Figure 43. XRD patterns of Si-MCM-41 (compare chapter 4.1.1) before (black) and after (red) pressing to pellets.	68
Figure 44. Scheme of the water vapor conductivity cell. ²⁰²	69
Figure 45. HTZ200 conductivity cell from University of Bremen. ²⁰³	70
Figure 46. Classes of adsorption isotherms. ²⁰⁷	75
Figure 47. Possible interactions between the incident beam and the sample. ²¹³	80
Figure 48. Course of beam in SEM and TEM. ²¹³	81
Figure 49. Principle of EDXS. ²¹³	83
Figure 50. Principle of thermogravimetric analysis TGA. ²¹⁴	85
Figure 51. Grafting reaction with surface silanol groups. ²⁴	91
Figure 52. Principle of co-condensation, exemplarily with MPMS. ²⁰³	93
Figure 53. Oxidation of surface SH groups to SO ₃ H groups. ¹⁹⁷	95
Figure 54. Peptide bond formation for imidazole anchorage. ¹⁶⁴	96
Figure 55. Mechanism forming a peptide bond between imidazole-2-carboxylic acid and surface-bond amine using DCC. ²²⁰	97
Figure 56. In-situ imidazole formation reaction. ⁶²	98
Figure 57. Formation of an N,N-acetale of a surface-bond aldehyde with ammonia. ²²¹	98

Figure 58. Condensation reaction of a nitrogen-nucleophile with a carbonyl resulting in an aldimine. ²²¹	99
Figure 59. Imidazole ring formation. ²²¹	99
Figure 60. N-imidazole anchorage reaction. ¹⁴⁸	100
Figure 61. Phosphonic acid formation. ²²²	101
Figure 62. X-ray powder pattern of calcined Si-MCM-41.	104
Figure 63. N ₂ sorption isotherm for synthesized Si-MCM-41.	104
Figure 64. Pore size distribution of synthesized Si-MCM-41.	105
Figure 65. SEM image of synthesized Si-MCM-41.	106
Figure 66. TEM micrograph showing the pores of synthesized Si-MCM-41.	107
Figure 67. XRDs showing the effect of the detemplation method on Si-MCM-41. Template containing Si-MCM-41 (black), after calcination (red), after ethanol/HCl extraction (green), after ion exchange with NH ₄ NO ₃ (bright blue), after microwave extraction (dark blue).....	107
Figure 68. SEM image of Si-SBA-15.	109
Figure 69. X-ray powder pattern of calcined Si-SBA-15.	110
Figure 70. N ₂ sorption isotherm for synthesized Si-SBA-15.	110
Figure 71. Pore size distribution of synthesized Si-SBA-15.	111
Figure 72. TEM micrograph of synthesized Si-SBA-15.	112
Figure 73. SEM image of synthesized Si-SBA-16.	113
Figure 74. XRD pattern of Si-SBA-16.	114
Figure 75. N ₂ sorption isotherm of synthesized Si-SBA-16.	115
Figure 76. Cage diameter of Si-SBA-16 estimated from nitrogen adsorption.	116
Figure 77. XRD pattern of synthesized nano-Si-MCM-41.	117
Figure 78. N ₂ sorption isotherm for synthesized nano-Si-MCM-41.	118
Figure 79. Pore size distribution of synthesized nano-Si-MCM-41.	119
Figure 80. SEM and (HR)TEM images of synthesized nano-Si-MCM-41.	119
Figure 81. IR spectra of mesoporous silica (black line) and SH functionalized silica (dotted line).	122
Figure 82. XRDs for SH-MCM-41 with decreasing intensities for pristine Si-MCM-41 (black) and SH functionalized Si-MCM-41 after 5 mmol (dotted), 10 mmol (red) and 20 mmol (blue) grafting.....	123
Figure 83. N ₂ adsorption isotherms for pristine Si-MCM-41 (■) and SH functionalized Si-MCM-41 after 5 mmol (□), 10 mmol (■) and 20 mmol (■) grafting.	124
Figure 84. IR spectra of pure Si-MCM-41 (black line), SH-MCM-41 (dotted line) and SO ₃ H-MCM-41 (dashed line).....	125
Figure 85. TGA (black line) and DTA (dashed line) of SO ₃ H-MCM-41 after 20 mmol/g grafting with MPMS and subsequent oxidation.	126
Figure 86. Water uptake of pristine Si-MCM-41 (■), SH-MCM-41 (○) and SO ₃ H- MCM-41 (■) after 20 mmol/g grafting and oxidation.....	127
Figure 87. Proton conductivities at 100 % RH of SO ₃ H-MCM-41 (□), SO ₃ H-SBA-15 (○) and SO ₃ H-SBA-16 (Δ) after 5 mmol/g grafting and oxidation. The lines are only to guide the eyes and have no physical meaning.....	129

- Figure 88.** Proton conductivities at 100 % RH of SO₃H-MCM-41 (■), SO₃H-SBA-15 (●) and SO₃H-SBA-16 (▲) after 20 mmol/g grafting. The lines are only to guide the eyes and have no physical meaning. 131
- Figure 89.** Model of the situation inside a pore of Si-MCM-41 after grafting and oxidation. carbon (blue), oxygen (red), hydrogen (white), sulfur (yellow). Pore diameter and chains sizes are in the correct relation. 132
- Figure 90.** Proton conductivities for SO₃H-MCM-41 0mmol100 (■), 5mmol100 (□), 10mmol100 (■) and 20mmol100 (■). The lines are only to guide the eyes and have no physical meaning. 133
- Figure 91.** Arrhenius plots for SO₃H-MCM-41 0mmol100 (■), 5mmol100 (□), 10mmol100 (■) and 20mmol100 (■) with additional fitting line for calculation of the given activation energies. 134
- Figure 92.** Proton conductivities for 20mmol0 SO₃H-MCM-41 (□), 20mmol50 (■), 20mmol100 (○) and 20mmol100 2nd (●).The lines are only to guide the eyes and have no physical meaning. 135
- Figure 93.** Energy barrier plot for the proton transfer between oxygen atoms belonging to two methyl SO₃H molecules (inset). ▼ (DFTB), Δ (DFT), □ represent the curve for the case with 1 water molecule in between the two methyl SO₃H molecules calculated via DFTB. 137
- Figure 94.** Proton conductivities for SO₃H-MCM-41 0mmol100 (■), 5mmol100 (□), 10mmol100 (■) and 20mmol100 (■) compared to Nafion (□) running dry. The lines are only to guide the eyes and have no physical meaning. 138
- Figure 95.** Enhancement of proton conductivity of SO₃H-MCM-41 by more offered MPMS (□). Increasing IECs are shown additionally (●). The lines are only to guide the eyes and have no physical meaning. 139
- Figure 96.** IR spectra of pure Si-MCM-41 (black line) and Cl functionalized Si-MCM-41 (dotted line). 140
- Figure 97.** XRDs for Cl-MCM-41 with decreasing intensities. Pure Si-MCM-41 (black), 5 mmol (dotted), 10 mmol (red), 20 mmol (blue)..... 141
- Figure 98.** N₂ adsorption isotherms for pristine Si-MCM-41 (■) and Cl functionalized Si-MCM-41 with 5 mmol (□), 10 mmol (■) and 20 mmol (■) CITMS. 142
- Figure 99** IR spectra of pure Si-MCM-41 (black line), Cl-MCM-41 (dotted) and N-imidazole-MCM-41 (dashed). 143
- Figure 100.** Proton conductivities for different N-imidazole-MCM-41 at 100 % RH. 5 mmol (□), 10 mmol (■), 20 mmol (■) compared to pristine Si-MCM-41 (■) 0 mmol. The lines are only to guide the eyes and have no physical meaning. 143
- Figure 101.** Proton hopping in N-imidazole systems. 144
- Figure 102.** IR spectra of pristine Si-MCM-41 (black line) compared to NH₂-MCM-41 (grey) and peptide-imidazole-MCM-41 (dotted line) after 20 mmol grafting and peptide bond formation. The imidazole-spectrum is enlarged for better signal observation. 145
- Figure 103.** XRDs for peptide-imidazole-MCM-41 with decreasing intensities. Pure Si-MCM-41 (black), 5 mmol (dotted), 10 mmol (red), 20 mmol (blue)..... 146

- Figure 104.** N₂ adsorption isotherms for pristine Si-MCM-41 (■) compared to peptide-imidazole functionalized Si-MCM-41 after 5 mmol (□), 10 mmol (■) and 20 mmol (■) grafting with APTES followed by peptide bond formation. 147
- Figure 105.** Proton conductivities for different peptide-imidazole-MCM-41 at 100 % RH. 5 mmol (□), 10 mmol (■), 20 mmol (■) compared to pristine Si-MCM-41 (■) 0 mmol. The lines are only to guide the eyes and have no physical meaning. 148
- Figure 106.** IR spectra of pristine Si-MCM-41 (black line) compared to CHO-MCM-41 (grey) and imidazole-MCM-41 (dotted line) after 20 mmol TESBA grafting and in-situ imidazole formation. 150
- Figure 107.** XRDs for imidazole-MCM-41 with decreasing intensities. Pure Si-MCM-41 (black), 10 mmol (red), 20 mmol (blue). 151
- Figure 108.** N₂ adsorption isotherms for pristine Si-MCM-41 (■) compared to aldehyde functionalized Si-MCM-41 after 10 mmol (■) and 20 mmol (■) grafting with TESBA. 152
- Figure 109.** Proton conductivities for different imidazole-MCM-41 at 100 % RH, 10 mmol (■), 20 mmol (■) compared to pristine Si-MCM-41 (■) 0 mmol. The lines are only to guide the eyes and have no physical meaning. 153
- Figure 110.** Maximum proton conductivities (□) and IECs (●) of imidazole functionalized Si-MCM-41 depending on the amount of TESBA offered in the grafting step. 154
- Figure 111.** Proton conductivities for different imidazole-MCM-41 at 50 % RH, 10 mmol (■), 20 mmol (■). The lines are only to guide the eyes and have no physical meaning. 155
- Figure 112.** Proton conductivities of functionalized Si-MCM-41 at 100 % RH and 20 mmol grafting with (Δ) N-imidazole, (▼) peptide-imidazole, (*) imidazole and (○) SO₃H groups, compared to pristine Si-MCM-41 (■). The lines are only to guide the eyes and have no physical meaning. 156
- Figure 113.** DTA curves, normalized by the largest signal. 20% SH-MCM-41-extr (black); 20% SO₃H-MCM-41-mw (red); 30% SO₃H-MCM-41-mw (green); 40% SO₃H-MCM-41-mw (blue). 159
- Figure 114.** Nitrogen adsorption isotherms on the pristine Si-MCM-41 (■) and on functionalized samples 20 (■), 30 (■) and 40 % (■) SO₃H-MCM-41-mw. 160
- Figure 115.** Schematic picture of a pore of 40 % SO₃H-MCM-41-mw, atoms: carbon (blue), oxygen (red), hydrogen (white), sulfur (yellow). Pore diameter and chain sizes are shown in the correct relation. 161
- Figure 116.** XRDs for 20 % (red) and (blue) 40 % SO₃H-MCM-41-mw samples, and for calcined 20 % (red dotted) and 40 % (blue dotted) SO₃H-MCM-41-calc samples. 162
- Figure 117.** TEM images of 40 % SO₃H-MCM-41-mw. 163
- Figure 118.** SEM picture of 20 % SO₃H-MCM-41-mw (upper left) and EDX mapping for oxygen (upper right), silicon (middle right) and sulfur (lower right). The EDX spectrum (lower left) was performed over the whole sample, the carbon signal results from the graphite slice from sample preparation. 164

- Figure 119.** Proton conductivity measured at 100 % RH for 0 % (■), 20 % (■), 30 % (■) and 40 % (■) SO₃H-MCM-41-mw compared to 20 mmol grafted SO₃H-MCM-41(□). The lines are only to guide the eyes and have no physical meaning. 165
- Figure 120.** Illustration of the environment inside the pores of Si-MCM-41 after functionalization with SO₃H groups. 3-A: after co-condensation, 3-B: after grafting. Atoms: carbon (blue), oxygen (red), hydrogen (white), sulfur (yellow). Pore diameters and chain sizes are shown in the correct relation. 166
- Figure 121.** Arrhenius plots for 20 % (■), 30 % (■) and 40 % (■) SO₃H-MCM-41-mw with additional fitting line for calculation of the given activation energies. 167
- Figure 122.** Dependence of proton conductivity for 40% SO₃H-MCM-41 on the relative humidity (0% (□), 50% (■), 100% (■)) in the measurement cell. The lines are only to guide the eyes and have no physical meaning. 168
- Figure 123.** Radial distribution functions for the distances between oxygen donor atom and oxygen acceptor atoms for different densities of conducting groups per area at T = 400 K. Red line (1 group/nm²), green line (2.04 groups/nm²) and blue line (4 group/nm²). 169
- Figure 124.** IR spectra of phosphonic acid diethyl ester (black line) and phosphonic acid functionalized Si-MCM-41 (dotted) prepared via co-condensation, extraction and HCl transformation. 171
- Figure 125.** XRD patterns of 20 % (red) and 30 % (green) PO₃H₂-MCM-41 compared to pure Si-MCM-41. 171
- Figure 126.** Proton conductivity measured at 100 % RH for 20 % (■) and 30 % (■) PO₃H₂-MCM-41 compared to pure Si-MCM-41 (■). The lines are only to guide the eyes and have no physical meaning. 172
- Figure 127.** XRD patterns of 20 % (red), 30 % (green) and 40 % (blue) imidazole-MCM-41 compared to pristine Si-MCM-41. 174
- Figure 128.** Nitrogen adsorption isotherms of functionalized samples 20 (■), 30 (■) and 40 % (■) CHO-MCM-41. 175
- Figure 129.** Proton conductivity measured at 100 % RH for 20 % (■), 30 (■) and 40 % (■) imidazole-MCM-41 compared to pure Si-MCM-41 (■). The lines are only to guide the eyes and have no physical meaning. 176
- Figure 130.** Proton conductivity measured at 100 % RH for pure Si-MCM-41 (■), 40 % Imi-MCM-41 (■), 30 % PO₃H₂-MCM-41 (■) and 40 % SO₃H-MCM-41 (■) compared to Nafion measured under the same conditions (●) running dry. The lines are only to guide the eyes and have no physical meaning. 177
- Figure 131.** SEM and HRTEM images of Si-MCM-41 nanoparticles after 10 % (a and b) and 20 % (c and d) co-condensation. 179
- Figure 132.** High-resolution SEM (HRSEM) images of SH functionalized mesoporous Si-MCM-41 nanoparticles by pre-hydrolysis strategy after template extraction. 180
- Figure 133.** XRD patterns for pure nano-Si-MCM-41 (black) compared to 10 % (brown) and 20 % (red) nano-SO₃H-MCM-41. 181
- Figure 134.** Nitrogen adsorption isotherms for pure nano-Si-MCM-41 (black) compared to 10 % (brown) and 20 % (red) nano-SO₃H-MCM-41. 182
- Figure 135.** TEM images and FFT calculation for 20 % nano-SO₃H-MCM-41. 183

- Figure 136.** EDX spectrum of 20 % nano-SO₃H-MCM-41. 184
- Figure 137.** EEL spectrum of 20 % nano-SO₃H-MCM-41. 184
- Figure 138.** Proton conductivities under 100 % RH for 10 % (●) and 20 % (●) nano-SO₃H-MCM-41. The lines are only to guide the eyes and have no physical meaning. 185
- Figure 139.** Comparison of the proton conductivities under 100 % RH after (a) 10 % co-condensation for 10 % nano-SO₃H-MCM-41 (●) and μm-SO₃H-MCM-41 (■); and after (b) 20 % co-condensation for 20 % nano-SO₃H-MCM-41 (●) and μm-SO₃H-MCM-41 (■) also compared to 30 % μm-SO₃H-MCM-41 (■). The lines are only to guide the eyes and have no physical meaning. 186
- Figure 140.** Comparison of the proton conductivities under 100 % RH of 20 % nano-SO₃H-MCM-41 (■, IEC 1.78 mmol/g) to SO₃H functionalized Aerosil[®] (■, IEC 1.45 mmol/g) and 20 % μm-SO₃H-MCM-41 (■, IEC 1.6 mmol/g). The lines are only to guide the eyes and have no physical meaning. 187
- Figure 141.** Comparison of activation energies of 20 % nano-SO₃H-MCM-41 (■, IEC 1.78 mmol/g) to SO₃H functionalized Aerosil[®] (■, IEC 1.45 mmol/g) and 20 % μm-SO₃H-MCM-41 (■, IEC 1.6 mmol/g). 188
- Figure 142.** SEM micrographs of particle free polysiloxane membrane (a) and 17.1 wt.-% SO₃H-MCM-41 particle containing polysiloxane composite membrane (b)... 191
- Figure 143.** Water adsorption isotherms of polysiloxane composite membranes containing 17.1 wt.-% Si-MCM-41 (■) or SO₃H-MCM-41 (■), compared to pure polysiloxane membrane (■). 192
- Figure 144.** TG analysis of composite membranes of polysiloxanes containing unfunctionalized Si-MCM-41 (green), SO₃H functionalized Si-MCM-41 (blue) compared to pure polysiloxane membranes (black) and Nafion[®] 117 (red). 193
- Figure 145.** Proton conductivities measured under decreasing RH (●) of composite membranes of polysiloxanes with 9.6 wt.-% Si-MCM-41 (■), 9.6 wt.-% SO₃H-MCM-41 (■) and 17.1 wt.-% SO₃H-MCM-41 (■) compared to pure polysiloxane membrane (■) and Nafion[®] (■). The lines are only to guide the eyes and have no physical meaning. 194
- Figure 146.** Scheme of a MEA prepared with polysiloxane-MCM-41 composite membrane. The black layers represent the electrocatalyst, and the thin beige layer depicts the polyetheretherketone fleece. In between, the composite membrane is shown. 196
- Figure 147.** Polarization curves of prepared MEAs of Si-MCM-41 containing polysiloxane composite membranes. 197
- Figure 148.** SEM images of polyoxadiazole-SO₃H-MCM-41 composite membrane with cross-section (right). 199
- Figure 149.** Ionic conductivity of pristine polyoxadiazole membrane (■) and composite membrane with SO₃H-MCM-41 (■) as a function of relative humidity measured at 120°C. The lines are only to guide the eyes and have no physical meaning. 199
- Figure 150.** H₂ permeation through a functionalized silica polyoxadiazole composite membrane (5 wt.-%). 200

Figure 151. Trace of $\tan \delta$ vs. temperature as measured by DMTA at 1 Hz for the nanocomposite containing 2.5 wt.-% (■) or 5 wt.-% (■) sulfonated mesoporous silica, compared to the pure polymer (■).	202
Figure 152. TGA curve for the polyoxadiazole nanocomposite membranes containing 2.5 wt.-% (red), 5 wt.-% (green) and 10 wt.-% (blue) SO ₃ H-MCM-41 compared to the pure polyoxadiazole (black).	203
Figure 153. SEM images of composite membranes of Nafion [®] with SO ₃ H-MCM-41, right: cross-section of the approx. 20 μm thin composite membrane.	204
Figure 154. Proton conductivities of pure Nafion [®] (■) compared to composite membranes containing pristine Si-MCM-41 (■) and SO ₃ H-MCM-41 (■). The lines are only to guide the eyes and have no physical meaning.	205

C Tables

Table 1. Anode and cathode reactions in different fuel cell types.	12
Table 2. Nanoporous materials following IUPAC. ⁸⁷	40
Table 3. Functionalization chemicals used for grafting.	92
Table 4. Functionalization chemicals used for co-condensation.	94
Table 5. Structural data of Si-MCM-41.	106
Table 6. Lattice values of Si-MCM-41 after detemplation.	108
Table 7. Structural data of Si-SBA-15.	112
Table 8. Structural data of Si-SBA-16.	115
Table 9. Structural data of nano-Si-MCM-41.	117
Table 10. Structural data of peptide-imidazole functionalized Si-MCM-41 determined from nitrogen adsorption measurements.	147
Table 11. Structural data of imidazole functionalized Si-MCM-41 determined from nitrogen adsorption measurements.	152
Table 12. Structural properties of nanosized functionalized silica materials.	182
Table 13. Results of dynamic mechanical thermal analysis of polyoxadiazole-nanocomposite containing SO ₃ H-MCM-41.	201

D Chemicals

Name	Producer	Purity	CAS-No.
APTES	Merck	> 99 %	[919-30-2]
ammonia	Sigma-Aldrich	7N in methanol	[7664-41-7]
CITMS	Merck	> 98 %	[2530-87-2]
CTAB	Sigma-Aldrich	99 %	[57-09-0]
DCC	Merck	≥ 99 %	[538-75-0]
DCM, water free	Sigma-Aldrich	99.8 %	[75-09-2]
DPTES	ABCR	95 %	[757-44-8]
ethanol	Roth	99.8 %	[64-17-5]
ethyl acetate	Fluka	> 99.5 %	[141-78-6]
glyoxal	Sigma-Aldrich	40 % in water	[107-22-2]
hydrogen peroxide	Merck	30 %	[7722-84-1]
imidazole	Acros Organics	99 %	[288-32-4]
imidazole-2- carboxylic acid	Maybridge	97 %	[16042-25-4]
methanol	Roth	≥ 99.8 %	[67-56-1]
MPMS	Merck	≥ 95 %	[4420-74-0]
nitric acid	Roth	65 %	[7697-37-2]
Pluronic F127	Sigma-Aldrich	-	[9003-11-6]
Pluronic P123	BASF	-	-
sodium metasilicate	Sigma-Aldrich	-	[6834-92-0]
sulfuric acid	Acros Organics	96 %	[7664-93-9]
TEOS	Merck	> 98 %	[78-10-4]
TESBA	ABCR	90 %	[88276-92-0]
toluene	Riedel-de-Haën	99.7 %	[108-88-3]

E Publications arisen from this work

Journal Publications

- First Roland Marschall, Inga Bannat, Jürgen Caro, Michael Wark
“Proton conductivity of sulfonic acid functionalized mesoporous materials”
Microporous Mesoporous Mater. 99 (2007) 190.
- Second Roland Marschall, Michael Wark, Michael Jeske, Michaela Wilhelm, Georg Grathwohl, Jürgen Caro
“Functionalized mesoporous materials used as proton conductive additives for high temperature PEM fuel cell membranes”
From zeolites to porous MOF materials – The 40th anniversary of international zeolite conference,
Stud. Surf. Sci. Catal. 170, Part B (2007) 1540.
- Third Roland Marschall, Jiří Rathouský, Michael Wark
“Ordered functionalized silica materials with high proton conductivity”
Chem. Mater. 19 (2007) 6401.
- Fourth Rouven Scheffler, Andreas Huth, Gerold Hübner, Roland Marschall, Jürgen Caro, Michael Wark
“Präparation und Evaluation neuer Hybrid-Protonenleiter, Teil 2: Anorganische Nanoteilchen als Modifikator in Nafion-Hybridmembranen”
Chem. Ing. Tech. 79 (2007) 2035.
- Fifth Michaela Wilhelm, Michael Jeske, Roland Marschall, Welch Cavalcanti, Pia Tölle, Christof Köhler, Dietmar Koch, Thomas Frauenheim, Georg Grathwohl, Jürgen Caro, Michael Wark
“New proton conducting hybrid membranes for HT-PEMFC systems based on polysiloxanes and SO₃H functionalized mesoporous Si-MCM-41 particles”
J. Membr. Sci., (2008), in press.

-
- Sixth Roland Marschall, Jiří Rathouský, Michaela Wilhelm, Michael Wark
“Textural investigations of highly proton conductive functionalized mesoporous SiO₂”
Proceedings of the symposium NANOPOROUS MATERIALS-V, World Scientific Publishing, Singapore, (2008), in press.
- Seventh Welch L. Cavalcanti, Roland Marschall, Pia Tölle, Christof Köhler, Michael Wark, Thomas Frauenheim
“Insight into proton conduction of immobilized imidazole systems via simulations and impedance spectroscopy”
Fuel Cells, (2008), accepted.
- Eighth Dominique Gomes, Roland Marschall, Suzana P. Nunes, Michael Wark
“Development of Polyoxadiazole Nanocomposites for High Temperature Polymer Electrolyte Membrane Fuel Cells”
J. Membr. Sci., (2008), submitted.
- Ninth Roland Marschall, Welch L. Cavalcanti, Pia Toelle, Michaela Wilhelm, Christof Köhler, Thomas Frauenheim, Michael Wark
“Simulation and synthesis of highly proton conductive sulfonic acid functionalized mesoporous materials”
J. Am. Chem. Soc., (2008), submitted.
- Tenth Roland Marschall, Inga Bannat, Lianzhou Wang, Gao Qing (Max) Lu, Michael Wark
“Nanoparticles of mesoporous functionalized Si-MCM-41 with superior proton conductivity”
Chem. Commun. (2008), submitted.

Posters

- First Roland Marschall, Jiří Rathouský, Michael Wark, Jürgen Caro
“Mesoporous silica modified with sulfonic acid functionalities by grafting or co-condensation: effect on the proton conductivity“
2nd Workshop on IN-Situ Study and DEvelopment of Processes Involving PORous Solids, INSIDE POREs,
24.02.2007-28.02.2007, Thessaloniki.
- Second Roland Marschall, Michael Wark, Michael Jeske, Michaela Wilhelm, Georg Grathwohl, Jürgen Caro
“Functionalized mesoporous materials used as proton conductive additives for high temperature PEM fuel cell membranes”
15th International Zeolite Conference in Peking,
12.08.2007-17.08.2007.
- Third Roland Marschall, Michael Wark, Jürgen Caro
“Modified mesoporous silica: Inorganic proton conductors as additives for fuel cell membranes application”
EUROMAT 2007, 10.09.2007-13.09.2007, Nürnberg.
- Fourth Roland Marschall, Michael Wark, Michael Jeske, Michaela Wilhelm, Georg Grathwohl, Jürgen Caro
“Functionalized mesoporous materials used as proton conductive additives for high temperature PEM fuel cell membranes”
Nanoday 2007, 27.09.2007, Hannover.
- Fifth Roland Marschall, Michael Wark, Jürgen Caro
“Sulfonic acid and imidazole functionalized ordered mesoporous oxides as additives for new hybrid membranes in HT-PEMFC applications”
CARISMA workshop, 12.11.2007-14.11.2007, Stuttgart.
- Sixth Roland Marschall, Lianzhou Wang, Gao Qing (Max) Lu, Michael Wark
“Mesoporous silica (nano-)particles modified with sulfonic acid or imidazole functionalities by grafting or co-condensation: determination of proton conductivity properties
20. Deutsche Zeolith-Tagung, 05.03.2008-07.03.2008, Halle (Saale).

Talks on Conferences

- 20/03/2006 1st Workshop on IN-Situ Study and DEvelopment of Processes
Involving PORous Solids INSIDE POReS,
La Grande Motte, France
“Functionalized mesoporous materials for electrochemical
application”
- 07/03/2007 19th German Zeolite Conference, Leipzig, Germany
“Mesoporous silica modified with sulfonic acid functionalities by
grafting or co-condensation: effect on the proton conductivity”

F Curriculum vitae

Personal data

Name:	Roland Marschall
Date of birth:	24.05.1980
Place of birth:	Hannover
Family status:	single

School education

08/1986 – 07/1990	Gebrüder-Grimm-Grundschule Letter, Seelze
08/1990 – 07/1992	Erich-Kästner-Orientierungsstufe Letter, Seelze
08/1992 – 05/1999	Georg-Büchner-Gymnasium Letter, Seelze
05/1999	general qualification for university entrance (Abitur, excellent/sehr gut)

Military service

11/1999 – 08/2000	Panzergranadierbataillon 323, Schwanewede, Germany Basic military service
-------------------	--

University education

10/2000 - 04/2005	University of Hannover, Germany <i>Student of chemistry</i>
04/2005	University of Hannover, Germany Diplom Chemie (excellent, sehr gut) Study focus: Physical Chemistry Master thesis: "Evaluation of Dye-sensitized Solar Cells", supervisors: Dr. Torsten Oekermann, Prof. Dr. Jürgen Caro, On behalf of VOLKSWAGEN AG

05/2005 - today
Leibniz University Hannover
PhD student in Physical Chemistry
PhD thesis on: "New solid proton conductors:
Functionalized mesoporous SiO₂ materials for application
in high temperature PEM fuel cell membranes"
Founded by the Ministry of Science and Culture,
Niedersachsen, Germany, Georg-Christoph-Lichtenberg-
scholarship
Supervisors: Prof. Dr. Michael Wark,
Prof. Dr. Jürgen Caro

Peronal scholarships / awards

since 05/2005
Graduate student in the Graduate Program:
"New Materials with Tailored Properties"
Georg-Christoph-Lichtenberg scholarship
Ministry of Science and Culture, Land Niedersachsen

Research visits

12/2006
J. Heyrovsky Institute for Physical Chemistry of the
Academy of Sciences of the Czech Republic in Prague
Topic: "Nitrogen adsorption of functionalized mesoporous
silica by co-condensation methods"
Research partner: Dr. Jiří Rathouský

03/2007 – 06/2007
ARC Centre of Excellence for Functional Nanomaterials,
Australian Institute for Bioengineering and
Nanotechnology AIBN, University of Queensland,
Brisbane, Australia
Topic: "Synthesis and functionalization of mesoporous
nanoparticles"
Research partner: Prof. Dr. Gao Qing (Max) Lu